ORNL/TM-10079

ornl

OAK RIDGE
NATIONAL
LABORATORY

MARTIN MARIETTA

Ceramic Technology for Advanced Heat Engines Project Semiannual Progress Report for Period October 1985 Through March 1986

Prepared for
U.S. Department of Energy
Assistant Secretary for Conservation and Renewable Energy
Office of Transportation Systems
Advanced Materials Development Program

OPERATED BY
MARTIN MARIETTA ENERGY SYSTEMS, INC.
FOR THE UNITED STATES
DEPARTMENT OF ENERGY

Printed in the United States of America. Available from
National Technical Information Service
U.S. Department of Commerce
5285 Port Royal Road, Springfield, Virginia 22161
NTIS price codes—Printed Copy: A17 Microfiche A01

ORNL/TM-10079

METALS AND CERAMICS DIVISION

CERAMIC TECHNOLOGY FOR ADVANCED HEAT ENGINES PROJECT SEMIANNUAL PROGRESS REPORT FOR PERIOD OCTOBER 1985 THROUGH MARCH 1986

D. R. Johnson
Project Manager

Date Published: August 1986

NOTICE: This document contains information of a preliminary nature. It is subject to revision or correction and therefore does not represent a final report.

Prepared for
U.S. Department of Energy
Assistant Secretary for Conservation and Renewable Energy
Office of Transportation Systems
Advanced Materials Development Program

Prepared by the
OAK RIDGE NATIONAL LABORATORY
Oak Ridge, Tennessee 37831
operated by
MARTIN MARIETTA ENERGY SYSTEMS, INC.
for the
U.S. DEPARTMENT OF ENERGY
under Contract No. DE-AC05-84OR21400

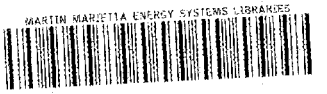

REPORTS PREVIOUSLY ISSUED

ORNL/TM-9325	Period March 1983–September 1983
ORNL/TM-9466	Period October 1983–March 1984
ORNL/TM-9497	Period April 1984–September 1984
ORNL/TM-9673	Period October 1984–March 1985
ORNL/TM-9947	Period April 1985–September 1985

CONTENTS

CERAMIC TECHNOLOGY FOR ADVANCED HEAT ENGINES PROJECT SEMIANNUAL PROGRESS REPORT FOR PERIOD OCTOBER 1985 THROUGH MARCH 1986

SUMMARY

The Ceramic Technology For Advanced Heat Engines Project was developed by the Department of Energy's Office of Transportation Systems (OTS) in Conservation and Renewable Energy. This project, part of the OTS's Advanced Materials Development Program, was developed to meet the ceramic technology requirements of the OTS's automotive technology programs.

Significant accomplishments in fabricating ceramic components for the Department of Energy (DOE), National Aeronautics and Space Administration (NASA), and Department of Defense (DOD) advanced heat engine programs have provided evidence that the operation of ceramic parts in high-temperature engine environments is feasible. However, these programs have also demonstrated that additional research is needed in materials and processing development, design methodology, and data base and life prediction before industry will have a sufficient technology base from which to produce reliable cost-effective ceramic engine components commercially.

An assessment of needs was completed, and a five-year project plan was developed with extensive input from private industry. The objective of the project is to develop the industrial technology base required for reliable ceramics for application in advanced automotive heat engines. The project approach includes determining the mechanisms controlling reliability, improving processes for fabricating existing ceramics, developing new materials with increased reliability, and testing these materials in simulated engine environments to confirm reliability. Although this is a generic materials project, the focus is on structural ceramics for advanced gas turbine and diesel engines, ceramic bearings and attachments, and ceramic coatings for thermal barrier and wear applications in these engines. This advanced materials technology is being developed in parallel and close coordination with the ongoing DOE and industry proof-of-concept engine development programs. To facilitate the rapid transfer of this technology to U.S. industry, the major portion of the work is being done in the ceramic industry, with technological support from government laboratories, other industrial laboratories, and universities.

This project is managed by ORNL for the Office of Transportation Systems, Heat Engine Propulsion Division, and is closely coordinated with complementary ceramics tasks funded by other DOE offices, NASA, DOD, and industry. A joint DOE and NASA technical plan has been established, with DOE focus on automotive applications and NASA focus on aerospace applications. A common work breakdown structure (WBS) was developed to facilitate coordination. The work described in this report is organized according to the following WBS project elements:

0.0 Management and Coordination

1.0 Materials and Processing

- 1.1 Monolithics
- 1.2 Ceramic Composites
- 1.3 Thermal and Wear Coatings
- 1.4 Joining

2.0 Materials Design Methodology

- 2.1 Modeling
- 2.2 Contact Interfaces
- 2.3 New Concepts

3.0 Data Base and Life Prediction

- 3.1 Structural Qualification
- 3.2 Time-Dependent Behavior
- 3.3 Environmental Effects
- 3.4 Fracture Mechanics
- 3.5 NDE Development

4.0 Technology Transfer

This report includes contributions from all currently active project participants. The contributions are arranged according to the WBS outline.

0.0 PROJECT MANAGEMENT AND COORDINATION

D. R. Johnson
Oak Ridge National Laboratory

Objective/scope

This task includes the technical management of the project in accordance with the project plans and management plan approved by the Department of Energy (DOE) Oak Ridge Operations Office (ORO) and the Office of Transportation Systems. This task includes preparation of annual field task proposals, initiation and management of subcontracts and interagency agreements, and management of ORNL technical tasks. Monthly management reports and bimonthly reports are provided to DOE; highlights and semiannual technical reports are provided to DOE and program participants. In addition, the program is coordinated with interfacing programs sponsored by other DOE offices and federal agencies, including the National Aeronautics and Space Administration (NASA) and the Department of Defense (DOD). This coordination is accomplished by participation in bimonthly DOE and NASA joint management meetings, annual interagency heat engine ceramics coordination meetings, DOE contractor coordination meetings, and DOE Energy Materials Coordinating Committee (EMaCC) meetings, as well as special coordination meetings.

Technical progress

During this reporting period ten research contracts were signed. In addition, formal coordination and/or review meetings were held as listed in Table 1.

Table 1. Formal coordination or review meetings involving the Ceramic Technology Project

Agency	Dates of meetings
Department of Energy (sponsor)	10/21 to 10/25; 10/31; 1/15; 2/20
Department of Energy (other programs)	10/11; 3/13 to 3/14
National Aeronautics and Space Administration	12/3; 12/10; 3/6
Defense Advanced Research Projects Agency	10/7 to 10/9
Department of Commerce	3/19
National Academy of Science/ National Materials Advisory Board	11/12
International groups	
IEA working group[a]	1/19

[a]Working group for the International Energy Agency's Annex II - Cooperative Programme On Ceramics For Advanced Engines and Other Conservation Applications.

1.0 MATERIALS AND PROCESSING

INTRODUCTION

This portion of the project is identified as project element 1.0 within the work breakdown structure (WBS). It contains four subelements: (1) Monolithics, (2) Ceramic Composites, (3) Thermal and Wear Coatings, and (4) Joining. Ceramic research conducted within the Monolithics subelement currently includes work activities on green state ceramic fabrication, characterization, and densification and on structural, mechanical, and physical properties of these ceramics. Research conducted within the Ceramic Composites subelement currently includes silicon carbide and oxide-based composites, which, in addition to the work activities cited for Monolithics, include fiber synthesis and characterization. Research conducted in the Thermal and Wear Coatings subelement is currently limited to oxide-base coatings and involves coating synthesis, characterization, and determination of the mechanical and physical properties of the coatings. Research conducted in the Joining subelement currently includes studies of processes to produce strong stable joints between zirconia ceramics and iron-base alloys.

A major objective of the research in the Materials and Processing project element is to systematically advance the understanding of the relationships between ceramic raw materials such as powders and reactant gases, the processing variables involved in producing the ceramic materials, and the resultant microstructures and physical and mechanical properties of the ceramic materials. Success in meeting this objective will provide U.S. companies with new or improved ways for producing economical highly reliable ceramic components for advanced heat engines.

1.1 MONOLITHICS

1.1.1 Silicon Carbide

Synthesis of High-Purity Sinterable Silicon Carbide Powders

J. M. Halstead, V. Venkateswaran [SOHIO Engineered Materials Company (Carborundum)] and B. L. Mehosky (SOHIO Research and Development)

Objective/Scope

The objective of this program is to develop a volume scaleable process to produce high purity, high surface area sinterable silicon carbide powder.

The program is organized in two phases. Phase I includes the following elements:

- Verify the technical feasibility of the gas phase synthesis route.
- Identify the best silicon feedstock on the basis of performance and cost.
- Optimize the production process at the bench scale.
- Fully characterize the powders produced and compare with commercially available alternatives.
- Develop a theoretical model to assist in understanding the synthesis process, optimization of operating conditions and scale-up.

Phase II, when authorized, will scale the process to 5 - 10 times the bench scale quantities in order to perform confirmatory experiments, produce process flowsheets and to perform economic analysis.

Technical Highlights

Background - The Gas Phase Synthesis Route

Given the objective of producing a submicron silicon carbide powder purer and with more controllable properties than could be produced via the Acheson process, Standard Oil-Carborundum evaluated three candidate process routes:

1) Sol-Gel
2) Polymer Pyrolysis
3) Gas Phase Reactions

A gas phase route utilizing plasma heating was chosen as having the most proven technology, the highest product yield and good scaleability potential.

Further, Carborundum had previously sponsored proprietary research in gas phase synthesis and had demonstrated the feasibility of the approach.

Workplan

A breakdown of major tasks and milestones is shown in Figure 1. Subtasks have been developed for Task 4 - Screening Experiments and will be developed for Task 5 - Extended Parametric Studies.

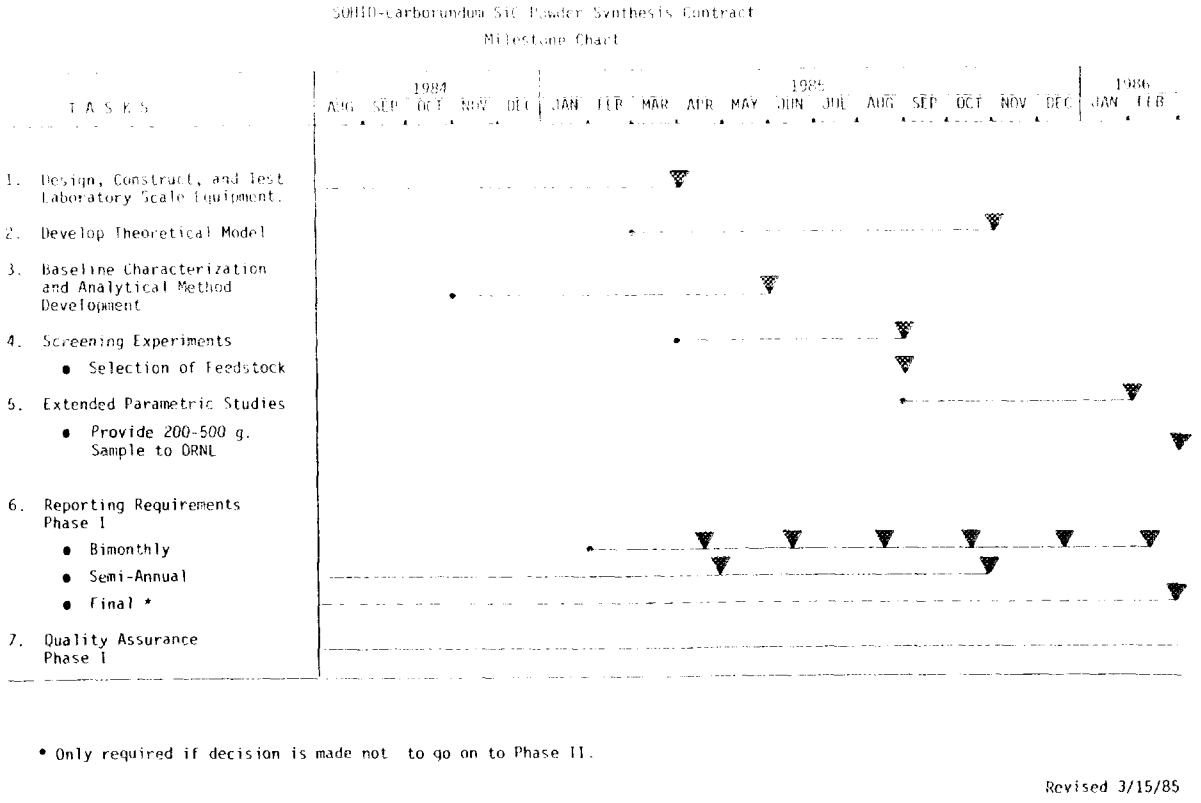

Figure 1. Milestone Chart

**ORNL has granted a no-cost extension of Phase I thru May 31, 1986.

Task 1. Design, Construct and Test Laboratory Scale Equipment

The Standard Oil Research and Development Center at Warrensville, Ohio was chosen as the site for the laboratory scale gas phase synthesis system due to the ready availability of applicable engineering and technical resources. The proximity to other related research which is being performed by Standard Oil on behalf of Standard Oil-Carborundum's structural ceramics effort was also a factor.

The design phase involved a complete review of the preliminary conceptual design and specifying appropriate subsystems in order to evaluate and control critical process parameters.

The conceptual design is shown in figure 1, a photographic overview is shown in figure 2.

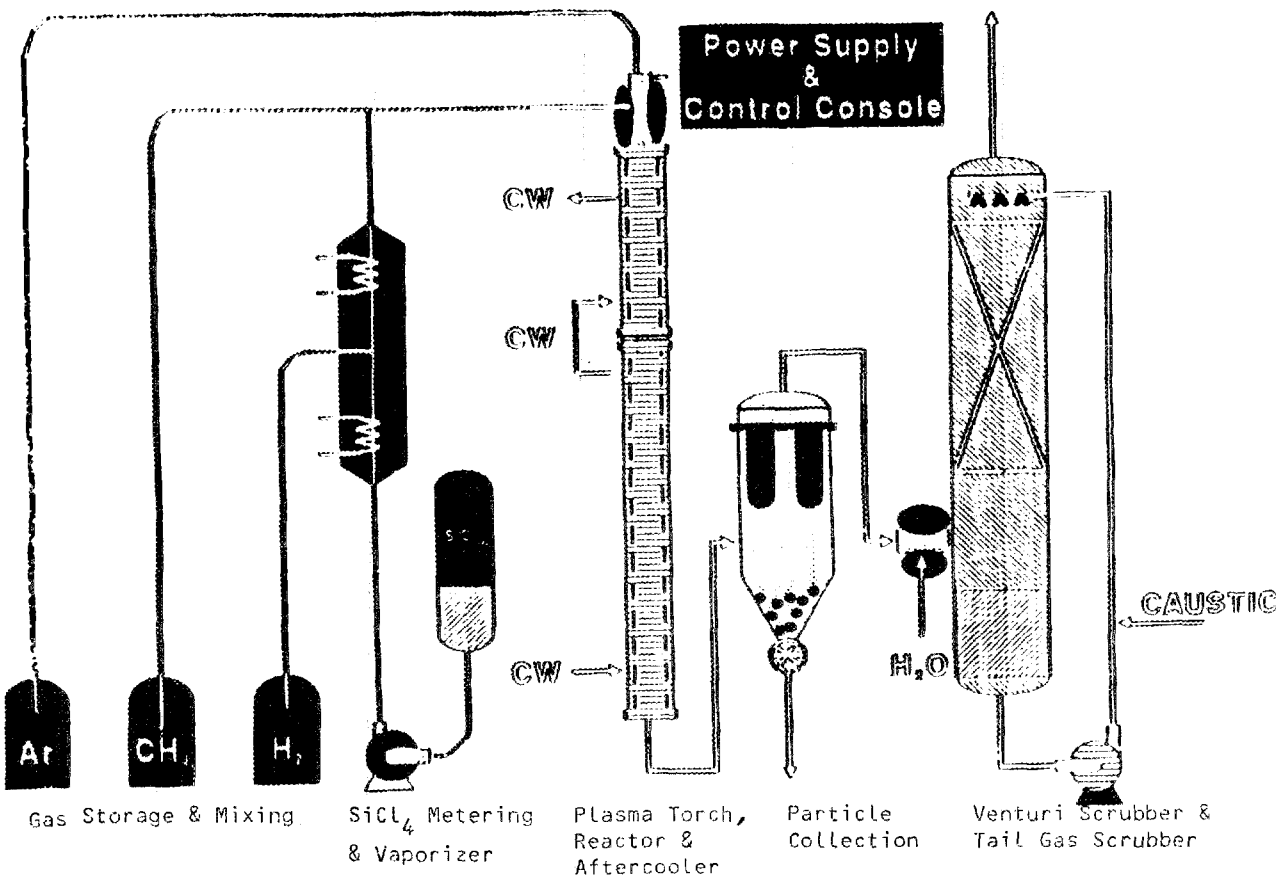

Figure 2. Conceptual Design and Simplified Process Flow Chart

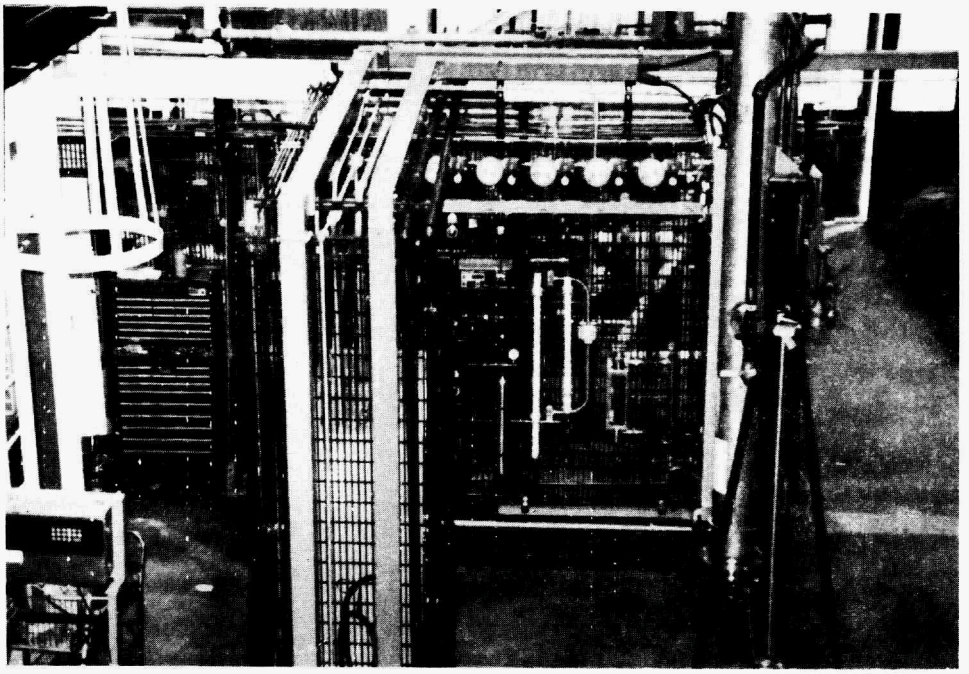

Figure 3. Photographic Overview of Laboratory Scale System

Plasma Torch Subsystem

The heart of the system is the plasma torch. This was obtained from Plasma Materials, Inc. with whom Standard Oil-Carborundum has previously worked. The torch system is rated at 50KW. This is significantly higher than required for this application, but the unit has excellent turn-down capability and will be sufficient for future scale-up. It is installed atop the reactor vessel which is constructed of copper and wrapped with copper tubing through which the cooling water flows. Thermocouples are installed along the entire length of the reactor. The plasma torch subsystem is shown in figures 3 and 4.

The DC power supply has a 75KW effective rating. A simple thimble type collector with an isolation valve is affixed to the lower end of the reactor. Alternative powder collection techniques will be evaluated in preparation for Phase II scale-up.

Task 2. Development of a Theoretical Model

The development of a theoretical model was intended to correlate particle surface area with major operational parameters. An expansion of previous Carborundum sponsored work, this developed a fundamental understanding of process reactions and will assist in the extended parametric studies and scale-up tasks.

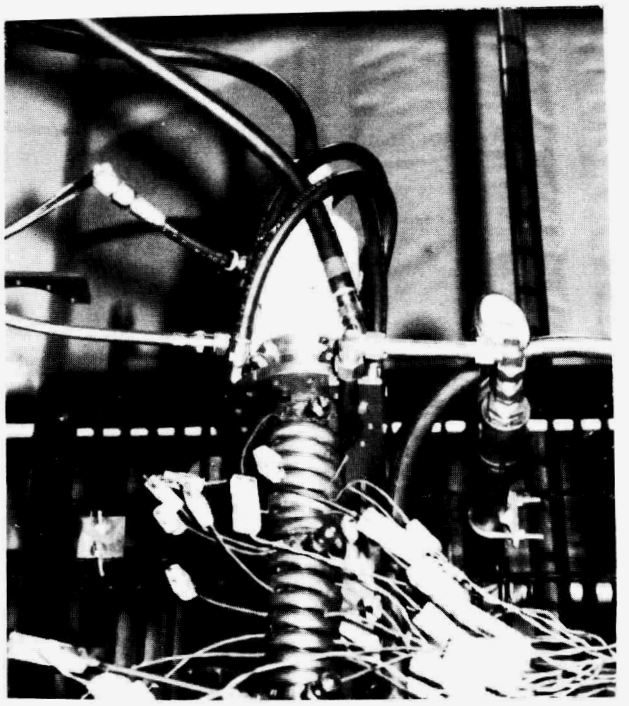

Figure 4. Plasma Torch Atop Water Cooled Reactor

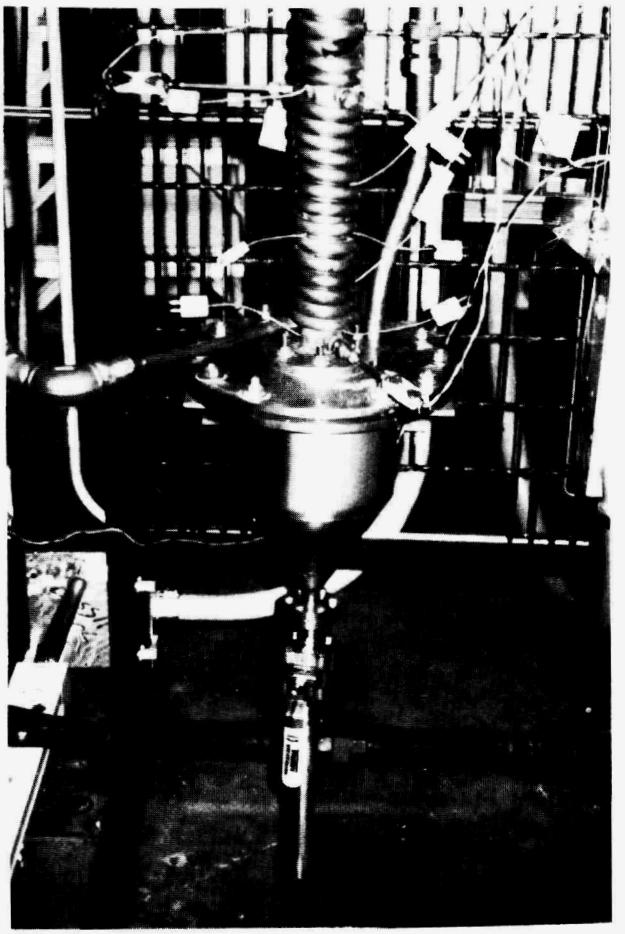

Figure 5. Exit End of Reactor with Simple Thimble Collector and Isolation Valve

After consultation with the ORNL Technical Monitor, the modeling work was subcontracted to International Thermal Plasma Engineering, Inc. (Professor Boulous - University of Sherbrooke, Quebec, Canada, et al).

The model was developed in stages:

1) Development of a model to describe the flow and temperature field in the reactor.
2) The calculation of thermodynamic equilibrium for the H_2-Ar-CH_4-$SiCl_4$ system and the study of the chemical kinetics of possible homogenous reactions occuring in the plasma process.
3) A literature review of nucleation and growth in an aerosol system which could be of relevance to this work.

Although a turbulent model was initially developed to describe the flow in the reactor, the actual flow experienced at the present operating conditions was found to be laminar. This necessitated the development of a laminar flow based model. The turbulent model is used to describe the flow and temperature fields in the entrance region of the reactor (first 150mm) and thereafter the laminar code is used. Since a mixture of hydrogen and argon is used in the present reactor, the transport properties have been calculated using the rule of mixtures. The model is being calibrated using measured temperatures and then used in a predictive mode to describe temperature and flow fields obtained under a wide range of operating conditions.

A final report is now being prepared by the subcontractor.

Task 3. Baseline Characterization and Analytical Method Development

The objectives for this task included:

- .. Firmly establish the methodologies to be used for powder characterization.
- .. Define basic powder characteristics which may be utilized to assess property control and improvements as the program progresses.

Initially, two commercially produced SiC powders were to be characterized: H.C. Starck, Inc. (West Germany), A10 Grade; and Standard Oil-Carborundum submicron alpha SiC.

As both of the above powders were alpha phase, it was decided to characterize one beta phase powder in addition, Starck B-10 Grade.

The parameters characterized and the methodologies used include the following:

Characteristic	Methodology
..Pressureless sinterability	--Percentage of theoretical density achieved with and without sintering aids.
..Surface area	--B.E.T. surface analysis.
..Degree of agglomeration	--Tap density.
..Particle size distribution	--Horiba particle size analyzer.
..Bulk composition	--Wet chemistry
..Phase distribution	--X-ray diffraction.

The results of the baseline characterization of the three powders is as follows:

	Starck A10	Starck B10	Standard Oil-Carborundum
Pressureless Sinterability (percentage of theoretical density)			
-without sintering aids	63.6%	N/A	51.01%
-with sintering aids	96.2%	94.3%	99.88%
Surface Area	14.3m^2/g	15.35m^2/g	9.47m^2/g
Degree of Agglomeration -tap density	0.847 g/cm^3	0.926 g/cm^3	0.962 g/cm^3

Particle Size Distribution

Size µm	Cumulative Percentage greater than the indicated particle size: Starck A10	Starck B10	Standard Oil-Carborundum
>7	0	4.2	0
7-6	2.4	4.7	0.4
6-5	11.4	5.8	3.8
5-4	23.4	8.7	7.0
4-3	29.8	11.8	9.8
3-2	38.2	21.0	24.3
2.1.8	41.4	24.6	27.3
1.8-1.6	45.7	29.0	32.2
1.6-1.4	50.9	36.1	39.1
1.4-1.2	58.0	43.2	49.9
1.2-1.0	66.4	49.2	65.4
1.0-0.8	68.2	61.5	67.1
0.8-0.6	76.7	69.9	76.2
0.6-0.4	85.7	84.0	87.9
0.4-0.2	97.2	97.4	97.7
0.2-0	100.0	100.0	100.0
-Mean Particle Size (d_{50})	1.4µm	1.0µm	1.2µm

Bulk Composition	Starck A10	Starck B10	Standard Oil-Carborundum
Chemical Analysis (wt %)			
Total Carbon	30.3	30.49	29.95
Free Carbon (corrected for oxidation)	1.54	1.83	0.36
Total Oxygen	0.76	0.90	0.27
Free Silicon	0.29	0.40	0.09
Si + SiO_2	1.73	1.71	0.60
SiO_2 (calculated from O_2)	1.44	1.31	0.51
SiC (calculated)	96.10	95.70	98.80
Emission Spectroscopy (wt %)	Aluminum .01 Calcium<.01 Iron 0.03 Magnesium<.01 Titanium .01	Aluminum .07 Calcium<.01 Iron .04 Magnesium<.01 Titanium<.01 Vanadium<.01 Boron .02	Aluminum<.01 Calcium<.01 Iron<.01 Magnesium<.01 Titanium<.01 Vanadium<.01

	Starck A10	Starck B10	Standard Oil-Carborundum
Elements less than .005%	Boron Chromium Copper Manganese Nickel Zirconium Cobalt Molybdenum Vanadium	Chromium Manganese Zirconium	Boron Chromium Copper Manganese Nickel Zirconium Molybdenum
Phase Distribution			
Major	6H	3C	6H
Low Trace	15R/4H	6H	15R

Task 4. Screening Experiments

Task 4 was divided into subtasks for management and reporting purposes.

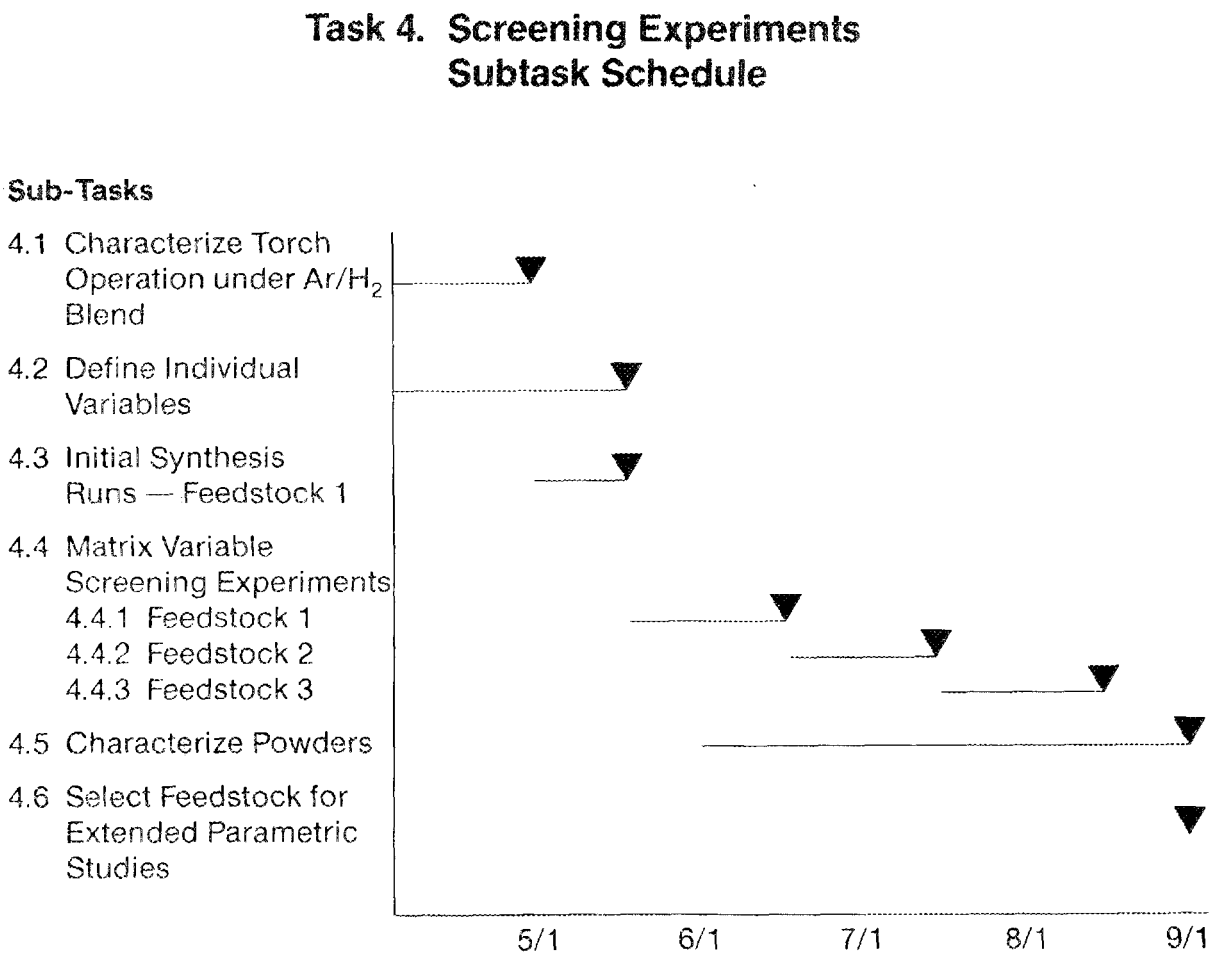

Figure 6. Subtask Schedule for Screening Experiments

The first subtask was to characterize the operation of the plasma torch using a hydrogen/argon blend. It should be noted that the original workscope included a short series of experiments to investigate the feasibility of using a hydrogen plasma in lieu of argon. This could be advantageous as hydrogen is a reactant (to scavenge chlorine from the silicon source) and the argon (necessary only as a carrier of energy) could potentially be reduced or eliminated.

As both Standard Oil-Carborundum and the torch vendor, Plasma Materials, Inc. were confident that the torch would operate with a very rich hydrogen to argon blend, it was decided to accomplish this subtask first.

Concurrent with that subtask, careful consideration was given to the choice of the individual variables for the screening experiments. The candidate feedstocks were described in the statement of work, but the values (or range of values) for temperature, carbon/silicon ratio and reactant concentration had to be established.

A matrix of screening experiments was developed to incorporate two levels of each of the variables for each feedstock. The candidate feedstocks are as follows:

Reactant 1: silicon tetrachloride ($SiCl_4$)
Reactant 2: dimethyl dichlorosilane [$(CH_3)_2SiCl_2$]
Reactant 3: methyl trichlorosilane (CH_3SiCl_3)

Proposed Test Matrix: Screening Experiments

Reactant	Temperature	Carbon/Silicon Ratio	Reactant Concentration
Reactant 1	Hi	Hi	Hi
			Lo
		Lo	Hi
			Lo
	Lo	Hi	Hi
			Lo
		Lo	Hi
			Lo
Reactant 2	Hi	Hi	Hi
			Lo
		Lo	Hi
			Lo
	Lo	Hi	Hi
			Lo
		Lo	Hi
			Lo
Reactant 3	Hi	Hi	Hi
			Lo
		Lo	Hi
			Lo
	Lo	Hi	Hi
			Lo
		Lo	Hi
			Lo

Figure 7. Screening Experiment Test Matrix

Once the plasma torch had been stabilized on a very rich H_2/Ar blend, silicon feedstock ($SiCl_4$) and methane were added to the system. Several short runs were made and powder was produced. Analysis later proved the powder to be beta silicon carbide.

Several debugging problems occurred which aborted many of the initial runs. Some of these problems included the silicon feed pump, the tail gas scrubber level transducer and a cooling water leak into the plasma torch. All items were satisfactorily resolved.

The torch and reactor system also experienced plugging problems which limited run times; some as short as 5 minutes. Minor anode configuration changes were made which has since allowed runs up to 3 hours in duration. Although this problem has not been completely solved, the present configuration is capable of running long enough to accomplish the tasks planned for Phase I. Runs of approximately one hour duration have generated representative material in sufficient quantities for analysis.

At this point, the workplan called for the initiation of screening experiments; a matrix of 24 variations of temperature, carbon to silicon ratio and reactant concentration (defined as hydrogen to chlorine ratio). However, a priority was placed upon establishing the consistency and reproducibility of the process. The workplan was modified to first run four pre-screening experiments to establish a consistent baseline; then to prioritize the screening experiments (focusing primarily on feedstock one). Eight experiments (six of Feedstock 1 and two of Feedstock 2) were initially run and the results analyzed. Upon completion of the analytical results of those powders, the remainder of the matrix was completed.

Table 1 summarizes the results of the screening experiments. The prime determinants of the quality of the powders produced were: Percent SiC, Percent Free Carbon, and Percent Free Silicon.

Conclusions - Screening Experiments

Based on the results of the screening experiments, methyl trichlorosilane was chosen as the best feedstock to be carried forward to the parametric studies.

Though the other feedstocks may also be suitable, methyl trichlorosilane provided the widest operating window.

Task 5. Extended Parametric Studies

This task is intended to further evaluate the process parameters of the feedstock selected at the conclusion of the screening experiments: Methyl trichlorosilane. Among other parameters, silicon feedstock flow rate will be varied in order to evaluate the effect of residence time and the best conditions for scaling up the selected process.

Sixteen parametric studies have been planned and about three-fourths have been run. Once these are completed, a limited number of experiments with dopant additions will be run.

TABLE 1
SUMMARY OF THE CHEMISTRY OF POWDERS FROM SCREENING EXPERIMENTS

Silicon Feedstock	Matrix No.	Power kw	Si/C Ratio	H/Cl Ratio	% SiC*	% Free Carbon	% Free Silicon
Silicon Tetrachloride ($SiCl_4$)	1	20	1.2	20	81.4	2.89	1.33
	2	20	1.2	15	75.0	3.61	1.21
	3	20	1.0	20	43.9	3.51	3.63
	4	20	1.0	15	70.4	6.33	2.17
	5	17	1.2	20	70.4	6.03	2.46
	6	17	1.2	15	77.1	3.03	1.04
	7	17	1.0	20	66.6	3.00	1.30
	8	17	1.0	15	54.4	9.32	1.88
Dimethyl Dichlorosilane $\{(CH_3)_2SiCl_2\}$	9	20	1.2	20	46.8	3.52	8.38
	10	20	1.2	15	76.7	2.03	1.45
	11	20	1.0	20	90.9	0.60	0.24
	12	20	1.0	15	83.9	1.60	0.29
	13	20	0.5	20	91.2	3.20	0.16
	14	20	0.5	15	82.1	4.46	0.59
	15	N/A	N/A	N/A	N/A	N/A	N/A
	16	17	1.2	15	85.9	3.10	0.24
	17	N/A	N/A	N/A	N/A	N/A	N/A
	18	N/A	N/A	N/A	N/A	N/A	N/A
	19	N/A	N/A	N/A	N/A	N/A	N/A
	20	N/A	N/A	N/A	N/A	N/A	N/A
Methyl Trichlorosilane (CH_3Cl_3Si)	21	20	1.2	20	89.4	1.46	0.32
	22	20	1.2	15	92.9	1.21	0.28
	23	20	1.0	20	97.9	1.09	0.03
	24	20	1.0	15	81.3	3.23	0.49
	25	17	1.2	20	84.1	1.85	1.04
	26	17	1.2	15	83.0	1.98	0.75
	27	17	1.0	20	76.1	2.80	0.88
	28	17	1.0	15	87.6	1.99	0.54

*computed from total carbon and free carbon analysis

N/A - five experiments originally planned were not run, or did not produce sufficient powder for analysis.

One of the first activities for this task was to produce a substantial amount of powder by running methyl trichlorosilane at the best known conditions in order to perform some initial sinterability studies.

Approximately 80 grams of powder were produced, analyzed, and sintering trials were performed.

Analysis of the powder revealed very good chemistry:

Percent SiC	98.5
Percent Free Carbon	0.15
Percent Free Silicon	0.13

Sintering to 89% and 92% of theoretical density was achieved with normal sintering additives. Though sintering conditions for beta SiC powders have not been optimized; these initial results are considered to have established the ability to sinter the powder produced by this process. Photomicrographs of the sintered specimens are shown in Figure 8.

Subsequent to the chemical analysis of all the powders produced during the parametric studies; a large quantity of powder will be produced for a further sinterability tests and to provide a 200-500g sample to ORNL.

This will conclude Phase I on the contract.

Status of Milestones

Task 1.	Design, Construct and Test Laboratory Scale Equipment	- Complete
Task 2.	Develop Theoretical Model	- Complete
Task 3.	Baseline Characterization and Analytical Model Development	- Complete
Task 4.	Screening Experiments	- Complete
	.. Selection of Feedstock	- Complete
Task 5.	Extended Parametric Studies	- To be completed approximately April 30
	.. Provide 200-500g Sample to ORNL	- Scheduled for - May 31, 1986
Task 6.	Reporting Requirements	- On schedule
Task 7.	Quality Assurance	- Ongoing

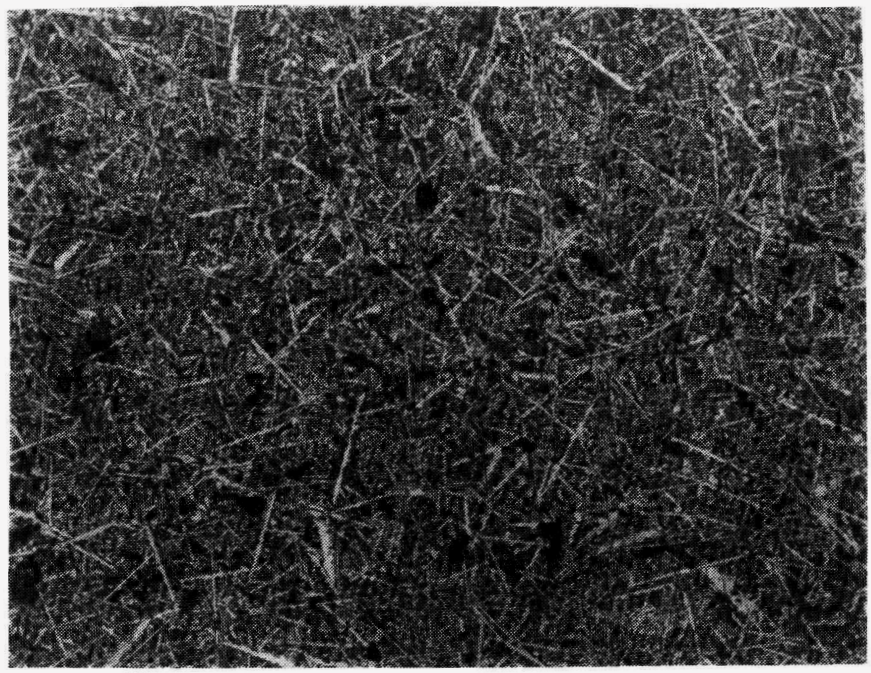

89% Theoretical Density

92% Theoretical Density

Figure 8. Photomicrographs of sintered speciments (200x)

1.1.2 Silicon Nitride

Sintering of Silicon Nitride
G. E. Gazza (Army Materials Technology Laboratory)

Objective/Scope:

The program is concentrating on sintering compositions in the Si3N4-Y2O3-SiO2 system using a two-step sintering method where the N2 gas pressure is raised to 7-8MPa during the second step of the process. During sintering, dissociation reactions are suppressed by the use of high N2 pressure and cover powder of suitable composition over the specimens. Variables in the program include the sintering process parameters, source of starting powders, milling media and time, and specimen composition. Resultant properties determined are room temperature modulus of rupture, high temperature stress-rupture, oxidation resistance, and fracture toughness. Successful densification of selected compositions with suitable properties will lead to densification of injected molded or slip cast components for engine testing.

Technical Progress:

Sintering studies are continuing to concentrate on compositions near the Si3N4-Y2Si2O7 join. Since the starting Si3N4 powders have oxygen contents in the range of 1.0-1.5%,the SiO2 content of the powder mixture must be increased to obtain the desired compositions. This can be accomplished by adding SiO2, such as Cabosil, and/or by oxidizing the powder at temperatures near 1000C and determining the increase in SiO2 from weight gain measurements. The starting Si3N4 powders principally being used in this study are Toyo-Soda (TS-7), UBE(SN-E-10), and KemaNord Siconide (P95). The surface area of the Toyo-Soda and UBE powders are approximately 12-13m2/g while the Siconide powder is 8m2/g.A higher surface area (12m2/g) Siconide powder, M-1246, will also be evaluated. Powders are milled in polyethylene or polypropylene jars using either Si3N4 or WC balls. The Si3N4 balls, obtained from ASEA, were fabricated by hot isostatic pressing. Milling times up to 100 hours are being studied. Milling criteria of primary concern are; using sufficient milling time to produce homogeneous mixing of the powders and controlling impurity pickup from the milling media. One source of contamination is the abrading of material from the milling jar by the milling balls into the powder. Impurity, such as polyethylene, should be removed from the powder before sintering. One method is to heat treat the powder at 600-700C in air after milling to eliminate the polyethylene and resultant carbon while not oxidizing the powder, i.e., not increasing the SiO2 content. Impurity from the milling balls themselves is more difficult to control. The use of high purity, HIPPED, Si3N4 balls with Y2O3 additive eliminates this problem for the compositions of interest in this study. Other milling media, such as WC, ZrO2, Y2O3, and Al2O3 have also been used to a certain extent. A limited evaluaton of Y2O3 milling media indicated that a non-uniform distribution of Y2O3 resulted in the powder being milled apparently due to the low abrasion resistance of the Y2O3 balls.

Al2O3 would appear to be satisfactory if Al2O3 containing compositions were being prepared. Inconclusive results were obtained with ZrO2. The use of WC media is being pursued further as its use appears to enhance densification of the powder compacts.The complete mechanism by which this occurs appears not to be fully defined. Also, there may be an upper limit on the amount of WC which can be incorporated into the powder without adversely affecting sintering or the resultant properties of the densified material.

Sintering of the cold pressed powder compacts is being performed in a covered RBSN crucible with the specimens embedded in cover powder. The cover powder is used to protect the specimens from the carbonaceous atmosphere (graphite heating elements are used in the furnace) and to suppress the formation of SiO, formed by the Si3N4+SiO2 reaction, at the specimen/cover powder interface. The cover powder typically consists of Si3N4 powder (usually from the same source as that being used in the compact to be sintered), Y2O3 and SiO2 powders with a Y2O3/SiO2 ratio near that of the compact composition, and BN (in the range of 25-40%). The specimen compositions being primarily studied are 85.5-86.5m/o Si3N4, 4.5-5.5m/o Y2O3, and 8.5-9.5m/o SiO2. The total amount of combined additive ranges from 8-13v/o. Sintering of Si3N4 with only Y2O3 and SiO2 as additives appears to require higher processing temperatures than when another additive, such as Al2O3, is also present. A problem associated with this is microstructural control. Figure 1 shows a microstructure of a sintered specimen containing 85.8m/o Si3N4-4.7m/o Y2O3-9.5m/o SiO2. The total volume percent additive is approximately 10-11%. The powder was milled with Si3N4 balls and the compact was sintered using the following schedule: 1960C for 75 min. under 2MPa N2 pressure, 1960C for 45 min. under 8MPa N2 pressure, 1200C for 60 min. under 7-8MPa N2 pressure. At 5000x magnification, both a-Si3N4 grains and second phase, principally Y2Si2O7, can be observed. The microstructure appears duplex with grains 2-3f diameter (many represent a cross-section of longer grains) and elongated grains,up to 25f long. The use of finer particle size, i.e., higher surface area, powders with a narrower size distribution should help produce more uniform microstructures. In Figure 2, an SEM photomicrograph (5000x) shows the microstructure produced by using WC milling media (approximately 1.3% WC incorporated into the starting powder estimated by weight loss of the milling balls) and using a sintering schedule of 1960C-75 min.-2MPa followed by 2000C-15 min.-8MPa. Some decomposition of the Si3N4 into Si has occurred. The dark black color associated with hot pressed or sintered Si3N4 is associated with the formation of free Si in the specimen.

Powder compacts have been scaled-up to 2" diameter x 0.385-0.5" thick for sintering in order to machine bars from them for determination of mechanical properties and oxidation resistance. Under proper sintering conditions, the density and weight change measured for the scaled-up compacts are similar to those values obtained for the smaller specimens.

Status of Milestones:

(a) Optimize process and composition----Sintering parameters and conditions have been established to the point where near full density can be achieved with various compositions in the area of interest in the phase diagram. One problem involves the use of Si_3N_4 powder with low oxygen content where more SiO_2 must be added to achieve the desired compositions. It is felt that a non-uniform distribution of SiO_2 occurs when a high volume of SiO_2 powder addition must be used. Pre-oxidation of powder compacts before sintering can alleviate this problem.

(b) Scale-up of compacts----Scale-up of specimens is being accomplished using powder compositions milled with Si_3N_4 balls or WC balls. High specimen densities have been obtained with both types of processed powders. Also, the use of recently obtained Si_3N_4 powder from Toyo-Soda and UBE are being primarily used as starting materials. Bars are being machined from the densified compacts for property evaluation, i.e., RT MOR and high temperature stress-rupture. Some bars are being evaluated for oxidation resistance at temperatures between 700C and 1250C.

(c) Mechanical property evaluation----Some properties at room temperature (MOR) and high temperature (1200C) stress-rupture have been generated and previously reported. MOR values ranged from 480 to 650MPa. Variability was caused by residual pores or pore clusters produced by binder removal in the "green" compact. Compacts are currently being formed without binder. The ability to withstand stress-rupture was influenced by crystallization treatments on the specimens. Oxidation rates at 1200C were found to be in the range of 10-12 to 10-13.

Publications

"Effect of Oxidation on the Densification of Sinterable RBSN", MTL TR86-1.

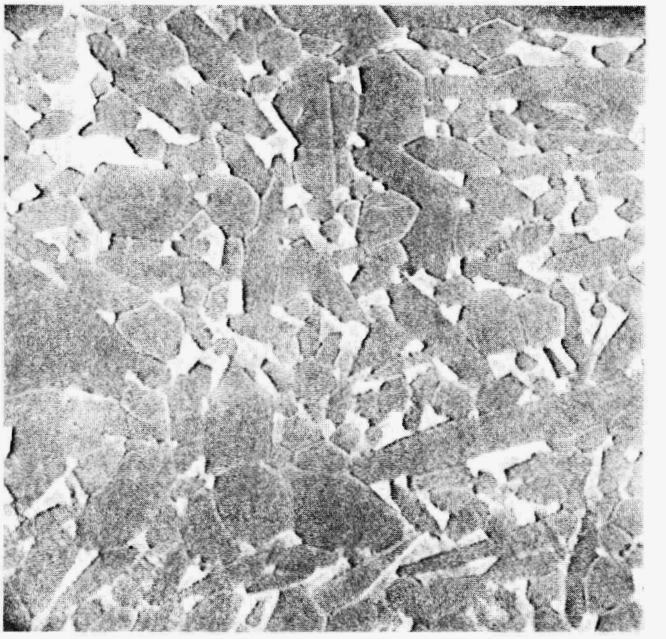

Figure 1 - Sintered Si_3N_4-7.8%Y_2O_3-1.3%SiO_2 composition showing two-phase, duplex microstructure (5000x). Powder milled with Si_3N_4 balls.

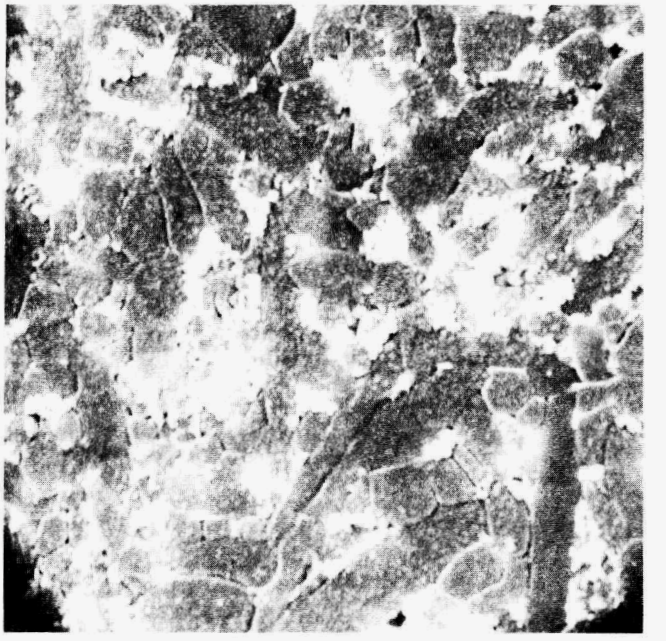

Figure 2-Microstructure of specimen of similar composition to that shown in Figure 1 except powder milled with WC balls and sintered at higher temperature (5000x).

Synthesis of High Purity Sinterable Si_3N_4 Powders

G. M. Crosbie (Ford Motor Company)

Objective/scope

The goal of this task is to achieve major improvements in the quantitative understanding of how to produce sinterable Si_3N_4 powders having highly controlled particle size, shape, surface area, impurity content and phase content. Through the availability of improved powders, new ceramic materials are expected to be developed to provide reliable and cost-effective structural ceramics for application in advanced heat engines.

Of interest to the present powder needs is a silicon nitride powder of high cation and anion purity without carbon residue.

The process study is directed towards a modification of the low temperature reaction of $SiCl_4$ with liquid NH_3 which is characterized 1) by absence of organics (a source of carbon contamination) and 2) by pressurization (for improved by-product extraction efficiency).

Technical progress

Si_3N_4 powder was produced with phase content, particle size and shape which are close to those characteristics considered desirable for pressureless sinterability. Specifically, the powder derived by thermal decomposition of an intermediate imide product (from reaction of $SiCl_4$ with liquid NH_3 at 0^oC and 75 psig) was principally alpha silicon nitride with particle size less than 1 micron and mostly equi-axed particle shape. A micrograph is shown as Figure 1.

By design, no organic diluent was present during the imide-forming reaction to control the silicon tetrachloride-ammonia reaction heat evolution. Instead, a non-reactive carrier gas was used to bring the $SiCl_4$ into contact with liquid ammonia. Consequently, contamination from organics contacting the amorphous imide is minimized.

An expected process feature (which is important for heat transfer scalability) has been supported by observations while running the reaction with the carrier gas diluent. For the operating conditions used in making the above alpha Si_3N_4, we have observed an overall endothermic reactor heat for the imide intermediate synthesis. In operation, in an ice bath, layers of ice built up on the reactor zone. An overall endotherm is predicted by an approximate thermodynamic model for these conditions. In this model, the (exothermic) heat

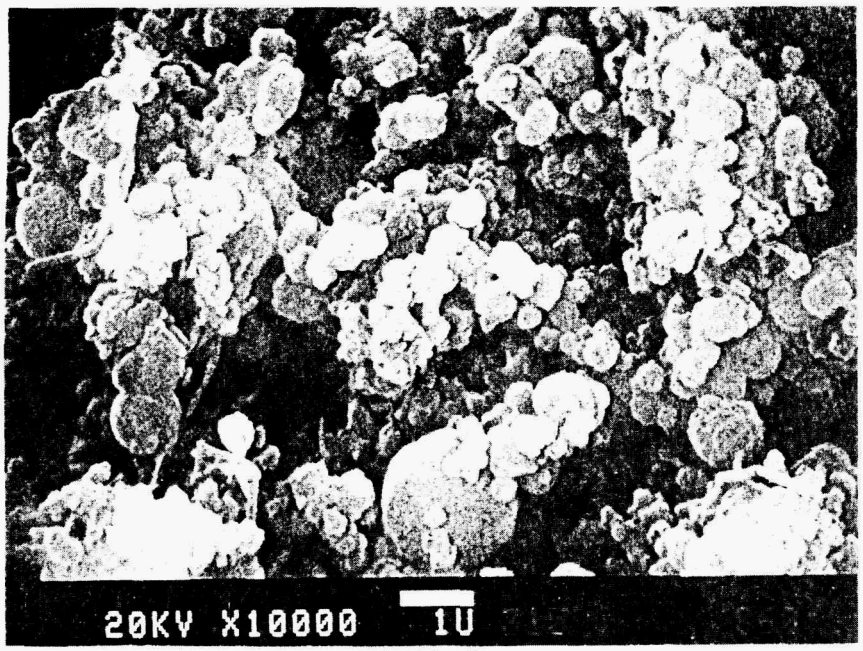

Figure 1. Scanning electron micrograph of powder produced. By x-ray diffraction, the major phase is alpha-Si_3N_4 with Si_2N_2O detected.

of the chloride-ammonia reaction is more than offset (at 0^oC) by the latent heat of vaporization of NH_3 into the residual carrier gas. Potential scalability problems related to heat transfer can therefore be minimized.

Earlier in this period, the imide reactor was assembled, pressure tested, and used with liquid ammonia alone. Various apparatus design modifications were carried out. Operating sequence checklists were prepared and computer programs were implemented for multiple-access logging of temperatures, flows, and operator actions.

As part of the process flowsheeting task requirements, a diagram was prepared from photographs of the pressurized $SiCl_4$-NH_3 reactor apparatus. The diagram has also been adapted for an operator's console display with an overlay of continually updated readouts of temperatures and flows at various locations.

A design was implemented (and subsequently upgraded) for transfer of the air-sensitive imide solids. The imide-containing slurry was produced by the reaction of $SiCl_4$ with liquid ammonia. In the present equipment, the slurry is stored in a pressure vessel after low-temperature synthesis. The imide-ammonia slurry is transferred to a controlled atmosphere furnace. The anaerobic transfer is accomplished with a pressure differential and a volume expansion on boiling of NH_3. A workable degree of pressure control has been achieved by valving to limit the maximum NH_3 volume on each unit transferred.

The following table summarizes considerations for operation of a process with silicon imide synthesis under pressure:

Advantages:
.Benefits of operating temperature closer to ambient (greater by-product solubility, lower thermal gradients and lower unit cooling costs)
.Pressurization keeps impurities out in spite of any trace leaks
.NH_3 engineering pressure data are available (material compatibilities, safety stds, from refrigeration eng'g)

Disadvantages:
.System complexity increased (for air-sensitive reactants and products, special transfer methods are needed)
.Reduced visibility as glass apparatus cannot be used
.Hazards of handling corrosive liquids heightened under pressure

Status of milestones

The milestone "complete construction and commission synthesis equipment" for December 1985 has been met on time in this semi-annual report period. The following milestones are on schedule for this program:

Complete process flow sheet analysis	April 1986
Demonstration of sinterability of synthesized Si_3N_4 powder	July 1986
Demonstration of proof of scalability	November 1986
Complete draft technical report describing the process	March 1987

Publications

G. M. Crosbie, "Synthesis of High Purity Sinterable Powder Si_3N_4," manuscript submitted for Post-Conference Proceedings of the 1985 Automotive Technology Development Contractors' Coordination Meeting.

G. M. Crosbie, "Preparation of Silicon Nitride Powders," presented at the 13th Automotive Materials Conference ("Processing of Automotive Ceramics"), November 6-7, 1985, Ann Arbor, Michigan. (Conference sponsored by the Michigan Section of the American Ceramic Society and the University of Michigan.)

G. M. Crosbie, "Silicon Nitride Synthesis -- A Progress Report," abstract submitted for presentation at the American Ceramic Society Annual Meeting, April 27 - May 1, 1986, Chicago, Illinois.

G. M. Crosbie, "Preparation of Silicon Nitride Powders," manuscript submitted for publication in the conference proceedings of the 13th Automotive Materials Conference (Processing of Automotive Ceramics), November 6-7, 1985, Ann Arbor, Michigan.

1.2 CERAMIC COMPOSITES

1.2.2 Silicon Nitride Matrix

Transformation-Toughened Silicon Nitride

H. W. Carpenter (Rocketdyne Division, Rockwell International) and
F. F. Lange (Rockwell Science Center)

Objective/scope

The objective of this program is to develop high toughness, high strength refractory ceramic matrix composites that can be made at low cost and to near net shape for heat engine applications. The composite system selected for development is based on a silicon nitride matrix toughened by dispersions of ZrO_2, HfO_2, or $(Hf,Zr)O_2$ modified with suitable additions of other refractory ceramics to control the physical behavior. The desired microstructure and optimum mechanical properties will be developed by expeditious laboratory methods including colloidal suspension, press forming, sintering, and hot pressing. Once the best composition and microstructure have been demonstrated, parameters will be optimized for producing samples by the injection molding process.

Technical progress

Y_2O_3-Stabilized ZrO_2 Dispersoids - The intent of this initial study is to retain a transformable form of tetragonal ZrO_2 in the Si_3N_4 matrix that will significantly toughen the composite material by a martensitic transformation mechanism without decreasing strength. The problem experienced in the past with using partially stabilized ZrO_2 is that Si_3N_4 and ZrO_2 react to form Zr-oxynitride, an undesirable compound because it depletes the ZrO_2 content without increasing toughness and it oxidizes at intermediate temperatures to monoclinic ZrO_2. The monoclinic ZrO_2, in turn, results in serious surface cracking. F. F. Lange (Ref. 1) has shown evidence that the formation of Zr-oxynitride can be prevented or retarded and that a transformable tetragonal ZrO_2 phase can be obtained by using ZrO_2 alloyed with Y_2O_3. A range of Y_2O_3-ZrO_2 alloys has been investigated, including 13.7%, 12.0%, 10.3%, 8.0% and 4.5% (by wt.) Y_2O_3. The basic composite composition selected for evaluation was 30% by vol. ZrO_2 alloy plus 70% Si_3N_4. Two or 4% (by wt.) Al_2O_3 was also added as a sintering aid. Submicron powders free of hard agglomerates were obtained by multiple sedimentation processes and the selected components were mixed with ultrasonic energy while still suspended in water. Disc-shaped samples were formed by pressure filtration, dried (green density of these samples was 40% of theoretical), and either sintered or hot pressed. Hot pressed samples did not contain Al_2O_3 additions.

Results have shown that compositions containing ZrO_2 with alloy additions below 6.0 m/o Y_2O_3 are subject to an intermediate-temperature (around 700C) oxidation problem due to the formation of the monoclinic ZrO_2 phase. On the other hand, the oxidation problem is not evident in compositions containing ZrO_2 with alloy additions above 6.0 m/o Y_2O_3 even after 64 h at 700C in air.

Fracture toughness values obtained by the diamond indentation method ranged from 6.1 to 7.1 MPa $m^{1/2}$ calculated using Evans' relationship (Ref. 2) and 4.1 to 7.1 MPa $m^{1/2}$ using Anstis' relationship (Ref. 3). The results obtained by the more recent Anstis' relationship are considered to be more accurate so, henceforth, only Kc values calculated by that relationship will be reported. For reference, toughness was measured on two NC 132 samples. Values averaged 6.1 (Ref. 2) and 4.1 MPa $m^{1/2}$ (Ref. 3). The latter values are in good agreement with fracture toughness data published in the literature.

Samples of a key composition, Si_3N_4 + 30 v/o ZrO_2 alloyed with 6.6 m/o Y_2O_3, were prepared by hot pressing so that test bars could be obtained expeditiously. Samples were first prepared by ball milling as-received powders but the hot pressed bars contained inclusions, possibly an impurity picked up in the as-received powders or from the milling operation. The strengths of bars in the as-hot-pressed condition were 59.0, 61.0, and 57.3 ksi while those in the oxidized (700C, 64h) condition were 10% higher, 62.8, 68.0, and 66.2 ksi. New samples were prepared using colloidally processed powders to eliminate the black impurities. Disc-shaped specimens were press formed, dried, and hot pressed at 1700C, 1 h. The densities of two discs hot pressed simultaneously were 4.01 and 4.04 g/cc. Calculated theoretical density is 4.06 g/cc. Thirteen MOR bars were machined and they will be used to determine (1) strength in the as-hot-pressed and in the oxidized (700C for 64h) conditions, and (2) fracture toughness using the method described by Cook and Lawn (Ref. 4), which is to use an MOR bar with 3 microindents located in the high stress area.

CaO-Stabilized Zirconia Dispersoids - Theoretical considerations (Ref. 1) imply that alloying ZrO_2 with a divalent cation may lead to higher toughness, and preliminary results indicate that this is the case. Samples of the compositions (1) Si_3N_4 + 30 v/o ZrO_2 (5 w/o CaO) and (2) Si_3N_4 + 30 v/o ZrO_2 (7 w/o CaO) were prepared by adding 2 1/2 w/o MgO as a densification aid, ball milling the as-received powders, and hot pressing at 1700C for 1 h. Fracture toughness in the as-hot-pressed condition was 7.1 and 7.0 MPa $m^{1/2}$, respectively, which is a 75% increase over Si_3N_4 without a dispersoid. A sample that was heat treated at 1350C for 2 h exhibited even higher toughness values, 12.5 MPa $m^{1/2}$ near the surface and 8.9 MPa $m^{1/2}$ in the center of the sample. These compositions, however, exhibit a low temperature oxidation problem. The average as-hot-pressed MOR was 119 ksi (6 samples) while that of bars oxidized at 700C for 64 h was only 45 ksi (4 samples). The effect of the 1350C treatment on the low temperature oxidation phenomenon is being evaluated.

MgO-Stabilized ZrO_2 Dispersoids - Powder of the composition Si_3N_4 + 30 v/o ZrO_2 alloyed with 5 w/o MgO + 2 1/2 w/o MgO as a densification aid was prepared by ball milling as-received powders and hot pressing at 1700C for 1 h. Fracture toughness measurements were 7.4 and 7.8 MPa $m^{1/2}$, an 85% improvement over the matrix material. Strength values exhibited a large scatter, 100.5, 46.8, and 20.3 ksi, presumably from inclusions introduced by ball milling and from a crack

that formed during hot pressing. Strengths of samples oxidized at 700C for 64 h were 89.7, 20.7, and 14.7 ksi. Since this composition densified so easily at 1700C another was hot pressed at 1600C. This sample also compressed to near full density but it cracked in two pieces during the hot press operation. The strengths of MOR bars machined from the remaining pieces were 93.0 and 81.5 ksi. A third sample was hot pressed at 1550C for 15 minutes to full density, 4.08 g/cc compared to 3.91 and 3.87 g/cc for the prior samples, without cracking. These samples are being evaluated.

HRMO Dispersoid - Small samples of Si_3N_4 + 30 v/o HRMO + 4 w/o Al_2O_3 as a sintering aid were prepared. HRMO is a hafnia-rich mixture of oxides containing 60 m/o HfO_2 + 20 m/o ZrO_2 + 20 m/o TiO_2 that exhibits zero thermal expansion to 2000F. Small cold pressed samples were sintered at 1750C but the density was only 75% of theoretical. A new supply of HRMO material was procured from a vendor so that larger samples can be made.

Status of milestones

All milestones are on schedule.

References

1. F.F.Lange, L. K. L. Falk, and B.I. Davis, "Structural Ceramics Composites Based on Si_3N_4-ZrO_2(+Y_2O_3) Compositions", unpublished, October 1985.

2. Evans, A.G. and E. A. Charles, "Fracture Toughness Determinations by Indentation," Jour. Amer. Ceram. Soc., 59(7-8), 371, 1976.

3. Anstis, G.R., et al., "A critical Evaluation of Indentation Techniques for Measuring Fracture Toughness; I Direct Crack Measurements Strength Method," Jour. Amer. Ceram. Soc., 64 (9), 533-538, 1981.

4. Cook, R.F., and B.R. Lawn, "A Modified Indentation Toughness Technique," Communications of the Amer. Ceram. Soc., C-200, Nov. 1983.

Silicon-Nitride-Metal Carbide Composites

S. T. Buljan (GTE Laboratories, Inc.)

Objective/Scope

The objective of this program is to develop silicon nitride-based composites of improved toughness, utilizing SiC and TiC as particulate or whisker dispersoids, and to develop and demonstrate a process for near net shape part fabrication. Near net shape process development will explore forming by injection molding and consolidation by hot isostatic pressing or conventional sintering.

Technical Progress

Summary

Work during the preceding reporting period had focused on detailed characterization of properties and fractographic analyses of both whisker and particulate composites. The results for the Si_3N_4-SiC (whisker) system indicate notable strength and fracture toughness improvements. Composites with TiC whiskers and particulate additions of both systems show, at this point of development, only marginal toughness improvements. The analyses of these materials have indicated that modest increases in fracture toughness are, for the most part, a consequence of underdeveloped microstructure.

Si_3N_4-TiC System

Examination of composites containing TiC particulates have shown that addition of up to 30 v/o of dispersed TiC of an average diameter of about 2 μm produces no change in fracture toughness despite observed crack-dispersoid interaction (Figure 1).

The crack-particle interaction was studied on composites containing single crystal TiC dispersoids and compared to an equivalent Al_2O_3-TiC composite. The residual strain produced by thermal expansion mismatch in these two composites is expected to be of opposite sign.

In order to assess the residual state of stress at the interface between TiC and ceramic matrices (Si_3N_4, Al_2O_3), a computer modeling approach has been used. Figure 2 shows the model, which represents a spherical particle that is integrally bonded to the ceramic continuum. The model has been reduced to a two-dimensional analysis because of the symmetrical nature of the problem. The material properties used to compute the residual stresses are listed in Table 1.

Table 1: Material Properties Used for Finite Element Analyses

	Properties			
Materials	E(x10^6 psi)	σ ult. ten. x10^3 psi	ν	α x 10^{-6} in/in/°C*
Si_3N_4	43	100	0.27	2.7
Al_2O_3	54	20	0.23	8.5
TiC	65	70	0.19	7.2

*Linear Thermal Expansion Coefficient (Room Temperature to 800°C)

Noteworthy are the differences between thermal expansion coefficients, which are responsible for the thermal strain mismatch at the matrix/particle interface. Figure 2 shows how the residual stress distribution differ when a temperature reduction of 800°C is applied to each of the ceramic composite systems. Inspection of the principal stress distributions for the Al_2O_3/TiC material reveals hoop tensile stresses in the Al_2O_3 matrix, which increase at the interface. The principal compressive stresses are radial through the TiC particle and matrix with an additional tensile hoop component in the particle region. In direct contrast is the Si_3N_4/TiC composite, which completely reverses the tensile and compressive principal stress distribution. The magnitude of the normal stresses across the particle/matrix interface is greatest for the Si_3N_4/TiC system. The resulting shear stress (stress xy) is essentially invariant, which results from the symmetrical problem definition. These residual stress data constitute a first step towards understanding how thermal strain mismatch can contribute to composite material performance, in particular, fracture behavior. Future work with SiC as the particle is planned, which may include the whisker geometry.

Two basic TiC single crystal morphologies were observed in the composite microstructures, elongated rectangular grains with {100} planes parallel to the straight edges of the grain and more equiaxed pseudohexagonal cross sections of crystal whose habit is defined by a combination of {100} and {120} planes. For the Si_3N_4 matrix composite, crack deflection around these grains was not observed. However, cleavage steps (deflection) were observed within some rectangular grains (Figure 3b). Crack penetration of the TiC crystal without deflection around the grains was the primary interaction in the majority of the cases observed.

For the Al_2O_3-TiC material, the crack-dispersoid interaction was observed to be dependent on dispersoid morphology. Cracks were observed to penetrate rectangular grains (Figure 1e) and deflect around pseudo hexagonal grains (Figure 3d). Deflection-induced crack branching was also observed.

These observations indicate that the sign of the thermal expansion mismatch stress affects the tendency for crack deflection to occur for TiC crystals which cleave readily on {100} planes. The radial thermal expansion mismatch stress for TiC in a Si_3N_4 matrix is tensile. The addition of the tensile stress field of the advancing crack to the residual stress may produce TiC cleavage and allow the crack front to propagate through the dispersed phase as observed. For the Al_2O_3-TiC composite, the radial thermal expansion mismatch stress is compressive. Apparently this reduces the tendency for cleavage with the appropriate crack-dispersoid orientation (Figure 3d), although crystal cleavage may still occur if the crack front encounters cleavage planes in specific direction (Figure 3e).

The investigations have demonstrated effective crack-dispersoid interaction and crack deflection in both composite systems. The effectiveness of TiC dispersoid as a toughening agent is diminished by the reaction with the matrix. The presence of Ti in the matrix glass, as well as presence of dispersoid phase, reduces Si_3N_4 grain growth, resulting in a matrix of considerably finer structure (Table 2) and due to a predominantly intergranular fracture mode, in a reduced amplitude of crack deflection in the matrix material (Figure 4). This effect can be reduced through adjustment of processing parameters or eliminated with the utilization of coated TiC dispersoids.

Table 2: Quantitative Microstructural Analyses (TEM, Mag 25KX) of Silicon Nitride-Based Composites

	β-Si_3N_4 Grain Size (μm)	No. of Grains Counted
AY6	0.36 ± 0.26	1205
AY6 + 30 v/o TiC	0.17 ± 0.14	1655
AY6 + 20 v/o SiC	0.40 ± 0.26	895

Si_3N_4-SiC System

Dispersoid-toughening of composite systems with complex polycrystalline matrices requires careful consideration of the minimum effective size of the dispersoid as well as concentration. In the Si_3N_4-SiC (particulate) system, it was observed that increasing concentration of fine (≈0.5 μm APD) SiC particulates results in a decrease in fracture toughness, while additions of coarser (8 μm APD) SiC show an increase (Figure 5).

Best results were obtained with the additions of SiC whisker. While particulate SiC composites exhibit only a modest increase in fracture toughness with increasing dispersoid concentration up to 30 v/o, whisker-containing composites show up to 40% improvement in fracture toughness with concomitant increase of fracture strength. While

several densification schedules were explored, studies have, in general, shown that increased concentration of SiC whisker requires extended time for full densification (Figure 6). The densification rate of particulate composites is equivalent to that observed for 10 v/o whisker materials. The room and elevated temperature K_{IC} and MOR of the composites processed according to the conditions given in Figure 6 are presented in Figure 7. In all cases, the fracture toughness and strength of the Si_3N_4-30 v/o SiC whisker composite is increased relative to the monolithic base material and approaches the targeted values.

By virtue of densification method and the shape of dispersed-phase, densified composites exhibit limited anisotropy in mechanical properties (Table 3). The indentation fracture toughness in a plane perpendicular to the hot pressing direction was lower in all cases than that measured parallel to the hot pressing direction. This is apparently due to whisker and Si_3N_4 grain alignment in planes perpendicular to the hot pressing direction. The preferential orientation of acicular grains is also reflected in Young's modulus values for two directions. The observed toughening may be attributed to both crack deflection and whisker pullout. SEM photomicrographs in Figures 8 and 9 illustrate the fracture mode. The whisker pullout cavities, protruding whiskers, and depressions caused by crack deflection around the whisker are clearly visible.

Table 3: Indicated Anisotropy in Hot Pressed Silicon Nitride-Based Materials

	Cross Section				Plane ⊥ HPD	
	IFT ($MPa \cdot m^{1/2}$)		Young's Modulus*(Gpa)		IFT ($MPa \cdot m^{1/2}$)	
Material	∥ HPD	⊥ HPD	∥ HPD	⊥ HPD	1	2
AY6	4.1 ± 0.2	3.4 ± 0.2	297	299	3.6 ± 0.2	3.7 ± 0.2
AY6 + 10 v/o SiCP (8 μm)	3.9 ± 0.3	3.2 ± 0.2			3.8 ± 0.2	3.8 ± 0.2
AY6 + 20 v/o SiCP (8 μm)	4.1 ± 0.2	3.0 ± 0.1			3.8 ± 0.2	3.8 ± 0.2
AY6 + 30 v/o SiCP (8 μm)	3.7 ± 0.2	3.0 ± 0.2			4.0 ± 0.2	4.0 ± 0.2
AY6 + 10 v/o SiCW (SC-9)	3.7 ± 0.2	3.5 ± 0.1			3.4 ± 0.1	3.5 ± 0.2
AY6 + 20 v/o SiCW (SC-9)	4.0 ± 0.1	2.9 ± 0.3	311	325	3.8 ± 0.1	3.6 ± 0.2
AY6 + 30 v/o SiCW (SC-9)	4.8 ± 0.2	3.0 ± 0.2	333	340	4.7 ± 0.2	4.6 ± 0.2

*Pulse-echo ultrasonic measurement

Quantitative analyses indicate that, while existent powder preparation process provides excellent dispersion, the whisker aspect ratio is severely reduced during homogenization (Table 4). It is thus anticipated that the process refinement to reduce comminution of the whiskers will further enhance mechanical properties. In another aspect of process optimization, the influence of time/temperature effects on matrix microstructure development and its consequence on the composite toughness is being further examined.

Table 4. Characterization of SiC Whiskers (SC-9)
(Average Diameter = 0.5 ± 0.2)

Processing Step	Average Length (μm)/Counts	Aspect Ratio
As-Received	18 ± 12/1574	33
After Sedimentation	18 ± 9/1430	33
After Homogenization	5 ± 3/1439	10
Hot Pressed Composite	6 ± 3/1780	12

Status of Milestones

Milestone 122301, Task 1.2, fabrication of initial specimens, was completed by December 1, 1985. Overall program execution is on schedule.

Publications

S.T. Buljan, J.G. Baldoni, and M.L. Huckabee, "Silicon Nitride-Silicon Carbide Composites," presented at 88th Annual Meeting of American Ceramic Society, Chicago, Ill., April 28 - May 1, 1986.

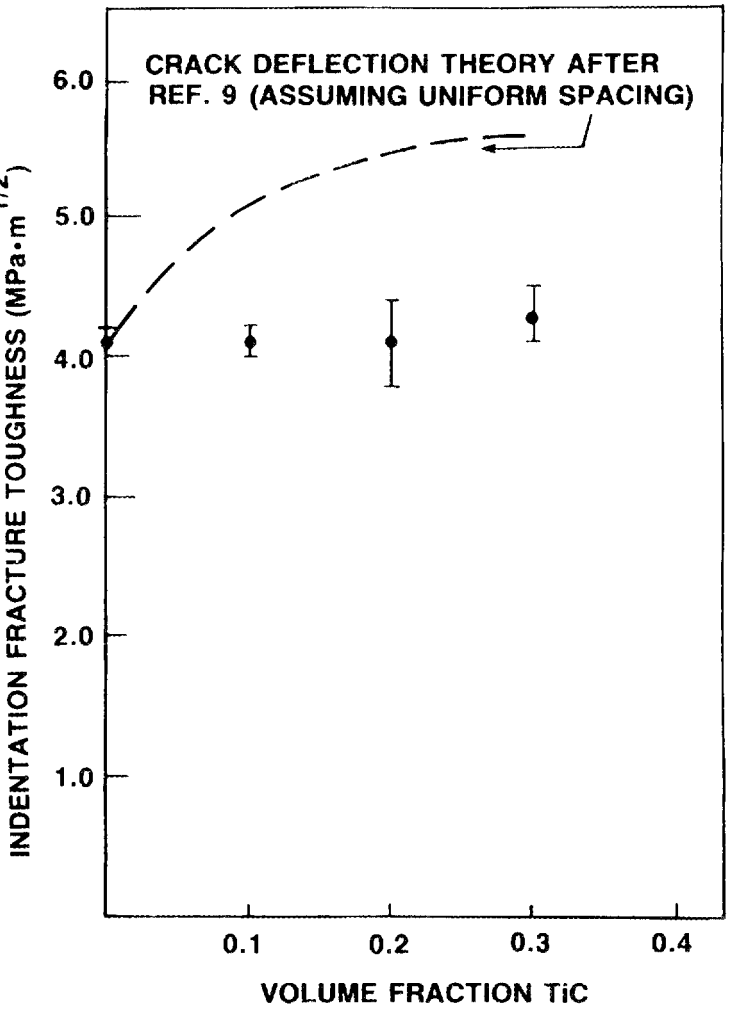

Figure 1: Indentation Fracture Toughness of Si_3N_4-TiC Particulate Composites

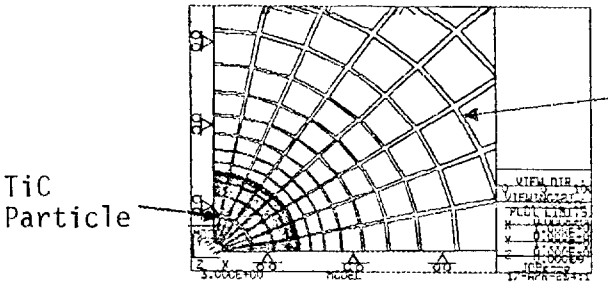

(a)

Comparison of Principal Stresses

Al_2O_3 Matrix

Si_3N_4 Matrix

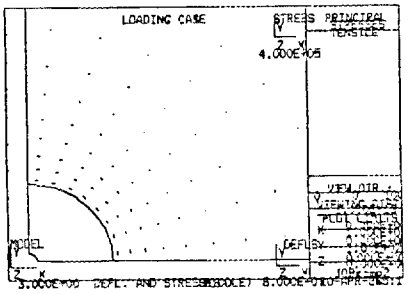

Tensile

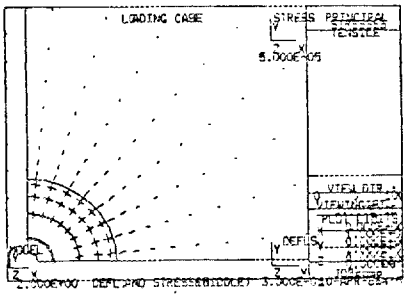

(b)

(c)

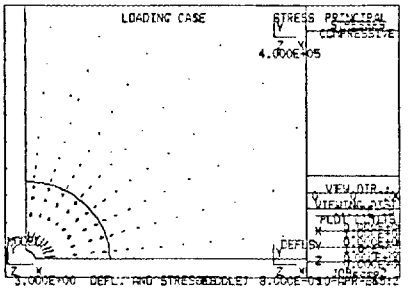

Compressive

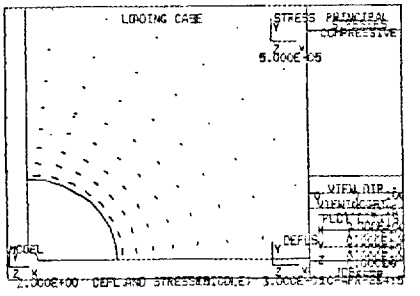

(d)

(e)

Comparison of Normal Stresses

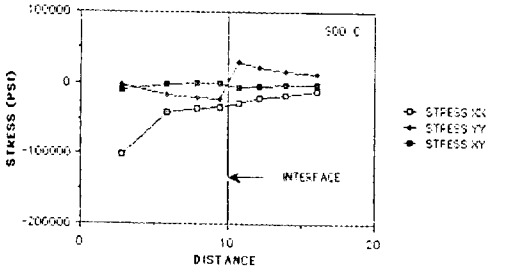

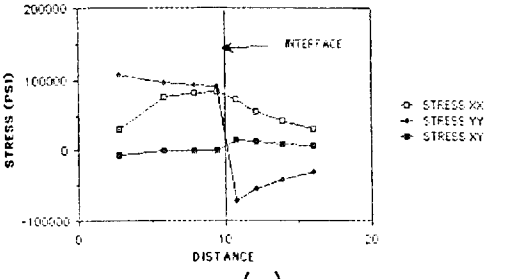

(f)

(g)

Figure 2: Two Dimensional Finite Element Model of Ceramic Composite Microstructure

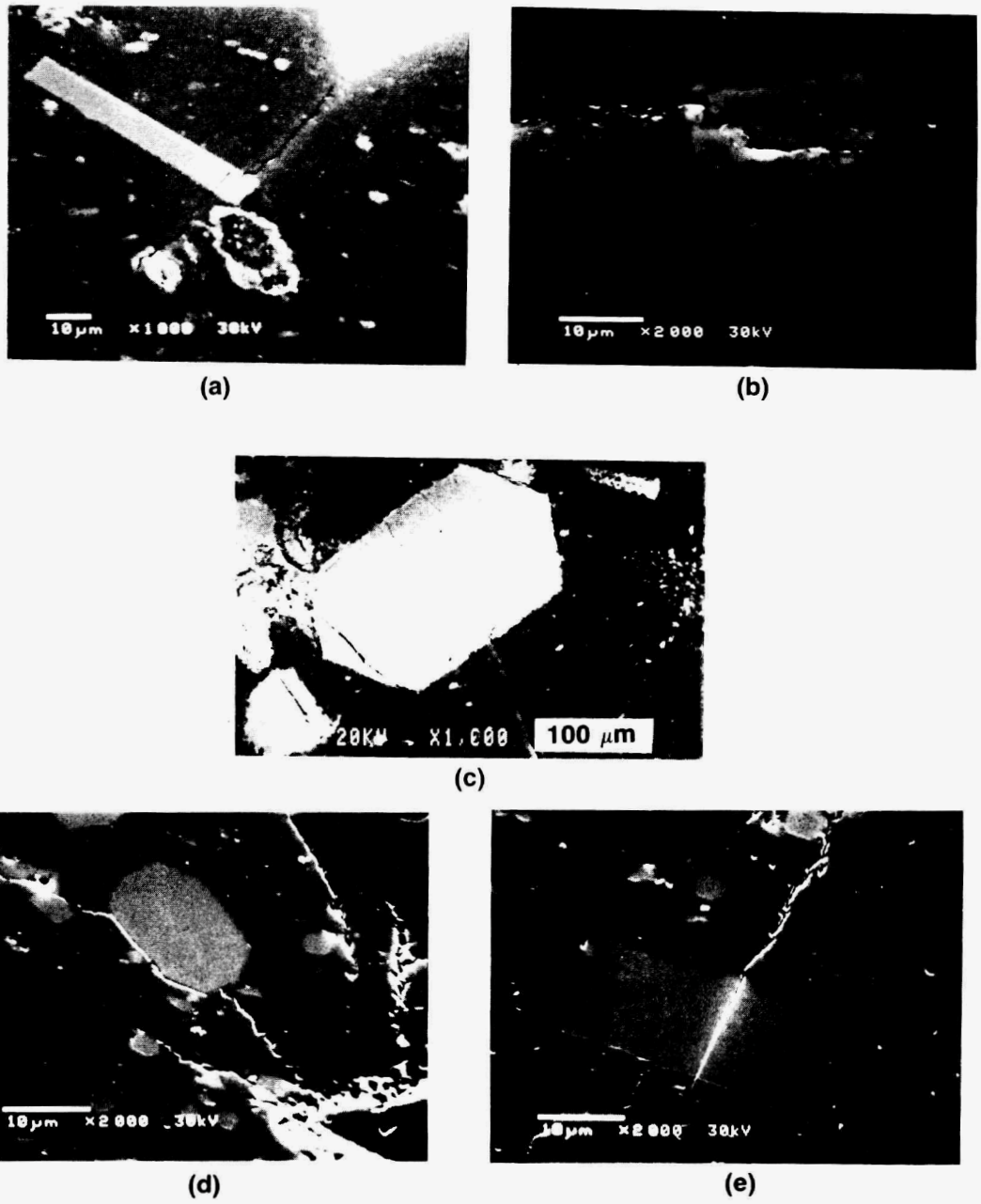

Figure 3: Crack-Dispersoid Interactions in Si_3N_4-TiC Composites (a-c) and Al_2O_3-TiC d,e)

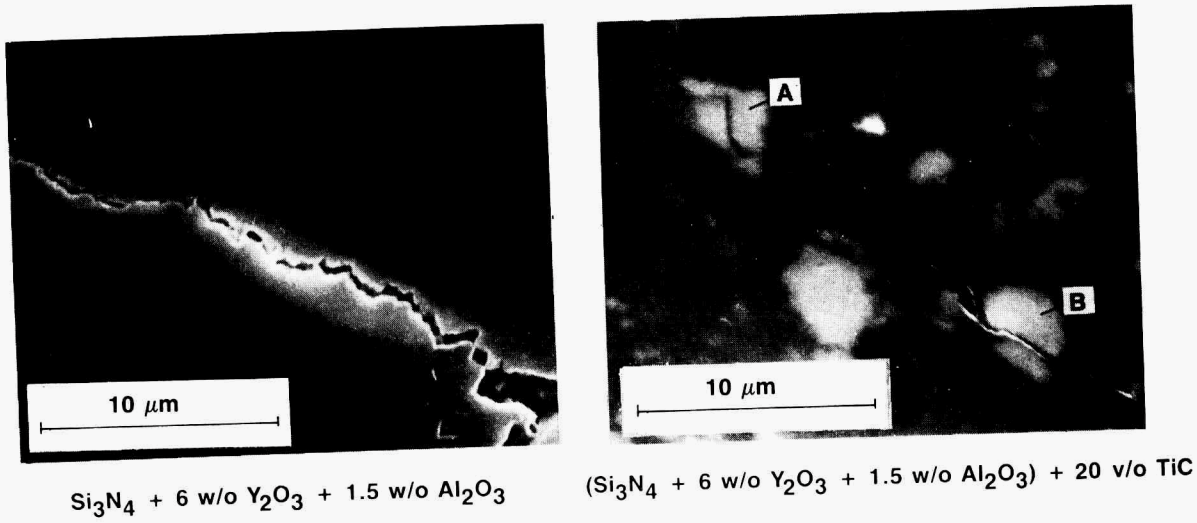

Figure 4: Observed Crack Trajectories in IFT Samples at Room Temperature in A) Si_3N_4 and B) Si_3N_4 + 20 v/o TiC Composites

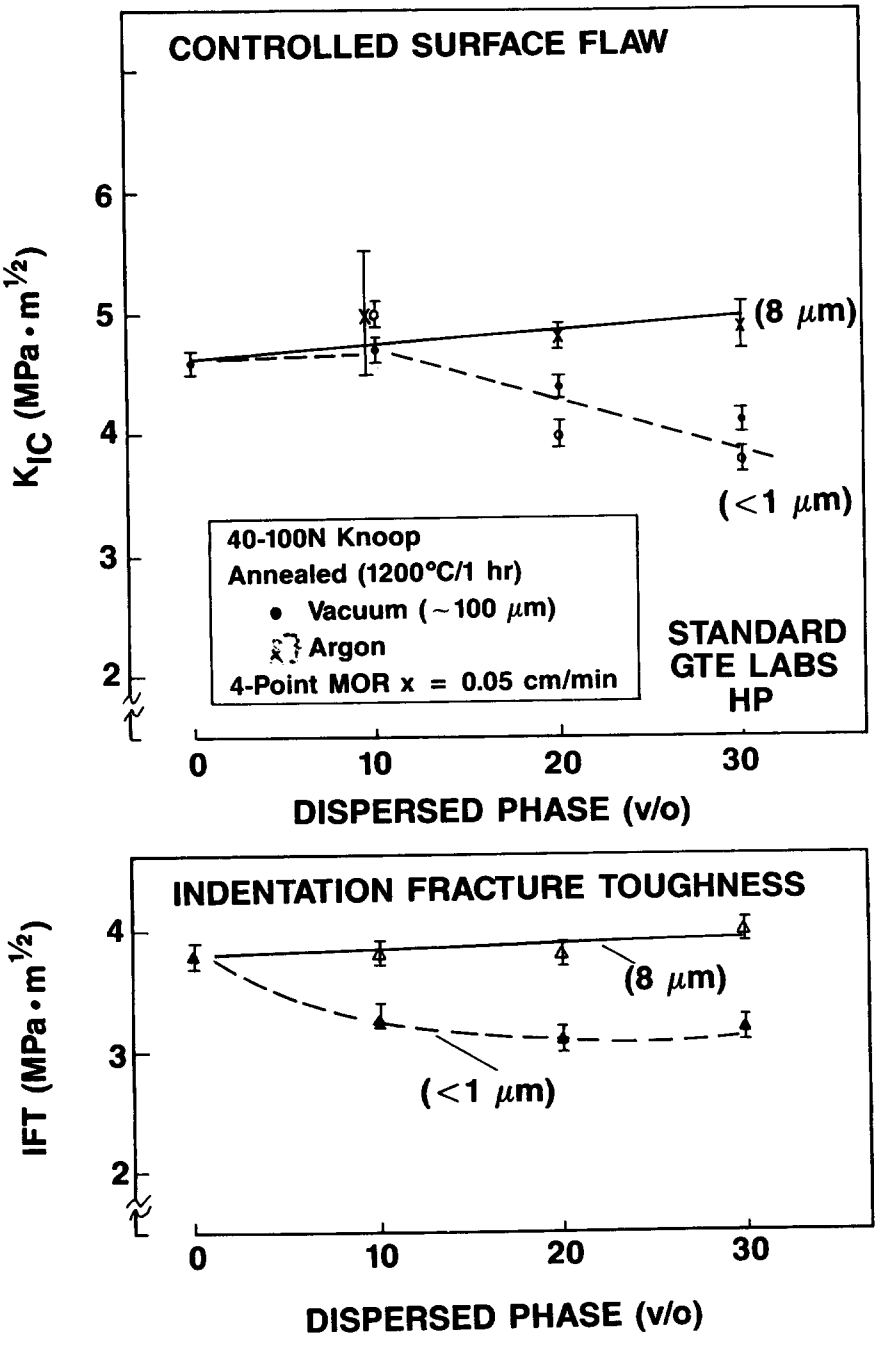

Figure 5: Fracture Toughness of Si_3N_4-SiC Particulate Composites

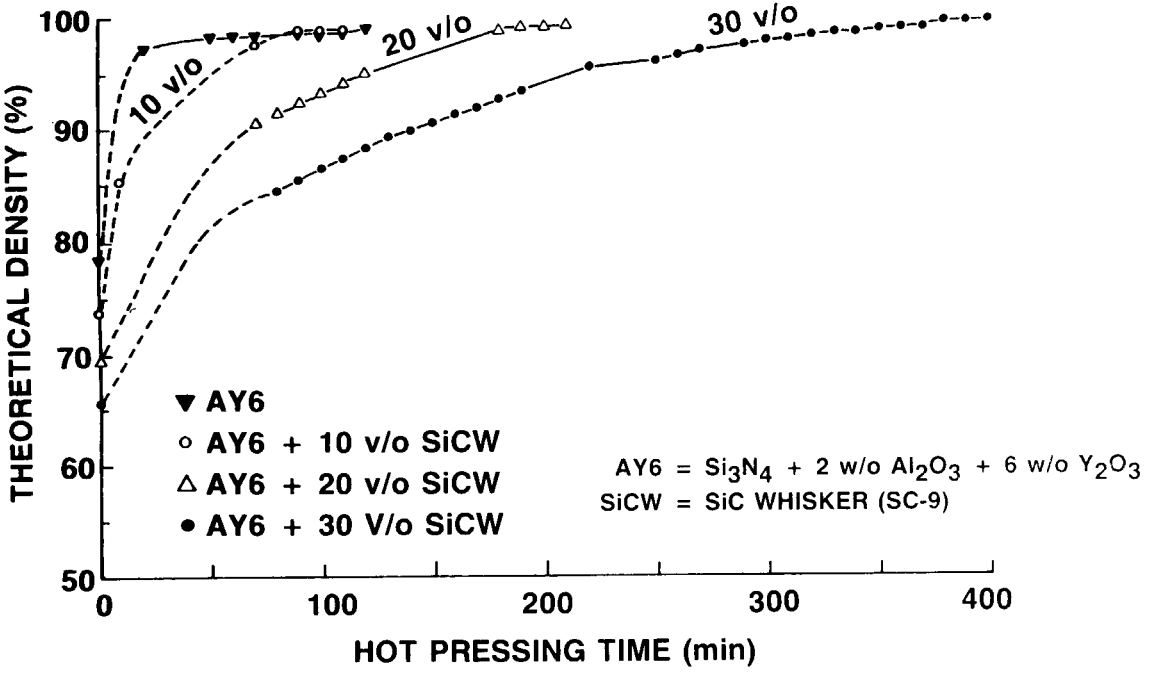

Figure 6: Densification of Si_3N_4-Based Materials

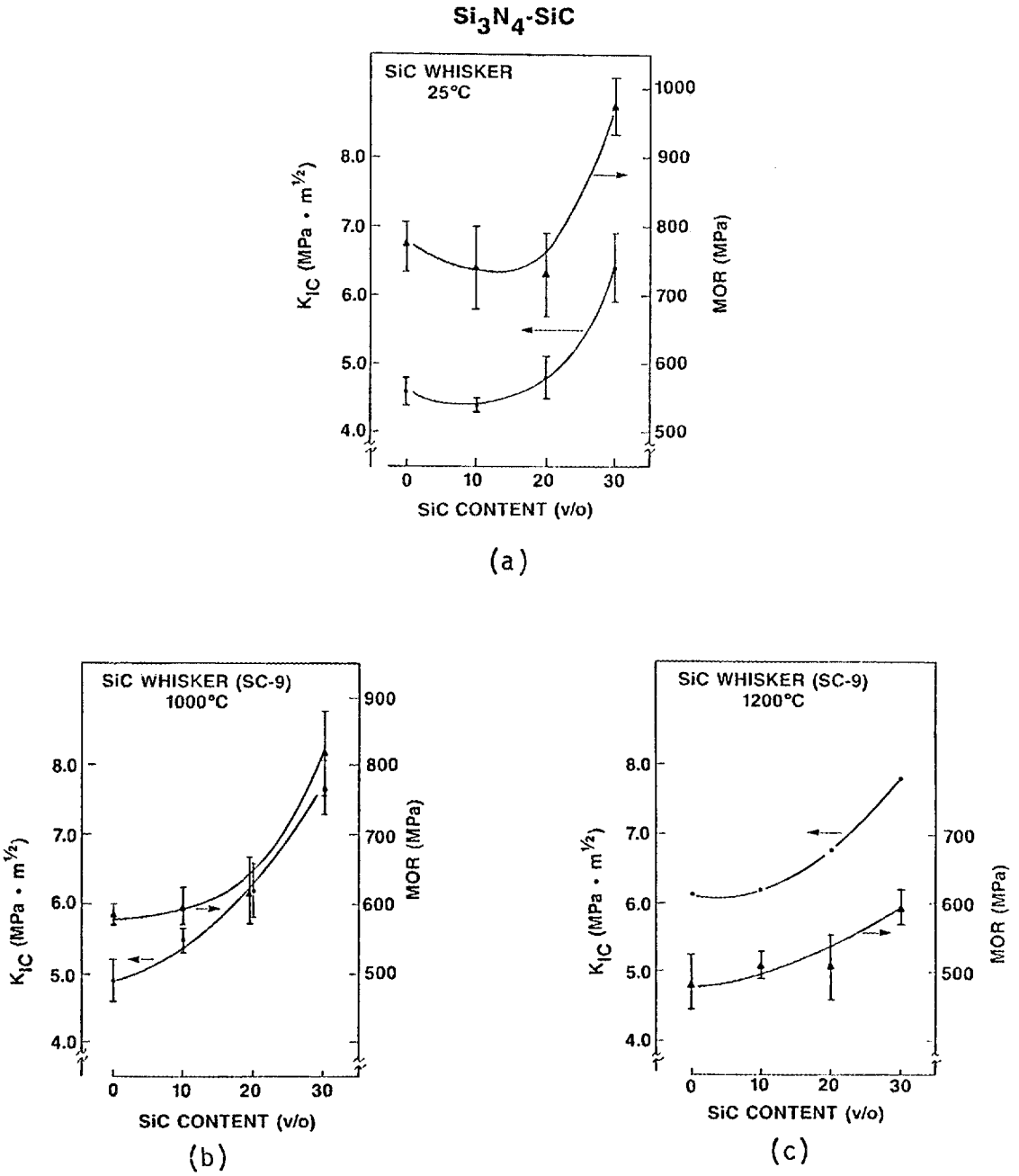

Figure 7: Room and Elevated Temperature K_{IC} and MOR of Si_3N_4-SiC Whisker Composites

$[Si_3N_4 + 2\ w/o\ Al_2O_3 + 6\ w/o\ Y_2O_3] + 30\ v/o\ SiCW\ (SC\text{-}9)$

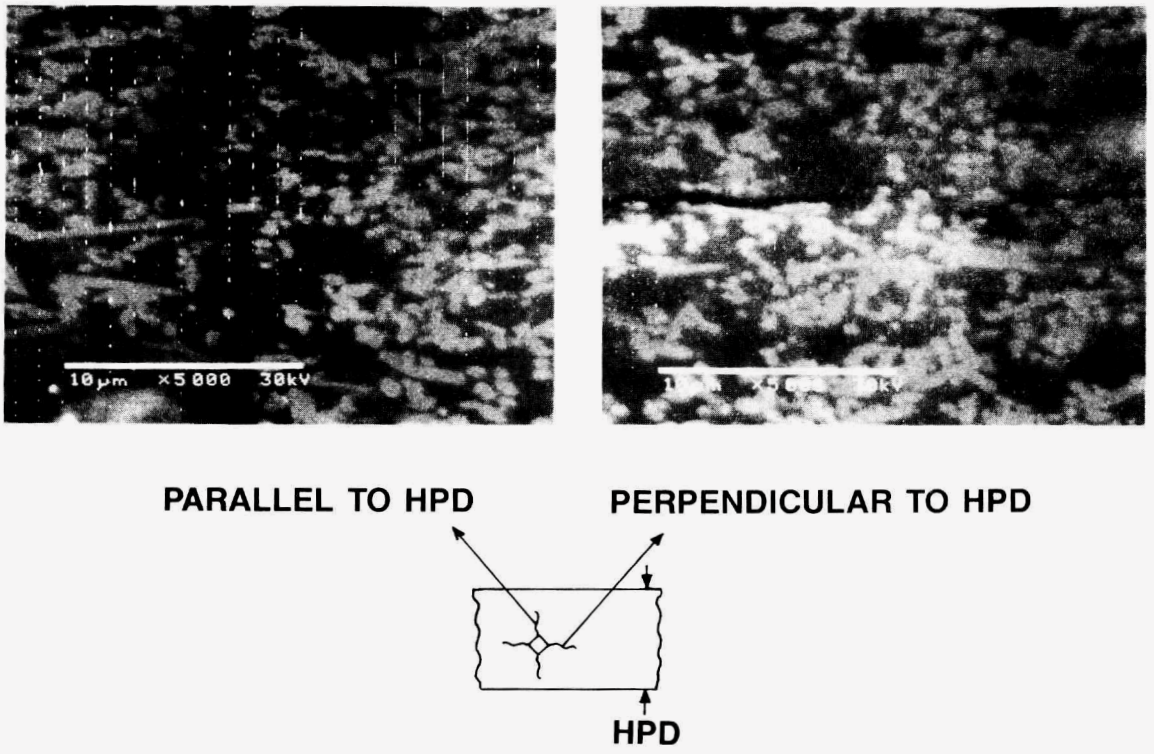

Figure 8: Indentation-Induced Crack Propagation

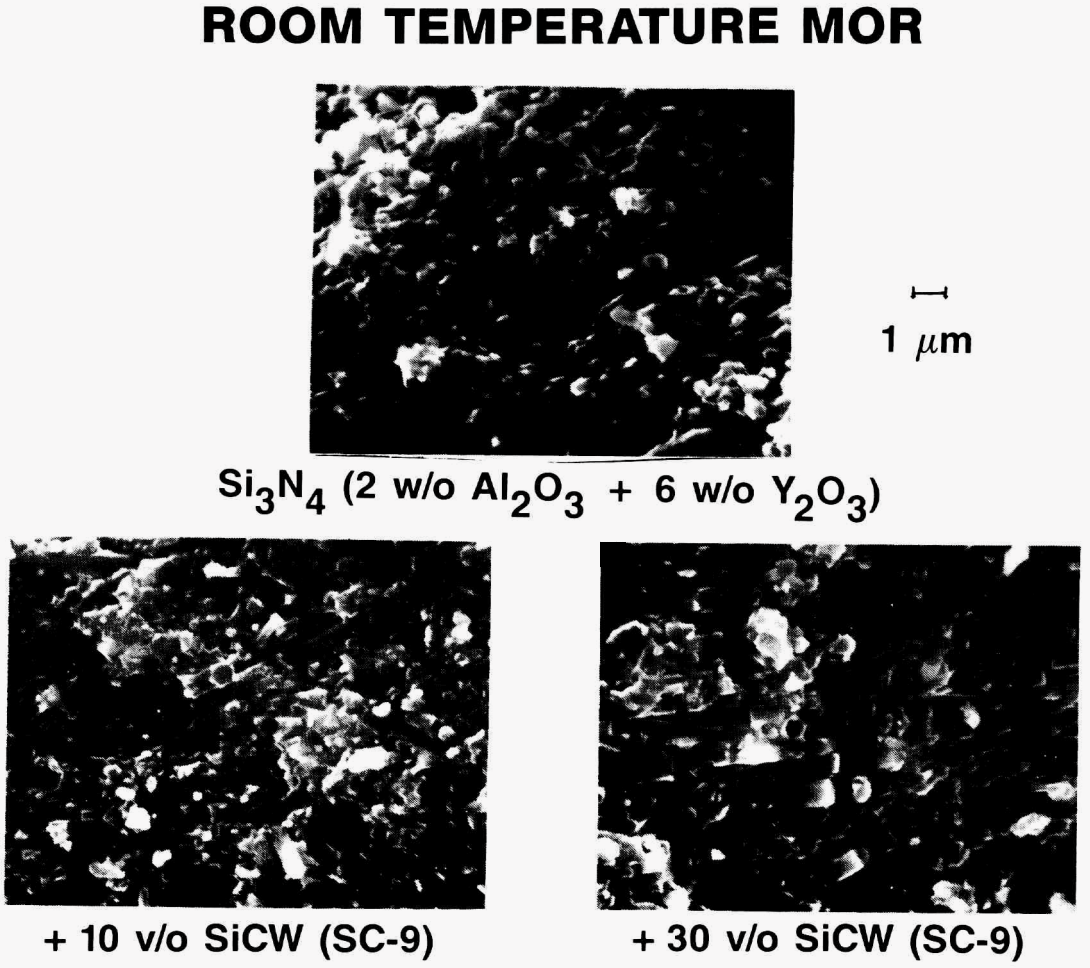

Figure 9: Fracture Surfaces of Silicon Nitride-Based Materials

SiC-Whisker-Toughened Silicon Nitride

K. Haynes, M. Martin, and H. Yeh (AiResearch Casting Company)

Objective/Scope

The objective of this twenty-four month program is to develop the technology base for fabricating a ceramic composite consisting of silicon carbide whiskers dispersed in a dense silicon nitride matrix. This is to be accomplished by slip casting as the green shape forming method, and sintering or sinter/HIP as the densification method. An iterative experimental approach is used throughout the entire program.

The recommended starting matrix composition is Si_3N_4 + 6% Y_2O_3 + 2% Al_2O_3 and four types of SiC whiskers are to be evaluated. Feasibility, as gauged by doubling the fracture toughness compared to the matrix Si_3N_4 containing no whiskers, will be demonstrated in Task 1. Once the feasibility has been demonstrated, systematic optimization studies will be conducted in Task 2 to develop optimum process parameters, microstructure, and mechanical properties. A full characterization of the optimized material will be carried out in Task 3.

Technical Highlights

Materials and Procedures

Specimens prepared in Iteration 4 using ARCO SC-9 and Tateho SCW #1 silicon carbide whiskers were encapsulated in tantalum cans. Processing parameters for these specimens were based upon processing results from Iteration 2A.

No processing was continued with Iteration 5 (forming samples via cold isostatic pressing) due to the inability to successfully form test samples using SiC/ Si_3N_4 composite materials.

Iteration 6 involved preparing ARCO SC-9 silicon carbide whiskers (20% by weight) in a silicon nitride matrix. The composite material was slip cast into billets, presintered and encapsulated in niobium cans. (Delays in receiving the niobium cans from the vendor were experienced).

Powders were prepared for Iteration 7 using 30 percent Tateho SiC whiskers. Slips were then cast into billets which were then pre-sintered. These were encapsulated in niobium as well.

Specimens were prepared using sinterable reaction bonded silicon nitride (SRBSN) with and without SiC. ARCO SC-9 and Tateho SCW #1 SiC were used in these samples at 15% loadings. The compositions and as-nitrided densities are listed in Table 1.

Tateho SCW #1-S silicon carbide whiskers were received. Powder preparation was initiated, with the composite powder containing 20% Tateho SCW #1-S. (Iteration 8).

Encapsulation and HIP

Iteration 2A

The remaining tantalum encapsulated specimen from Iteration 2A containing 20 volume percent ARCO SC-9 was processed at 1750°C and 28 ksi pressure argon (HIP run 460). This run yielded the best densities to date for formulations with 20 volume percent SiC whiskers (3.18 g/cc).

Iteration 4

Two HIP runs were made using tantalum encapsulated samples from Iteration 4. Based on the results of Iteration 2A, which were run at 1750°C, these samples were run at 1800°C in an effort to increase the HIP'ped density.

HIP run 485 was carried out using a sample containing 20% ARCO SC-9 SiC. This sample experienced incomplete densification due to a weld failure. A density of only 2.45 g/cc was achieved. A wafer of this material was cut and analyzed for fiber degradation.

HIP run 488 was carried out using a sample containing 20% Tateho SCW #1 SiC. Incomplete densification occurred in this sample due to reaction products. As seen in Figure 1, the tantalum can started collapsing around the sample. At some point the volatiles caused the can to bloat and fail as seen in the upper portion of the photo.

Iteration 6 and 7

Two HIP runs were made using niobium encapsulated samples. Both HIP runs were taken to 1800°C.

HIP run #501 was performed using a sample containing 30% Tateho SCW #1. Complete densification of the sample was achieved without failure of the niobium can. (Figure 2; left can). A density of 3.23 g/cc was achieved.

HIP run #502 was carried out using two samples; one sample contained 20% ARCO SC-9 while the other sample contained 30% Tateho SCW #1. The Tateho SCW #1 sample did not densify as well as the Tateho sample in run #501. A defect in the weld of the niobium can was identified. However, the ARCO SC-9 sample showed successful and complete collapsing of the niobium can (Figure 2; right can) as indicated by a density of 3.24 g/cc for the ARCO SC-9 sample.

Removal of the niobium from the ARCO and Tateho samples showed densified samples with a similar dark green color. (Figure 3; Tateho SCW #1 on left, ARCO SC-9 on right). The Tateho SCW #1 sample is slightly smaller in height and diameter compared to the ARCO SC-9 due to green casting density. The Tateho SCW #1 sample was cast at a green denisty of 1.73 g/cc, while the ARCO SC-9 started with a density of 2.04 g/cc. Both samples were cast in plaster molds with identical dimensions.

Encapsulation and HIP Summary

In comparing tantalum encapsulation to niobium encapsulation, niobium appeared to be a better encapsulation material to tantalum. The weld integrity of the niobium was much better compared to tantalum, especially after observing the condition of the cans through Hot Isostatic Processing (HIP) (Figure 1 vs. Figure 2). In addition, the tantalum would be more reactive to the nitrogen in the furnace atmosphere resulting in a very brittle can that would fail under pressure. Niobium would maintain its ductility through HIP.

A more significant observation showing the success of niobium encapsulation versus tantalum encapsulation are visual and density comparisons of the respective samples. Visually, the tantalum encapsulated samples would be dark gray to black indicating some reaction with the furnace atmosphere (failure of the tantalum can). The niobium encapsulated samples have shown a dark green color after HIP inidcating the niobium integrity through HIP. Density results with tantalum have shown a maximum of 3.18 g/cc for 20% ARCO SC-9/Si_3N_4. Niobium encapsulants have shown maximum densities of 3.23 g/cc for 30% Tateho/Si_3N_4 and 3.24 g/cc for 20% ARCO SC-9/Si_3N_4.

Evaluations

The baseline Si_3N_4 and the Si_3N_4/20 volume percent ARCO SiC billets from Iteration 2A were machined into test bars. Machining the billets into test bars proved to be a time consuming process. The specimens tested for MOR and fracture toughness were nominally 1/4" X 1/8" X 2". MOR testing employed a 4 point bend method. For the fracture toughness measurements, a single notch test method was used. The notch depth was approximately 0.060 inch. The results of the MOR testing are compiled in Table 2. The average strength for the baseline material was 103.8 ksi while the 20% ARCO SiC/Si_3N_4 material was 90.7 ksi, representing a decrease of 12.6%.

Fracture toughness results from Iteration 2A are compiled in Table 3. The average toughness for the baseline was 7.2 ksi$\cdot in^{\frac{1}{2}}$, and the average of the composite material was 10.0 ksi$\cdot in^{\frac{1}{2}}$, an increase of 38.9%.

Additional fracture toughness evaluations were done on Iteration 2A samples using a chevron notch technique. The average fracture toughness for the monolithic Si_3N_4 and the composite were 2.8 and 1.7 ksi•in$^{\frac{1}{2}}$ respectively (the averages exclude specimens which did not exhibit stable crack growth). The chevron notch data is inconsistent with previous measurements using single edge notch beam specimens (7.2 ksi•in$^{\frac{1}{2}}$ for Si_3N_4 and 10.0 ksi•in$^{\frac{1}{2}}$ for Si_3N_4/20% SiC). The inconsistency may be due to precracking of the chevron notch specimens. These specimens had a triangular ligament measuring only approximately 0.125" across the base and approximately 0.065" in height and may easily crack on handling. The test technique and specimen size are being re-evaluated by Garrett Turbine Engine Company through the University of Washington and ORNL.

Samples from Iteration 2A, containing 20% ARCO SiC, were analyzed using SEM and polished micrographs. Polished micrographs of the as nitrided SRBSN were also prepared.

Polished micrographs of a representative MOR specimen are shown in Figures 4A and 4B. These photos show the orientation of the SiC to be quite random and the distribution to be uniform. The fracture surface of this same specimen was examined using SEM as seen in Figure 5A. The fracture origin seemed to be nondensified Si_3N_4. This was representative of approximately half the specimens examined. The remaining specimens showed fracture origins consisting of inclusions or agglomerates not appearing to consist of silicon carbide whiskers.

A higher magnification view is shown in SEM Figure 5B. Whiskers can be resolved as well as pull outs indicative of the toughening mechanisms. An approximately 40% increase in fracture toughness was found in this material system versus the monolithic.

The effect of eliminating Al_2O_3 in a sintered reaction bonded silicon nitride (SRBSN) were studied in samples under the cost share effort. Polished micrographs representative of the as nitrided SRBSN samples are shown in Figures 6A and 6B. The whiskers visible in these photos may be a result of the polishing process. Due to the lower density of the material, the whiskers may be more easily removed.

From the data presented in Table 1, the density of the as nitrided samples without Al_2O_3 are lower than those containing Al_2O_3. This is also true in the case of Code 7a in which La_2O_3 has been substituted for Al_2O_3. This trend along with MOR and fracture toughness properties will be further evaluated after sintering.

Microphotos of both the ARCO SC-9 (Iteration 6) and Tateho SCW #1 (Iteration 7) were taken at 400X (Figures 7A and 7B). Despite the low quality of the pictures, both the ARCO SC-9 and the Tateho SCW #1 samples showed good uniform dispersion in the silicon nitride matrix. The dark inclusions show probable pullout of the silicon carbide from the silicon nitride matrix or possible gas formation during hot isostatic pressing.

SEM Photographs

Two sets of samples were sent to Signal Research Center (SRC) for Scanning Electron Microscopy (SEM). Sample set #1 consisted of four types of as received silicon carbide whiskers (listed below). Sample Set #2 contained green density samples from four slip cast compositions of 20 volume percent silicon carbide whiskers in a silicon nitride matrix.

Sample Set #1: Silicon Carbide Whiskers

Material	Pictures Included
A) ARCO SC-9	Figure 8A-C
B) Tateho SCW #1	Figure 9A-C
C) Tateho SCW #1-S	Figure 10A-C
D) Tokai 'Tokamax'	Figure 11A-C

Sample Set #2: Slip Cast Samples

Material	Pictures Included
A) ARCO SC-9	Figure 12A-B
B) ARCO SC-9 with BN Coating	Figure 13A-B
C) Tateho SCW #1	Figure 14A-B
D) Tokai 'Tokamax'	Figure 15A-B

Silcon Carbide Whisker Analysis

All silicon carbide whiskers at 200X showed agglomerated clusters approximately 100 microns in diameter. A more detailed accounting of the individual whiskers is shown at 2,000X and 10,000X. All silicon carbide whiskers showed a wide mixture of whisker length (up to approximately 100 micron) as well as variations in whisker diameter (1 micron diameter maximum). Tokai silicon carbide whiskers appear to be more irregularly shaped and have the greatest variations in whisker diameter. Tateho SCW #1 and SCW #1-S do not show any significant difference in agglomeration behavior, whisker diameter or whisker length based on SEM comparisons. Tateho had indicated (meeting with ACC on 1-28-86) SCW #1-S would be a more 'deagglomerated' silicon carbide whisker.

Slip Cast Sample Analysis

In contrast to the silicon carbide whisker micrographs, all the slip cast samples (20% volume silicon carbide in a silicon nitride matrix) showed good distribution of silicon carbide whiskers throughout the silicon nitride without whisker agglomeration. Any pores seen in the samples (especially Tateho SCW #1) could have resulted from entrapped air in the samples during slip casting.

Impurity Analysis of Silicon Carbide Whiskers

Samples of ARCO SC-9, Tateho SCW #1 and Tokai Tokamax silicon carbide whiskers were sent to Signal Research Center (SRC) for chemical analysis. (Table #4). In addition to their analysis, SRC included data previously compiled by ORNL on the chemical analysis of silicon carbide whiskers. In correlation to the SEM photographs, the analysis tends to indicate Tokai Tokamax silicon carbide whiskers are processed differently compared to ARCO or Tateho whiskers.

PROBLEMS ENCOUNTERED

ARCO Metals has discontinued supplying ARCO SC-9 silicon carbide whiskers. The current supply of ARCO SC-9 (3 pounds) was supplied from Garrett Turbine Engine Company. The remaining supply of ARCO SC-9 will be used to finish any ongoing iterations that have incorporated

ARCO SC-9. Any further iterations will utilize Tateho SCW #1-S silicon carbide whiskers as the primary silicon carbide whisker.

STATUS OF MILESTONES

Milestone 122102 (Evaluate Alternate SiC Whiskers and Coated Whiskers in Si_3N_4 Matrix Composites) is behind schedule. Fully dense samples have been fabricated. Evaluation techniques have been inconsistant. Delays in testing have resulted while these techniques themself are re-evaluated. Sample preparation is now in progress and testing should be completed during the April - May bi-monthly period.

COMMUNICATION/VISITS/TRAVEL

The 1985 Twenty-third ATD/CCM in Dearborn, Michigan, October 21-24, 1985, was attended.

Representatives of Tateho were at ACC to present updated information on their SiC whiskers. They indicated that oxidation of their whiskers starts at 750°C in air.

PUBLICATIONS

A paper entitled "Si_3N_4 Matrix Composite Development" by K. Haynes and H. Yeh was presented at the 1985 Twenty-third ATD/CCM in Dearborn, Michigan, October 21-24, 1985.

TABLE 1

SILICON CARBIDE AND SRBSN COMPOSITIONS

CODE	Si_3N_4	Y_2O_3	Al_2O_3	Fe_2O_3	SiC WHISKERS	AS-NITRIDED DENSITY
9	93	6	0	1	15% ARCO	2.33 g/cc
7	91	6	2	1	15% ARCO	2.45 g/cc
7	91	6	2	1	15% Tateho	2.56 g/cc
7[a]	91	6	2*	1	15% ARCO	2.34 g/cc
7	91	6	2	1	0	2.69 g/cc

*La_2O_3

TABLE 2

Iteration 2A Modulus of Rupture Results

Material	Sample Number	M.O.R. (ksi)	Average
Baseline Si_3N_4	1	113.5	
	2	96.3	
(Density: 3.13 g/cc)	3	110.0	
	4	116.1	
	5	100.8	
	6	112.0	
	7	84.7	
	8	98.8	103.8
	9	98.8	
	10	111.5	
	11	97.1	
	12	91.9	
	13	111.2	
	14	108.3	
	15	98.2	
	16	110.9	
Si_3N_4/20 v/o ARCO SiC	1	99.1	
	2	94.2	
(Density: 3.18 g/cc)	3	83.2	
	4	66.2	
	5	93.0	
	6	91.0	90.7
	7	84.0	
	8	104.3	
	9	90.7	
	10	78.6	
	11	109.7	
	12	93.9	

TABLE 3

Iteration 2A Fracture Toughness Results

Material	Sample Number	K_{IC} (ksi•$in^{\frac{1}{2}}$)	Average
Baseline Si_3N_4	1	7.5	
	2	7.9	
(Density: 3.15 g/cc)	3	8.8	
	4	4.0	7.2
	5	3.6	
	6	8.3	
	7	8.6	
	8	9.4	
Si_3N_4/20 v/o ARCO SiC	1	6.4	
	2	12.5	
(Density: 3.18 g/cc)	3	11.6	10.0
	4	10.1	
	5	10.3	
	6	8.9	

TABLE 4

WHISKER IMPURITY ANALYSIS

Element	Tateho SCW #1[1]	Tokai 'Tokamax'[1]	ARCO SC-9[1]	ORNL SC-9[2]	ORNL F-9[2]
Ca	0.099	(3)	0.160	0.010	0.100
Mn	0.015	0.005	0.110	0.010	0.100
Al	0.120	0.050	0.081	0.020	0.070
Fe	0.045	0.023	0.050	0.010	0.100
Mg	0.007	0.005	0.059	0.030	0.030
Cr	(3)	(3)	0.014	0.005	0.100
Na	0.400[4]	0.400[4]	0.400[4]	0.003	0.003
Co	(3)	0.290	(3)	(5)	(5)
Zr	0.110	(3)	(3)	(5)	(5)
Ni	0.014	0.014	0.014	(5)	(5)
Cu	0.005	0.005	0.005	(5)	(5)
Zn	(3)	(3)	0.180	(5)	(5)
Ti	0.090	0.140	(3)	(5)	(5)

Notes:

(1) Analyzed by Signal Research Center (SRC) via emission analysis.
(2) Data on material from ORNL Semiannual Report for October 1983 to March 1984.
(3) Analysis indicated no trace.
(4) 0.400% is lowest detection limit for Na. Values are not indicative of actual amount of Na in the material.
(5) Not measured or not indicated.

Analyses for V, Sn, Pb, Mo, B, Ba and Sr by Signal showed no trace.
Analyses by ORNL for K on ORNL SC-9 and F-9 showed 0.002% for SC-9, higher % for F-9. SRC did not analyze for K.

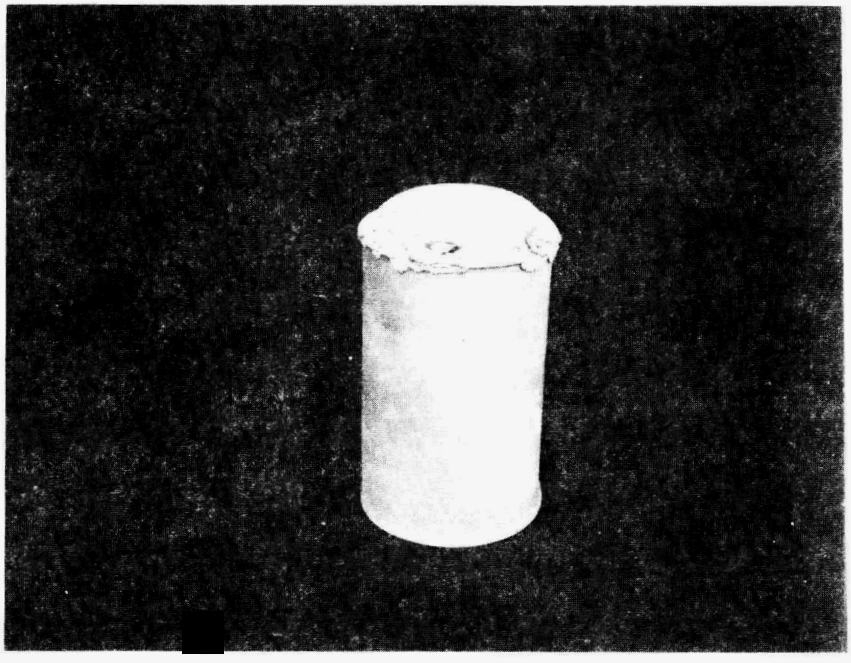

Figure 1: Encapsulated Si_3N_4/Tateho SiC sample (HIP run #488).

Figure 2: Nb encapsulated Si_3N_4/SiC whisker samples (after HIP).
Left Can: Si_3N_4/Tateho SCW #1.
Right Can: Si_3N_4 ARCO SC-9.

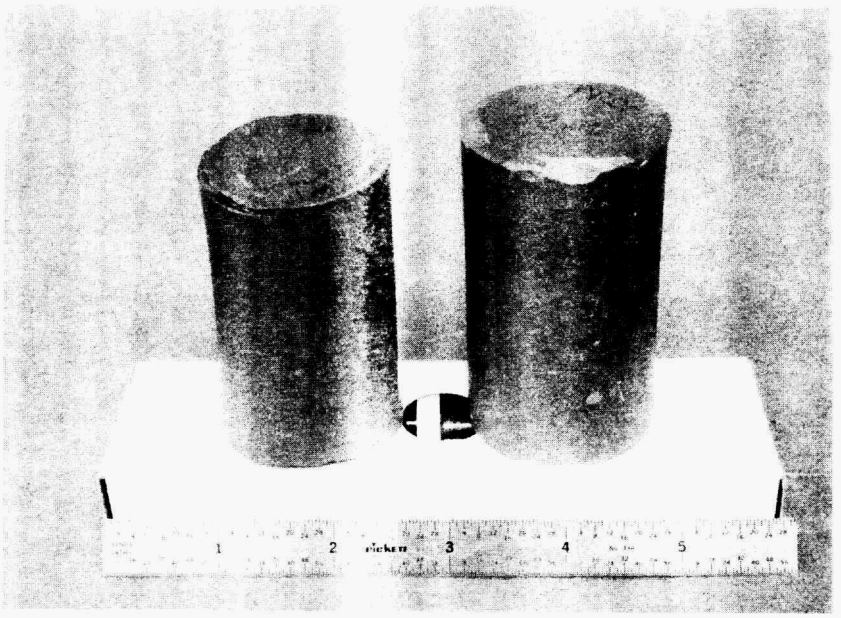

Figure 3: HIP'ped Si_3N_4/SiC whisker samples with Nb encapsulant removed.
Left Sample: Si_3N_4/Tateho SCW #1.
Right Sample: Si_3N_4/ARCO SC-9.

4A

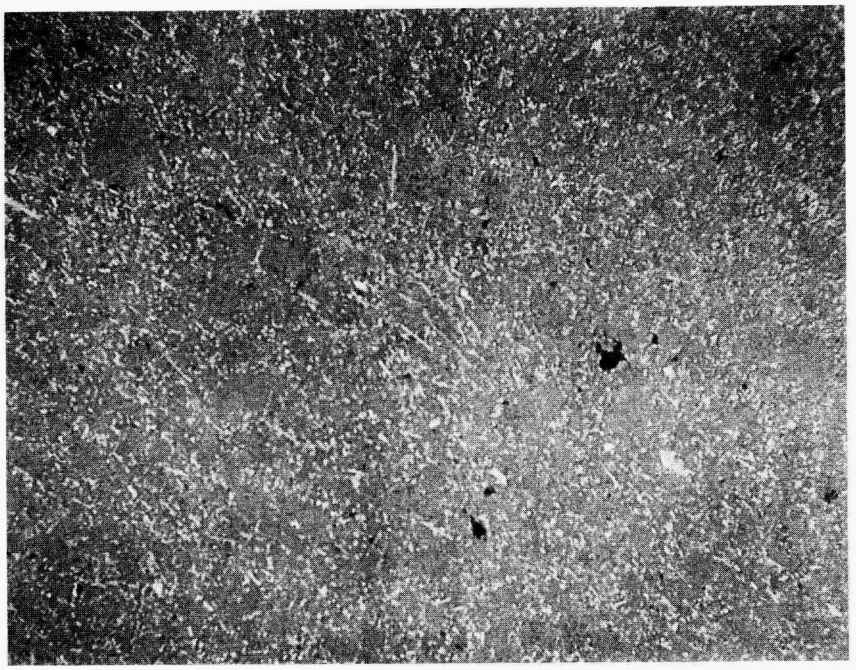

400X

4B

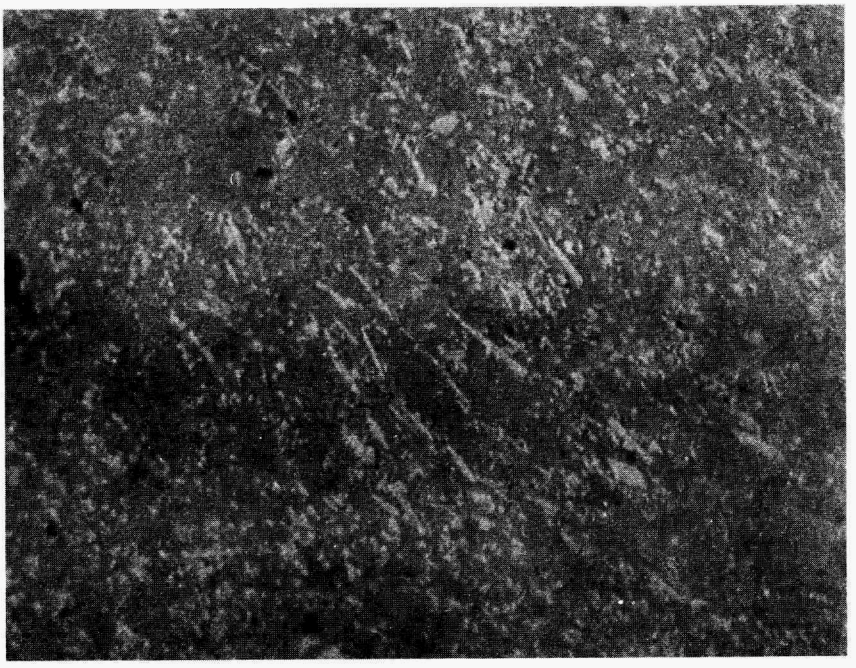

1000X

Figures 4A & 4B: Polished micrographs of SiC orientation and distribution in sample containing 20% ARCO SiC.

5A

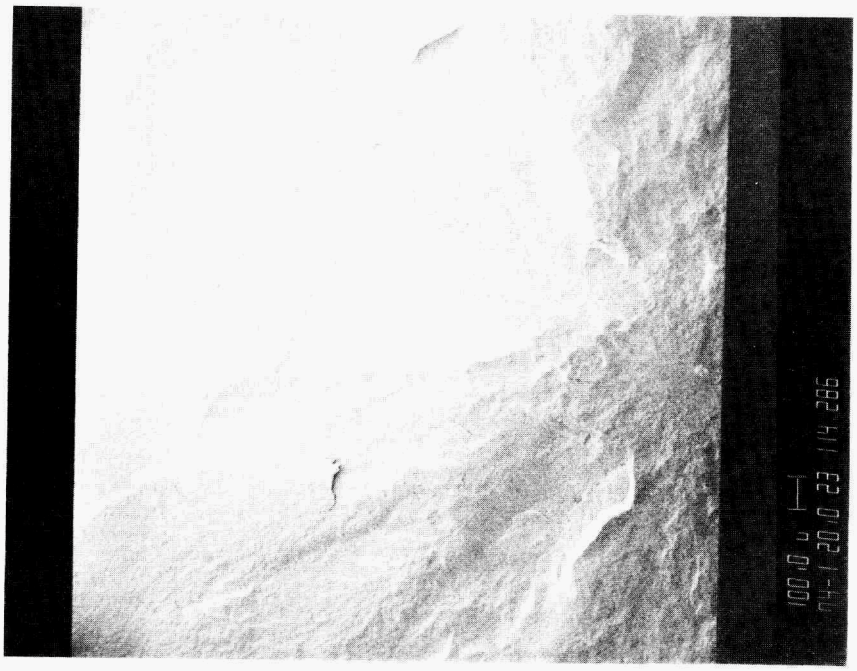

5B

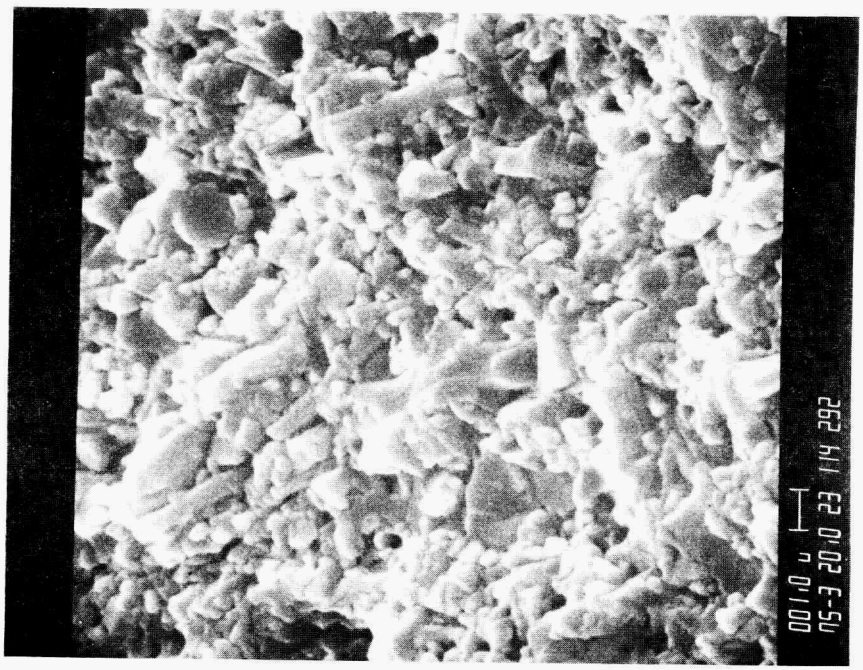

Figures 5A & 5B: SEM of fracture surface of sample containing 20% ARCO SiC.

6A

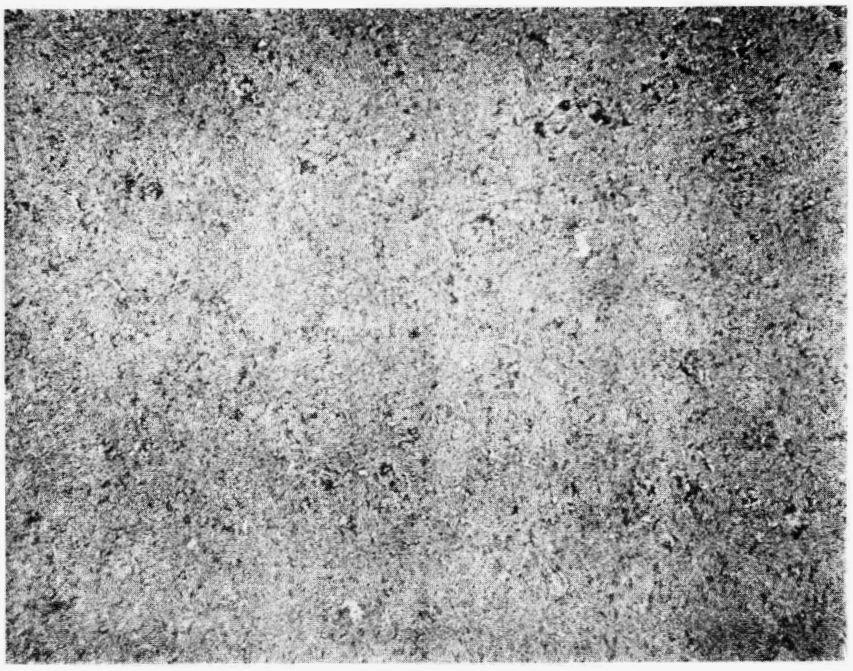

400X

6B

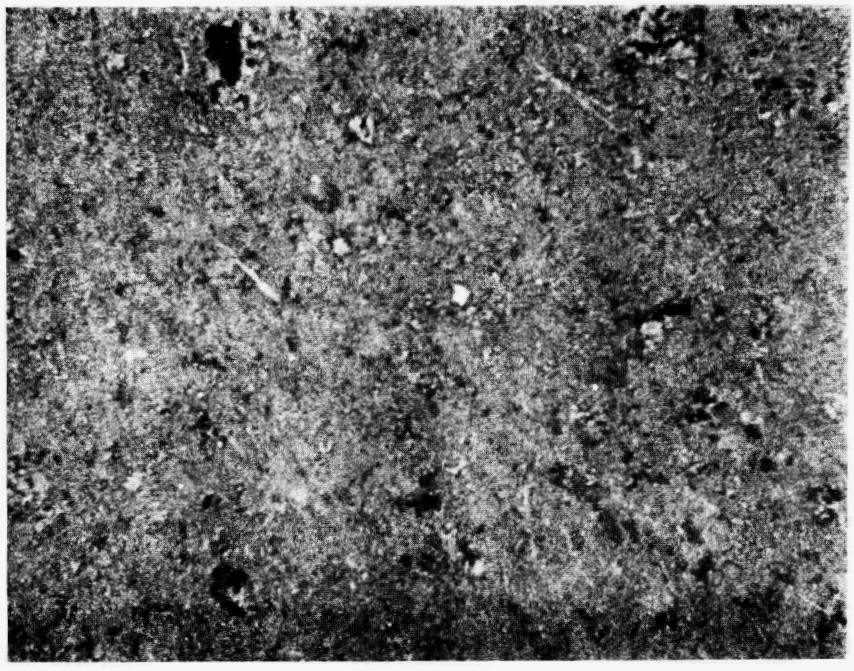

1000X

Figures 6A & 6B: Polished micrographs of as nitrided SRBSN containing 15% ARCO SiC.

Figure 7A: HIP'ped Si_3N_4/ARCO SC-9 (400X).

Figure 7B: HIP'ped Si_3N_4/Tateho SCW #1 SiC (400X).

8A

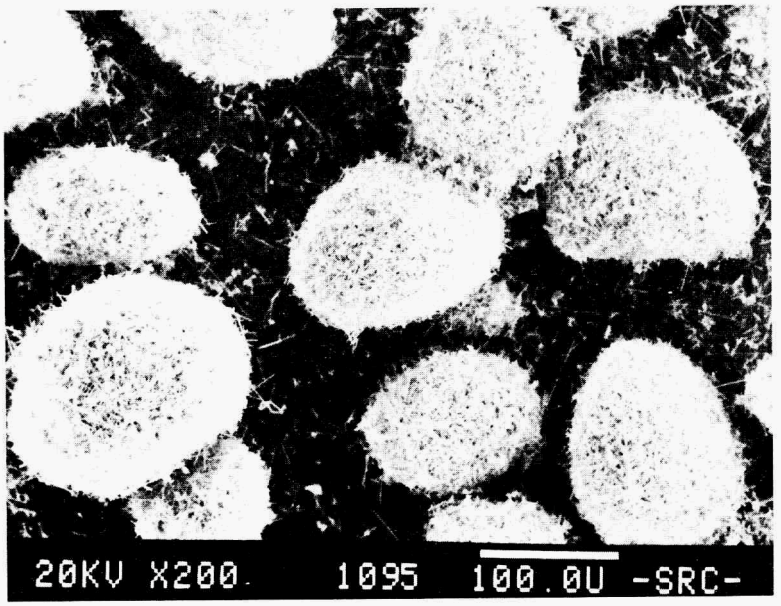

8B

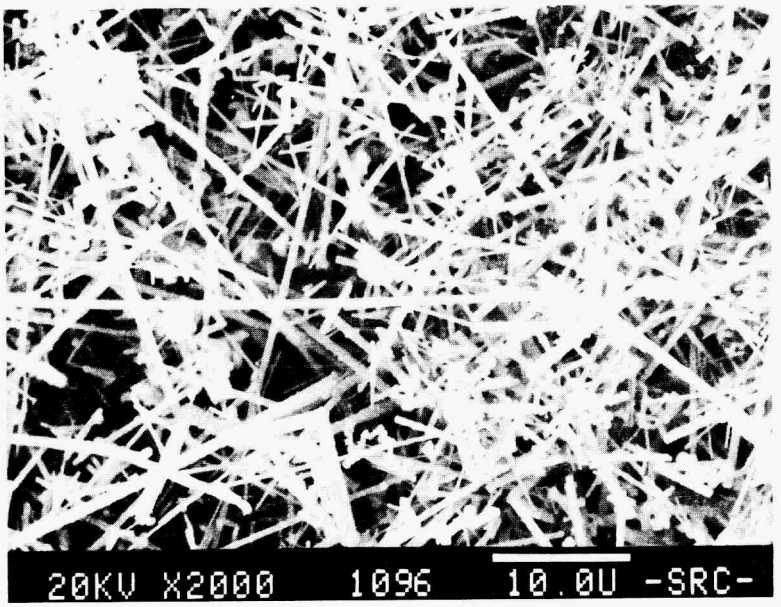

Figures 8A & 8B: ARCO SC-9 silicon carbide whiskers.

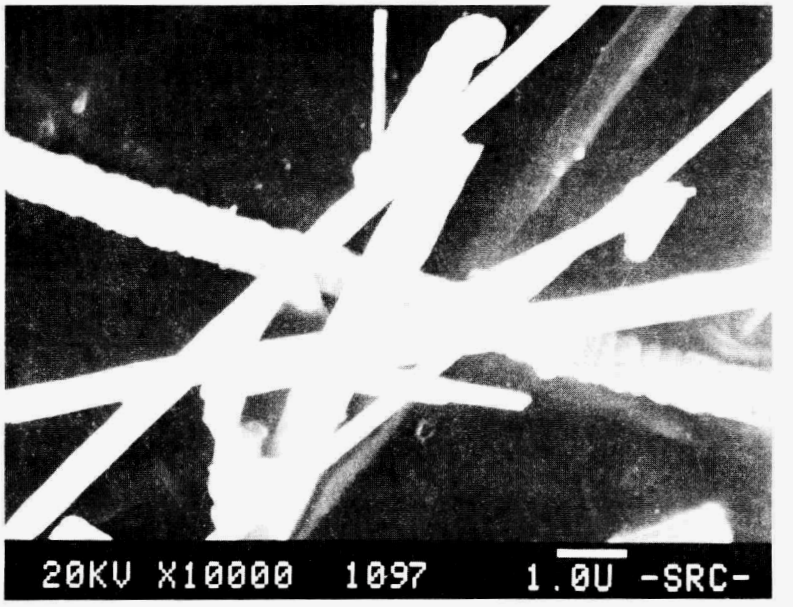

Figure 8C: ARCO SC-9 silicon carbide whiskers.

9A

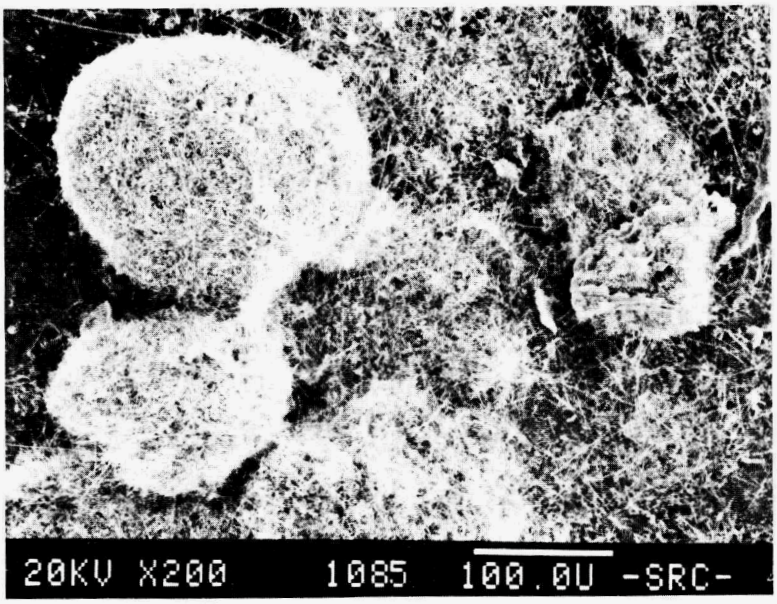

9B

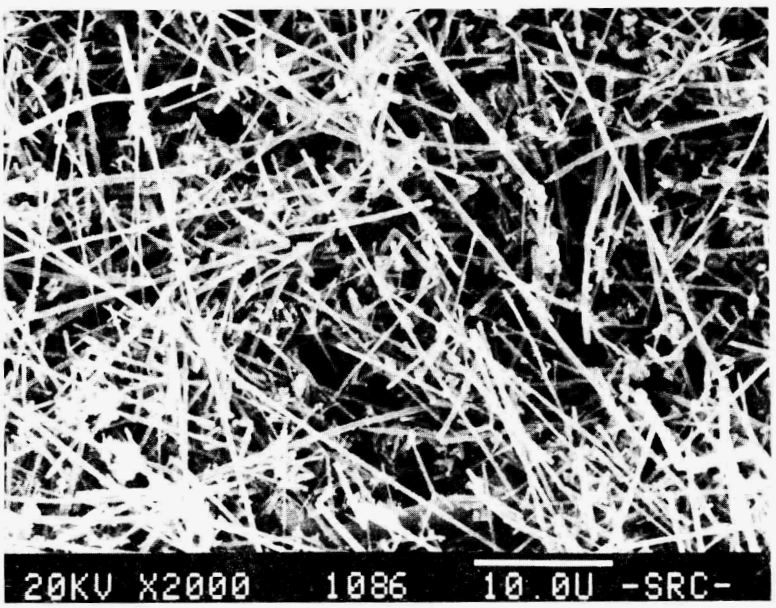

Figures 9A & 9B: Tateho SCW #1 silicon carbide whiskers.

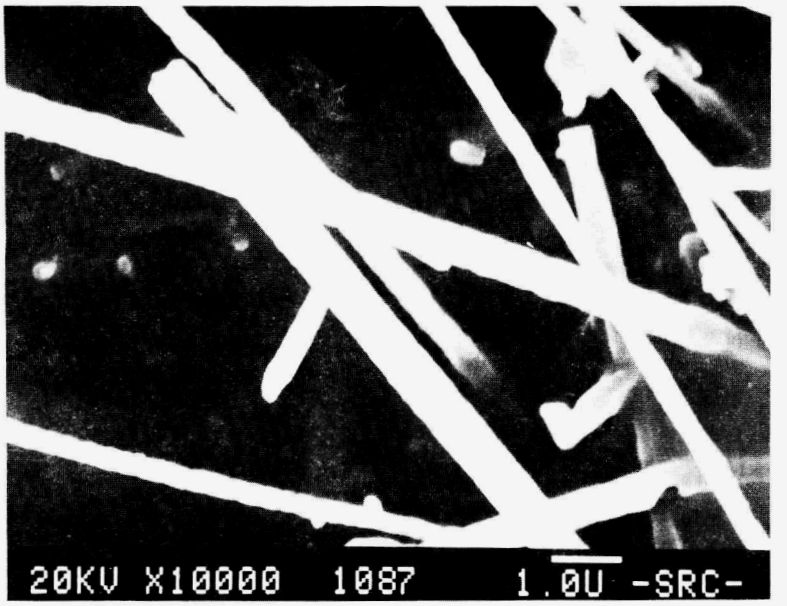

Figure 9C: Tateho SCW #1 silicon carbide whiskers.

10A

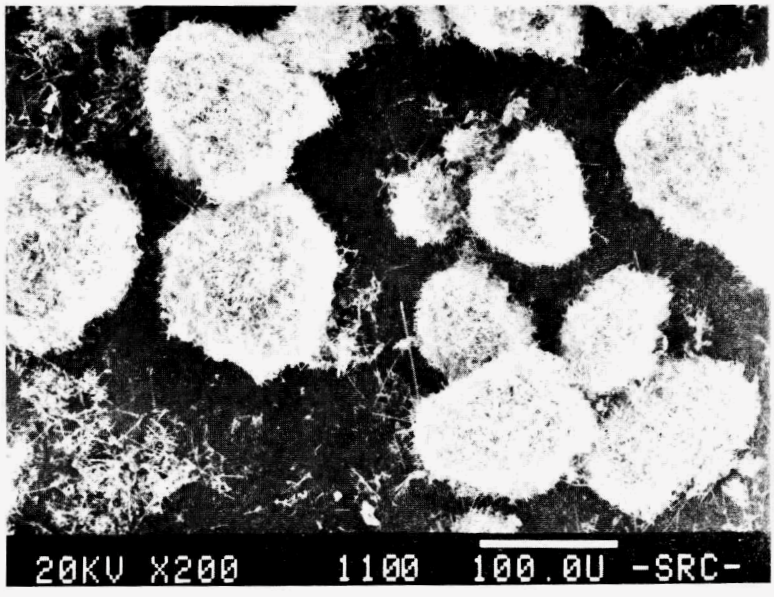

10B

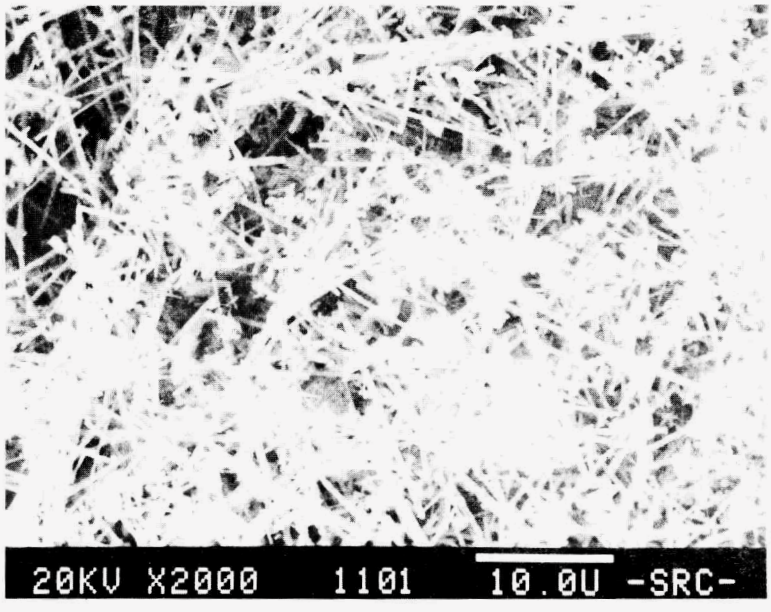

Figures 10A & 10B: Tateho SCW #1-S silicon carbide whiskers.

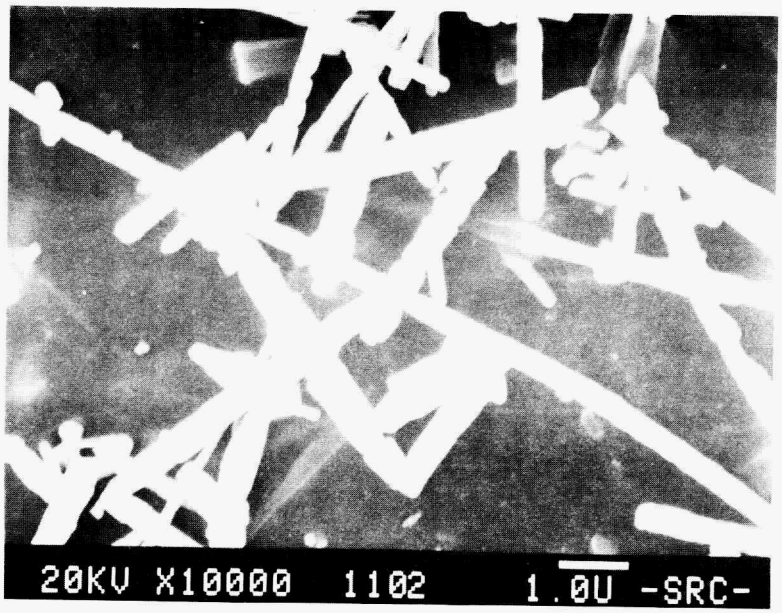

Figure 10C: Tateho SCW #1-S silicon carbide whiskers.

11A

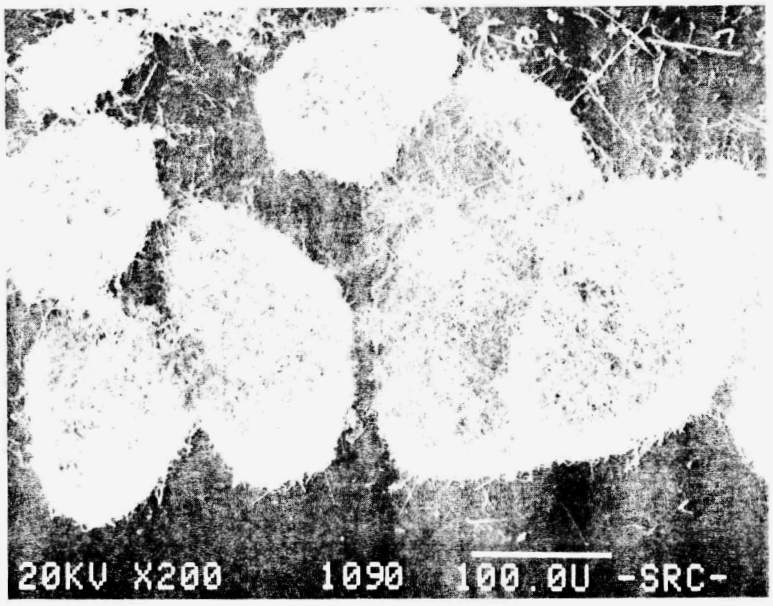

11B

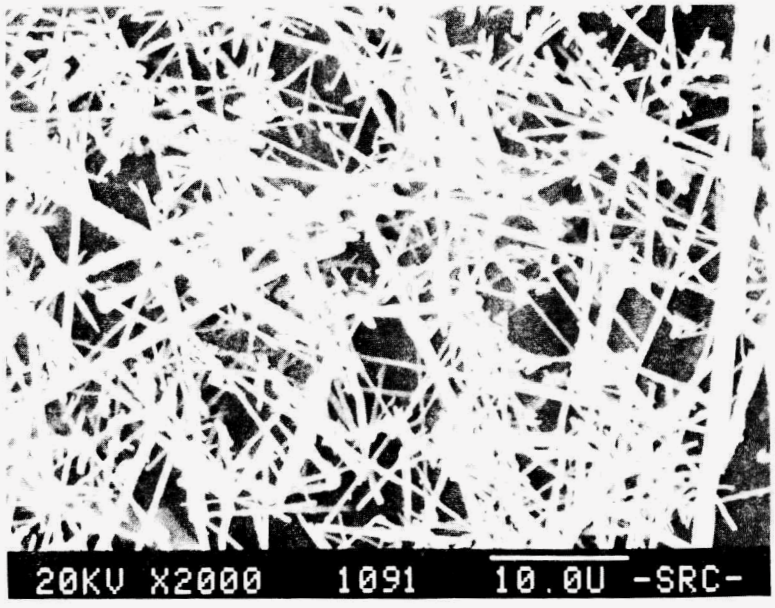

Figures 11A & 11B: Tokai Tokamax silicon carbide whiskers.

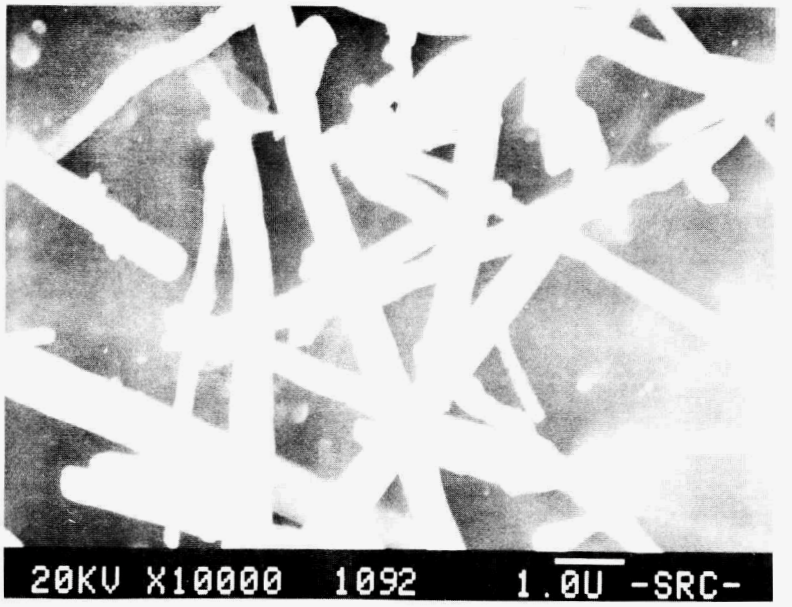

Figure 11C: Tokai Tokamax silicon carbide whiskers.

12A

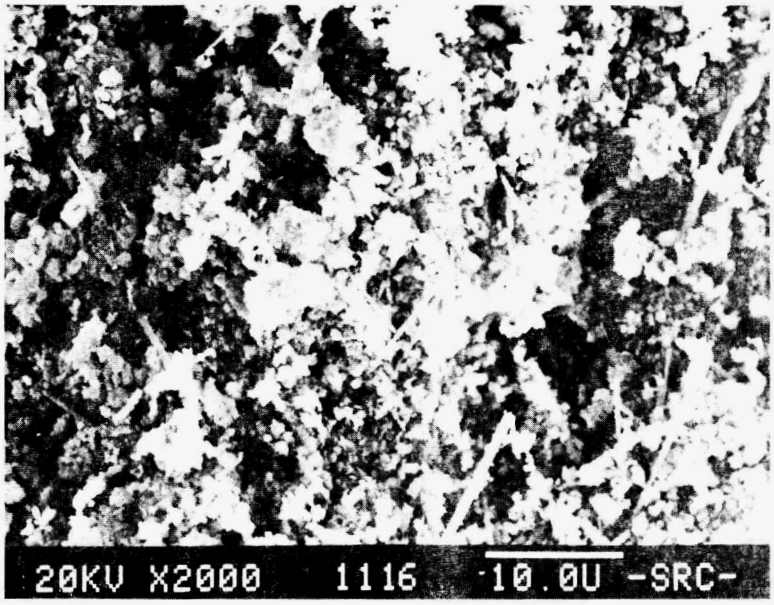

12B

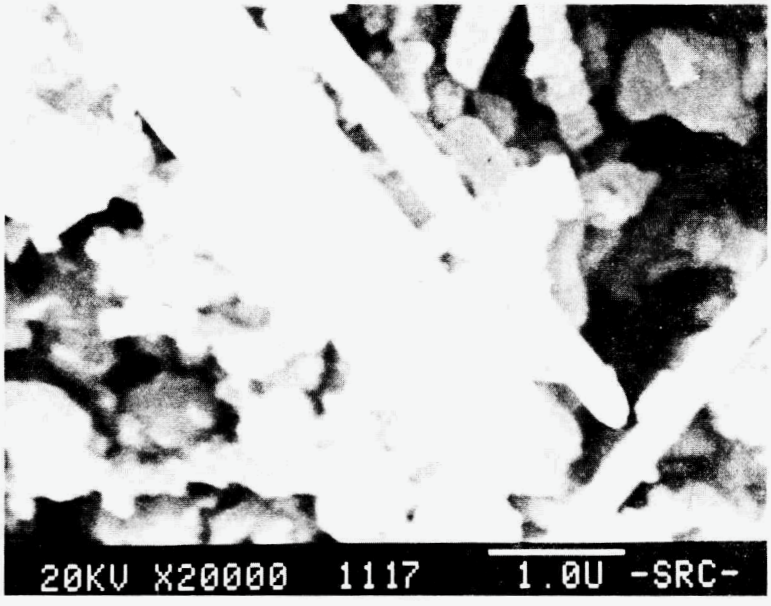

Figures 12A & 12B: Slip cast Si_3N_4/ARCO SC-9 SiC whiskers.

13A

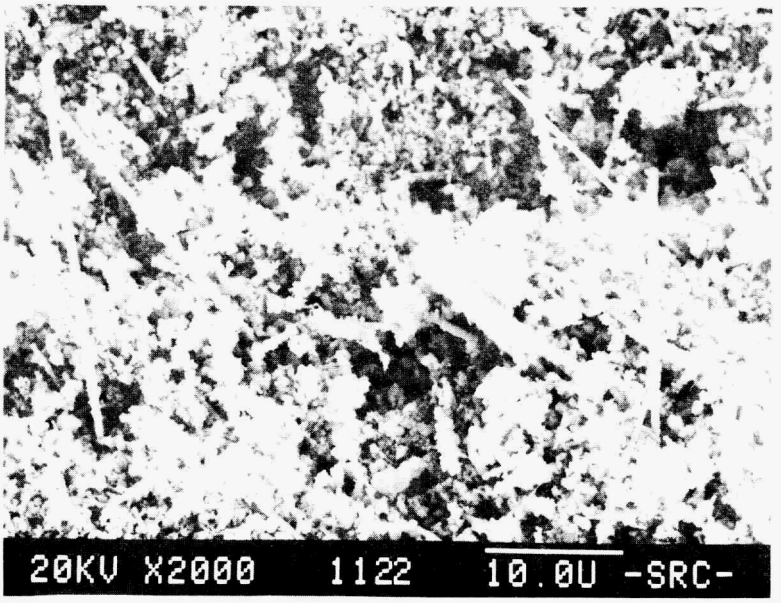

13B

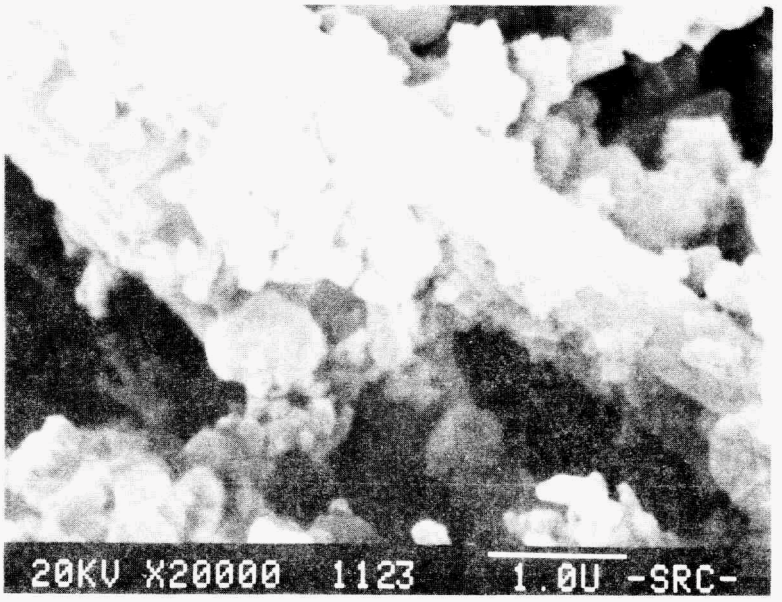

Figures 13A & 13B: Slip cast Si_3N_4/coated ARCO SC-9 SiC whiskers.

14A

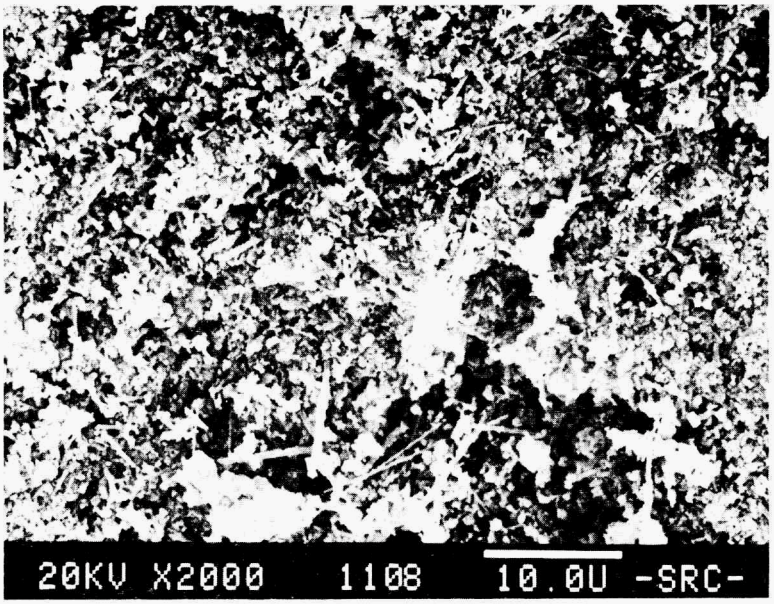

14B

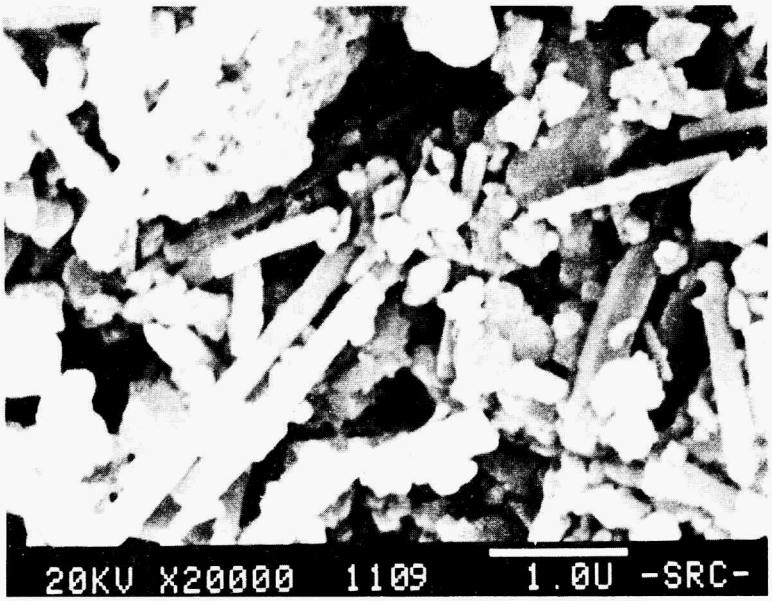

Figures 14A & 14B: Slip cast Si_3N_4/Tateho SCW #1 SiC whiskers.

15A

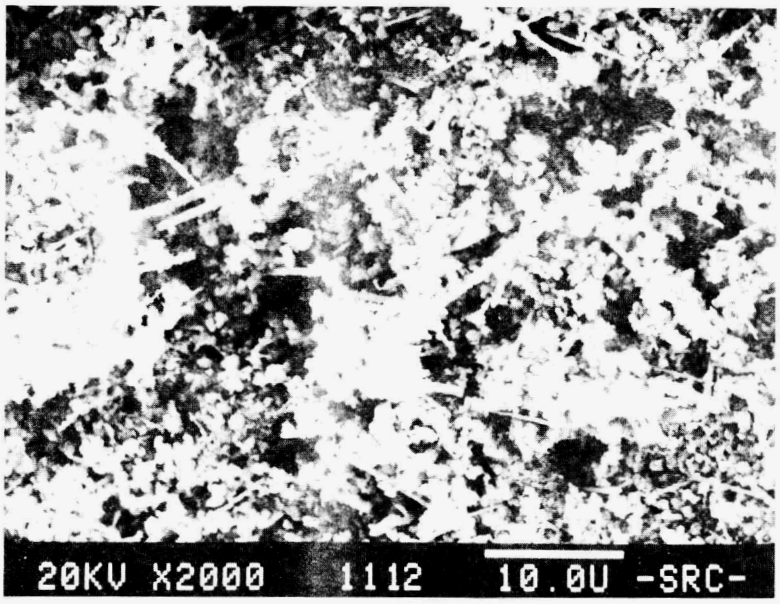

15B

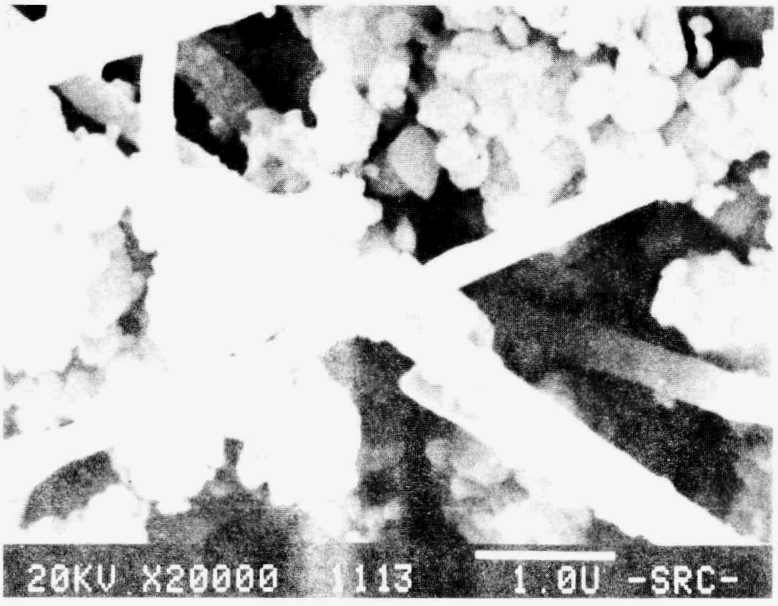

Figures 15A & 15B: Slip cast Si_3N_4/Tokai Tokamax SiC whiskers.

1.2.3 Oxide Matrix

SiC-Whisker-Reinforced Ceramic Composites

T. N. Tiegs, P. F. Becher, and L. A. Harris (Oak Ridge National Laboratory)

Objective/scope

This work involves development and characterization of SiC-whisker-reinforced oxide composites for improved mechanical performance. To date, most of the work has dealt with alumina as the matrix because it was deemed a promising material for initial study. However, optimization of matrix materials is also explored. The approach to fabrication is to first use hot pressing to identify compositions for toughening and then to explore pressureless sintering for fabrication to near net shape.

Technical progress

SiC whiskers

As part of a program to study the whisker–alumina matrix interface, we undertook an initial examination of the whiskers of interest and a preliminary transmission electron microscopy (TEM) examination of a hot-pressed composite.

X-ray photoelectron spectroscopy (XPS) scans were made of the surfaces of three groups of SiC whiskers identified as ARCO, LANL, and Tateho. Table 1 contains quantitative data on the SiC whiskers computed from high-resolution XPS scans. The LANL whiskers had considerably less oxygen on their surfaces than either of the other whiskers but did contain nitrogen and fluorine. The nitrogen is believed to be related to the synthesis process, whereas fluorine is probably due to the hydrofluoric acid treatment used to remove excess silica from the whiskers. The elemental concentrations on the surfaces of the ARCO and Tateho whiskers show strong

Table 1. Elemental concentrations on the surfaces of SiC whiskers

Sample	Elements					
	Si	C	O	N_2	F	Ca
ARCO[a]	22.25	51.69	25.76			0.31
LANL[b]	26.73	56.90	12.22	3.10	1.05	
Tateho[c]	21.01	49.35	29.63			

[a]ARCO Chemical Co., Greer, S.C.

[b]Los Alamos National Laboratory, N. Mex.

[c]Tateho Chemical Co., Japan.

similarities especially with respect to silicon and carbon. However, the Tateho whiskers are much richer in oxygen and do not appear to contain any detectable minor elements such as the calcium found in the ARCO material.

In addition to the elemental composition of the whisker surfaces, XPS supplies information about the chemical state of the elements. Table 2 lists the bonding energies (B.E.) for the major constituents: silicon, carbon, and oxygen. These B.E. values have been adjusted to compensate for possible charging normally associated with insulator material. A comparison of B.E. for elements on LANL and ARCO whiskers reveals strong similarities; the silicon B.E. value of 100.5 eV is in agreement with values we obtained for silicon in single crystals of SiC. Particularly noteworthy are the carbon B.E. peaks at about 282 eV and 284 eV; the first value we believe is carbon in SiC while the second value (higher B.E.) is due to free carbon. The dual peaks are most prominent in the LANL whiskers. Additional similarities between ARCO and LANL whiskers exist for oxygen B.E. values. In contrast, Tateho fibers have silicon and oxygen B.E. values that suggest the presence of silica.

Table 2. Bonding energy of major elements on the surfaces of SiC whiskers (eV)

(Bonding energy peak positions have been corrected for charging)

Phase identification	Sample	Elements		
		Si	C	O_2
α/β SiC	ARCO	100.5	282 284	532.05
β SiC + C	LANL	100.5	282 284	531.5
α/β SiC	Tateho	103.05	284	532.8

Examination by TEM of a hot-pressed alumina–20 vol % SiC whisker composite made with ARCO whiskers showed little interaction between the whiskers and the matrix. In addition, no evidence of matrix microcracking was observed around the whiskers.

Oxidation of SiC-whisker-reinforced composites

As reported previously, considerable oxidation of alumina–SiC whisker composites occurs at temperatures of 800 to 1200°C, resulting in degradation of flexural strength. Apparently there is sufficient oxygen transport through the alumina matrix. Review of some literature indicated that oxygen transport through a mullite matrix should be significantly lower. Consequently, specimens of a hot-pressed mullite–20 vol % SiC whisker composite were subjected to isothermal oxidation at elevated temperatures. The

results are summarized in Table 3. As shown, the mullite-matrix composites had considerably lower weight gains than the alumina-matrix composites. Thus oxidation of SiC-whisker-reinforced ceramic composites may be minimized by the use of mullite matrices or by the formation of a protective mullite coating on alumina-matrix composites. We are planning to determine any strength degradation in the mullite-matrix composites and to perform isothermal heating tests.

Table 3. Results of isothermal oxidation for 500 h of 20 vol % SiC whisker–ceramic matrix composites

Ceramic matrix	Oxidation temperature (°C)	Weight gain (g/m^2)
Mullite	800	~0[a]
Mullite	1000	0.329
Alumina	800	0.738
Alumina	1000	1.774

[a]Measurements at detection limit of instruments.

Hot pressing

As reported previously, hot-pressed alumina composites made with SiC whiskers from different sources had considerably different mechanical properties. A new batch of SiC whiskers from Tateho that apparently had lower oxygen content than previous batches was tested as an alternate source of whiskers. Hot-pressing results at 1850°C (typical for previous composite studies) were not encouraging; however, at lower hot-pressing temperatures (~1600°C) whisker degradation appeared to be minimized. In addition, the whiskers appeared to survive during pressureless sintering of alumina–SiC whisker composites. Mechanical property tests on the composite hot pressed at 1600°C, along with a comparable one made with ARCO whiskers, are summarized in Table 4. As shown, the composite fabricated with Tateho SiC whiskers was not as tough or strong as the composite made with the ARCO whiskers. Although the properties are somewhat poorer, the composite with the new Tateho whiskers is better than one made initially with Tateho whiskers.

Table 4. Summary of mechanical properties for alumina–20 vol % SiC whisker composites made with different whiskers

Source of SiC whiskers	Fracture toughness, K_{Ic} (MPa·m$^{1/2}$)	Flexural strength[a] (MPa)
Tateho	5.1	535
Arco	7.8	700

[a]Four-point flexural test.

Examination of the fracture surfaces showed the Tateho whiskers to be intact. However, some interaction between the whiskers and the matrix was evident. This may have resulted in increased bonding between the whiskers and matrix, thus diminishing the effect of crack deflection toughening.

Pressureless sintering

Alumina–SiC whisker composites containing 5, 10, 15, and 20 vol % whiskers were fabricated by pressureless sintering and then machined into mechanical test specimens. A summary of the fabrication route used is shown in Fig. 1. Flexural strengths at room temperature and elevated temperature (1000°C) are given in Tables 5 through 8.

As shown, the flexural strength is dependent on the sintered density and flaw size of the samples, which is typical for ceramic materials. The flaws inadvertently introduced in compositions SCW-132, -135, -136, and -137 were due to a poor binder selection (the effect was large voids >100 μm in diameter), although good densities were achieved. Thus, as with all ceramic materials, the importance of processing cannot be underestimated. With good powder and whisker preparation, sample forming, binder removal, and firing, high densities [>94% of theoretical density (T.D.)] were achieved with good flexural strengths. An average of about 330 MPa was obtained for pressureless sintered alumina–10 vol % SiC whisker composites with densities of at least 94% T.D. and no major flaws.

The flexural strength data at 1000°C are limited but do show a relative decrease in strength, which is consistent with that observed in the hot-pressed composites. The fracture toughness, K_{Ic}, of numerous alumina–10 vol % SiC whisker composites was determined (Fig. 2). As shown, the toughness for the composites with the higher densities is on the order of 7 MPa·m$^{1/2}$. This is comparable to the toughness observed for hot-pressed composites with the same whisker loading.

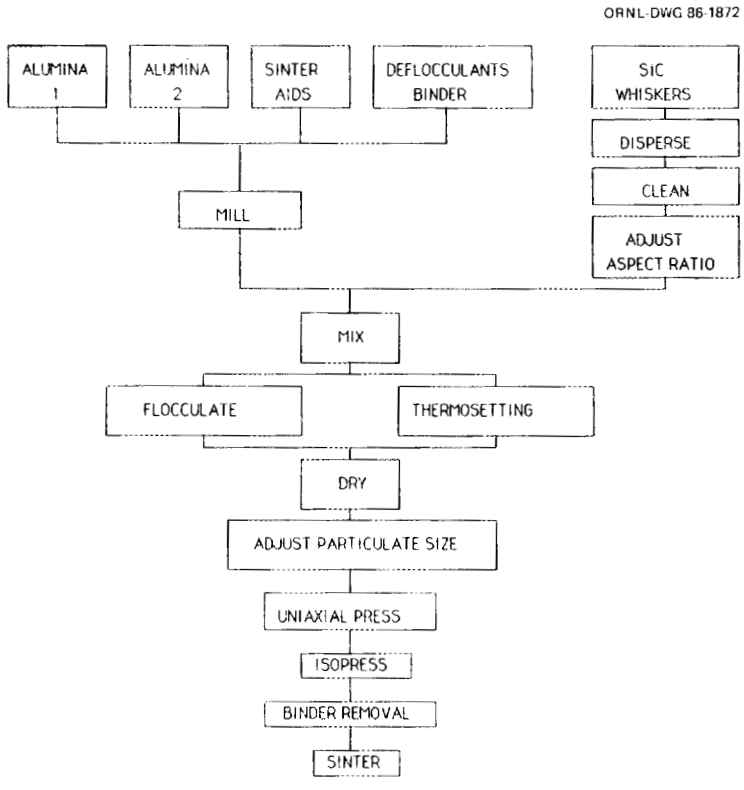

Fig. 1. Summary of fabrication route for pressureless-sintered alumina-SiC whisker composites.

Table 5. Summary of flexural strength of pressureless-sintered alumina-5 vol % SiC whisker composites

Sample	Density (% T.D.)	Flexural strength[a] (MPa)
SCW-51-4	97.9	280
SCW-62-1	98.2	340
SCW-62-2	98.2	360
SCW-62-3	98.2	275
SCW-136-10[b]	99.0	275
SCW-136-13[b]	99.4	290

[a]Four-point flexure test.

[b]Major flaws introduced during processing.

Table 6. Summary of flexural strength of pressureless-sintered alumina–10 vol % SiC whisker composites

Sample	Density (% T.D.)	Flexural strength[a] (MPa)
SCW-68A	92.0	295
SCW-68-60	93.0	280
SCW-69-5	93.0	260
SCW-83-1	92.6	275
SCW-83-60	96.0	310
SCW-90-60	94.8	310
SCW-108-10	95.2	370
SCW-114-7	94.2	315
SCW-114-9	88.2	200
SCW-115-3	96.4	370
SCW-115-4	96.4	310
SCW-115-10	93.0	305
SCW-115-12	93.0	305
SCW-119-6	92.2	250
SCW-127-1	96.5	370
SCW-132-4[b]	93.3	290
SCW-132-5[b]	95.5	275
SCW-132-6[b]	94.1	290
SCW-135-4[b]	95.3	270

[a]Four-point flexure test.

[b]Major flaws introduced during processing.

Table 7. Summary of flexural strength of pressureless-sintered alumina composites with 15 and 20 vol % SiC whiskers

Sample	SiC whisker content (vol %)	Density (% T.D.)	Flexural strength (MPa)[a]
SCW-70B	15	78.4	195
SCW-70-60	15	81.8	190
SCW-137-4[b]	15	83.5	215
SCW-125-3	20	80.9	230
SCW-125-4	20	89.9	365
SCW-125-5	20	78.5	200

[a]Four-point flexure test.

[b]Major flaws introduced during processing.

Table 8. Summary of elevated-temperature flexure strength of alumina–SiC whisker composites

Sample	SiC whisker content (vol %)	Flexure strength (MPa)[a]	
		Room temperature	1000°C
SCW-108-10	10	370	280
SCW-115-12	10	305	210
SCW-119-6	10	250	240
SCW-132-4[b]	10	290	240
SCW-132-6[b]	10	290	240
SCW-135-4[b]	10	270	320
SCW-136-10[b]	5	275	240

[a]Four-point flexure test.

[b]Major flaws introduced during processing.

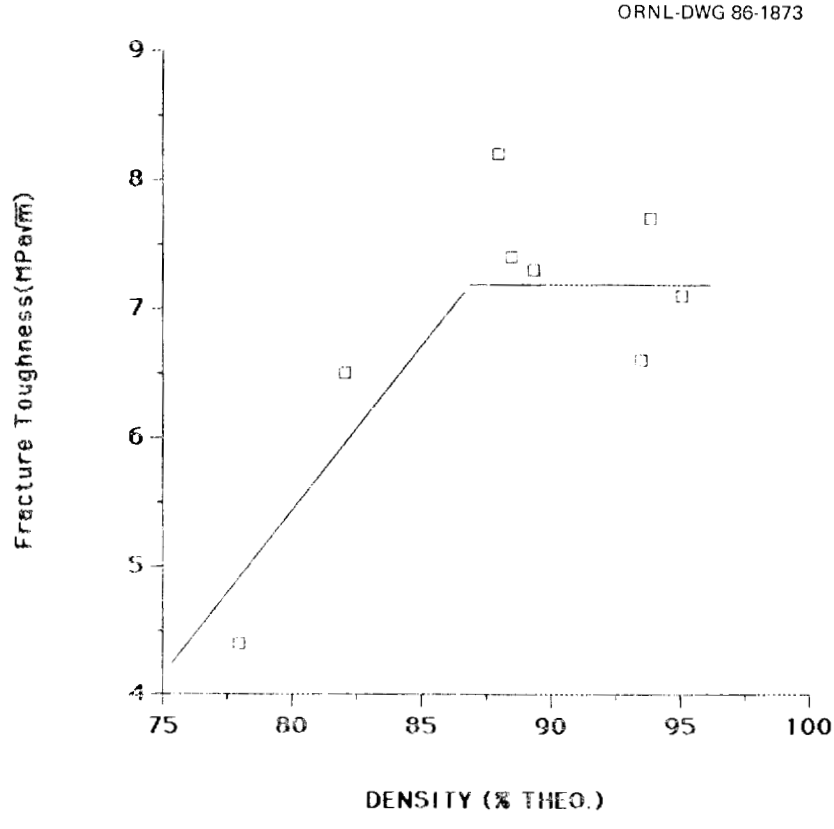

Fig. 2. Summary of fracture toughness of pressureless-sintered alumina–10 vol % SiC whisker composites.

Status of milestones

Milestone 123103 was completed this reporting period, "Complete Study of Mechanical Properties of Pressureless Sintered Whisker Reinforced Ceramic Matrix Composites." All other milestones are on schedule.

Publications

T. N. Tiegs and P. F. Becher, "Alumina-SiC Whisker Composites," to be published in proceedings of the 1985 23rd Automotive Technology Development Contractors' Coordination Meeting by the Society of Automotive Engineers.

Sol-Gel Oxide Powder

W. D. Bond, P. F. Becher, and T. N. Tiegs (Oak Ridge National Laboratory)

Objective/scope

Sol-gel processes have the potential for the synthesis of materials that can be processed at modest temperatures while obtaining highly uniform composition in dense, fine-grain ceramics that incorporate dispersed second phases to increase fracture toughness. This research emphasizes the determination of the feasibility of sol-gel processes for (1) synthesizing powders of phase stabilized zirconia and alumina and (2) coating whiskers to control their interface properties to matrix phases. Sol-gel processes take advantage of the high degree of homogeneity that can be achieved by mixing on the colloidal scale and the surface properties of the colloidal particles. The excellent bonding and sintering properties of colloids are a result of their very high specific surface energy.

The work reported here is performed in a collaborative effort in the Material Sciences Program tasks of the Structural Ceramics Group in the Metals and Ceramics Division. The synthesis of sol-gel materials is carried out in the Ceramics for Advanced Heat Engines Project. The densification, characterization, and mechanical properties studies on compacts of the sol-gel powders are performed in the Materials Sciences Program.

Technical progress

Studies in this report period were concerned with (1) the sol-gel process parameters that influence the uniformity of yttria and (2) the preparation of colloidal zirconia and hafnia by hydrothermal reactions in an autoclave at 175 to 200°C. It was clearly shown that the pH of the precursor Al_2O_3-ZrO_2-Y_2O_3 sols governs the homogeneity of Y_2O_3 in gel-derived powders. Initial studies show that hydrothermal precipitation of ZrO_2 and HfO_2 at elevated temperatures is a promising method for the synthesis of highly crystalline colloidal oxides.

Studies are continuing on the sol-gel process parameters that influence the uniformity of yttria distribution in zirconia. Results are showing that materials derived from sols having pH values of 7 or less are reasonably uniform in Y_2O_3 distributions, whereas those derived from sols of pH 4 or less are nonuniform.

The uniformity in composition was determined by measuring the alumina, zirconia, and yttria energy peaks as a function of position on the samples by using the electron microprobe operating with an effective beam diameter of 1 to 2 μm. The composition ratios were determined by translating the specimens in 2-μm increments for a total translation of 50 μm with 2 to 3 such scans at different regions of the samples. Both calcined gel powders and dense ceramic composite pieces were analyzed. The results given here are for the dense ceramics because only minor differences were found for powders and dense pieces. The dense ceramics were fabricated from Al_2O_3-ZrO_2-Y_2O_3 gels that were prepared by the relatively slow evaporation of water from the bulk sols at various pH levels at 80°C.

Uniformity of the Y_2O_3 content was reflected both by plots of Y/Zr ratios (or mol % Y_2O_3 in ZrO_2) as a function of microprobe beam position and by obtaining the magnitude of one standard deviation of the mean of the mol % Y_2O_3 in the ZrO_2. For sols prepared at low pH values (pH ≤4, acidic conditions) the results showed that the scatter in the Y/Zr ratios or mol % Y_2O_3 in the ZrO_2 was quite large. Typically one standard deviation from the mean mol % Y_2O_3 in ZrO_2 was at least ±50% of the mean value. On the other hand, dense samples obtained from sols prepared at pH values of 7 or higher had much more uniform Y_2O_3 distributions (Fig. 1). In most cases, standard deviation from the mean mol % Y_2O_3 was ±20% or less of the mean value. Some samples showed wider variation in Y_2O_3 contents. However, any nonuniform distributions of Y_2O_3 in these samples were localized to regions of 10 μm or less in size in the microstructure, and the overall Y_2O_3 distribution was substantially more uniform for the higher-pH sols.

The reason for the nonuniform Y_2O_3 distribution in gels prepared from sols having low pH values can best be attributed to the observed increase in Y_2O_3 solubility with decreased pH. The greater solubility of Y_2O_3 at low pH means that the Y_2O_3 is removed from the ZrO_2 particles in the sol and some of the Y_2O_3 exists as a solute in the aqueous medium. The soluble Y_2O_3 content of the aqueous medium increases with decreasing pH. When the sol is gelled, more of the soluble Y_2O_3 reprecipitates out as the aqueous medium is evaporated. Thus, the initial portion of the sol to gel has a lower Y_2O_3 content than the final portion to gel. When these gels are then calcined and milled to form powders, significant variations in Y_2O_3 content result.

On the other hand with sols prepared at pH values of 7 to 9.5, the Y_2O_3 solubility in the aqueous medium is extremely low (e.g., $\geq 1 \times 10^{-3}$ mmol at pH ≥7.6). Therefore, the Y_2O_3 is not significantly redistributed during slow gelation, and much more uniform Y_2O_3 distributions are obtained.

Complete hydrothermal precipitation of the colloidal oxides of ZrO_2 and HfO_2 occurred when 0.25 to 1.0 M solutions of the metal salts were heated in an autoclave for 4 h at 200°C. At 175°C the precipitation was complete for ZrO_2 but was incomplete for HfO_2. The ZrO_2 was precipitated from zirconyl nitrate solution whereas HfO_2 was precipitated from hafnyl chloride. Hydrosols of ZrO_2 or HfO_2 were formed from the precipitates after appropriate removal of acid (HNO_3 or HCl) from the solids-liquid reaction products that were formed hydrothermally in the autoclave. The bulk of the acid was removed from the reaction product by separating the mother liquor from the precipitate by centrifugation. Final adjustment to effect sol formation was accomplished by making batch additions of anion exchange resin (hydroxide form) to an aqueous slurry of the separated precipitate to remove additional acid. When the final acidity was reduced to a pH of 4, highly stable sols were formed. The resin particles (50–100 mesh) were removed from the sol by filtration. No separation of solids has occurred from these sols after 2 months of storage. These colloidal oxides are highly crystalline (8–10 nm), whereas ZrO_2 and HfO_2 oxides prepared by conventional precipitation methods at 25 to 80°C are amorphous. The use of high temperatures (175 to 200°C) promotes rapid crystal growth.

ORNL-DWG 86-1902

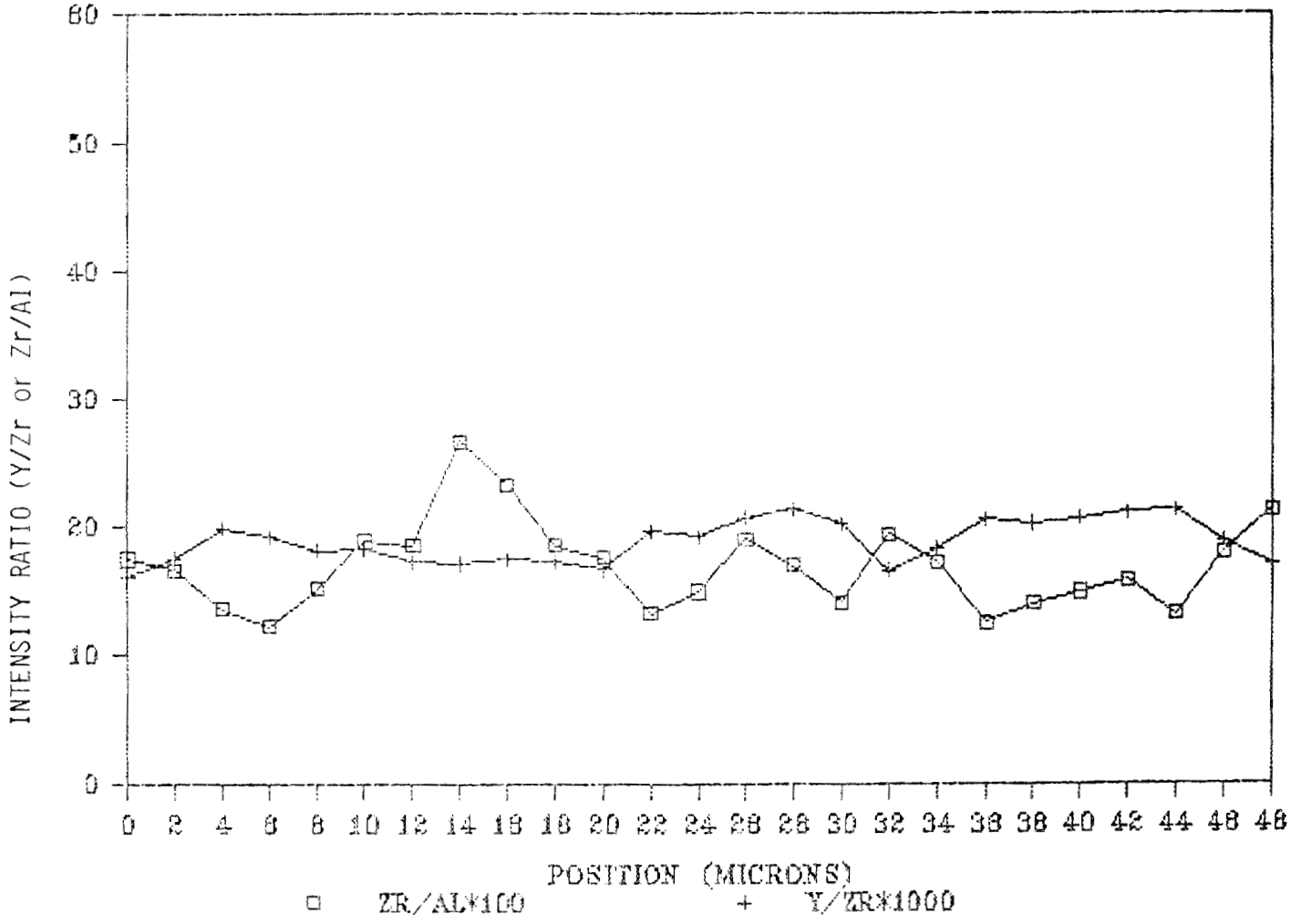

Fig. 1. Uniformity of yttria distribution in ceramic composites derived from oxide sols of pH 7 or higher.

Status of milestones

Progress on gel powder synthesis variables (Milestone 12 33 03) is on schedule.

Publications

None.

Processing of Improved Transformation-Toughened Ceramics

G.A.Rossi, C.E.Knapp, K.E.Manwiller (Norton Company)

Objective/Scope

The objective of this program is the production of zirconia toughened ceramics (ZTC) which exhibit strength and fracture toughness superior to those of the "state-of-the-art" toughened ceramics, particularly at high temperature and after prolonged aging at high temperature. In addition, such ceramics should possess low thermal conductivity to minimize heat losses in engine applications.

The scope includes powder synthesis and characterization, powder processing and shape forming, pressureless sintering, characterization of the sintered ceramics and reporting of results.

The main shortcomings of the existing ZTC materials are: rapid drop in mechanical properties vs. temperature, high temperature creep induced by intergranular glassy phases and microstructural instability during prolonged aging at high temperature.

It is, therefore, the aim of this program to develop ceramics with the desired combination of purity, chemical composition and microstructural features, which will exhibit maximum property retention at high temperatures and thermal stability upon aging.

In order to meet the program objectives, two types of powders will be used. The first type is obtained by rapid solidification from the melt, followed by milling, whereas the second type is made by wet chemical synthesis from chemical precursors.

The main advantages of the rapidly solidified (R/S) powders are excellent chemical homogeneity and high particle density. Those of the chemically derived (C/D) powders are high purity and small crystallite size.

Major emphasis in this program will be placed on powder processing and shape forming methods, especially wet forming methods, where the agglomeration problem of the dry powder is circumvented.

The systems to be investigated are: $MgO-ZrO_2$, $Y_2O_3-ZrO_2$ and $ZrO_2-Al_2O_3$.

In the $MgO-ZrO_2$ system we will evaluate the potential of fine grained Mg-PSZ ceramics and will try to produce and characterize the Mg-TZP, analogous to the Y-TZP materials.

In the $Y_2O_3-ZrO_2$ system we will try to improve on the inherent limitations of this system, i.e. low fracture toughness at high temperature, by optimizing the microstructure and doping with MgO or Al_2O_3.

In the $ZrO_2-Al_2O_3$ system we will try to maximize the retention of t-ZrO_2 at room temperature by improvements in the powder synthesis, powder processing and shape forming methods and to enhance the high temperature properties and thermal stability on aging by additions of CeO_2 and /or HfO_2. In addition, Cr_2O_3 additions to Al_2O_3 will be used to lower the thermal conductivity.

Technical Progress

1. Rapidly solidified (R/S) powder

1.1 $MgO-ZrO_2$ system

Four batches of $MgO-ZrO_2$ powder were made by rapid solidification and milling to submicron size. Two of the batches were prepared using baddeleyite and MgO single crystal as feed materials (2.2 w/o and 3.0 w/o MgO). The other two batches (2.8 w/o and 3.1 w/o MgO), of higher purity, were made using E-10 zirconia powder from Magnesium Electron and MgO single crystal. Green bodies were cold isostatically pressed at 207 MPa and sintered in the 1500°C-1600°C range. The results of the characterization of the sintered specimens can be summarized as follows:

A) A lower percentage of MgO results in smaller grain size in the sintered samples.

B) A duplex microstructure was observed in all sintered samples.

C) Lenticular intragranular precipitates (almost certainly t-ZrO_2) were observed in all samples sintered at 1500°.

D) Shrinkage curves obtained by dilatometry have shown that the powders made with baddeleyite densify at a lower temperature.

E) The lenticular precipitates were not detected in samples sintered at 1600°C.

Most of the characterization work was performed on the samples made with the 3.14 w/o $MgO-ZrO_2$ powder obtained by melting zirconia E-10 and MgO, since they showed the most interesting microstructural features. Density measurements and aging/microstructural evaluation were begun and the main results are as follows:

a) An enrichment in $m-ZrO_2$ was detected by XRD on the surface of the sintered pieces. No $m-ZrO_2$ was, however, detected on the polished interior surface. Samples sintered while buried in their own powder showed substantially reduced $m-ZrO_2$ formation on the as fired surface. Loss of MgO on the surface is believed to be the cause of the $m-ZrO_2$ formation.

b) A duplex microstructure was observed in a sample of 3 w/o $MgO-ZrO_2$, with small grains (probably $t-ZrO_2$) averaging 1-2 um and larger grains (almost certainly $c-ZrO_2$) averaging 5-10 um. Furthermore, intragranular $t-ZrO_2$ precipitates were observed in samples aged at 1400°C. The 3 w/o $MgO-ZrO_2$ sample was sintered at 1500°C for 1 hour and had a He density of 5.74 g/cc. From this sample specimens were cut, polished and aged at 1400°C in air for 1 hour and 5 hrs. (The aging had also the purpose of thermally etching the surface.) A control sample was aged at 1400°C for 5 hours and <u>then</u> polished and chemically etched with hot phosphoric acid (130°C) for 3 minutes, to be sure that the microstructure visible in the thermally etched samples was not simply a surface effect.

Fig. 1 shows the sample sintered at 1500°C, polished and aged at 1400°C for 1 hr.

Fig. 2 shows the sample sintered at 1500°C, polished and aged at 1400°C for 5 hrs.

Fig. 3 shows the sample sintered at 1500°C, aged at 1400°C for 5 hrs, polished and chemically etched.

Since the $t-ZrO_2$ intragranular precipitates are more evident in the specimens aged for a longer time, it is concluded that probably they were nucleated during aging, rather than during the cooling period after sintering at 1500°C. TEM analysis of this sample is planned to confirm the nature of the phases present.

Fig. 4 shows the sample sintered at 1600°C, polished and thermally etched at 1400°C, 1 hr.

For the sake of comparison, SEM photomicrographs of samples made with the other three batches are shown in Figs. 5, 6, and 7.

Work is in progress to optimize the microstructure by identifying the best firing and aging conditions, after which the strength and fracture toughness will be measured.

The sintered samples from the 3.1 w/o $MgO-ZrO_2$ batch made with the E-10 powder have shown room temperature MOR (3 pt) around 700 MPa, measured on 1x1x10mm bars.

Preliminary mechanical testing is conducted on these small bars, for which the influence of process related flaws is minimized, only for the purpose of establishing a bench mark for materials evaluation.

1.2 Y_2O_3-ZrO_2 system

1.2.1 4 w/o Y_2O_3-ZrO_2 TZP's

This composition is known to produce TZP ceramics with exceptional strength and good fracture toughness. The submicron powder obtained by milling of the R/S material was either cold isostatically pressed or used to prepare aqueous slips from which billets were slip cast.

The room temperature MOR (4 pt) was measured on .125" x .128" x 1.125" chamfered bars obtained from specimens sintered at 1600°C. For the ceramic made by cold isostatic pressing an average MOR of 875 MPa (22 bars) was measured, with a standard deviation of 158 MPa. For the ceramics made by slip casting an average MOR of 950 MPa (21 bars) with standard deviation of 145 MPa was obtained. Hot isostatic pressing of the sintered samples resulted in much higher strengths, typically in the 1380-1515 MPa range. K_{IC} was measured at room temperature with the microindentation method and typically values around 8 MPa. $m^{1/2}$ were obtained.

The high temperature (1000°C) MOR (3 pt) was also measured in these materials. An average value of 311 MPa (6 bars) with a standard deviation of 27 MPa was measured for sintered samples, whereas an average of 539 MPa (2 bars) with standard deviation of 73 MPa was obtained for samples sintered and then HIPed in Ar at 207 MPa, 1500°C, 1 hr.

1.2.2 20 w/o Al_2O_3/4 w/o Y_2O_3-ZrO_2 composite

It has been reported[1] that alumina addition to Y-TZP's dramatically enhances the strength in HIPed ceramics, and that the peak in strength is obtained for 20 w/o Al_2O_3 addition.

We have tried to disperse submicron alpha alumina powder (20 w/o) in a matrix of R/S 4 w/o Y_2O_3-ZrO_2. In the first attempt two well dispersed slurries of the two powders were ultrasonically mixed and the resulting suspension was slip cast. SEM evaluation of the sintered samples has shown clumps of alpha-alumina exhibiting exaggerated grain growth and areas of well dispersed particles. In these areas a reduction of the grain size of the Y-TZP matrix was noticed, compared to alumina-free Y-TZP's sintered under similar conditions. A second attempt was made using a combination of ultrasonic and milling steps to disperse the two phases. Preliminary inspection has shown a good dispersion of alpha alumina. SEM analysis is under way, as well as mechanical property evaluation, at room temperature and at 1000°C.

1.3 ZrO_2-Al_2O_3 system

Three batches with the following compositions were prepared by melting and rapid solidification:

a) 15 w/o ZrO_2-Al_2O_3
b) 27 w/o ZrO_2-1.2 w/o Y_2O_3-Al_2O_3
c) 38 w/o ZrO_2-1.4 w/o Y_2O_3-Al_2O_3

Composition a) has been used by other researchers (2), (3) to produce ZTA ceramics with maximum strength and fracture toughness. Composition c) is close to the eutectic and b) represents an intermediate situation.

XRD of the as solidifed materials is underway. Small lots of the three batches were milled to a submicron powder and sintering studies have commenced. Samples of the as solidified materials b) and c) were also split into various size fractions. The fine size portions from these two compositions were milled to a submicron powder to compare phases present and properties achieved with the all size versions of both runs. Preliminary results have shown room temperature MOR (3 pt) of 1378 MPa measured on 1x1x10mm bars.

2.0 Chemically derived (C/D) powders

Two methods have been used for the coprecipitation of doped zirconia powders from solutions of chemical precursors.

Method I, for which a patent was issued(4), consists in mixing an ethanolic solution of $ZrCl_4$ and M salt (M=Y, Mg,...) with an ethanolic solution of NaOH.

After the coprecipitation, the slurry is filtered, dried and washed to remove the salt.

Method II, for which a patent application was submitted, consists in mixing an aqueous solution of Zr and M salts with an ethanolic solution of hexamethylenetetramine, which is the ammonia donor. The subsequent steps are similar to those used for method I.

In the preliminary experiments, it was found that part of the stabilizing oxide, either Y_2O_3 or MgO, was lost during washing with method II.[2] Consequently, method I was used for powder preparation, but it was recently found that MgO is partially lost also with this method, whereas Y_2O_3 is not dissolved.

2.1 $MgO-ZrO_2$ system

Two batches were prepared with method I, both of nominal composition 3.5 w/o MgO. Atomic absorption analysis has shown, however, 2.7 w/o and 1.3 w/o MgO. These powders are being tested for sinterability, microstructure and mechanical properties.

2.2 $Y_2O_3-ZrO_2$ system

2.2.1 4 w/o $Y_2O_3-ZrO_2$

About 1 kg of powder of this composition was prepared with method I. Atomic absorption analysis has shown no Y_2O_3 loss. The powder, calcined at 700°C, was milled and tiles were pressed and sintered at 1500°C. 1x1x10mm bars were broken in 3 pt bending and an average room temperature MOR (20 bars) of 1080 MPa was obtained, with a standard deviation of 110 MPa. Standard (.125" x .128" x 1.125") chamfered bars will be tested at room temperature and 1000°C for MOR and K_{IC} (multiple controlled flaw method). Three sintered tiles were hot isostatically pressed at 1500°C, 1 hr., in 207 MPa Ar. Two came out cracked and the third one uncracked but non-uniform in color. This tile will be tested for MOR and K_{IC}.

From the same powder, hydrothermally crystallized at 275°C instead of calcined at 700°C, tiles were made by pressing and also by slip-casting from aqueous dispersions containing Darvan 821 A (ammonium polyacrylate) as dispersing agent. The pressed tiles developed cracks upon sintering, whereas the slip-cast ones cracked upon drying.

It is believed that cracking arises from non-uniform shrinkage stresses which are caused by the low green density and, possibly, by density gradients in the green body; a concomitant cause could be the relatively high water content (5-7 w/o) of the autoclaved powder.

Dilatometry studies, supported by TGA, are underway to understand and solve the cracking problem. Fig. 8 shows the shrinkage curves, obtained by dilatometry, for green bars (pressed at 35 MPa) made with C/D and R/S powders of the same composition. Curves 1 and 2 were obtained from autoclaved and calcined (700°C) powders, respectively. Curve 3 was obtained from the R/S powder and curve 4 from a Toyo-Soda powder with 3 w/o Y_2O_3, as control.

2.2.2 4 w/o Y_2O_3-1 w/o MgO-ZrO_2

A batch of this (nominal) composition was prepared with method I. Atomic absorption analysis has shown 4.4 w/o Y_2O_3 and 0.5 w/o MgO.

The powder, calcined at 700°C, was milled and pressed into tiles, which were sintered at 1500°C. The sintered tiles (d=5.80 g/cc) were all cracked. The XRD pattern of the as fired surface has shown a high m-ZrO_2/t-ZrO_2 ratio. This result is not understood. Microstructural analysis is under way to determine the possible cause of the cracking.

2.2.3 10 w/o Al_2O_3-90w/o (4 w/o Y_2O_3-ZrO_2) composite

This batch was also prepared with method I, using $AlCl_3$ as precursor of Al_2O_3 (10 w/o Al_2O_3 was chosen, and not 20 w/o as with the R/S Al_2O_3 powder, since $Al(OH)_3$ has a very high tendency to gel in contact with water, which results in the coarsening of the powder).

Tiles were pressed and sintered at 1500°C, using the powder calcined at 700°C. The sintered density was in the 5.65-5.70 g/cc range, or about 98-99% of TD. (The calculated TD for this composition is 5.79 g/cc.) The phase composition, microstructure and mechanical properties are being evaluated. The analysis of Y_2O_3 and Al_2O_3 by atomic absorption has shown 4 w/o Y_2O_3 and 10.2 w/o Al_2O_3.

2.3 ZrO_2-Al_2O_3 system

No powders were prepared by wet chemical methods in this system, where alumina constitutes the major component.

3.0 Powder processing and shape forming methods

Only powders pressing and slip-casting were tried until now for both the R/S and C/D powders. A colloid

press made of stainless steel has been received and tested. It can make a 3" diameter disc and is composed of a cylinder, a short base and a long piston. Base and piston have rubber O-rings and internal channels to allow pressing under vacuum or with a flowing gas for drying purposes. The colloid press is intended for pressing thick pastes or gels, either at room temperature or at the highest temperature usable with the O-ring gaskets.

The R/S and C/D powders behave very differently upon pressing or slip-casting. With the R/S powders much higher green densities can be obtained, either by pressing or slip-casting of aqueous suspensions. The difference in behavior seems to be related to differences in particle density, surface area and surface chemistry. Typically, upon isostatically cold pressing, the R/S 4 w/o Y_2O_3-ZrO_2 powder gives green densities around 53% of TD, whereas the C/D powder of the same composition, either calcined at 700°C or hydrothermally crystallized, gives densities around 40% of TD.

Even more dramatic is the differences for slip-cast bodies. With the R/S powders aqueous slips with solids loadings up to 50 v/o have been prepared, whereas with the C/D powders only about 30 v/o can be attained and the green bodies develop cracks upon drying. Experiments are under way to increase the particle density and decrease the retained water in the powders crystallized in the autoclave.

The use of dispersing agents has been tried with both types of powders, for example, Darvan C, Darvan 821 A, Pluronic P104, Pluronic 10R5. The best results were obtained with the R/S powders using Darvan 821 A (ammonium polyacrylate), which has allowed to prepare aqueous slips with up to 50 v/o solids; such slips gave slip cast bodies with densities of 62% of TD. The same additive has not shown obvious beneficial effect in slips prepared with the C/D powders.

pH control was also tried for slip preparation, but ph stabilized slips could not be prepared with 50 w/o solids loading using the R/S powders.

Status of Milestones

All milestones are on schedule. The milestone titles, dates and a brief summary of the results are reported below.

1. (Mechanical properties of Mg-PSZ's and Mg-TZP's (4/30/86)

Mg-TZP ceramics have not been made yet. For the

fine grained Mg-PSZ materials preliminary results indicate that RT MOR (3 pt) around 700MPa can be achieved with 1x1x10mm bars for a 3.1 w/o MgO composition.

Optimization of the phases present via aging followed by mechanical property evaluation is planned as soon as possible.

No mechanical properties for the ceramics made with the C/D powders are at present available.

2. (Construction of melting/rapid solidification apparatus) (5/31/86)

The R/S material can be prepared either by feeding a powder to the plasma torch or by immersion of a water cooled spinning disc into the molten charge. Atmosphere control is possible. Estimates were received from potential vendors. A test program has been initiated with the most probable company to run zirconia and zirconia/alumina materials for evaluation of their apparatus. If chosen, this vendor will continue testing until our unit can be installed in house.

3. (Comparison of R/S and C/D powders) (7/31/86)

The R/S powders give green bodies with high density, both by powder pressing and slip-casting. The C/D powders give lower green densities due to agglomeration, lower particle density, higher surface areas and different surface chemistry.

Y_2O_3 and MgO are partially lost with method II, whereas only MgO is partially lost with Method I. The applicability of these two methods to the synthesis of powder in the ZrO_2-Al_2O_3 system, where alumina is the major component, has not been tried yet.

4. (Mechanical properties of Y-TZP ceramics) (8/31/86)

Room temperature MOR (4 pt) of pressureless sintered ceramics made with the R/S powder is in the 875-950 MPa range, for both dry pressed and slip-cast parts sintered at 1600°C in air. If these parts are HIPed after sintering, the average MOR increases to 1380-1515 MPa.

The MOR at 1000°C for the same Y-TZP ceramics, sintered or sintered/HIPed, drops to about 1/3 of the room temperature value, with the sintered/HIPed specimens always showing a higher value.

5. (Choice of the two best forming methods) (10/31/86)

For the R/S powder (4 w/o Y_2O_3-ZrO_2) slip casting gives sintered Y-TZP's with slightly higher (about 9%) strength, when compared to cold isostatic pressing.

However, a firm conclusion about which one is the best method cannot be drawn, since optimization has not been done yet.

For the C/D powders, drying cracks were observed in the green parts obtained from the autoclaved powders by slip-casting; in many instances, cracking also occurred during the firing of the pressed bodies. It is believed that an increase in density will solve the problem.

6. (Property evaluation of ZTA ceramics) (10/31/86)

Preliminary tests on 1x1x10mm bars indicated room temperature strengths (3 pt) of 1378 MPa. Processing variables and phase assemblages are being optimized for these R/S powders before comprehensive property evaluation is begun.

ZTA ceramics derived from the C/D powders have not been prepared yet.

Publications

None.

References

1. K.Tsukuma and K.Ueda: "Strength and fracture toughness of isostatically hot pressed composites of Al_2O_3 and Y_2O_3-partially stabilized ZrO_2". Comm. Am. Ceram. Soc., Jan. 1985, C-4, C-5.

2. P.F.Becher: "Transient thermal stress behavior in ZrO_2-toughened Al_2O_3", J. Am. Ceram. Soc. Vol. 64, 37-39 (1981).

3. T.Y.Tien: "Transformation toughened ceramics-A potential material for light diesel engine application", Semi-annual report, Oct. 1983-March 31, 1984. (Contract No. DAAG46-84-K-0001)

4. G.A.Rossi: U.S. Pat. 4,501,818

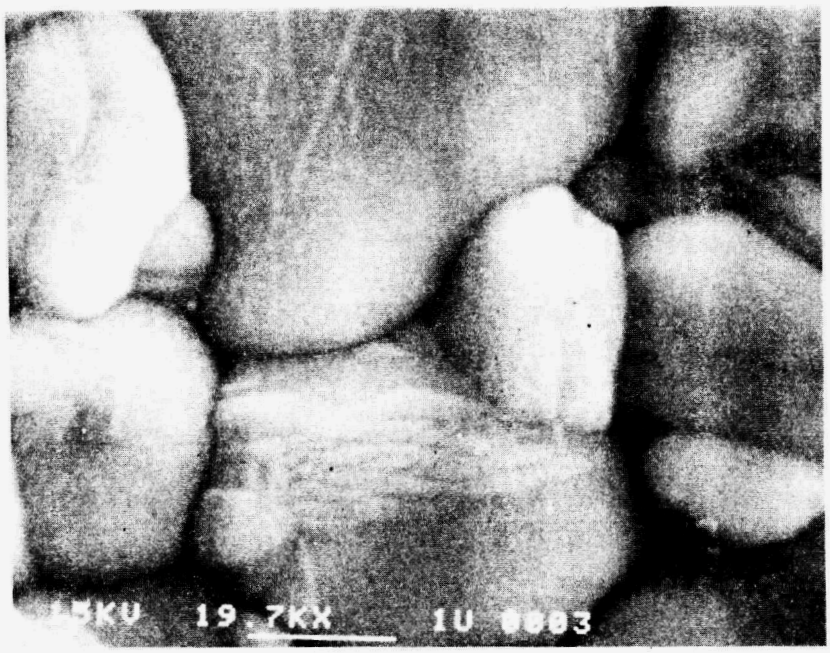

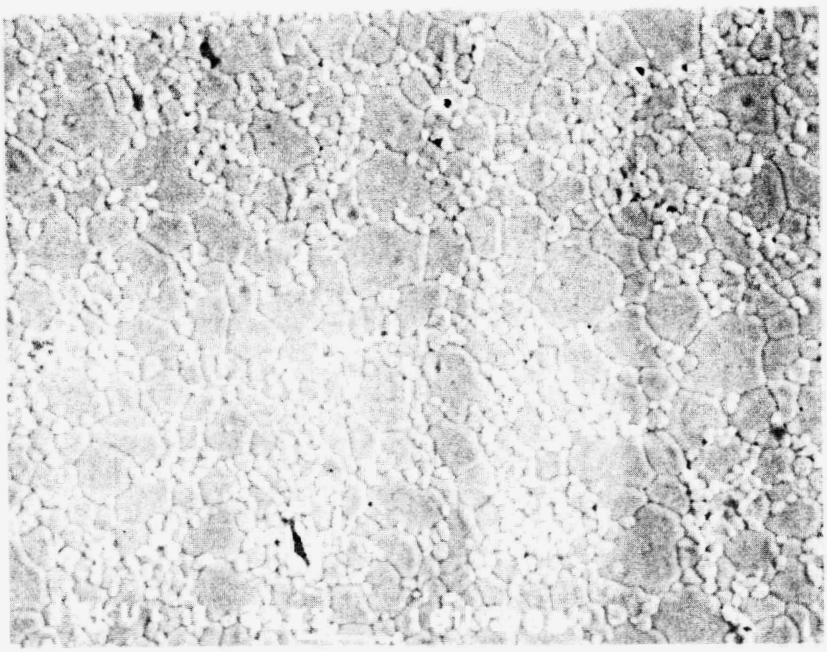

Fig. 1: 3.1 w/o $MgO-ZrO_2$, made by melting E-10 ZrO_2 and MgO, sintered at 1500°C, polished and aged at 1400°C for 1 hour.

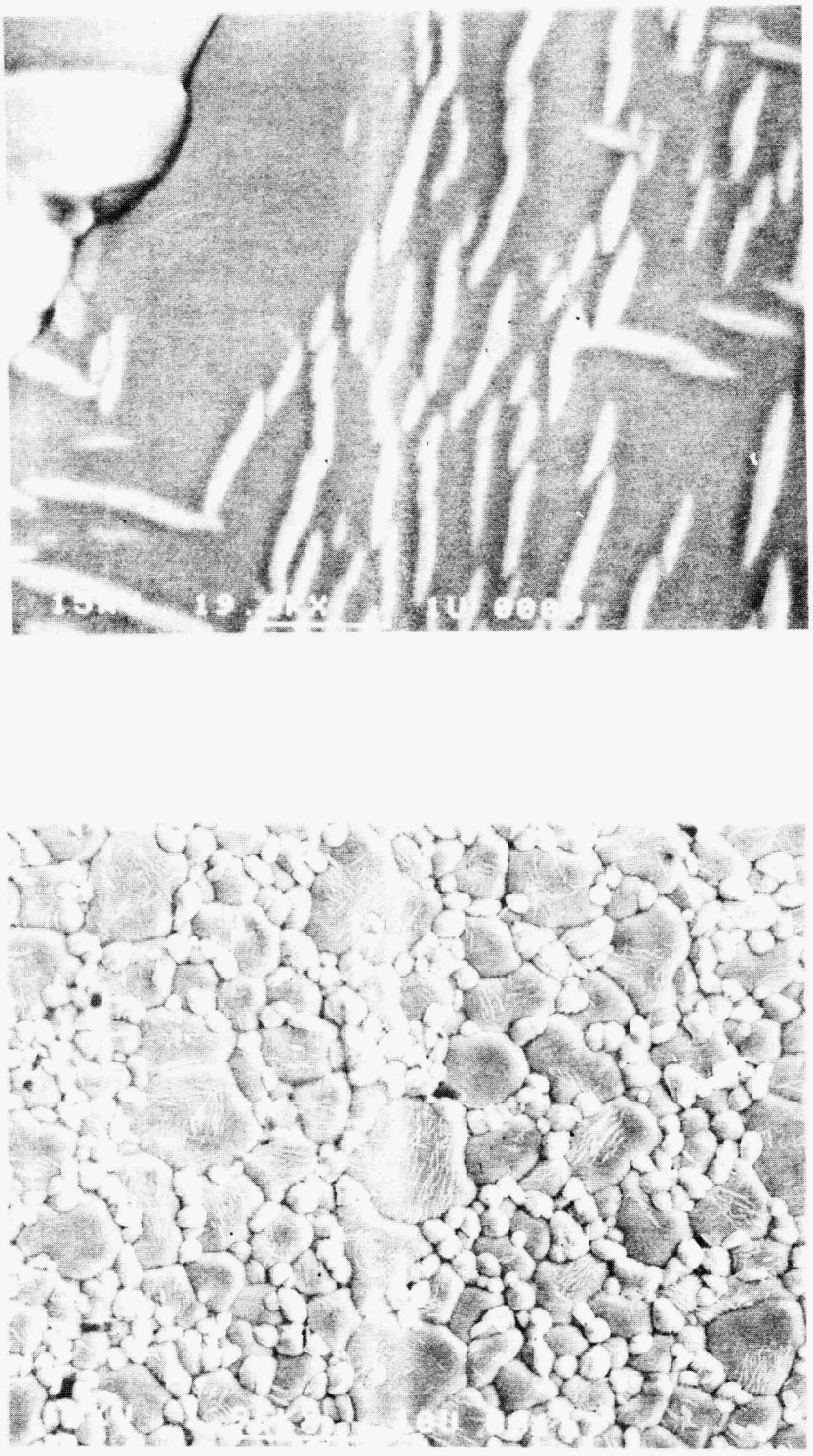

Fig. 2: 3.1 w/o MgO-ZrO_2, made by melting E-10 ZrO_2 and MgO, sintered at 1500°C, polished and aged at 1400°C for 5 hrs.

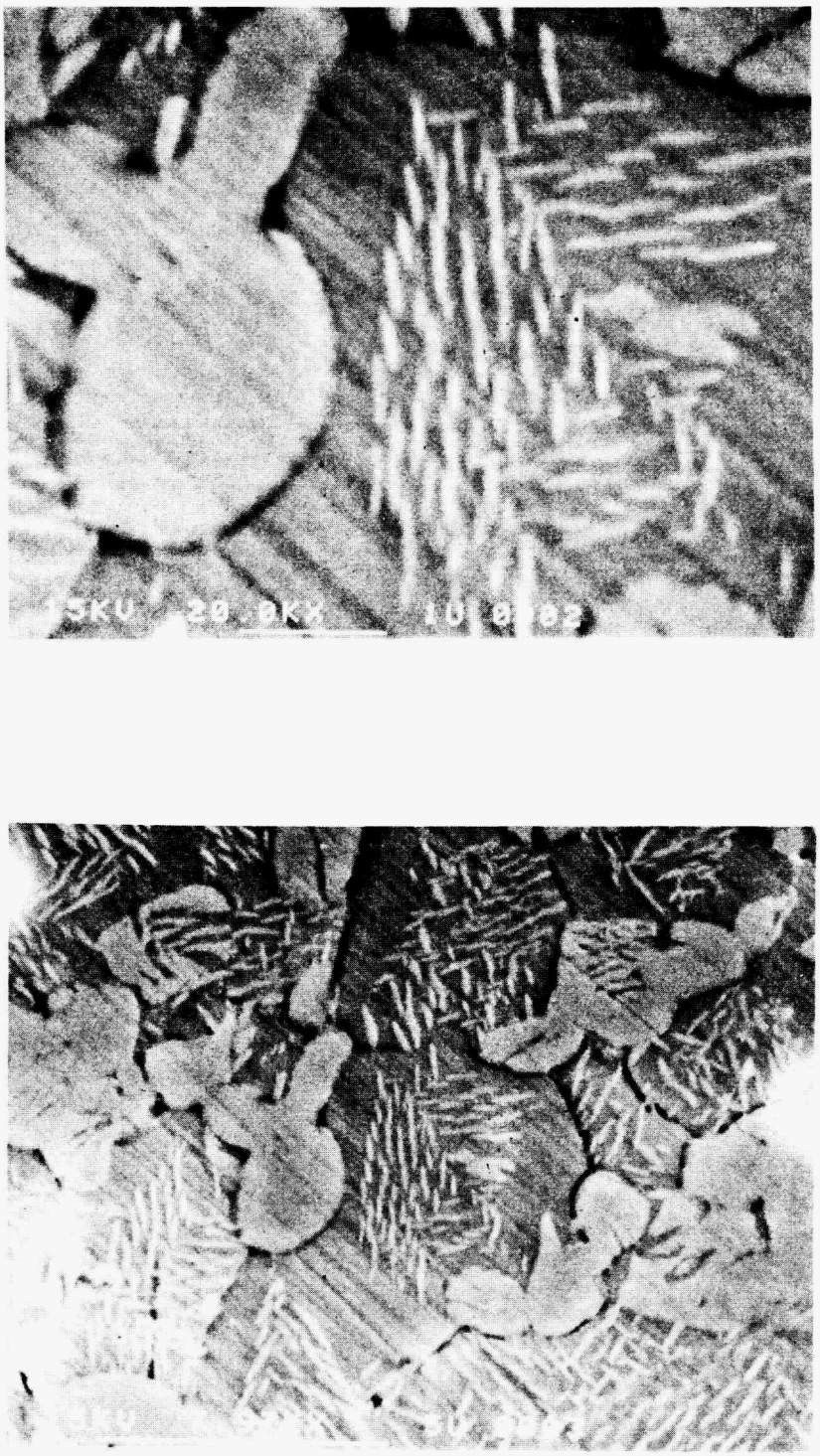

Fig. 3: 3.1 w/o $MgO-ZrO_2$, made by melting E-10 ZrO_2 and MgO, sintered at 1500°C, aged at 1400°C for 5 hrs., polished and chemically etched.

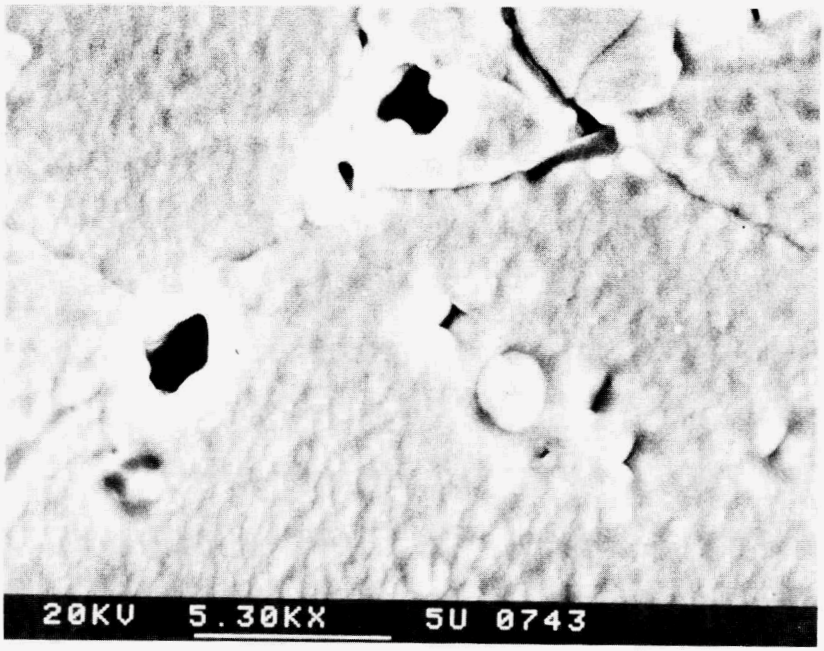

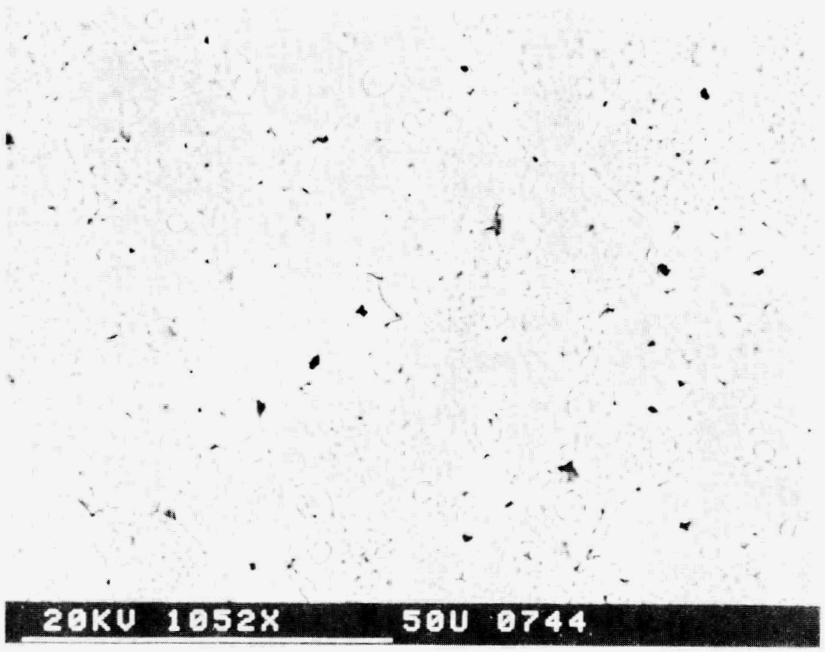

Fig. 4: 3.1 w/o MgO-ZrO_2, made by melting E-10 ZrO_2 and MgO, sintered at 1600°C, polished and aged at 1400°C for 1 hour.

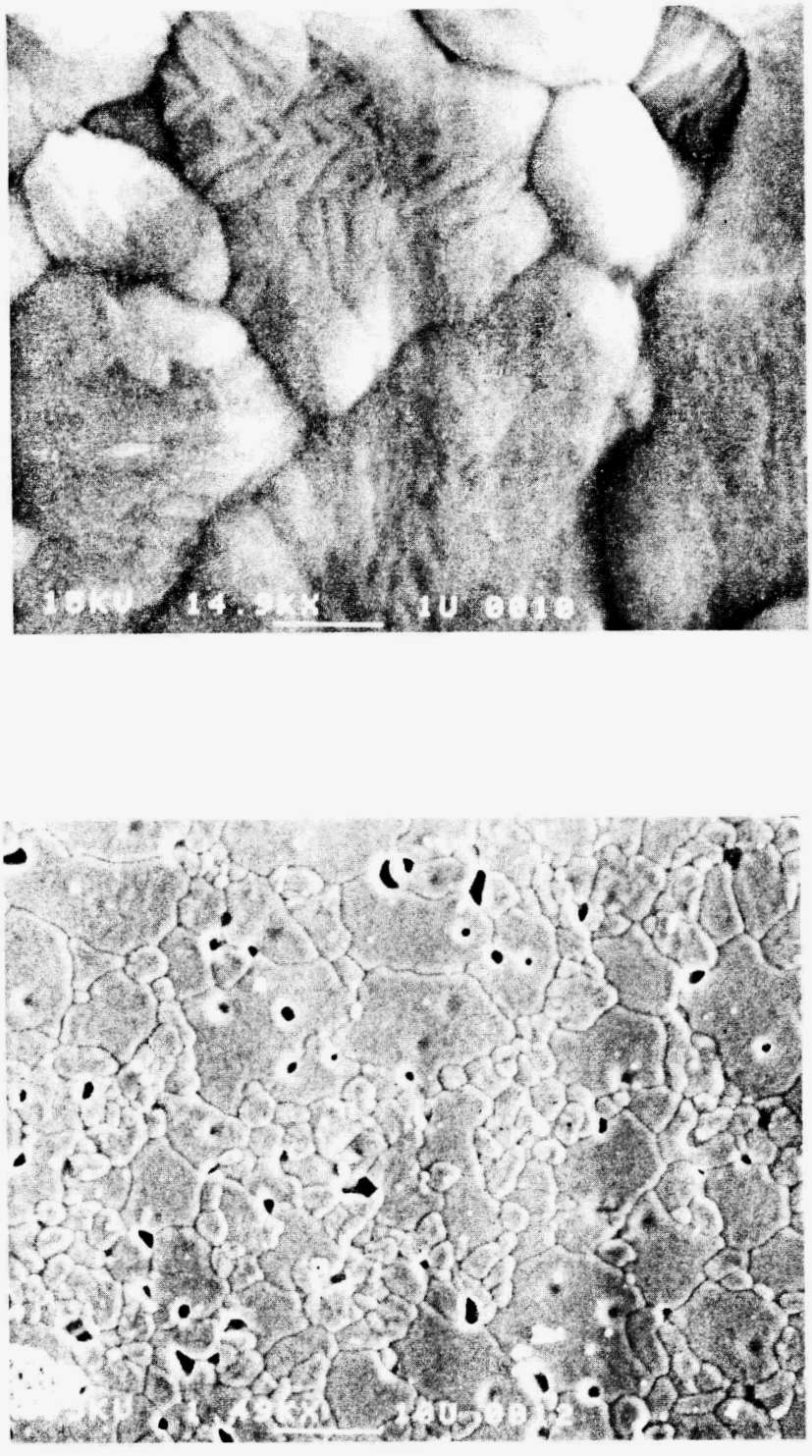

Fig. 5: 2.8 w/o $MgO-ZrO_2$, made by melting E-10 ZrO_2 and MgO, sintered at 1600°C, polished and aged at 1400°C for 1 hour.

Fig. 6: 3.0 w/o $MgO-ZrO_2$, made by melting baddeleyite and MgO, sintered at $1600^{o}C$, polished and aged at $1400^{o}C$ for 1 hour.

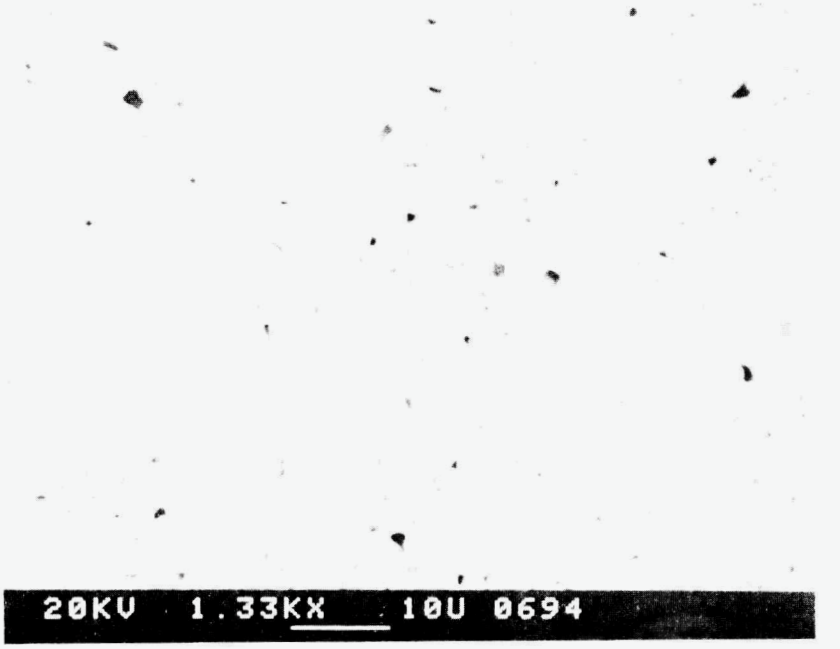

Fig. 7: 2.2 w/o $MgO-ZrO_2$, made by melting baddeleyite and MgO, sintered at 1600°C, polished and aged at 1400°C for 1 hour.

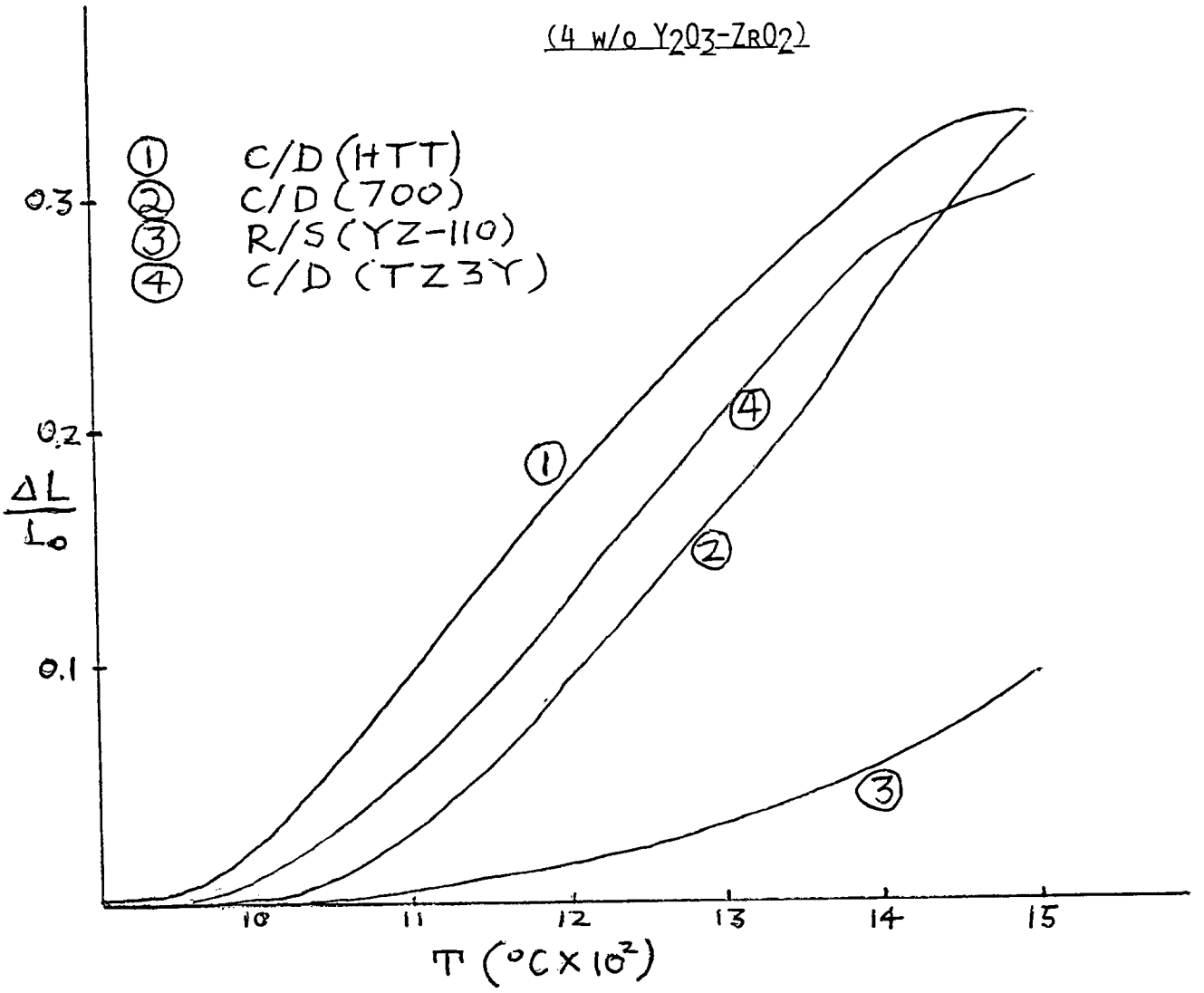

GREEN DENSITY (5 KSI)	TYPE OF POWDER	FIRED DENSITY (1500°C)
1.78 G/CC	C/D (HTT)	6.03 G/CC
1.72 G/CC	C/D (700)	5.83 G/CC
3.17 G/CC	R/S (YZ-110)	5.80 G/CC
2.33 G/CC	C/D (TZ3Y)	5.93 G/CC

Fig. 8: Comparison of shrinkage behavior of pressed bars made with the chemically derived and rapidly solidified powders.

Advanced Transformation-Toughened Oxides

T. Y. Tien (University of Michigan)

Objective/Scope

The objective of this project is to develop a thermal insulating material has sufficient strength and toughness for heat engine applications. The approach is to explore the composite materials in the system Al_2O_3:CrO_2/ZrO_2:HfO_2.

Technical Highlight

The goal of the present work is to optimize the strength and toughness of the materials in the system Al_2O_3:Cr_2O_3/ZrO_2:HfO_2. Previous results indicated that the toughness could be increase by the increase of the dispersed phase (ZrO_2:HfO_2). Unfortunately, there is a strength decrease with increasing dispersed phase. However, it has also been demonstrated that the strength decrease can be avoided if the dispersed particle contain higher HfO_2 content (>30 mole %) and are not large enough to cause micro-cracks.

A manuscript of a paper is attached to this report as a subsection.

Technical Progress

The current research will develop procedures to produce material with increased toughness by increasing the dispersed phase while maintaining acceptable strength levels by controlling the dispersed phase composition and particle size.

The experimental work has concentrated on the methods of sample preparation. The steps developed for sample preparation are:

1) The starting powders are co-precipitated from ethanol solutions. The powders are dried and calcined. Fine, homogeneous, crystalline particles of the desired composition were obtained.

2) Composites of alumina/chromia matrix containing15 vol % of the dispersed particles have been prepared. The alumina matrix phase contains 20 mole % Cr_2O_3 and the dispersed particles are ZrO_2/15 Mole % HfO_2 and ZrO_2/30 mole % HfO_2.

3) The powders are dispersed in distilled water using a surfactant (Darvon 821-A).

4) A disc is slip cast from the suspended powder using vacuum filtration.

5) The slip casted disc is slowly dried in air under controlled humidity and then isostatically pressed to 26 ksi.

6) The pressed disc is sintered in a carbon resistance furnace under a low oxygen potential atmosphere at 1500°C for 20 minutes. The sintered specimens have a density greater than 99% of the theoretical.

7) After sintering, phases presence were determined by X-ray diffraction. It was found that 50% of the zirconia particles are in the tetragonal form. It should be noted that when the dispersed particles have tetragonal to monoclinic ratio of 1: to 1:2 exhibited the maximum toughness. Therefore, it is planned that specimens be heat treated to obtain the desired tetragonal/monoclinic ratio.

The final step in our sample preparation was to cut and grind "four point bend test" bars from the sintered discs. A new surface grinder is currently being installed which will allow such test bars to be machined in our laboratory. The four point test bars produced will be used to measure the fracture toughness and bend strength at room temperature as well at elevated temperatures.

Status of milstones

The project is on schedule.

Publications

1) T. Y. Tien, Ceramic Compositions, U. S. Patent 4,533,647. August 6, 1985.

2) T. Y. Tien, T. K. Brog and A. K. Li, "Toughened Ceraimics in the System Al_2O_3:Cr_2O_3/ZrO_2:HfO_2," submitted to the International Journal of High Technology Ceramics.

Toughened Ceramics in the System Al_2O_3:Cr_2O_3/ZrO_2:HfO_2: Microstructure Development.

A. K. Li and T. Y. Tien
Materials Science and Engineering
The University of Michigan
Ann Arbor, Michigan 48109

Abstract:

Sintering behavior and growth kinetics of the matrix alumina:chromia solid solution grains and the dispersed zirconia:hafnia solid solution particles of the two-phase composites in the system Al_2O_3:Cr_2O_3 / ZrO_2:HfO_2 were studied. Starting materials were prepared by co-precipitation from mixed aqueous solutions. Precipitates were calcined at 1050°C and well crystallized alpha-alumina and zirconia were obtained. Composites of near full density with a matrix grain size <1μm and a dispersed particles size <0.3 μm were obtained at 1550°C without soaking time. The growth rate of the dispersed phase seems to be determined by the grain growth rate.

Fracture toughness of specimens containing different size distribution of ZrO_2:HfO_2 dispersed particles were measured. It was found that when the dispersed phase has a monoclinic to tetragonal ratio closed to 1:1 exhibited a maximum toughness.

Introduction:

Sintering and grain growth studies of two-phase materials became an active research topic in the past few years (1,2), probably because of the emerging technical importance of the material "transformation toughened" ceramics. A typical material of this kind is a high density alumina containing fine dispersed zirconia particles (3). As mentioned by Coble and Cannon (4), because of the complexity of the problem and the lack of data base needed to interpret the kinetics and mechanism of the sintering process, quantitative treatment of sintering of relatively pure single phase solid is not possible. Therefore no attempt was made in this paper to elucidate the sintering mechanism of two-phase materials. This paper will report the effect of solid solution in both the matrix phase and the dispersed phase on the kinetics of sintering and grain and particle growth. Co-precipitated powders were used for this study, and it is assumed that all metal ions were mixed in atomic scale, therefore, the problem of non-uniform distribution of the two phases could be eliminated.

Sample Preparation:

Compositions studied in this investigation were Al_2O_3:Cr_2O_3 solid solutions as the matrix phase and ZrO_2:HfO_2 solid solutions as the dispersed phase. The dispersed particle content was 15 volume %. The compositions of the composites can be expressed as $(Al_{1-x}Cr_x)_2O_3/(Zr_{1-y}Hf_y)O_2$, where 100x = 0, 2, 5, 10, 20 and 30 and 100y = 0, 10, 30 and 50. The compositions of the composites in this study are designed as 100x-15-100y, (i.e. x mole% of Cr_2O_3 in the matrix phase - volume% of dispersed particles - y mole% of HfO_2 in the dispersed phase). Mixed oxides powders were prepared by co-precipitation as metal hydroxides from aqueous solutions of the mixed salts. One molal aqueous solutions of aluminum nitrate, chromium nitrate, zirconium oxychoride and hafnium oxychloride were prepared. Solutions were mixed according required compositions of the composites and further diluted with equal volume of ethanol. Mixed metal hydroxides were precipitated by adding the mixed metal salts solution, while stirring, to ammonium hydroxide solution. The pH value of the precipitating mixtures were maintained between 6.8 to 7.3. The pH value used was previously determined to obtain maximum amount of hydroxides precipitates from the mixed metal salts solutions.

Mixed metal hydroxides precipitates were filtered, washed with dilute ammonium hydroxide solution. The gelatinous filter cakes were dried at 110°C for 10 hours and were then calcined at 1050°C for four hours. Calcined powders were alpha alumina with corundum structure, determined by x-ray diffraction. Calcined powders were dry ground in an alumina rotary mill for 10 hours with 5 wt.% of stearic acid as grinding additives. Ground powders were isostatically pressed at 25,000 psi and were heated at 650°C for 2 hours to remove the organic additives. Green densities of these compacts were greater than 50% of theoretical. Chromia containing compositions were

sintered in an induction furnace with graphite susceptor filled with 15μm over pressure of argon. Chromia free compositions were sintered in air in a furnace with $MoSi_2$ heating elements. Both furnaces were heated at a rate of 750°C per hour and cooled at a rate of 600°C per hour. Sintering temperatures used ranged from 1400°C to 1650°C and the soaking time at top temperature ranged from zero to 480 minutes. All specimens after sintering showed two phases: alpha alumina and tetragonal and/or monoclinic ZrO_2.

Results and Discussion:

Sinterting:

Apparent densities of sintered specimens were measured using Archimedes principle (water as the liquid media). True densities used to compute relative density values were obtained from the lattice parameter data of both series of the solid solutions (5,6) assuming the dispersed zirconia particles are in the monoclinic form. Relative densities of specimens sintered at different temperatures as a function of soaking time are plotted in Fig.1. Specimens were sintered to full density at temperatures above 1550°C without holding time.

Compositions with higher chromia content sintered faster than those with lower chromia concentrations. As shown in these figures that specimens containing higher chromia concentrations reached higher sintered density than those containing lower chromia concentrations under the same sintering conditions. This could be explained by the a higher diffusion rate of chromium ions in the Cr_2O_3 crystals than that of aluminum ions in Al_2O_3 (7). Al_2O_3 and Cr_2O_3 crystallize in the same corundum structure and form complete solid solutions.

Hafnia content in the dispersed phase had no effect on the sintering rate of the composites.

Grain and Particle Growth:

Sintered specimens were polished and thermally etched. Average grain diameter (Dg) of the matrix phase and the average particle diameter (Dp) of the dispersed phase were measured on polished and etched surfaces using the lineal intercept technique (8). Measured average diameters of the matrix grains and of the dispersed particles are listed in Table I.

Growth of the grains of the matrix phase and the particles of the dispersed phase can be expressed by the following generalized empirical equation (9):

$$D = Kt^n \qquad (1)$$

where n is a constant (time exponent). K is the rate constant which follows the Arrhenious equation,

$$K = K_0 e^{-Q/RT} \qquad (2)$$

Growth data of some compositions are plotted in Figs. 2 in the form of log D vs. log t. Growth rate (D/t^n) vs. reciprocal temperature ($1/T°K$) data of these compositions are plotted in Figs. 3. The time exponent, n, the rate constant, K, and the activation energy, Q, were calculated using linear regression method from these data and the results are given in Table II and Table III respectively.

Growth rate data showed that the chromia contents in the matrix phase affected the growth rate of both of the matrix phase and the dispersed phase. The hafnia contents in the dispersed phase did not affect the growth rate of either phase.

There are three possible mechanisms (2) for the zirconia particle inclusions in the composites to grow: 1) intragranular particles grow by Ostwald ripening through bulk diffusion, 2) intergranular particles grow by Ostwald ripening through grain boundary diffusion, and 3) intergranular particles grow by coalescence. Microstructures of composites containing low chromia concentrations (<5 mole%) sintered at lower temperatures (<1400°C) showed the presence of small percentage of intragranular zirconia particles. For compositions containing higher chromia concentrations sintered at higher temperatures showed predominately intergranular zirconia particles. The data points presented in Table I are average values over both types of particles, i.e. inter— and intragranular particles. It should also be mentioned that coalesced particles at the triple points were counted as separate particles whenever grain boundaries were recognizable between zirconia particles.

The data in Tables II and III were given in the form of terms in equation 1, i.e. D, K, n and t. Both of the intercepts ($\ln K_0$) and the slopes (time exponents, n) were obtained by linear regression analysis using data points measured (see Table I). The time exponent, n, for the particle growth increased as chromia contents increased in the matrix phase and remained constant as the hafnia contents in the dispersed phase changed. The values of the time exponent, n, seems to be lower than it would be expected from the theoretical models, since Ostwald ripening through grain boundary diffusion should give a value of 1/4 and coalescence should give a value of 1/4. Since both Ostwald ripening and coalescence give a "n" value of 1/4, it is difficult to differentiate the growth mechanism through the classical time dependent value, n. Particle size disptribution and microstructural details have to be considered in order to clarified the mechanism for particle growth. At present time, values are being re—evalueated and some of the data points are being repeated. Detailed discussions will be presented when the values were confirmed. Data from Lange et.al. (1) and Kibbel et.al. (2) were also plotted and the time exponent, n, computed. The results from these two publications were very similar to that of the present work.

The activation energy for particle growth are given in Table III. The activation energy increased with the increase of chromia contents in the matrix phase and remained virtually constant while the hafnia content in the dispersed phase changed. The average value of the activation energy is about 48 Kcal/mole which is about the value for grain boundary diffusion.

Grain sizes are plotted against the particle sizes of the same specimen received the same heat treatment in Fig. 4. It shows a straight line relationship. This relationship follows the Zener's (10) suggestion that the limiting grain size (D_f) is related to the size of the inclusions (d) and their volume fraction (f) in a composite in the following form:

$$D_f = d / f \qquad (3)$$

It should be noted that both the time exponent and activation energy for grain growth and particle growth for the same composition are always the same.

The rate constant, K, for Ostwald ripening of the dispersed particles, according to Speight (11), is related to; interfacial energy between the matrix grains and the dispersed particles, grain boundary thickness, diffusion rate of the dispersed phase along the matrix grain boundaries, and solute concentration of the dispersed phase in the matrix phase, among other factors. All of the above factors mentioned could be varied as a function of compositions of both the matrix phase and the dispersed phase. All of the factors are being evaluated at present time and will be discussed in the future.

References:

1. F. F. Lange and M. M. Hirlinger, "Hindrance of Grain Growth in Al203 by Zr02 Inclusions," J. Am. Ceram. Soc. 67 [3] 164 – 8 (1984).

2. B. W. Kibbel and A. H. Heuer, "Ripening of Inter– and Intragranular Zr02 Particles in Zr02–Toughened Al203," p.415–425, Advances in Ceramics, Vol. 12, Sciences and Technology of Zirconia II, Ed. N. Claussen, M. Rühle and A. H. Heurer, Am. Ceram. Soc., Columbus, OH. 1984.

3. N. Claussen and M. Rühle, "Design of Transformation Toughened Ceramics," p.137, Advances in Ceramics, Vol. 3, Sciences and Technology of Zirconia, Ed. A. H. Heuer and L. W. Hobbs, Am. Ceram. Soc., Columbus, OH, 1981.

4. R. L. Coble and R. M. Cannon, "Current Paradigms in Powder Processing," p. 151 – 170, Processing of Crystalline Ceramics, Materials Science Research Vol. 11, Ed. H. Palmour, R. Davis and Hare, Plenum PPressw, New York, 1978.

5. E. N. Bunting, "Phase Equilibria in the System Al203–Cr203," J. Res. Nat. Bur. Stand., 6 [6] 947–49 (1931).

6. R. Ruh, H. J. Garrett, T. F. Domagala and N. M. Tallan, "The System Zirconia – Hafnia," J. Am. Ceram. Soc. 51 [1] 23–7 (1968).

7. W. D. Kinery, Introduction to Ceramics, 2nd Edition, p. 240, John Wiley & Sons, New York, 1976.

8. J. C. Wurst and J. A. Nelson, "Lineal Intercept Technique for Measuring Grain Size in Two–Phase Polycrystalline Ceramics," J. Am. Ceram. Soc. 55 [2] 109 (1972).

9. R. J. Brooks, "Controlled Grain Growth," p. 331–364, Treatise on Materials Science and Technology, Vol. 9. Ed. F. F. Y. Wang, Academic Press, New York, 1976.

10. C. Zener, quoted by S. C. Smith, "Grains, Phases, and Interfaces; An Interpretation of Microstructure," Metals Technol., 15 [4]; Trans. Met. Soc. AIME, 175, 15–51 (1948).

11. M. V. Speight, "Growth Kinetics of Grain Boundary Precipitates," Acta Mfetall.l, 16 [1] 133–35 (1968).

TABLE L Grain/Particle Size Measurement
(Unit in Micrometer)

1450°C	1/4 HR	1/2 HR	1 HR	2 HR	4 HR	8 HR	
02-15-0C	0.358/0.188	0.463/0.209	0.609/0.272	0.761/0.311			
05-15-0C	0.399/0.201	0.573/0.243	0.675/0.294	0.854/0.366			
10-15-0C	0.447/0.188	0.565/0.281	0.831/0.360	1.036/0.520			
20-15-0C		0.809/0.292	1.123/0.363	1.430/0.568			
30-15-0C	0.663/0.251	0.864/0.334	1.322/0.553	1.601/0.707			
1500°C							
02-15-0C	0.656/0.286	0.857/0.363	0.951/0.393				
05-15-0C	0.783/0.343	0.885/0.403	1.116/0.469	1.243/0.484	1.473/0.608	1.652/0.722	
10-15-0C	0.934/0.371	1.102/0.407	1.363/0.565	1.755/0.608	1.980/0.732	2.368/0.878	
20-15-0C	1.242/0.451	1.523/0.578	1.810/0.656	2.298/0.890	2.691/1.047	3.456/1.243	
30-15-0C	1.291/0.493	1.557/0.692	1.851/0.824	2.583/1.069	3.401/1.324	4.247/1.707	
1550°C							
02-15-0C	0.973/0.452	1.146/0.455	1.385/0.504	1.495/0.603			
05-15-0C	1.065/0.457	1.206/0.496	1.381/0.550	1.856/0.694	2.035/0.760	2.393/0.922	
10-15-0C	1.175/0.493	1.492/0.587	1.853/0.691	2.316/0.876	2.953/0.973	3.586/1.185	
20-15-0C	1.884/0.763	2.671/0.824	2.994/0.981	3.782/1.345	5.228/1.666	6.212/1.977	
30-15-0C	2.217/0.769	2.848/1.053	3.669/1.232	4.875/1.911	6.536/2.578	8.239/2.983	
1600°C							
02-15-0C		1.562/0.765	1.862/0.933	2.195/1.061	2.576/1.204		
05-15-0C		2.005/0.892	2.595/1.022	2.865/1.231	3.540/1.397		
10-15-0C		2.027/0.970	2.583/1.196	3.244/1.502	4.321/1.875		
20-15-0C		3.647/1.416	4.914/1.889	6.606/2.507	10.68/3.570		
30-15-0C		3.556/1.525	5.047/2.182	7.764/3.472	11.99/5.508		

TABLE II. Grain Growth Data* in the System Al_2O_3:Cr_2O_3/ZrO_2:HfO_2 Sintered at 1550°C.

POWDER	a (Intercept)	b (Slope = n)	r (Corr. Coeff.)
GRAIN			
02-15-0C	-O.590	0.213	0.987
05-15-0C	-0.620	0.244	0.991
10-15-0C	-0.707	0.324	0.999
20-15-0C	-0.250	0.339	0.993
30-15-0C	-0.256	0.385	0.999
PARTICLE			
02-15-0C	-1.216	0.140	0.929
05-15-0C	-1.627	0.206	0.987
10-15-0C	-1.691	0.253	0.989
20-15-0C	-1.580	0.295	0.995
30-15-0C	-1.365	0.408	0.992

* The data are presented in the form of $\ln D = a + n \ln t$, where D is the grain(or particle size), a is the intercept of the regression analysis, n is the time exponent in the grain/particle growth kinetics.

TABLE III. Grain Growth Activation Energies* in the System

Al_2O_3:Cr_2O_3/ZrO_2:HfO_2

POWDER	n (Intercept)	a(=lnk_o) (Intercept)	r. (Corr. Coeff.)	Q(Kcal/Mol) (Slope x R)
GRAIN				
02-15-0C	0.213	1.608	-0.999	44.4
05-15-0C	0.244	4.580	-0.957	55.5
10-15-0C	0.324	0.422	-0.999	42.2
20-15-0C	0.339	7.263	-0.999	65.7
30-15-0C	0.385	10.837	-0.998	79.5
PARTICLE				
02-15-0C	0.140	3.275	-0.975	51.1
05-15-0C	0.207	1.314	-0.947	45.9
10-15-0C	0.253	2.071	-0.961	49.3
20-15-0C	0.296	6.199	-0.993	64.4
30-15-0C	0.408	7.660	-0.986	72.1

*The data are presented in the form of $\ln(D/t^n) = a + (Q/R) / T$, where D is the grain(or particle size), t is the sintering time in min., n is the time exponent from Table II., a is the intercept of the regression analysis, Q is the activation energy of grain(or particle) growth, R and T have their usual meanings.

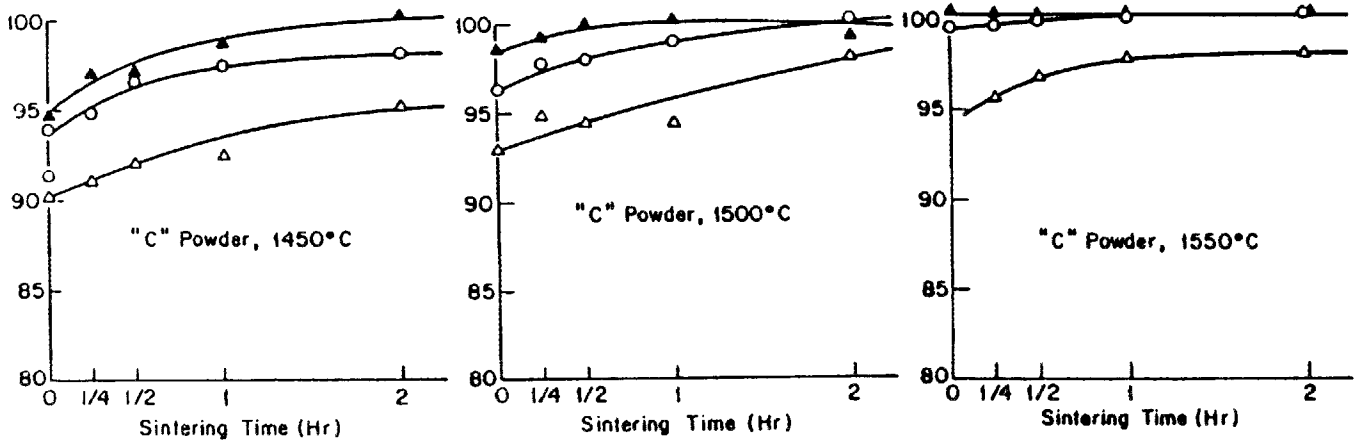

Fig. 1. Relative Densities of Composites in the System Al_2O_3:Cr_2O_3/ZrO_2:HfO_2, Sintered at 1450°C, 1500°C, 1550°C.

Composition Designation:

Cr_2O_3 Content – Vol % ZrO_2 – HfO_2 Content – Starting Powder.

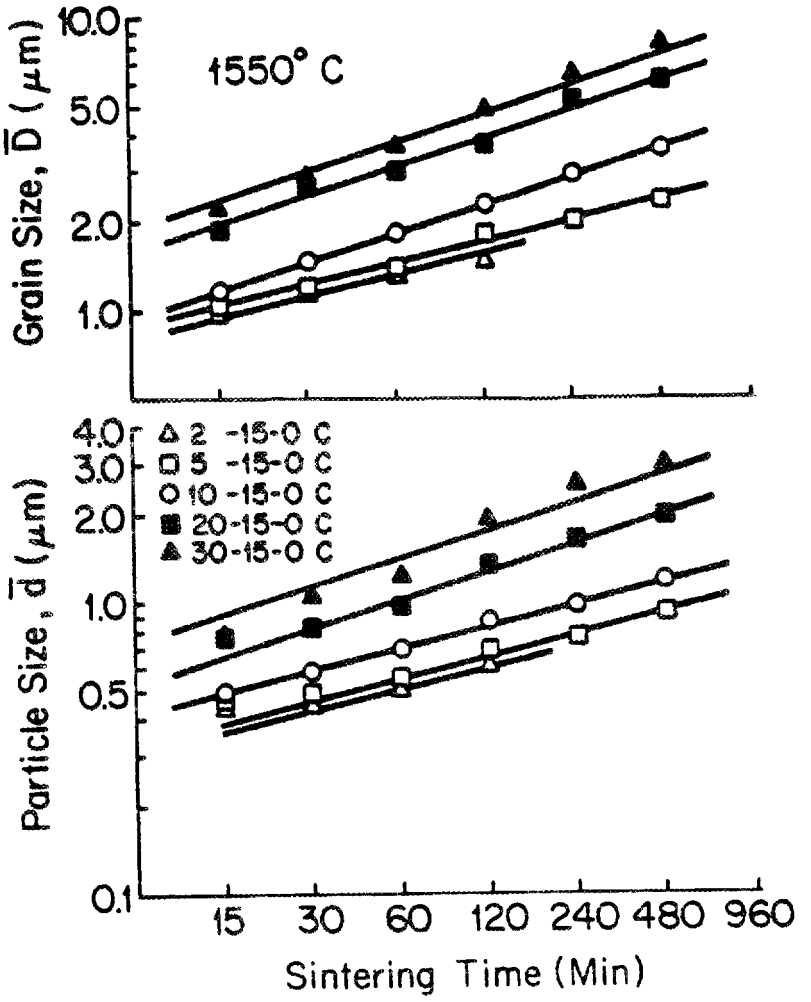

Fig. 2. Grain and Particle Growth Data for Compsoties Sintered at 1550°C., Starting Powder Used: "C" – Alpha Alumina

Composition Designation:

Cr_2O_3 Content – Vol % ZrO_2 – HfO_2 Content – Starting Powder.

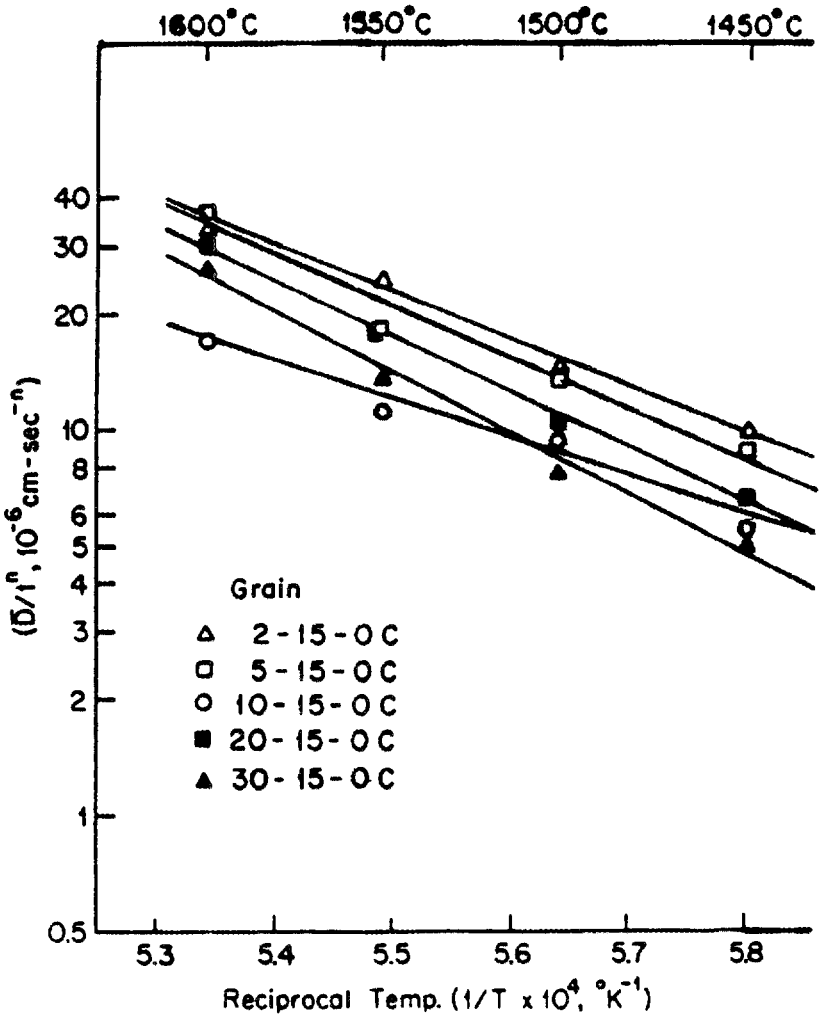

Fig. 3a. Temperature Dependence of the Grain Growth Rate.
Composition Designation:
Cr_2O_3 Content – Vol % ZrO_2 – HfO_2 Content – Starting Powder.

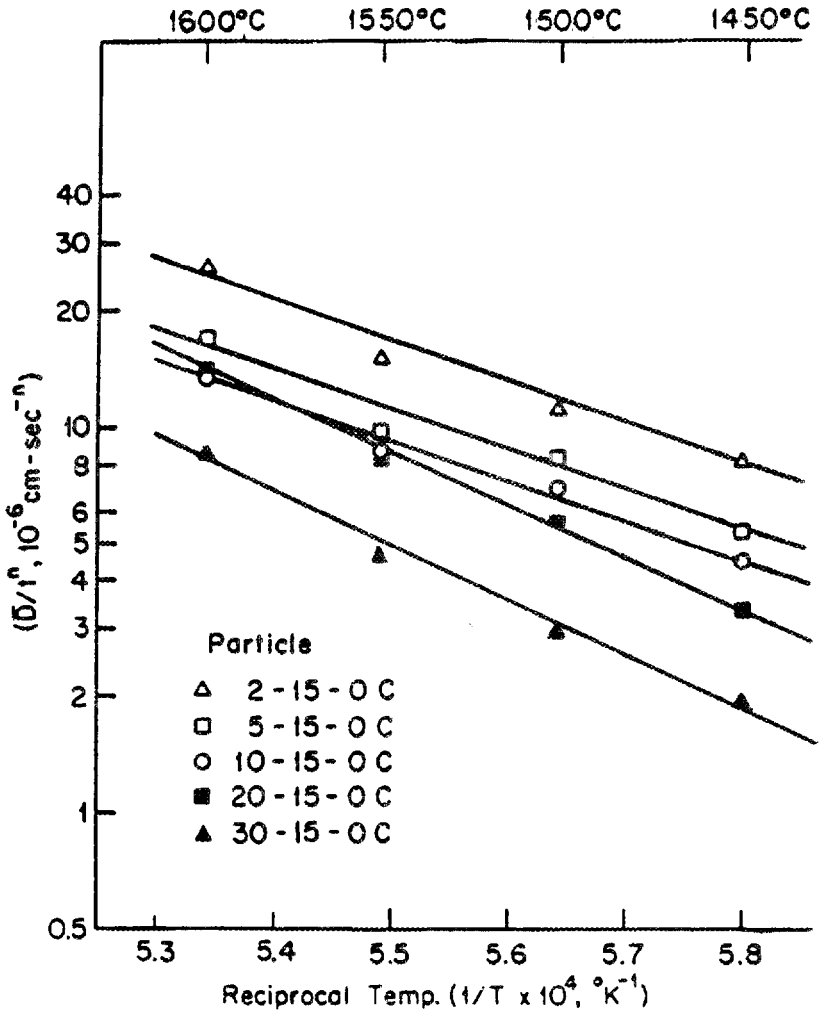

Fig. 3b. Temperature Dependence of the Grain Growth Rate.
Composition Designation:
Cr_2O_3 Content – Vol % ZrO_2 – HfO_2 Content – Starting Powder.

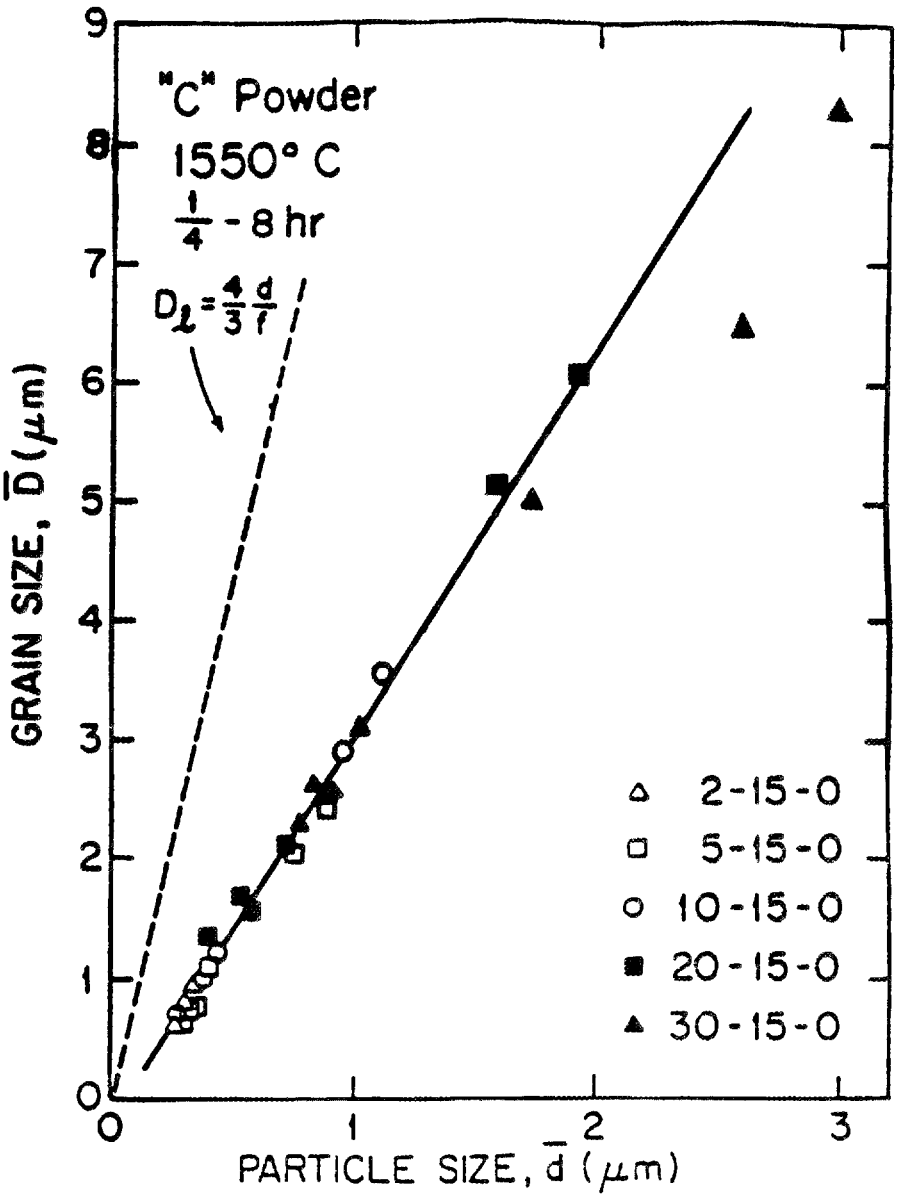

Fig. 4. Grain Size vs. Particle Size for Specimens Sinter at 1550° C.
Composition Designation:

Cr_2O_3 Content – Vol % ZrO_2 – HfO_2 Content

Processing and Characterization of Transformation-Toughened Ceramics With Strength Retention to Elevated Temperatures

R. A. Cutler and J. D. Bright (Ceramatec, Inc.)

Objective/Scope

Previous work[1] has shown that it is possible to increase the strength of Al_2O_3-ZrO_2 ceramics by incorporating transformation-induced residual stresses in sintered specimens consisting of three layers. The outer layers contained Al_2O_3 and unstabilized ZrO_2, while the central layer contained Al_2O_3 and partially stabilized ZrO_2. When cooled from the sintering temperature, some of the zirconia in the outer layers transformed to the monoclinic form while zirconia in the central layer was retained in the tetragonal polymorph. The transformation of zirconia in the outer layers led to the establishment of surface compressive stresses and balancing tensile stresses in the bulk. In theory, the residual stresses will not decrease with temperature until the monoclinic to tetragonal transformation temperature is reached since monoclinic and tetragonal ZrO_2 polymorphs have nearly the same coefficients of thermal expansion. The demonstration of the retention of residual stresses with temperature is a primary purpose of this project.

Previous work was accomplished using dry pressing techniques. The development of slip casting technology for layered composites will allow for better dispersion of zirconia in alumina and thereby facilitate higher volume monoclinic ZrO_2 in outer layers without strength degrading microcracking. A comparison between slip casting and dry pressing techniques will be made to identify higher strength materials for more detailed characterization during the second year of the project.

Technical Highlights

Experimental Procedures

Al_2O_3-10 vol. % ZrO_2 powders with 2.6% Y_2O_3 and Al_2O_3-10 vol. % ZrO_2 (no zirconia stabilizer added) were dispersed, vibratory milled, and spray dried. The dried powders were screened through a 170 mesh screen, and monolithic and three layered "sandwich" (see Figure 1) Al_2O_3-10ZrO_2 composite bar specimens were fabricated. Three layer composites were made by loading a predetermined volume of "outer layer" (Al_2O_3-10ZrO_2) powder into a steel die, followed by "inner layer" (Al_2O_3-10ZrO_2(2.6 mole % Y_2O_3)) powder and a second addition of "outer layer" powder. The layered bars were all made so that the thickness after grinding would be 6 mm with outer layer thickness of 250, 500, 1000, and 2000 micrometers. The layered composites were uniaxially pressed at 35 MPa, followed by isostatic pressing at 207 MPa. Monolithic bars were made of the inner and outer

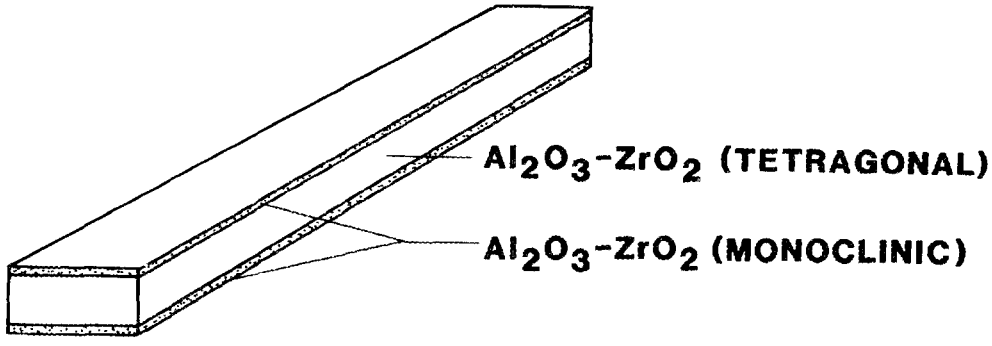

Figure 1. Schematic of Three Layered Composite.

layer compositions. The 160 test bars were sintered at 1587°C for 60 minutes and hot isostatically pressed (HIP) at 1500°C for 30 minutes in 175 MPa Ar overpressure, with properties as shown in Table 1.

X-ray diffraction (XRD) to determine the polymorph type[2] was used to calculate the theoretical density. Sintered densities were between 97.3 and 97.6 % of theoretical density and HIPped densities were greater than 99.8% of theoretical. Shrinkage was identical between the inner and outer layers. The bars were diamond ground on all four sides with a 220 grit wheel. The ground dimensions were 6 mm by 12 mm by 43 mm. A thickness of 6 mm was chosen since outer layer thicknesses below 250 microns are difficult to make using a powder pressing technique. The interfaces between the inner and outer layers were not completely smooth and varied up to 200 microns in the thickness direction of the bar. This variation arises due to die wall-powder interactions, flow of the spray dried powder into the die cavity, and distortion (warping) during sintering and subsequent grinding. Slip casting in a uniaxial direction minimizes the problem and control to within 50 microns is possible.

The bars were broken in 4-point bending (20 mm inner span and 40 mm outer span) at a crosshead speed of 0.5 mm/min. Hardness and indentation fracture toughness[3,4] were determined on one fractured specimen (picked at random) after polishing to a 1 micron polish. Two bars of each type (see Table 1) were polished to a one micron finish and the toughness measured by a multiple-flaw indentation technique[5]. Double cantilever beam (DCB) specimens and short-rod[6] fracture toughness specimens were made for monolithic materials. Residual stresses were measured using a strain gage technique developed by Virkar[1].

Table 1
Physical Properties of Al_2O_3-10ZrO_2

Code	d_1[a] (μm)	Shrinkage (%)	Density(g/cc)		Monoclinic(5)[b]	
			Sintered	HIP	Sintered[c]	Ground[d]
A	---[e]	16.6	4.09	4.19	0.0	4.2
B	---[f]	16.5	4.08	4.19	37.8	65.7
C	250	16.7	4.09	4.19	35.2	62.3
D	500	16.7	4.09	4.19	38.1	64.8
E	1000	16.7	4.08	4.18	36.9	---[g]
F	2000	16.7	4.09	4.18	36.7	---[g]

a. Outer layer thickness of 6 mm thick bars.
b. Percent monoclinic ZrO_2 (balance is tetragonal) as determined by XRD[2].
c. As-sintered or hot isostatically pressed (HIP).
d. As-ground with a 220 grit wheel after "sparking out."
e. Monolithic inner composition.
f. Monolithic outer composition.
g. Not measured (similar to B-D).

Results and Discussion

XRD diffraction showed that the monoclinic content of the ZrO_2 in the outer layer was only 36% (the remainder being tetragonal) and that the zirconia in the inner material was entirely tetragonal. As expected, the monoclinic content increased substantially upon grinding in the near surface region of Al_2O_3-10 ZrO_2 composites containing unstabilized zirconia (see Table 1).

Mechanical property data are summarized in Table 2. The strength of monolithic and three layer bars are shown in Figure 2. The strength and Weibull modulus of sintered bars increased substantially upon hot isostatic pressing (see Figure 3) and there was no difference between the strength of the "inner" (Code A) and "outer" (Code B) layer monolithic materials. Fractography of HIPped bars showed that 40% of the "inner" layer bars failed from chamfers, 33% from inclusions, and 27% from the tensile surface (away from the chamfer). while 60% of the "outer" layer bars failed from chamfers, 33% from the tensile surface, and 7% from inclusions. Code C bars with compressive stress arising from the 250 micron outer layer showed a 20% increase in strength over the monolithic bars. although both the

Table 2
Mechanical Property Data

Code	d_1 (μm)	Strength Data(MPa)[a]				H(GPa)[b]		K_c(MPa-$m^{1/2}$)	
		#[c]	$\bar{x}$[d]	s[e]	m[f]	$\bar{x}$	s	K_c[g]	K_c[h]
A-Si[i]	---	10	363.0	64.3	5.4	--[j]		---[j]	---[j]
A	---	15	505.9	75.1	6.9	17.8	0.38	3.89±0.45	4.06
B-Si[i]	---	10	385.7	94.8	3.7	--[j]		---[j]	---[j]
B	---	15	538.1	75.7	7.3	17.7	0.66	4.44±0.34	4.82
C	250	15	643.6	104.3	6.0	17.5	0.14	5.87±0.29	---[j]
D	500	15	678.7	101.4	6.1	18.0	0.63	5.72±0.18	7.82
E	1000	15	649.6	119.9	4.9	17.5	0.95	5.96±0.59	6.77
F	2000	17	692.6	57.4	12.2	17.1	0.63	5.38±0.69	5.83

a. Four point bend strength on 6 mm x 12 mm x 43 mm bars.
b. Vicker's hardness determined at loads between 75 and 225N.
c. Number of bars broken.
d. Mean value.
e. Standard deviation.
f. Weibull modulus.
g. Indentation toughness[3].
h. Fracture toughness (codes A&B) or apparent toughness (codes C-F) as determined using multiple indent technique[5].
i. As-sintered (Before HIP).
j. Not determined.

standard deviation and Weibull modulus increased. Fractography showed that 40% of the bars failed from chamfers, 33% from inclusions (two of these were within the inner layer), and 27% from the tensile surface. The bend strength of layered bars having 500 micron thick outer layers was 27% higher than monolithic materials (see Figure 2) and fractography showed that 73% of the bars failed from chamfers, 20% from inclusions (the three highest strengths), and 7% from the tensile surface. Code E bars having outer layers 1000 microns thick had strengths similar to Code C and D bars (see Table 2) with 53% of the bars failing from chamfers, 27% from the tensile surface, and 20% from voids or inclusions (all within the outer layer). The Code F bars (all three layers equal in thickness) had strengths 29% higher than the monolithic bars with a substantial increase in the Weibull modulus (see Figure 3). Fractography showed that 47% of the bars failed from the tensile surface, 42% failed from chamfers, and 11% failed from voids or inclusions.

An examination of bars failing from chamfers showed no consistent trend in the initiation location. It is anticipated that a smaller specimen cross-section (i.e., 3 mm x 4 mm) rather than the larger specimen cross-section (6 mm x 12 mm) used for room temperature measurements may decrease the tendency to fail from chamfers since much lower loads will be needed to break the samples.

Electron microscopy of selected samples showed that the average flaw size was 25 to 75 microns when bars failed from inclusions or voids. Impurities from spray drying, primarily CeO_2, were detected by energy dispersive spectroscopy as the inclusions in the samples. Optical microscopy clearly

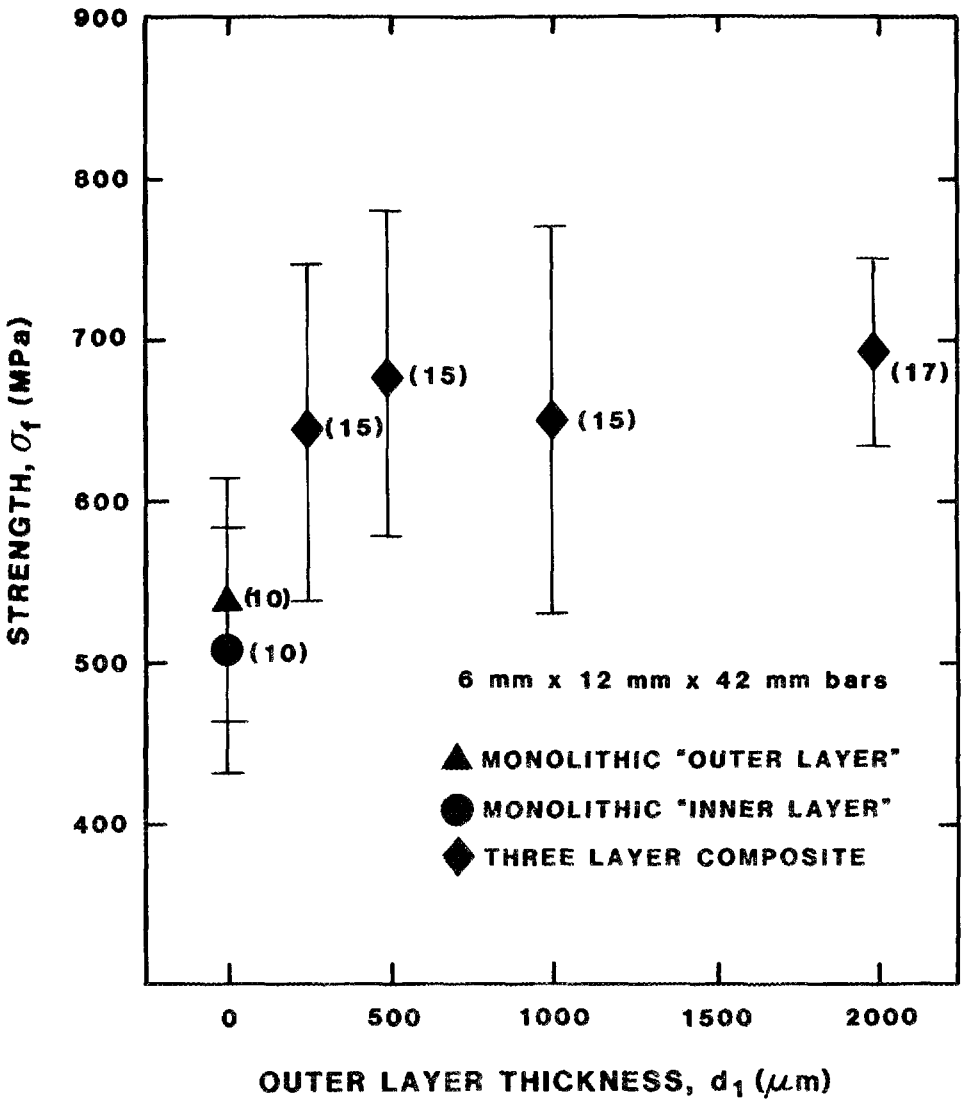

Figure 2. Room Temperature Strength Comparison Between Monolithic and Three Layer Al_2O_3-10ZrO_2 Composites.

showed inclusions distributed throughout the microstructure and no porosity at the interface. Improved processing will significantly increase the strength.

Figure 4 shows a schematic of strains introduced in unconstrained and constrained outer layers assuming a square wave distribution. The residual stresses in the outer and inner layers were calculated assuming $\Delta\epsilon_o$ to be 7.0×10^{-4} (assuming the 10 vol. % ZrO_2 to consist of 43% monoclinic and taking the volume change from the tetragonal to monoclinic transition as 4.9%[6]), ν = 0.25, and E to be 365 GPa.

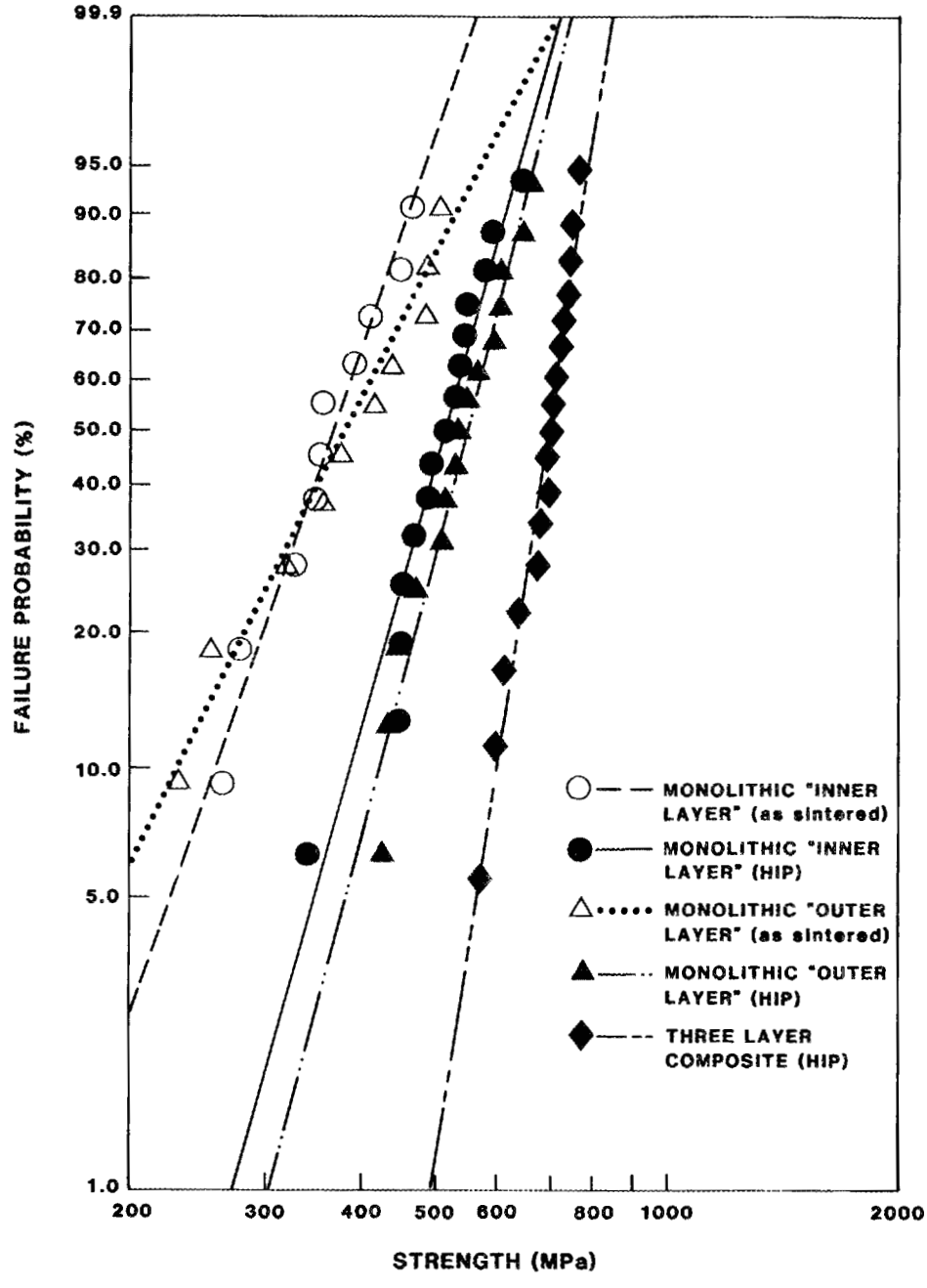

Figure 3. Failure Probabilities of Sintered and Sintered/HIPped Monolithic Materials in Comparison to Sinter/HIPped Three Layer Composite (d_1=2000 microns). See Table 2 for Weibull moduli.

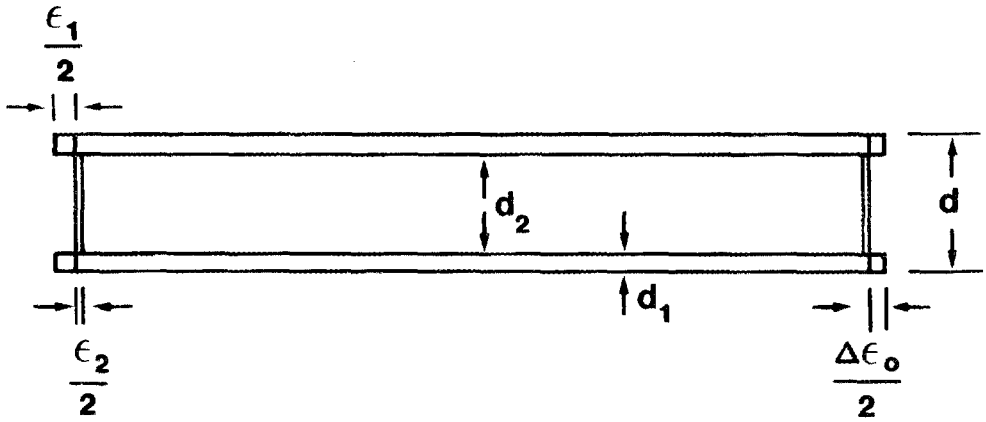

Figure 4. Schematic of Strains Introduced in Unconstrained and Constrained Outer Layers[1].

The residual compressive stress (σ_c) in the outer layer is given by

$$\sigma_c = -d_2 E \Delta\epsilon_o / d(1-\nu) \qquad (1)$$

where d_1 is the thickness in the outer layer, d_2 is the thickness of the inner layer, d is the total thickness of the bar, ϵ_1 is the strain in the outer layer, ϵ_2 is the strain in the inner layer, and $\Delta\epsilon_o$ is the change in strain between the inner and outer layers[1]. Table 3 shows that the transformation-induced residual compressive stresses decrease as the thickness of the outer layer increases.

The monolithic and three layer bars were strain gaged and ground[1] to determine the magnitude of residual surface compressive stresses. Figure 5 shows that residual stresses decrease with increasing outer layer thickness, for three layer bars with constant total thickness. Strain gage data for the C and D bars were erratic due to the variation in thickness of the outer layers. Compressive residual stresses were calculated to be 324 MPa, 171 MPa, 110 MPa, and 83 MPa for three layer bars with nominal thicknesses of 250 (code C), 500 (code D), 1000 (code E), and 2000 (code F) microns, respectively. Both monolithic materials (codes A and B) showed no measurable residual stresses, as expected. The residual stresses measured using the strain gage technique[1] were within 50% of the calculated values for transformation-induced stresses (see Table 3).

The coefficients of thermal expansion of the inner and outer layer monolithic materials between 25 and 1000°C were measured as $8.4 \times 10^{-6}/°C$ and $7.8 \times 10^{-6}/°C$, respectively.

Table 3
Calculated Compressive Stresses and Predicted Strengths

d_1[a] (μm)	Calculated Stresses (MPa)			Predicted Strengths (MPa)			
	Transformation[b]		Temp[c]	Surface[d]			Interface[e]
	σ_c[f]	σ_t[g]	σ_c	T-I[i]	Tg	T-I+T[h]	
250	-286	26	-254	824	792	1078	524
500	-259	52	-231	797	769	1028	545
1000	-208	104	-185	746	723	931	603
2000	-104	207	-93	642	631	735	897

a. Outer layer thickness. Total thickness of all bars is 6mm.
b. Transformation-induced stresses from Equation (1).
c. Temperature-induced stresses from Equation (2).
d. Failure from the surface assuming an outer layer strength of 538 MPa (see Table 2).
e. Failure from the tensile region immediately below the interface using Equation (3) and an inner layer strength of 506 MPa.
f. Assuming transformation-induced stresses are the only stresses present.
g. Assuming temperature-induced stresses are the only stresses present.
h. Assuming both transformation and temperature stresses are present.

The lower thermal expansion coefficient of the outer material would lead to temperature-induced residual compressive stresses in the outer layer given by

$$\sigma_c = -E(\alpha_2 - \alpha_1)\Delta T d_2/d(1-\nu) \qquad (2)$$

where α_1 and α_2 are the coefficients of thermal expansion of the outer and inner layers. respectively. and ΔT is the temperature difference over which the stresses exist. Assuming a temperature gradient of 1000°C, the calculated temperature-induced residual stresses are given in Table 3. As in the case of surface failure in transformation-induced stresses, the residual compressive stresses decrease as the outer layer thickness increases.

As reported previously[1], if failure occurs from within the region of compressive tensile stresses (i.e., just below the interface of the outer and inner layers), the predicted failure stress is given as

$$\sigma_f = (\sigma_f^o - \sigma_t)d/d_2 \qquad (3)$$

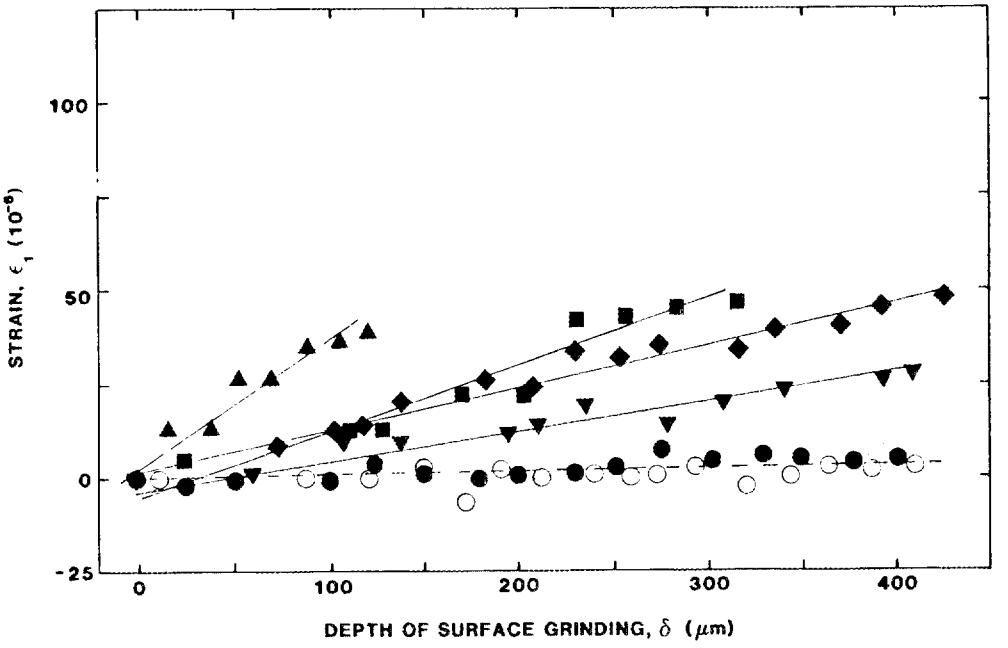

Figure 5. Strain Determination in the Outer Layer of Al_2O_3-$10ZrO_2$ bars (solid circles-inner layer monolithic (code A). open circles-outer layer monolithic (code B), triangles-code C, squares-code D, diamonds-code E, and inverted triangles-code F).

where σ_f^o is the failure stress of the inner material. As shown in Table 3 this strength increases with increasing outer layer thickness, similar to the trend observed in Table 2. Since failure in very few specimens initiated from within the tensile region, it is obvious that either the stress distribution is more complicated that assumed, or grinding flaws controlled failure. Since grinding was identical in both monolithic and layered bars it appears that the 150-180 MPa increase in strength is due to the transformation-induced stresses. If the temperature stresses were significant, as calculated in Table 3, the strength would not be high for Code F bars. It is therefore anticipated that the strength increase due to the compressive stresses will be retained to the transformation temperature. High temperature measurements will be made on bars having layers of equal thickness.

Fracture toughness for the monolithic inner layer material (Al_2O_3-10 vol. % ZrO_2(2.6 mole % Y_2O_3)) was measured using indentation[3.4]. multiple-flaw indentation[5], double

cantilever beam (DCB) and short-rod[6] techniques. The agreement was good between the different techniques with values of 3.89 ± 0.45[3], 3.76 ± 0.46[4], 4.06[5], 4.58(DCB), and 4.00 ± 0.36(short-rod) MPa-$m^{1/2}$. Fracture toughness for the monolithic outer layer material was measured by all of the above techniques, except the short-rod method, with resulting values of 4.44 + 0.34[3] 4.40 + 0.32[4], 4.82[5], and 4.09 ± 0.09(DCB) MPa-$m^{1/2}$. Since fracture toughness, K_{Ic}, is a material property, it is independent of residual stresses. The apparent toughness, K_{Ic}^a, as measured by indentation or by a technique in which the flaw size is much less than the residual zone size, however, increases with increasing compressive residual stresses as

$$K_{Ic}^a = K_{Ic} + K_{Ic}^R \tag{4}$$

where K_{Ic}^R is the stress intensity factor due to residual stresses[8]. The apparent toughness will therefore increase with increasing crack length[9,10] for surface cracks contained well within the outer layer region and is given by

$$K_{Ic}^a = K_{Ic} - \sigma_c \, 2\sqrt{c} \, / \sqrt{\pi} \tag{5}$$

where c is the crack radius. The data in Table 2 are for cracks approximately 150 micrometers in length (c = 75 microns). The apparent toughness. as measured by the multiple flaw technique[5], increases significantly with increasing residual stresses (see Figure 6). in agreement with the WC-Co system previously studied[7]. The difficulty in polishing the large bars prevented the acquisition of more data via the multiple indent technique. No data were obtained for code C bars since the inner layer was exposed after removing only 50 microns during grinding and polishing. Since apparent toughness changes with crack length and the magnitude of residual stresses present, one should be careful to distinguish it from the material property. However, higher apparent toughness should lead to improvement in heat engines components exposed to contact loading or thermal shock.

Monolithic and three layer Al_2O_3-10 vol % ZrO_2 specimens were pressed, sintered. and HIPped as before[2] for use in high temperature testing. Specimens approximately 3 mm x 4 mm x 50 mm will be tested at elevated temperatures with all three layers of the "sandwich" being of equal thickness. This geometry was chosen based on the good room temperature strength of the code F specimens (see Table 2). Elevated temperature 4-point bend testing at 500°C, 750°C, and 1000°C will begin in April.

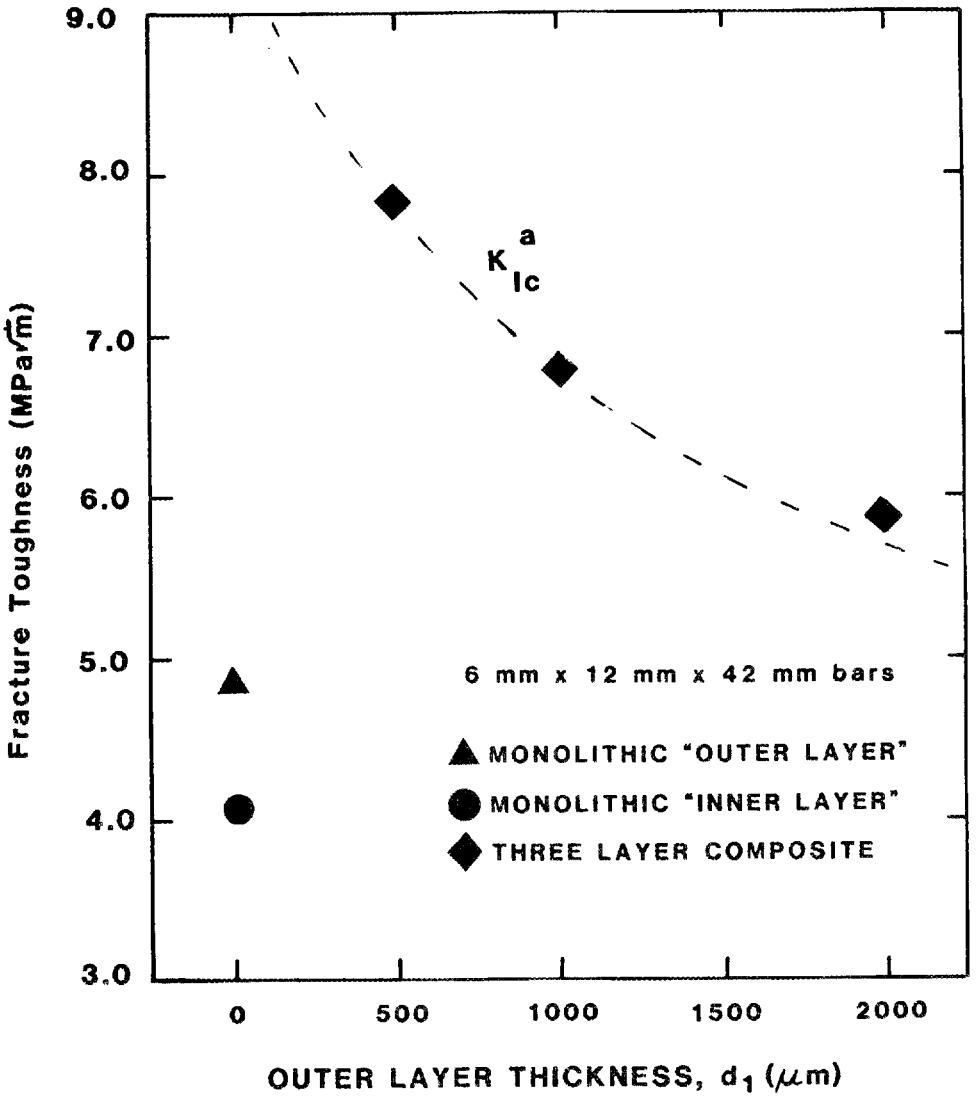

Figure 6. Apparent Toughness Increases With Increasing Residual Compressive Stresses.

Status of Milestones

The following milestone was scheduled for completion in this reporting period.

Milestone: Complete the room temperature characterization (i.e., phase determination. thermal expansion coefficient determination, room temperature strength and toughness testing. and evaluation of porosity) of monolithic and layered Al_2O_3-10ZrO_2.

The milestone was completed with results as summarized above. All other milestones are on schedule.

References

1. A. V. Virkar, J. L. Huang, and R. A. Cutler, "Strengthening of Oxide Ceramics by Transformation Induced Stresses," submitted to Am. Ceram. Soc. for publication.

2. H. Toraya, M. Yoshimura, and S. Somiya, "Calibration Curve for Quantitative Analysis of the Monoclinic-Tetragonal ZrO_2 System by X-Ray Diffraction," J. Am. Ceram. Soc., 68 C-119-C-121 (1984).

3. A. G. Evans and E. A. Charles, "Fracture Toughness Determinations by Indentation," J. Am. Ceram. Soc., 59[7-8] 371-72 (1976).

4. G.R. Anstis, P. Chantikul, B.R. Lawn, and D.B. Marshall, "A Critical Evaluation of Indentation Techniques for Measuring Fracture Toughness: I, Direct Crack Measurements," J. Am. Ceram. Soc.. 64[9] 533-38 (1981).

5. R.F. Cook and B.R. Lawn, "A Modified Indentation Toughness Technique," J. Am. Ceram. Soc., 66[11] C-200--C-201(1983).

6. L. M. Barker, "Short Rod K_{Ic} Measurements of Al_2O_3," Fracture Mechanics of Ceramics. Vol. 3. edited by R. C. Bradt, D. P. H. Hasselman and F. F. Lange, (Plenum Pub. Co., New York. 483 1977).

7. W.M. Kriven, "The Transformation Mechanism of Spherical Zirconia Particles in Alumina," Advances in Ceramics. Vol. 3, Science and Technology of Zirconia II, Edited by N. Claussen, M. Ruhle. and A.H. Heuer (Am. Ceram. Soc., Columbus, OH 64-77 1984).

8. R. A. Cutler and A. V. Virkar, "The Effect of Binder Thickness and Residual Stresses on the Fracture Toughness of Cemented Carbides," J. Mater. Sci., 20 3557-73 (1985).

9. Y. Ikuma and A. V. Virkar, Crack Size Dependence of Fracture Toughness in Transformation Toughened Ceramics," J. Mater. Sci., 19 2233-38(1984).

10. Y. Ikuma and A. V. Virkar, "Comments of Crack Size Dependence of Fracture Toughness in Transformation-Toughened Ceramics," J. Mater. Sci.. 20 4239-44(1985).

Injection Molded Composites

M. A. Janney (Oak Ridge National Laboratory)

Objective/scope

The goals of this activity are twofold: (1) to evaluate the ability of advanced ceramic-ceramic composites to be injection molded and processed using standard wax- and/or polymer-based binder systems; and (2) to develop advanced complex-shape forming technologies that will eliminate some of the problems associated with wax- and polymer-based binder systems such as long binder removal times, cracking, and low green strength.

Technical progress

Work this period focused on two major efforts: (1) rheology of SiC whisker-alumina slurries, and (2) establishing the Ceramic Technology Powder Characterization Laboratory.

Slurry studies

Whisker-reinforced ceramic composites show greatly improved fracture toughness and thermal shock resistance, so they are excellent candidate materials for use in advanced heat engines. Among the biggest unknowns with respect to these materials are the effects of the presence of whiskers on the processing of the materials. To help determine those effects, an investigation into the rheology of water-based slurries of alumina-SiC whisker slurries was conducted. Specifically, we were interested in the effects the whiskers might have on both fully dispersed and fully flocculated slurries including the effects of whisker content and total volume percent solids.

Previous work on the Al_2O_3-SiC whisker system showed that reasonably dispersed slurries could be achieved by using standard procedures and standard additives (e.g., Darvan 7,* citric acid, and Carbowax†). However, it was further observed that differential settling of the SiC and Al_2O_3 occurred; this could be prevented by flocculating the system (achieved by adjusting the pH to ~6).

Materials and methods. The following materials and procedures were used in this investigation. The alumina was Alcoa A16SG,‡ a calcined α-alumina with average particle size about 0.5 μm. The SiC whiskers were Tateho SCW-1S;** they were 0.25 to 0.50 μm in diameter and 10 to 20 μm long. The whiskers were cleaned in concentrated HCl, then washed with deionized water until the pH of the wash solution was about 7. This procedure removed most of the iron and nickel contamination in the whiskers (Fe ~300 ppm, Ni ~200 ppm, as received; Fe about ~20 ppm, Ni ~30 ppm, after washing).

---

*RT Vanderbilt Corp., Norwalk, Conn.

†Union Carbide Corp., Danbury, Conn.

‡Alcoa, Inc., Pittsburgh, Pa.

**Tateho Chemical Co., Ltd., Japan.

Darvan 7 and citric acid* were used as dispersants, and 1N HCl* and 10% tetramethylammonium hydroxide (TMAH)* were used for pH adjustment. Three different slurry preparation methods were used in this investigation; they are summarized in Table 1. Method 1 was to mix the whiskers and alumina in water, add TMAH to adjust to a pH of 11, then sonicate with a 300-W probe† for about 3 min to achieve mixing and dispersion. Method 2 was to mix the alumina and whiskers in a solution of 0.125% Darvan 7 and 0.06% citric acid (based on the weight of SiC and alumina). The pH of these slurries was typically 10.2 ± 0.1. The slurries were then sonicated for about 3 min to mix and disperse. Method 3 was to mix the alumina and whiskers in water (pH ~9.5 to 10), sonicate about 3 min to mix, then adjust to pH 6 with 1N HCl to cause flocculation. The rheological properties of the slurries were measured with a Rheometrics RFS 8400 fluids spectrometer.‡ A parallel plate test geometry was used with a gap of 1.8 mm between plates. This large gap was chosen to try to assure that continuum conditions were approximated during testing, even with the presence of the long (20-μm) whiskers. Rheological measurements were made to determine "equilibrium flow curves" for the slurries under test. This involved shearing the sample at constant strain rate until a constant stress was reached, and then measuring that stress. Typical times to reach a constant stress were: Method 1, 60 sec; Method 2, 30 sec; Method 3, 2 min. Strain rates from 0.5 to 50 sec^{-1} were used.

Results and Discussion. The three methods of slurry preparation described above produced three very different rheologies in the slurries. Method 1 produced somewhat fluid slurries; Method 2 produced very fluid slurries; and Method 3 produced very thick slurries. They are discussed in turn below.

Method 1 – Figure 1 shows the flow curves for slurries made by Method 1. The flow behavior appears to be anomalous in that the shear stresses decrease with increasing whisker content. One would think that the whiskers would increase the shear stresses required for flow. There is, however, a reasonable explanation. At pH 11, A16SG should have a zeta potential of about −10 mV. (A16SG has a point of zero zeta potential of about 9.5 to 10.) A zeta potential of such small magnitude would be expected to produce a flocculated, pseudoplastic or plastic slurry, which is observed to be the case in Fig. 1. On the other hand, the SiC whiskers, which are expected to have a silica surface, should have a large, negative zeta potential, say about −60 mV, at pH 11 and should form a stable, fluid slurry; this is observed qualitatively. An additional factor is the solubility of silica, which is low at acidic and neutral pH, but which increases rapidly above pH 10. Furthermore, it is well established that soluble silica specifically adsorbs on alumina under basic conditions to form a silica layer on the alumina surface. Hence, the following scenario would explain the decrease in shear stress observed with increasing SiC whisker content: as the whiskers are added to the alumina slurry, silica from the surface of the whiskers dissolves in the

---

*Fisher Scientific Co., Pittsburgh, Pa.

†Model 300, Fisher Scientific Co., Pittsburgh, Pa.

‡Rheometrics, Inc., Piscataway, N.J.

Table 1. Summary of slurry preparation methods

Method Number	Rheological control	Additive(s)	Mixing
1	Natural charge on solid at pH 11	TMAH[a] to pH 11	Sonication after pH adjustment
2	Charge on particle surface due to absorbed dispersants	Darvan 7, citric acid	Sonication
3	Flocculation at pH 6	1N HCl to pH 6	Sonication prior to pH adjustment; spatula at pH 6

[a]Tetramethylammonium hydroxide.

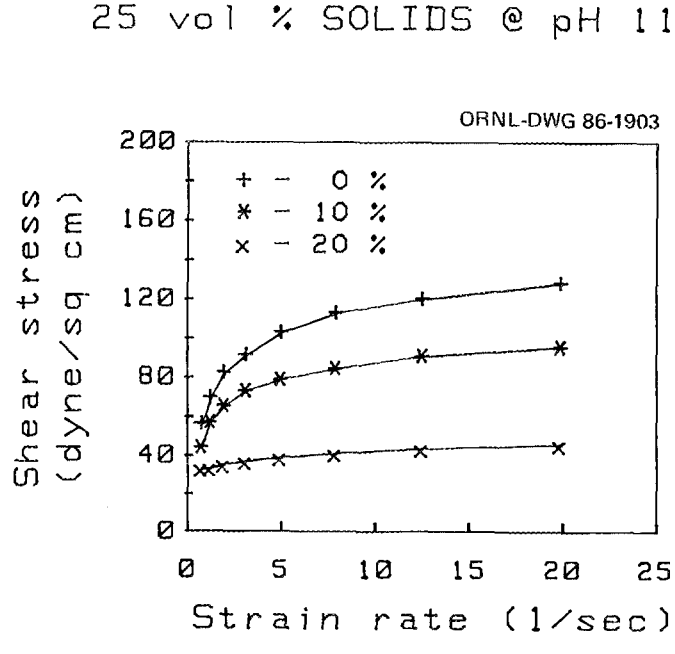

Fig. 1. Adding SiC whiskers to alumina slurries at pH 11 lowered the viscosity of the slurries.

pH-11 water, then adsorbs on the surface of the alumina; this changes the zeta-potential of the alumina particles from about −10 mV to about −60 mV, which, in turn, lowers the viscosity of the slurry of alumina and SiC whiskers with respect to that of pure alumina.

Method 2 – Method 2 produced very fluid slurries as shown in Figs. 2 through 5. At 25 vol % solids, Figs. 2 and 3, the slurries had viscosities below 2 poise, even with 30% SiC whiskers. The slurries became pseudoplastic with as little as 5% whiskers; both the plastic viscosity (slope of the τ-$\dot{\gamma}$ curve at high $\dot{\gamma}$) and the apparent yield point (τ_0) increased with increasing whisker content.

At 40 vol % solids, somewhat different behavior was observed. First, even with no whiskers added, a small yield point was observed (~5 dyne/cm^2). Second, the relative changes in shear stress were smaller at 40 vol % solids than at 25 vol % solids. For example, at a strain rate of 50 sec^{-1}, adding 30% SiC whiskers increased the shear stress from about 3 to to about 18 dyne/cm^2 for the 25 vol % solids slurry (6× increase); for the 40 vol % solids slurry, the same addition increased the shear stress from about 40 to about 80, only a 2× increase. Why the whiskers should have a greater relative effect at 25 vol % solids than at 40 vol % solids is not immediately clear. It may be that it is the absolute increase in shear stress that is important and not the relative effects, or it may be that "crowding" effects exist at 40 vol % solids that do not exist at 25 vol % solids. Evidence for "crowding" effects is shown in Fig. 4, which shows a large increase in shear stress between 30 and 40% whiskers. This is to be compared with the very modest increases in shear stress between 0, 20, and 30% whiskers (40% total solids) shown in Fig. 5.

Method 3 – At pH 6, the slurries with and without whiskers were highly flocculated. Adding whiskers had a much more marked effect on these flocculated slurries than on the dispersed slurries discussed above. In the flocculated slurries, whisker effects were observed at whisker loadings as low as 2% (Fig. 6). The whiskers appear to have two effects: first, they *decrease* the shear stress at low strain rate; then, they *increase* the shear stress at high strain rate. Such behavior is at first most confusing. By visual inspection in the beakers, the slurries with whiskers appear to be more viscous than those without whiskers. Why then this strange behavior? We believe the cause is slip at the wall of the rheometer. An unusual flow was observed in this material when it was being tested. At low strain rates, the material simply rotated as a disk in the gap between the parallel plates; all the shear occurred at the interface between the top plate and the test sample. At high strain rates, shear occurred both in the interfacial layer and in the bulk of the material. (The point of transition out of plug flow has not yet been determined.) Some sort of "phase separation" is thought to be responsible for this slip phenomenon. The particular nature of such slip phenomena can be quantified by testing the material with greater and lesser gap heights between the parallel plates. These and other analyses are in progress and will be reported in the next semiannual report.

Summary. Fluid slurries were achieved via standard additives and standard ceramic processing. The implications of work completed so far are that whisker-containing slurries process in a manner analogous to plain alumina slurries at up to 40 vol % solids and up to 40% whiskers.

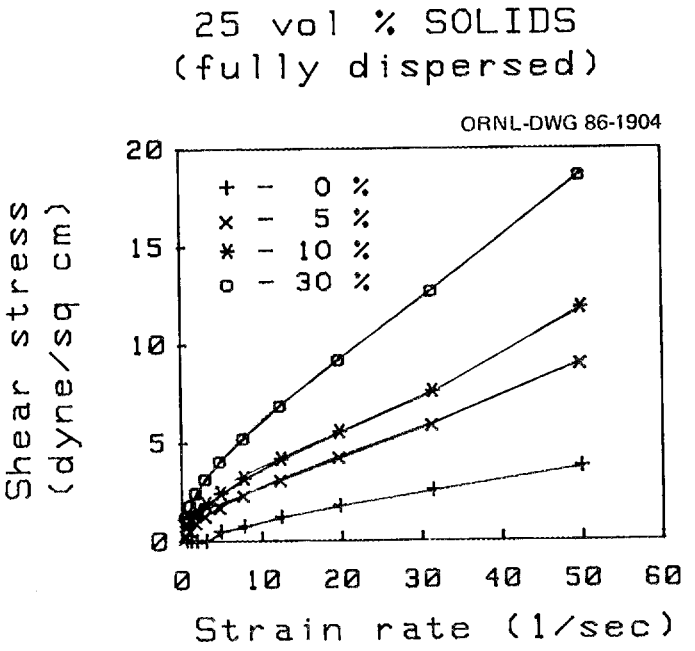

Fig. 2. Adding SiC whiskers to fully dispersed, 25 vol % slurries increased their viscosities and induced pseudoplasticity.

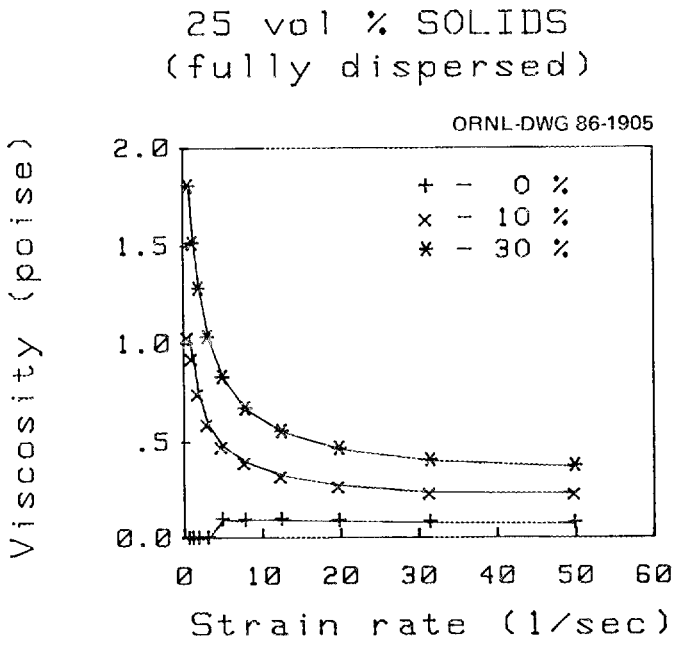

Fig. 3. Adding 30% SiC whiskers to a 25 vol % alumina slurry raised its viscosity only slightly.

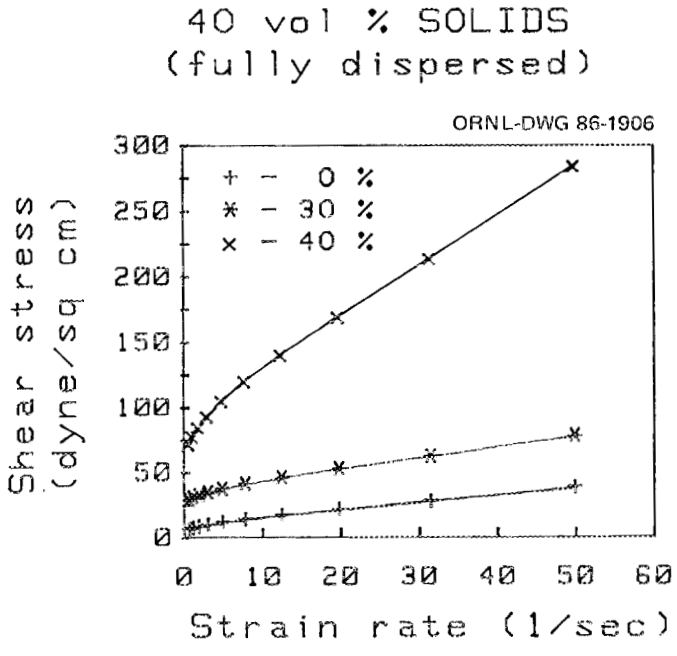

Fig. 4. Shear stress increased rapidly between 30% and 40% SiC whisker additions.

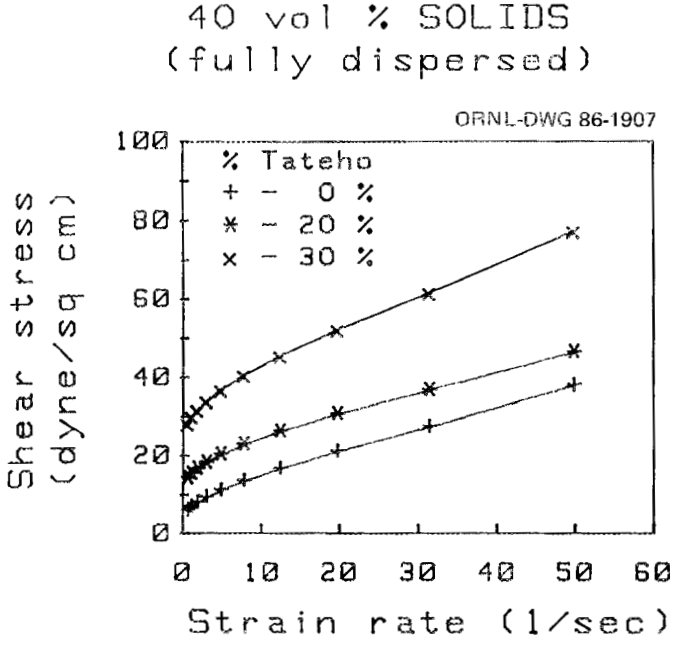

Fig. 5. Shear stress increased slowly between 0% and 30% SiC whisker additions.

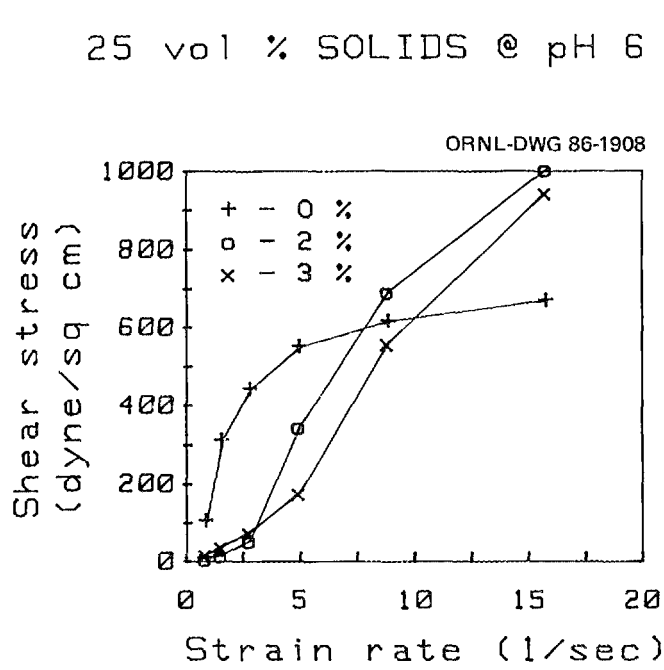

Fig. 6. Flow curves for 2% and 3% SiC whisker slurries indicate slip at the wall.

Flocculated slurries exhibited behavior consistent with "wall slip" or "phase separation" at whisker contents as low as 2%.

At pH 11, in the absence of other additives, the viscosity of SiC-whisker-containing slurries was lower than that of the plain alumina slurry. Dissolution of silica and its subsequent adsorption on the alumina, which increased its negative charge, is postulated to explain this phenomenon.

Powder characterization laboratory

A full description of the instruments included in the laboratory was given in the previous semiannual report. Since then, the Digilab FTS40 Fourier Transform Infrared Spectrometer was received and is operational, the large particle size modification to the Leeds and Northrup Microtrac particle size analyzer was received and is operational, and specifications were written for the soil mechanics triaxial test unit. In addition, modifications to our existing dilatometer have been ordered with funds from other programs to permit complete analysis of sintered density and rate of densification as functions of time and temperature (up to 2100°C, in reducing or neutral atmospheres), including determination of optimum rate-controlled sintering paths.

Status of milestones

No activity.

Publications

None.

1.2.4 Silicate Matrix

Mullite-SiC Whisker Composites

Solomon Musikant (General Electric Co., Space Systems Division)

Objective/Scope

The objective of this program is to develop high toughness, high strength, refractory ceramic matrix composites which are amenable to low cost, near net shape forming for application to automotive engines.

In this program, the General Electric Company, Space Systems Division, is pursuing the development of SiC whisker reinforced mullite (3 Al_2O_3 2 SiO_2) matrix ceramic composite. In addition, the enhancement of the mullite matrix fracture toughness by the incorporation of transformation toughening by additions of $Zr_{0.5}$ $Hf_{0.5}O_2$ is proposed. This mullite matrix composite can meet a very significant need in the ceramic heat engine technology. That specific need is for a low thermal conductivity, high strength, tough, hard and wear resistant ceramic with intrinsically good thermal shock resistance. The intrinsically good thermal shock resistance is due to mullite's moderately low modulus of elasticity, 30 X 10^6 psi (207 GPa), and relatively low coefficient of thermal expansion (CTE), 5 X 10^{-6}/°C, as well as good levels of strength. The thermal conductivity is low, being approximately equal to that of ZrO_2. Since the coefficient of thermal expansion (CTE) is about half that of of ZrO_2, mullite experiences far lower thermal stresses than ZrO_2 when exposed to the same thermal gradient.

Similarly, in comparison to alumina, mullite is intrinsically superior with respect to thermal shock because of mullite's lower CTE and lower modulus of elasticity. Any matrix with a high CTE tends to have lower resistance to thermal shock.

The initial aim of the investigation is to prepare a composite with fracture toughness of $\geq$ 4.0 MPa $\sqrt{m}$.

In order to achieve this goal, we have initiated investigation of mullite-SiC whiskers compositions with varying parameters. The major steps in this investigation are as follows:

1. Prepare mullite/SiC whisker compositions using fine particle size mullite powder. Whisker compositions may range between 15 and 30 wt %. Whiskers may be milled for size reduction before incorporating into a batch composition.
2. Investigate sintering aids which will assist in composite consolidation.
3. Investigate the addition of a transformation toughening agent, $Zr_{0.5}Hf_{0.5}O_2$, to mullite-SiC compositions to enhance the fracture toughness of the matrix material.
4. Consolidation methods include:
   (a) Cold isostatic pressing and sintering.
   (b) Hot isostatic pressing (HIP).
   (c) Cold isostatic pressing (CIP), sintering, and hot isostatic pressing (HIP).

5. Explore the application of coating materials to whiskers to control the bonding strength of whisker to matrix; incorporating diffusion barriers at the whisker/matrix interface to minimize chemical reactions between the matrix and whisker.
6. Characterize the composites for mechanical, physical, chemical and thermal properties at room temperature and at elevated temperatures.

Technical progress

MATERIALS AND PROCEDURE

The primary objective of the current program is to develop a dense (>95% theoretical density) mullite-SiC composite, having high fracture toughness and high flexural strength at room as well as elevated temperatures, using net shape processing without resorting to hot pressing.

During this reporting period (1st half FY1986), of this two-year program, technical efforts were focussed on preparing highly densified mullite-SiC whisker composites by hot isostatic pressing (HIP'ing) of sintered composite billets. As reported in the prior semi-annual report, it was found that mullite/SiC whisker (70/30 weight %) composites, prepared by cold isostatic pressing (CIP'ing) followed by sintering in air, yielded approx. 90-91% dense material with or without a sintering aid. In general, a sintered composite density needs to be improved to $\geq$ 95% (with no open porosity) in order for containerless HIP'ing of these material to be successful. For a net shape process, such a containerless HIP'ing procedure is preferred. However, if high enough density of material is not achieved after sintering, encapsulation or canning of the material in a refractory metal, such as Mo or Nb or a glass, such as, Vycor or fused silica is necessary for HIP'ing.

In our first attempt at HIP'ing we used an 88% dense mullite/SiC whisker composite (70/30 wt %) sintered at 1650°C/3 hrs. The sample was encapsulated in a molybdenum (Mo foil, 0.005" thick) capsule by electron beam (EB) welding and then HIP'ed at 1500°C, 15 KSI, 1/2 hour. Figure 1 shows the molybdenum capsule before and after HIP'ing. As seen, the capsule embrittled and failed with no measurable increased densification of the specimen.

Several mullite-SiC whisker composite samples were then HIP'ed after each material was vacuum encapsulated in a Vycor or silica glass (sometimes referred to as fused quartz glass) tube. They are described in Table I and photographs of the composite pieces as encapsulated or canned inside Vycor or fused quartz capsules are shown in Figure 2. As shown, some of the samples, prior to glass encapsulation, were wrapped in a Saffil ceramic fiber paper (Al_2O_3-5w%SiO_2, ICI Chemical Corp.) while others were surrounded by a mullite powder which had been cold isostatically pressed in place. The objective of these wraps was to minimize stresses on the capsule due to sharp edges of the specimens. These glass en-

capsulated samples were HIP'ed at 1650°C, 10 KSI, 1/2 hour. Only one specimen, with a composition of mullite/SiC whiskers/Nb_2O_5, 70/30/10 weight ratio (#1 in Table I, #1V in Figure 2), was effectively densified to about 98% theoretical density after HIP'ing. It is believed that HIP'ing of other specimens was unsuccessful because of the failure of glass cans or capsules during heat up.

In the next HIP runs, twelve specimens of sintered mullite-SiC whisker composites were hot isostatically pressed (HIP'ed) at Gorham International Inc., Gorham, Maine. Three HIP procedures were followed. Four of these composite specimens were vacuum encapsulated in niobium (Nb-1 w/o Zr) cans by helium-arc welding technique. Nb powder was used as a separator between the Nb can and the ceramic billet in these cans. Four other samples were vacuum encapsulated in Vycor glass capsules and the remaining four samples were HIP'ed while placed inside a silica glass powder surrounded in a graphite crucible. In all cases, HIP conditions were 1600°C, 30 Ksi argon, 0.5 hour. Table II, specimens Nos. 2-13, shows the compositions, processing methods and final density of the HIP'ed specimens. Figures 3 to 5 show photographs of the specimens after HIP'ing. The pictures show niobium metal cans containing the first group of specimens, the second group of four composite specimens already taken out of the Vycor glass cans and the third group of four smaller specimens still inside solidified silica glass melts.

As shown in Table II, only one specimen (No. 6, mullite/SC9/Glass I = 70/30/20, parts by wt.) out of four, encapsulated in Vycor glass cans, densified to <95% theoretical density. It is believed that for the other specimens, the Vycor glass capsules failed before reaching HIP conditions.

Among specimens HIP'ed inside silica glass melts, two composite samples containing (mullite/SC9/Glass I and mullite/SC9/Glass II, 85/15/15, parts by wt.) showed high densities (approx. 97-98% of theoretical). In the case of the niobium metal cans, HIP'ing of the samples was successful without any failure of the cans; however, extraction of the specimens out of these metal cans was difficult because the specimen surfaces were strongly bonded to the Nb. Also, the niobium metal powders used to fill in the spaces between the sample and the metal can (0.0625" wall) sintered into a hard and strong mass, thus thickening the can's wall.

The metal jackets of the Nb cans were cut off and usable portions of the billets selected for flexure bars. The HIP'ed billets with densities >95% of theoretical were then fabricated into flexure bars for mechanical test. These are redesignated and compositions are listed with the new billet Nos. on Table III for convenience of reference.

In regard to HIP'ing procedures, we believe that all three encapsulation techniques are usable. It is possible that the powdered glass approach as an encapsulation technique will prove to be the most cost effective of these three methods. However, for the remainder of this program we have decided to continue with the Nb canning technique as the most reliable for the purposes of the current study. However, the separating powder initially

selected, Nb, will be replaced with a SiC powder/whisker mix in future runs.

MECHANICAL TESTING

Mechanical testing on this study was performed at GE - Research and Development Center. An experimental set-up for high temperature four-point bend testing has been constructed. An overall schematic of the arrangement is shown in Figure 6. cooling jackets are provided at the top and bottom to protect the load cell and other metal hardware. A photograph of the apparatus is given in Figure 7 while the four point, SiC, load fixture is seen in Figure 8. A photograph of the lower cooling jacket is provided in Figure 9.

Four point bend tests have been conducted on mullite and mullite SiC composite specimens machined to the Type B specimen dimensions of MIL-STD-1942 (MR), 3 mm X 4 mm X 45 mm. Two such specimens are shown in Figure 10.

Fracture testing of the mullite specimens is intended to provide a baseline from which the improvement by whisker addition can be judged. Mechanical test data on the unreinforced mullite and the SiC whisker reinforced mullite matrix composites is shown in Table IV. The billets from which the mullite test bars were cut were prepared from the same Baikowski mullite starting powder without Al_2O_3 additions and consolidated by sintering in air.

The best specimens come from billets L1 and L7. Weight change upon thermal soak at 1000°C/100 hrs for these two billets was negligible as shown on Table V. In addition, a flexure specimen from billet L7 tested at 800°C provided an MOR higher than one of the two specimens tested at room temperature. Measurement of modulus of elasticity of L1 and L7 at room temperature showed values of 236.6 GPa and 221 GPa (average of two), respectively. In addition, for L7, displacement measurement at 800°C indicated very little change in modulus of elasticity at 800°C.

The remaining billets revealed either poor strength or poor thermal stability upon heating to 800°C or upon thermal soak, as indicated in Table IV.

Fracture toughness data is also given in Table IV. All data presented is based on multiple indent, 4 point flexure, technique except for the specimen from billet L1 where the single indent technique was employed. Based on the test data to date, the most promising approach is the use of Nb_5O_5 in the range of 5 w/o as an additive.

XRD RESULTS

The composites #L1 and #L7 were analyzed by x-ray diffraction (Figure 11). This XRD data showed the presence of mullite and SiC phases in L1 and mullite, SiC and NbC phases in L7 material.

The Nb_2O_5 evidently reacts with the SiC to form NbC probably degrading the whiskers to some extent. Future runs will attempt to coat the whiskers with carbon to act as a sacrificial layer to the NbC forming reaction and also to modify the interfacial

bond strength between the whiskers and the matrix.

MICROSTRUCTURES

The SiC whiskers after milling and cleaning are shown in Figure 12. Most of the shot has been eliminated and a relatively broad distribution of lengths is evident in this micrograph. Micrographs of L1, L3, L6, L7 and L10 are shown, respectively, in Figures 13, 14, 15, 16 and 17. These show fracture surfaces of shards of material. In all cases, good distribution of the whiskers in the matrix is evident.

Figure 18 shows a fractograph from a mullite (unreinforced) flexure bar revealing a typical polycrystalline fracture surface with river patterns.

Fractograph of a flexure bar taken from billet L7 is seen in Figure 19. The fractured whiskers are visible as circular features and there is an extensive network of microcracking in the fracture surface. L7 exhibited the highest flexural strengths of the specimens tested to date.

One can safely say that by virtue of the microcracking in the L7 fracture surface in contrast to the pure mullite fractograph (Figure 18) that much more energy is being asborbed in L7 during fracture because of the large amount of free surface area being created. There is still room, however, for considerable improvement in the L7 type material. There is little SiC whisker pullout which means that the SiC whiskers fractured shortly after the matrix failed. Micromechanical analysis indicates that large additional amounts of energy can be absorbed in some whisker pullout can be achieved.

Work in progress

In order to improve the mechanical performance of the mullite/SiC whisker composites several approaches are being implemented. These include:

1. Increased SiC whisker content.
2. Increased comminution of powders to achieve sub-micron particulates.
3. Additional powder preparation to minimize or eliminate coarse particulates.
4. Investigation of graphite coatings on SiC whiskers to
   (a) inhibit reaction of SiC with Nb_2O_5 sintering aid
   (b) reduce interfacial bonding between the whisker and the matrix.
5. Investigation of non-oxidizing sintering atmospheres, argon or nitrogen, and/or packing the green body in SiC powder as a protection against oxidation of the SiC whiskers.

The compositions of seven billets currently in preparation are given in Table VI. In all cases the SiC content is 30 w/o of the total. The rationale for these selections follows:

R1 This is the baseline, containing only Baikowski mullite and uncoated SiC whiskers.

R2 Similar to R1 with the inclusion of 4.7 w/o Nb_2O_5 as a sintering aid.

R3 Similar to R1 with the addition of $Zr_{0.5}Hf_{0.5}O_2$ as a transformation toughening agent.

R4 Similar to R1 except that part of the mullite is replaced with Glass I as a sintering aid and sufficient Al_2O_3 to convert the Glass I to mullite by additional heat treatment after HIP'ing, if needed.

R5 Similar to R2 with one half the Nb_2O_5 content.

R6 Similar to R2 with less SiC whisker content.

R7 Similar to R3 with the addition of Nb_2O_3 as a sintering aid.

The details of the processing of these billets (e.g. whisker coating and sintering atmospheres) will be modified as indicated by the results of 4 and 5 above.

Status of Milestones

Table VII lists the Milestone schedule for this study. Milestone 3.3.1 is partially complete and is currently being emphasized in the program.

Milestone 3.3.3 has been initiated and will be further developed as more mechanical test results become available.

Publications

A paper "Development of Mullite/SiC Whisker Composites for Application in the Ceramic Technology for Advanced Heat Engine Program " by S. Musikant, S. Samanta, P. Architetto & E. Feingold, was presented in the 10th Annual Conference on Composites and Advanced Ceramic Materials, January 19-24, 1986, Cocoa Beach, FL, sponsored by the Engineering Ceramics Div., Am. Ceramic Society.

TABLE I

VACUUM ENCAPSULATION OF COMPOSITES
IN A GLASS FOR HIP'ING

SAMPLE NO.	COMPOSITION	PROCESSING CONDITIONS	DENSITY, % THEORETICAL (SINTERED)	VACUUM SEALED IN	
				VYCOR	FUSED SILICA
1	M/SC9/Nb_2O_5 (70/30/10) Parts by wt.	Mullite and Nb_2O_5 first blended in a planetary mill for 15 minutes, dry; whiskers added and then blended for another 15 mins; the batch material then CIP-ed at 55 KSI and sintered at 1670°C for 3 hours; then HIP'ed at 1650°C, 10 KSI, 1/2 hour.	91.1	Sample* wrapped in a Saffil paper	Sample inside a layer of mullite powder - CIP'ed
3	M/SC9/Glass I (70/30/10)	Mullite and glass powders first blended together in planetary mill for 15 minutes and then blended for another 15 mins with whiskers added. The batch is then CIP-ed at 55 KSI and sintered at 1670°C/3 hrs and HIP'ed at 1650°C/10 KSI/½ hr.	87.7	Bare Sample	Bare Sample
4	M/SC9/Glass II (70/30/10)	"	87.1	Tube collapsed onto the sample by flame fusion before vacuum sealing.	Bare Sample

TABLE I (CONTINUED)

VACUUM ENCAPSULATION OF COMPOSITES
IN A GLASS FOR HIP'ING

SAMPLE NO.	COMPOSITION	PROCESSING CONDITIONS	DENSITY, % THEORETICAL (SINTERED)	VACUUM SEALED IN	
				VYCOR	FUSED SILICA
6	M/SC9 (70/30)	Prepared by wet dispersion mixing in a Waring blender at PH 11.0, re-adjusted the PH to 7.0, concentrated the slurry by boiling off water and then dried. Dry batch powder CIP-ed at 55,000 psi, and sintered at 1670°C/3 Hrs; then HIP'ed at 1650°C/10 KSI/½ hr	90.9	Sample inside a layer of mullite powder - CIP'ed	Sample wrapped in a Saffil paper

NOTE: *Only sample densified to a higher density (approx. 98%)

M = Baikowski mullite, 193 CR

Other Materials - same as in Table II

( ) - weight ratio of components

Saffil Paper - Al_2O_3-5w% SiO_2 fibrous paper with low content of binder (ICI Chemical Corp.)

TABLE II

MULLITE-SiC WHISKER COMPOSITES
(SINTERED & HIP'ED)

SPECIMEN NO.	(PARTS BY WEIGHT) MULLITE	SiC WHISKER	GLASS I	GLASS II	Nb_2O_5	Al_2O_3	PROCESSING CONDITIONS	DENSITY (% THEORETICAL)	REMARKS	BILLET DESIGNATION IN TABLE III
1	70	30	-	-	20	-	Planetary ball milled (PBM) wet, 5 minutes, dried, deagglomerated and then CIP'ed at 55 KSI, sintered at 1670°C/3 hours and then HIP'ed at 1600°C/19 KSI/0.5 hr.	97.9	HIP'ed without* encapsulation	1
2	70	30	-	-	-	-	Same as above up to sintering step; then HIP'ed at 160C°C/ 30 KSI/0.5 hour	99.4	HIP'ed inside Nb metal can	L1
3	70	30	-	-	10	-	"	90.2	HIP'ed in Vycor glass can	
4	70	30	20	-	-	48	"	98.2	HIP'ed in Nb metal can	L3
5	70	30	-	20	-	37	"	98.9	"	L4
6	70	30	20	-	-	-	"	96.5	HIP'ed in Vycor glass can	L5
7	70	30	-	20	-	-	"	90.9	"	L6
8	70	30	-	-	5	-	"	97.9	HIP'ed in Nb metal can	L7
9	85	15	15	-	-	-	"	98.1	HIP'ed in silica glass powder melt	
10	85	15	-	15	-	-	"	97.4	"	

TABLE II (CONTINUED)

SPECIMEN NO.	(PARTS BY WEIGHT) MULLITE	SiC WHISKER	GLASS I	GLASS II	Nb_2O_5	Al_2O_5	PROCESSING CONDITIONS	DENSITY (% THEORETICAL)	REMARKS
11	80	20	-	-	-	-	"	84.4	HIP'ed in Vycor glass can
12	70	30	10	-	-	-	Mullite and glass powder first blended together in PBM for 15 minutes and then blended for another 15 minutes with whiskers added; batch then CIP'ed at 55 KSI and sintered at 1670°C/3 hrs and then HIP'ed at 1600°C/30 KSI/0.5 Hr	80.3	HIP'ed in silica glass powder melt
13	70	30	-	10	-	-	"	80.0	"

*Specimen No. 1 HIP'ed at GE
All others HIP'ed at Gorham

NOTE:

Sintered and HIP'ed billets: 2¼" X 1" X 1" (Nos. 1-8); ≤ 1" X 1" X 1" (Nos. 9-13)

Raw Materials Used:

Mullte - New, deagglomerated mullite (193 CR) from Baikowski Corp.

SiC Whiskers - SILAR SC-9 from ARCO Metals Co.
Washed and cleaned by suspending the whiskers in deionized water and then decanting the blackish scum, floatables and fine particles in the top aqueous layer; good whiskers, settled at the bottom, were then dried, and planetary ball milled for ½ hour.

Nb_2O_5 -- 325 mesh, Kenametals Co.

Glass I - SiO_2/Al_2O_3, 95/5 mole %, melted and ground, -325 mesh

Glass II - SiO_2/Al_2O_3, 85/15 mole %, melted and ground, -325 mesh

Al_2O_3 - 38-900 grade, Norton Co.

TABLE III

MULLITE-SiC WHISKER COMPOSITES
(SINTERED & HIP'ED)

BILLET NO.	COMPOSITION, PERCENT BY WEIGHT						PROCESSING CONDITIONS	DENSITY (% THEORETICAL)	HIP CANNING		
	MULLITE	SiC WHISKER	GLASS I	GLASS II	Nb_2O_5	Al_2O_3			NONE	Nb	VYCOR
1	58.3	25	-	-	16.7	-	Planetary ball milled (PBM) wet, 5 minutes, dried, deagglomerated and then CIP'ed at 55 KSI, sintered at 1670°C/ 3 hours and then HIP'ed at 1600°C/19 KSI/0.5 hr.	97.9	X		
L1	70	30	-	-	-	-	Same as above up to sintering step; then HIP'ed at 1600°C/ 30 KSI/0.5 hour	99.4		X	
L3	41.7	17.9	11.9	-	-	28.5	"	98.2		X	
L4	44.6	19.1	-	12.7	-	23.6	"	98.9		X	
L5	58.3	25	16.7	-	-	-	"	96.5			X
L7	66.7	28.6	-	-	4.8	-	"	97.9		X	

NOTE:

Sintered and HIP'ed billets: 2¼" X 1" X 1"

Raw Materials Used:

Mullite - New, deagglomerated mullite (193 CR) from Baikowski Corp.

SiC Whiskers - SILAR SC-9 from ARCO Metals Co.
Washed and cleaned by suspending the whiskers in deionized water and then decanting the blackish scum, floatables and fine particles in the top aqueous layers; good whiskers, settled at the bottom, were then dried, and planetary ball milled for ½ hour.

Nb_2O_5 -- 325 mesh, Kenametals Co.

Glass I - SiO_2/Al_2O_3, 95/5 mole %, melted and ground, -325 mesh

Glass II - SiO_2/Al_2O_3, 85/15 mole %, melted and ground, -325 mesh

Al_2O_3 - 38-900 grade, Norton Co.

TABLE IV

MECHANICAL PROPERTIES OF COMPOSITES

BILLET NO.	SPECIMEN NO.	RT-MODULUS OF RUPTURE MPa	RT-MODULUS OF RUPTURE Ksi	RT-ELASTIC MODULUS GPA	RT-ELASTIC MODULUS MPsi	800°C - ARGON MODULUS OF RUPTURE MPa	800°C - ARGON MODULUS OF RUPTURE Ksi	RT-K_{IC} MPa m	COMMENT
1	1	282.3	41.0						Mullite/SiC Whisker/Nb_2O_5 70/30/20 Parts by Weight
	2	276.2	40.1						
	3	233.1	33.8						Specimens fractured during heat up to 800°C/ Argon.
	4	307.5	44.6						
	AVG OF 4	274.8	39.9						Severe surface pitting during 1000°C/100 hr soak in air.
	5*	393.3	57.0					2.5	
L1	1**	546.0	79.2						Mullite/SiC whisker 70/30 - parts by weight
	2**	596.3	86.5						
	AVG of 2	571.2	82.8						
	4***	377.4	54.7	236.5	34.3			3.8	
L3	1	300.3	43.5	205.0	29.7				Contains G-I sintering aid with Al_2O_3 additive.
	2	304.0	44.1	222.0	32.2				
	AVG OF 2	302.2	43.8	224.0	31.0				
	A					217	31.5		
	B					219	31.8		
	AVG OF 2					218	31.7		
L4	1	318.8	46.2	218.5	31.7				Contains G-II sintering aid with Al_2O_3 additive.
	2	281.7	40.8	228.0	33.1				
	AVG OF 2	300.3	43.5	223.3	32.4				
	7					206.5	29.9	3.0	
L5	1	192.8	28.0	153.6	22.3				Contains G-I sintering aid without alumina additive. Specimen fractured during heat up to 800°C/Argon. Specimens fractured during 1000°C/ 100 hr - soak in air.
	2	159.4	32.1	153.4	22.2				
	AVG OF 2	176.1	25.5	153.5	22.2			2.4	

TABLE IV (CONTINUED)

BILLET NO.	SPECIMEN NO.	RT-MODULUS OF RUPTURE MPa	Msi	RT-ELASTIC MODULUS GPa	MPsi	800°C - ARGON MODULUS OF RUPTURE MPa	Ksi	RT-K_{IC} MPa $\sqrt{m}$	COMMENT
L6	1	100.1	14.5	129.7	18.8				Contains G-I sintering aid without alumina additive.
	2	140.8	20.4	114.8	16.6				
	AVG OF 2	120.5	17.5	122.3	17.7				
L7	1	448.5	65.0	211.8	30.7				Mullite/SiC whisker/Nb_2O_5: 70/30/5 parts by weight.
	2	315.1	45.7	231.2	33.5				
	AVG OF 2	381.5	55.4	221.5	32.1				
	3					316.6	45.9	2.9	
M1	1	170.5		181.3	26.3				Sample fabricated from Baikowski mullite 193CR powder as received. CIP, sintered 1600°C/ 30 min.
	2			162.8	23.6				
	AVG OF 2			172.1	25.0			2.2	

NOTES

All flexure bars 3 mm X 4 mm X 45 mm
4 Point 40/20 mm span (as indicated on Figure 6) unless otherwise noted.

* 3 Point bend 40 mm outer span with single load point at 30/10 mm position.

** 3 Point bend 12.7 mm outer span (3 mm X 4 mm cross-section)

*** 4 Point bend 17.78/7.62 mm span (3 mm X 4 mm cross-section)

TABLE V

THERMAL SOAK IN AIR (1000°C/100 HRS) RESULTS ON COMPOSITES

SPECIMEN NO.	WEIGHT BEFORE THERMAL SOAK (gm)	WEIGHT AFTER THERMAL SOAK (1000°C/100 HRS) (gm)
#L1-1	0.6730	0.6728
-2	0.5758	0.5757
#L7-1	0.4545	0.4527

TABLE VI

MULLITE-SiC WHISKER COMPOSITES

COMPOSITION, PERCENT BY WEIGHT

No.	Mullite A	Nb_2O_5	ZrO_2-HfO_2 (1:1 molar)	Glass I	Al_2O_3	SiC Whisker
1	70.0	--	--	--	--	30.0
2	653	4.7	--	--	--	30.0
3	56.0	--	14.0	--	--	30.0
4	35.5	--	--	10.2	24.3	30.0
5	67.6	2.4	--	--	--	30.0
6	85.3	4.7	--	--	--	10.0
7	52.2	4.7	13.1	--	--	30.0

NOTE: Mullite A - Baikowski mullite, 193CR/Norton Alumina, 38-900 85/15 V% (81.8/18.2 W%); calculated Al_2O_3/SiO_2 = 74.0/26.0 W%

Glass I - SiO_2/Al_2O_3, 95/5 mole % (91.8/8.2 W%)

TABLE VII

Development of Ceramic Matrix Composites for Application in the Ceramic Technology for Advanced Heat Engine Program - Mullite Si C Whisker Composites Subcontract 86X-00218C

Milestone Schedule

Task		Date
1.	Feasibility demonstration	
1.1	Establish performance goals	12/14/84
1.2	Fabricate initial specimens	1/7/85
1.3	Characterize initial specimens	2/1/85
2.	Develop process flow sheets	
2.1	Develop low cost near net shape process	
	Fabricate initial liquid phase sintered specimens	4/1/85
	Fabricate initial HIP specimens	4/5/85
	Fabricate improved liquid phase sintered specimens	8/2/85
	Fabricate improved HIP specimens	8/2/85
	Select best process for optimization	1/3/86
2.2	Develop optimized process	
	Document optimized process flow sheet for intermediate level of optimization	5/2/86
	Document process flow sheet for final level of optimization	8/1/86
3.0	Property measurements	
3.1	Characterize microstructure of each stage of process development	
	initial	5/3/85
	improved	9/6/85

Task		Date
3.1	intermediate optimization	5/2/86
	final optimization	8/1/86
3.2	Submit detailed test plan to ORNL	2/1/85
3.3	Property measurements	
3.3.1	(a) Measure MOR, K_{IC} at RT and 1200C	5/3/85
	(b) Measure MOR, E, K_{IC} CTE, k at RT and 1200C.	9/6/85
	Thermal soak at 1000C/500 hrs. and repeat tests.	
	(c) Repeat (b)	7/4/86
3.3.2	Perform cyclic fatigue test and fatigue crack	5/16/86
	propagation test	
3.3.3	Model MOR of composite	5/16/85
3.3.4	Perform thermal shock analyis	8/15/86
4.0	Reports	
	Milestone schedule	12/1/84
	Bimonthly reports	1/15/85
		3/15/85
		5/15/85
		7/15/85
		9/15/85
		11/15/85
		2/10/86
		4/10/86
		6/10/86
		8/11/86
		10/10/86
	Semi annual reports	6/15/85
		12/15/85
		4/21/86
	Final report	11/18/86
		11/30/86

BEFORE HIP

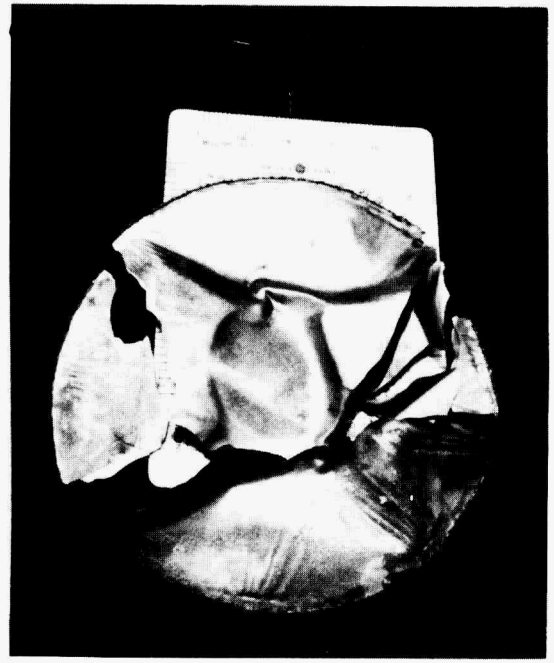

AFTER HIP

FIGURE 1 Molybdenum Foil Encapsulated Samples

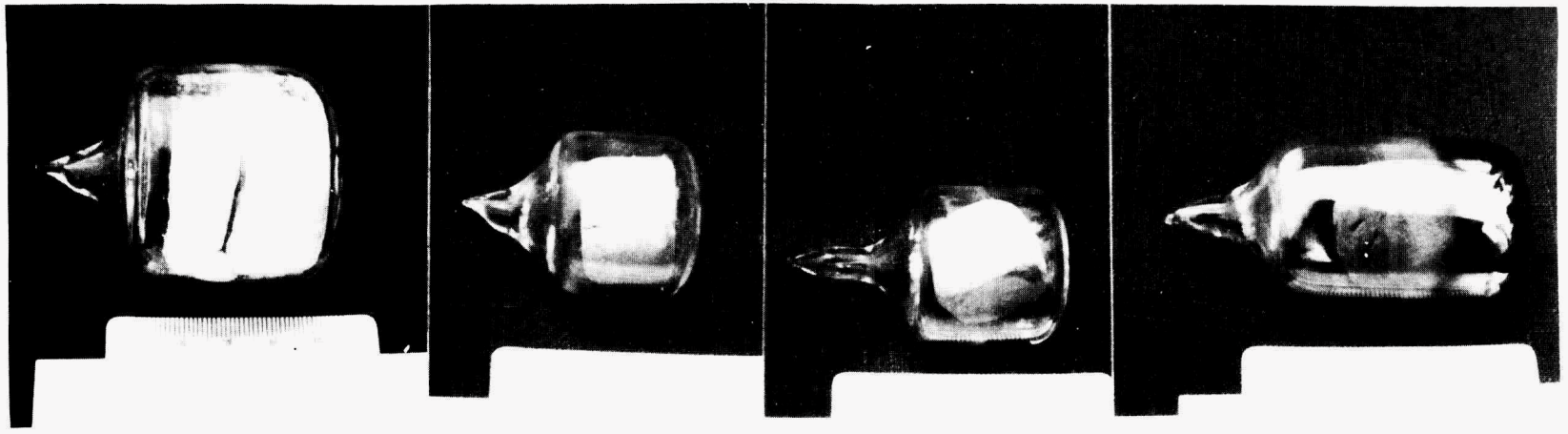

1Q
CIP'D MULLITE JACKET
QUARTZ CAPSULE

3Q
QUARTZ CAPSULE

4Q
QUARTZ CAPSULE

6Q
SAFFIL JACKET
QUARTZ CAPSULE

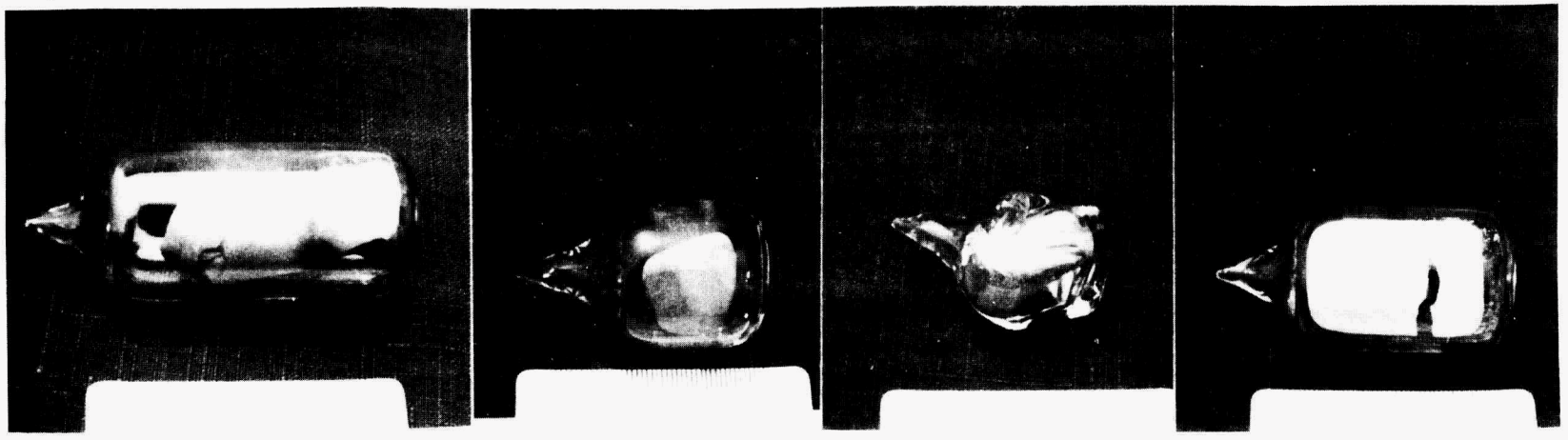

1V
SAFFIL JACKET
VYCOR CAPSULE

3V
VYCOR CAPSULE

4V
COLLAPSED
VYCOR CAPSULE

6V
CIP'D MULLITE JACKET
VYCOR CAPSULE

FIGURE 2 GLASS ENCAPSULATED SAMPLES

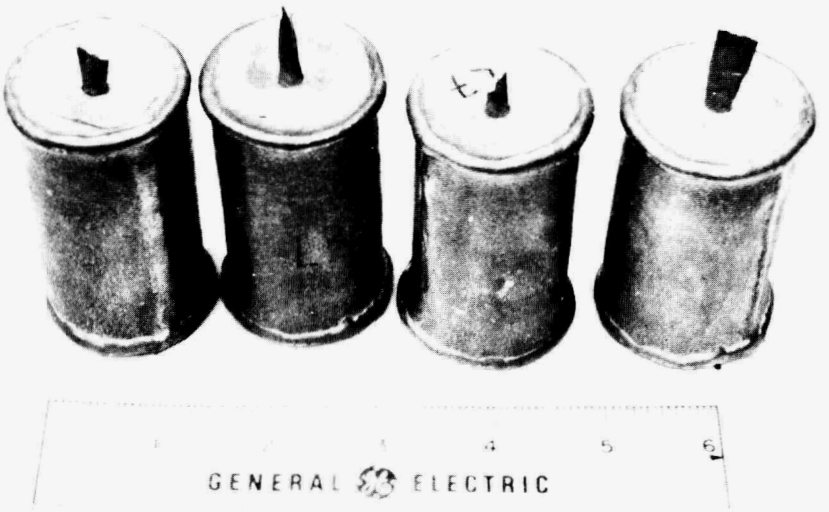

FIGURE 3 HIP'ED NIOBIUM METAL CANS WITH COMPOSITE SPECIMEN INSIDE

FIGURE 4 COMPOSITE SAMPLES HIP'ED IN VYCOR GLASS CANS

FIGURE 5 HIP'ED COMPOSITE SPECIMENS INSIDE SILICA GLASS MELTS

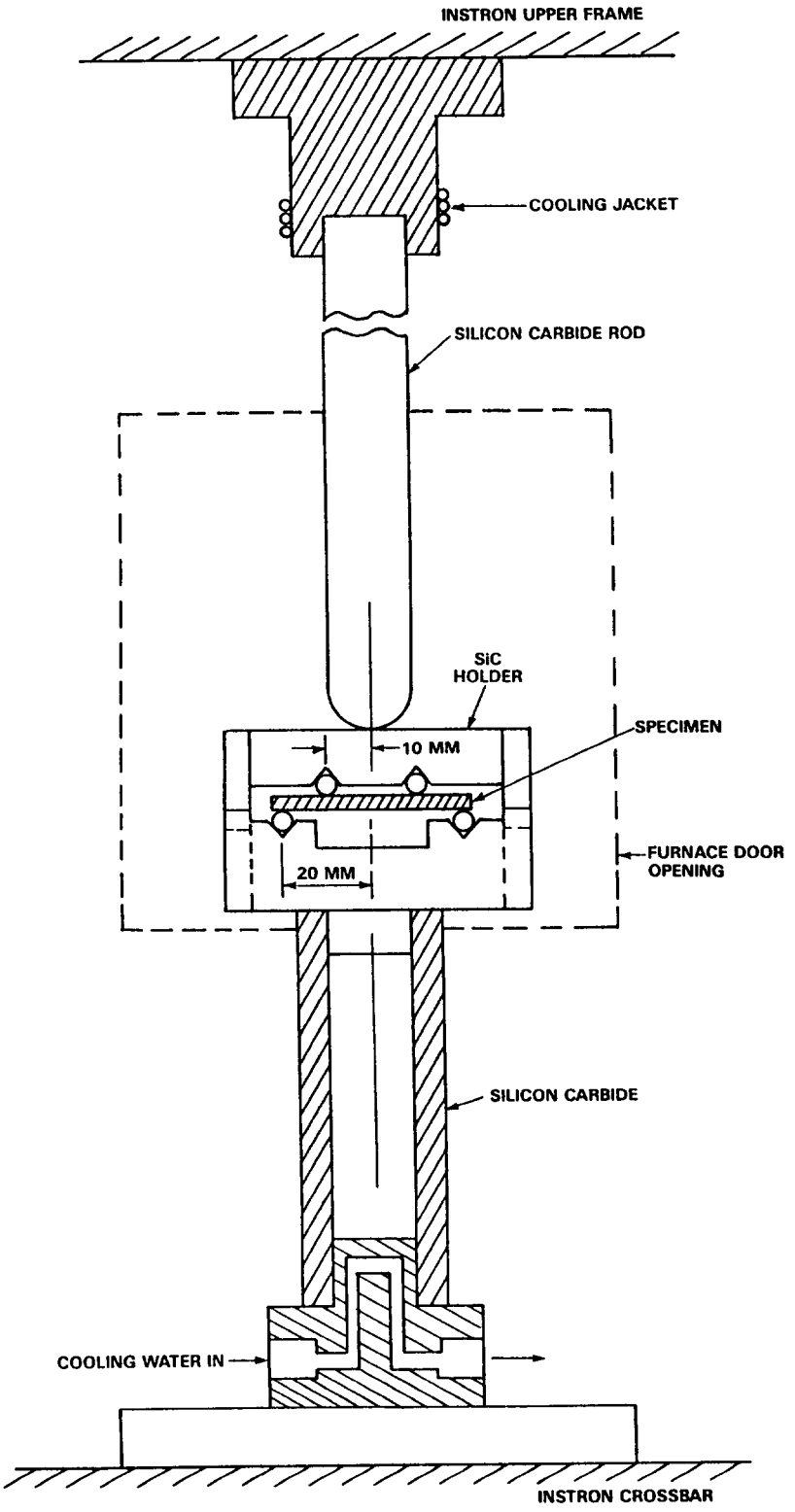

FIGURE 6 HIGH TEMPERATURE MECHANICAL TEST SET-UP - SCHEMATIC

FIGURE 7 INSTRON TEST FRAME AND HIGH TEMPERATURE FURNACE

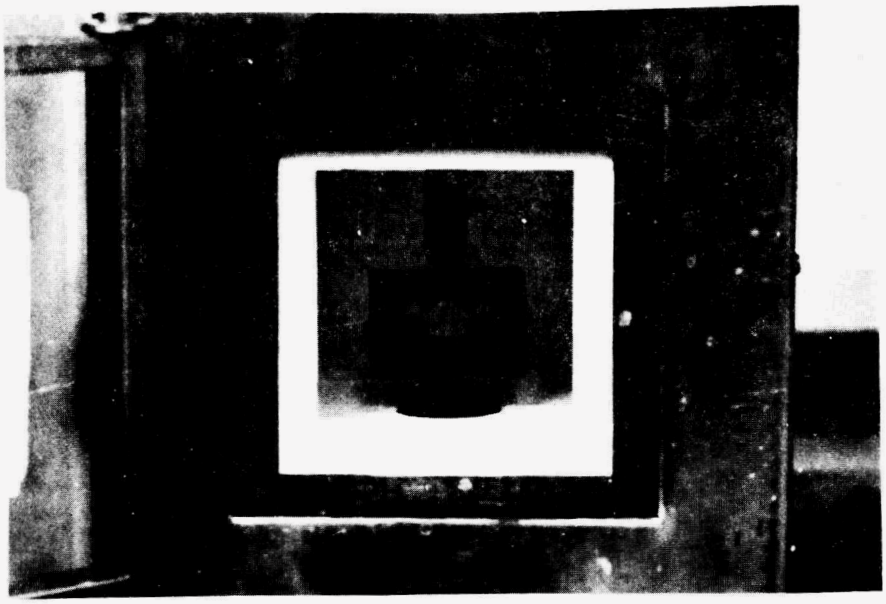

FIGURE 8 HIGH TEMPERATURE (SiC) 4-POINT FLEXURE FIXTURE IN FURNACE

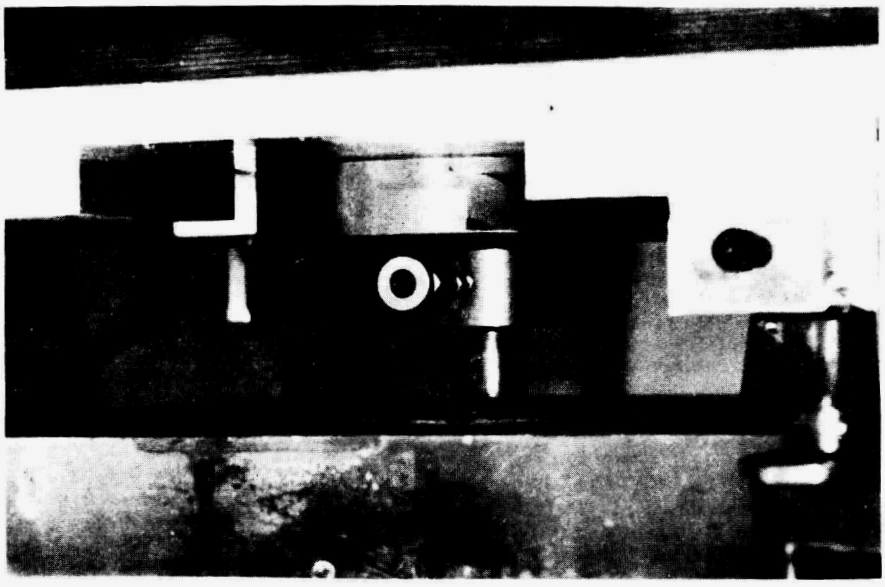

FIGURE 9 COOLING JACKET TO PROTECT LOAD CELL

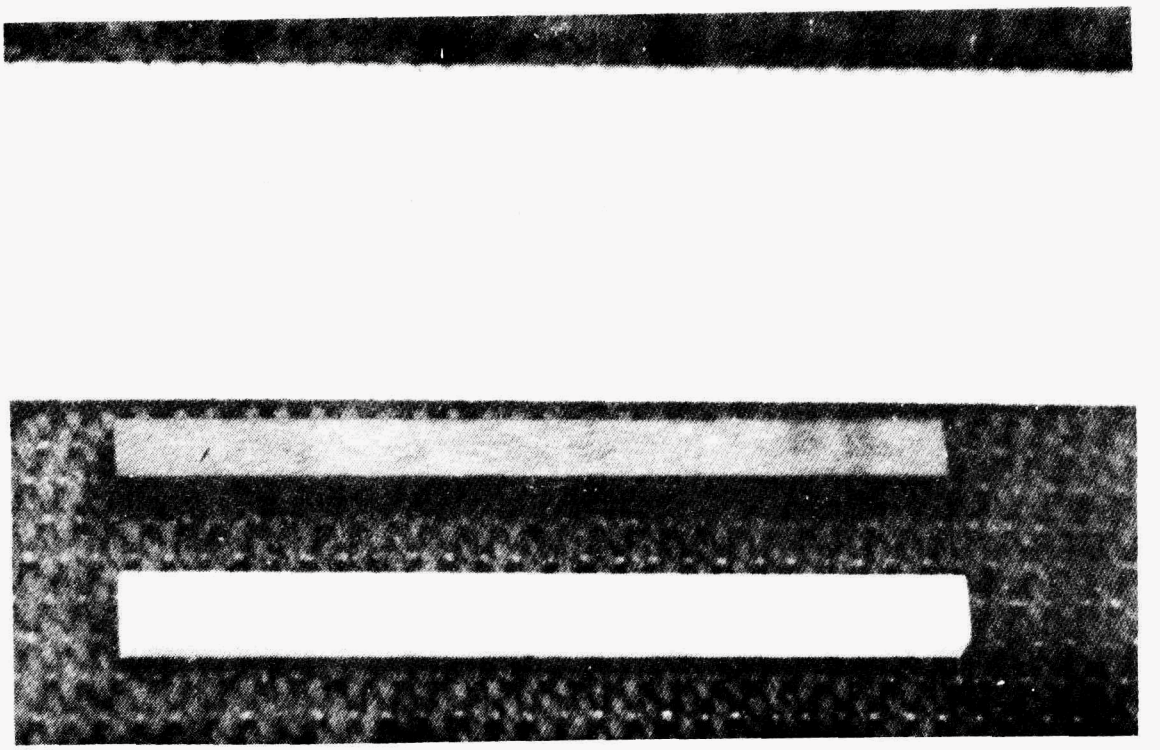

FIGURE 10 MULLITE-SiC WHISKER FLEXURE BAR (UPPER)
MULLITE FLEXURE BAR (LOWER)

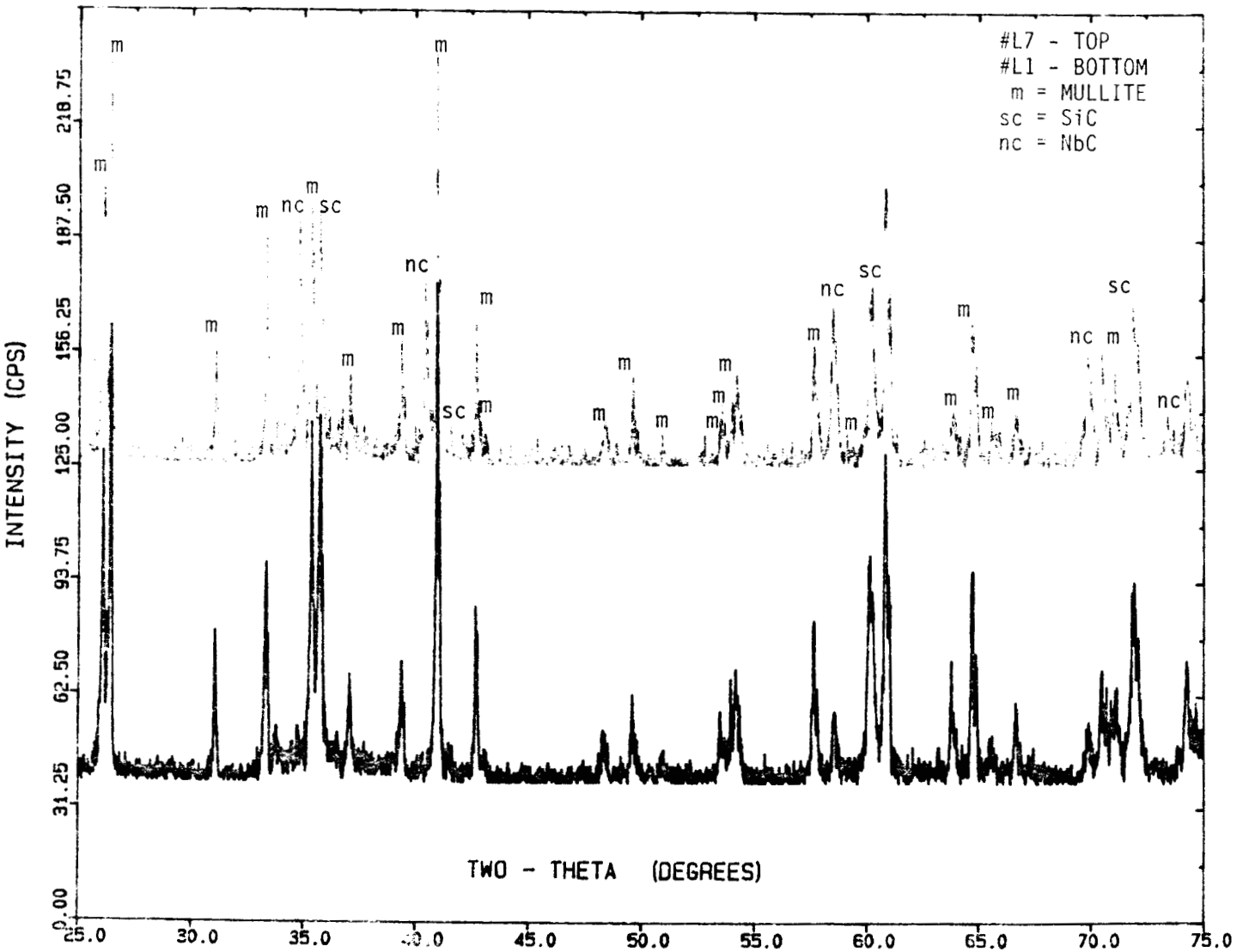

FIGURE 11 X-RAY DIFFRACTION PATTERNS OF COMPOSITES

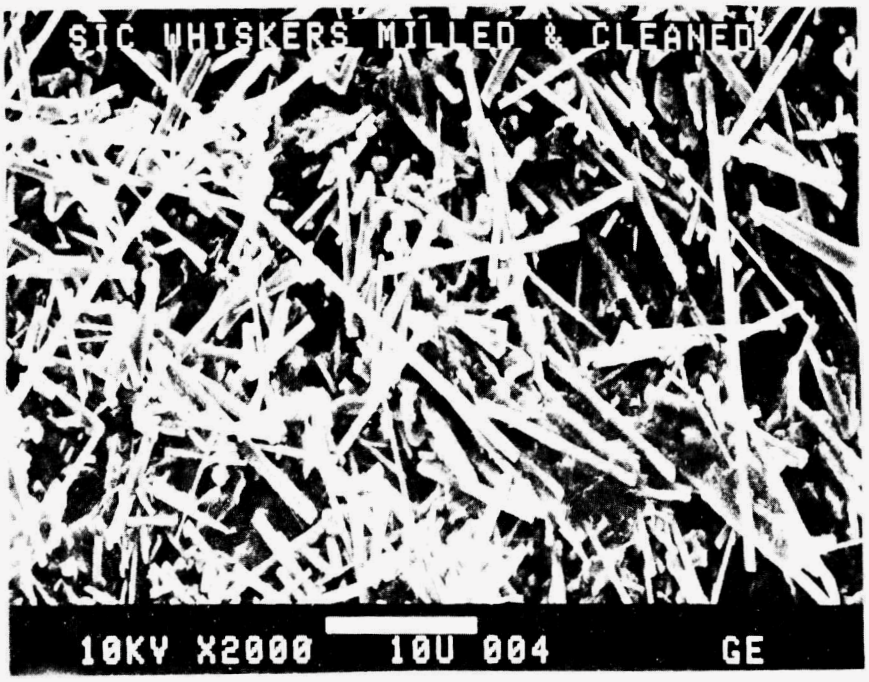

FIGURE 12. SiC WHISKERS 1/2 HR PLANETARY BALL MILLED, WASHED & CLEANED

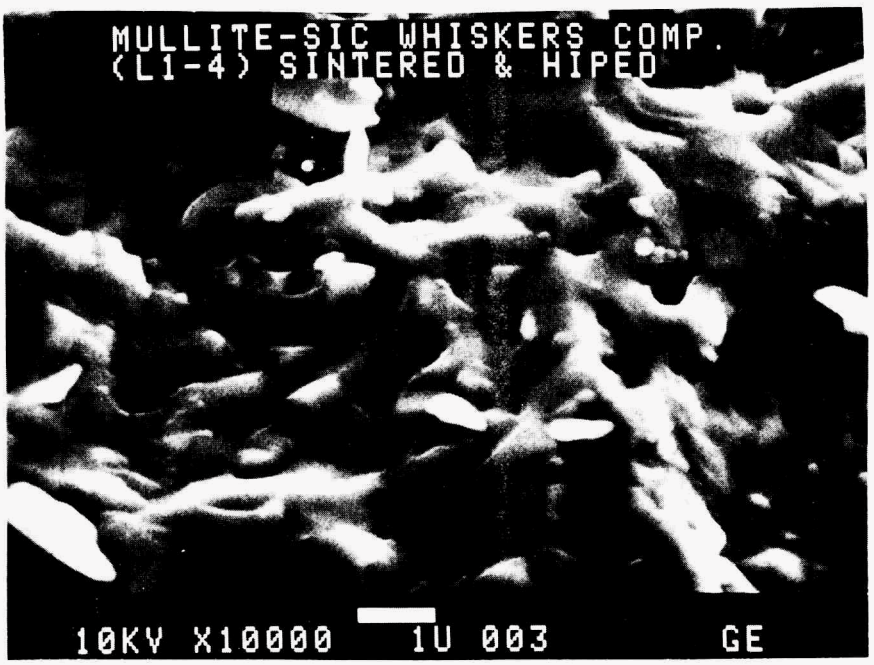

FIGURE 13B FRACTURE SURFACE SAME SPECIMEN AS BELOW

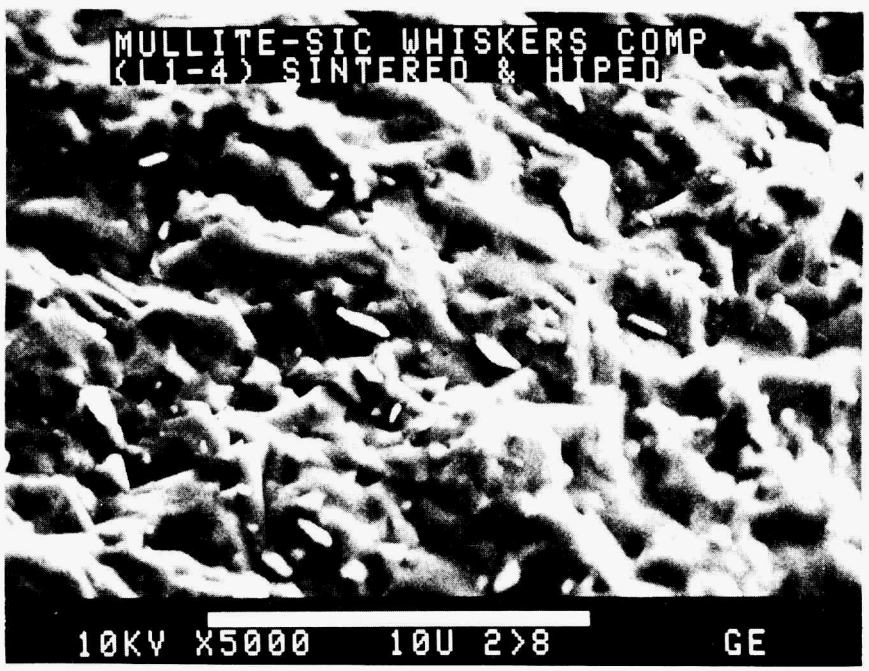

FIGURE 13 A FRACTURE SURFACE MULLITE-SiC
(70/30, WT %) COMPOSITE NO. L1

FIGURE 14B FRACTURE SURFACE (SAME AS BELOW)

FIGURE 14A FRACTURE SURFACE MULLITE-SiC WHISKER-GLASS I - AL_2O_3 (70/30/20/48 PARTS BY WEIGHT) SPECIMEN NO. L3

FIGURE 15 FRACTURE SURFACE MULLITE-SiC WHISKER-GLASS I (70/30/20 PARTS BY WEIGHT) SPECIMEN NO. L6

FIGURE 16B FRACTURE SURFACE (SAME AS BELOW)

FIGURE 16A FRACTURE SURFACE MULLITE-SiC WHISKER-Nb_2O_5 (70/30/5 PARTS BY WEIGHT) COMPOSITE NO. L7

FIGURE 17 FRACTURE SURFACE MULLITE-SiC WHISKER-GLASS-II 85/15/15 PARTS BY WEIGHT SPECIMEN NO. L10

FIGURE 18 FRACTURE SURFACE MULLITE

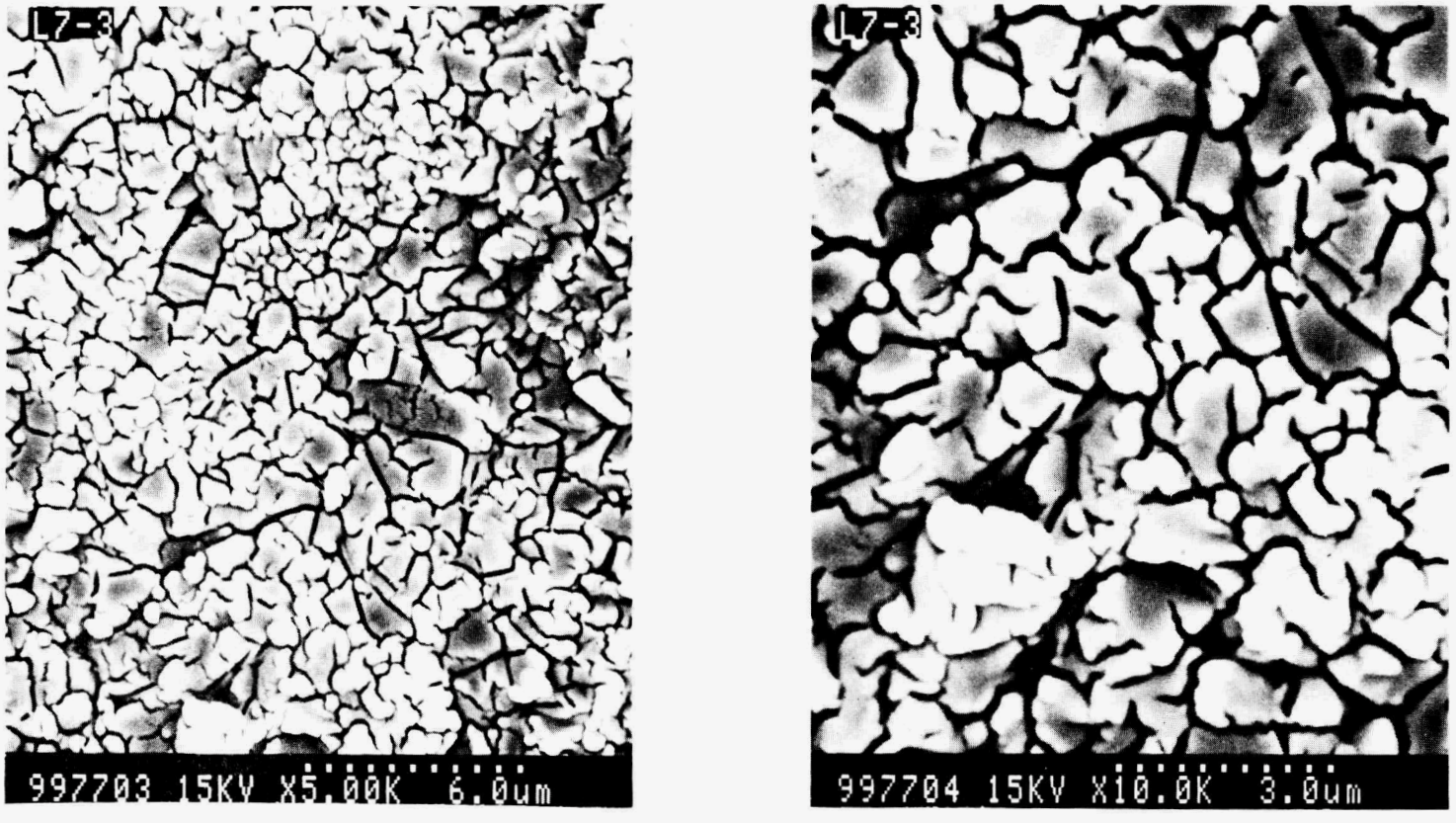

FIGURE 19 FRACTURE SURFACE COMPOSITE NO. 7

1.4 JOINING

1.4.1 Ceramic-Metal Joints

Active-Metal Brazing of PSZ to Iron
S. A. David (Oak Ridge National Laboratory)

Objective/scope

The objective of this task is to develop strong reliable joints containing ceramic components for application in advanced heat engines. Presently, this work is focused on the joining of partially stabilized zirconia to nodular cast iron by brazing. Joints of this arrangement will be required for attaching monolithic pieces of partially stabilized zirconia to cast iron piston caps in order for the ceramic to provide the insulation necessary for use in uncooled diesel engines. A novel method for brazing zirconia to cast iron has already been established. The emphasis of this activity for FY 1986 will be to improve the integrity of zirconia-to-cast-iron joints, to assess the mechanical properties of such joints at room temperature and elevated temperature (primarily by shear testing), and to investigate their thermal aging behavior.

Technical progress

Both active-substrate brazing and active-filler-metal brazing have been used to make joints of zirconia to cast iron during this reporting period. For active-substrate brazing the zirconia surfaces were coated with 0.6 μm of titanium prior to brazing. The titanium was deposited by a modified coating procedure that resulted in porosity-free, high-strength bond zones after brazing. The coated zirconia was brazed to either titanium or cast iron with vacuum grade BVAg-18 filler metal (Ag-30Cu-10Sn) in a muffle furnace fitted with an alumina tube that was evacuated to a pressure of 7×10^{-4} Pa before the heat cycle commenced. The maximum temperature experienced during this brazing cycle was 735°C.

Active-filler-metal brazing was done with a newly available alloy known as Incusil-15ABA. This alloy is produced by GTE-Wesgo and has a nominal composition of Ag-23.5Cu-14.5In-1.25Ti by weight. The manufacturer advised that the brazing temperature range was 750 to 770°C, that the alloy would wet uncoated ceramics and cast iron, and that ceramic surfaces should be polished before brazing. Our evaluation of Incusil-15ABA suggested that 775°C was the lowest temperature at which good bonding to zirconia could be obtained. These results will be discussed below. The details of the brazing cycle used for the Incusil filler metal were identical to those used for BVAg-18 except for the maximum temperature.

Shear testing was used to evaluate the strength of the braze joints at 25 and 400°C. The shear test apparatus has been described in previous reports. For the 400°C tests, specimens were placed in the testing apparatus at 25°C and the entire assembly was heated together. Testing was done in air and commenced as soon as the temperature stabilized at 400°C.

To test the effectiveness of the modified coating procedure used for the active substrate process, joints of zirconia to titanium and zirconia to cast iron were made for room temperature shear testing. Only one joint with titanium was made and tested at room temperature. The shear fracture strength of this joint was 251 MPa, compared with a fracture strength of 140 MPa for tests of similar joints made with previous procedures. Examination of the fracture surface of this specimen indicated that the fracture plane alternated between the interface of zirconia and filler metal and that of titanium and filler metal. No porosity was observed in this braze joint. A cross sectional view of a region where fracture occurred along the titanium surface is shown in Fig. 1. This view shows that considerable deformation of the bond zone occurred without any separation at the zirconia surface. Three zirconia-to-cast iron active-substrate braze joints were made with the modified coating procedure and shear tested at room temperature. The strength values of these joints were 189, 194, and 191 MPa. These values are about 35% higher than the strength values of identical joints made with the original processing. Examination of the fractured specimens indicated that the plane of fracture was about one-half through the copper electroplating and about one-half through the zirconia just below the braze interface. There was no indication that failure was associated with the titanium coating applied to the zirconia. The observations made on all four of these joints indicate that eliminating porosity improved their strength and promoted adhesion to the zirconia surfaces.

M22286

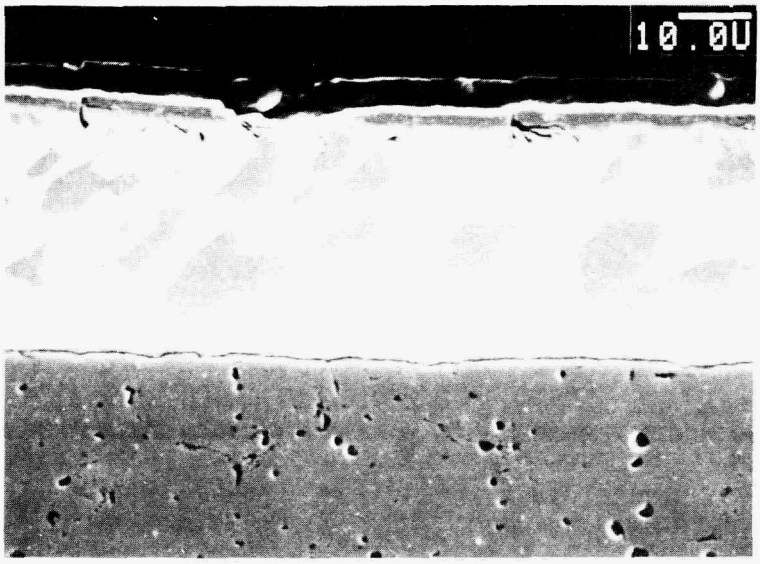

Fig. 1. Electron micrograph of cross section of zirconia-to-titanium shear test specimen. Fracture location was the interface between the bond zone and the titanium.

Evaluation of the active-filler-metal alloy Incusil-15 ABA first consisted of establishing a suitable brazing temperature. For our processing equipment and procedures this temperature was determined to be 775°C. Once this was established several braze joints were made and shear tested at room temperature. These results are presented in Table 1, and they suggest that much stronger zirconia-to-cast-iron joints are formed with unpolished zirconia contrary to the manufacturer's recommendation. Table 1 also shows that using copper-coated cast iron with unpolished zirconia can further improve shear strength.

Table 1. Shear strength of zirconia-to-cast-iron braze joints made with Incusil-15 ABA braze filler metal

Specimen	Pad	Bar	Shear strength (MPa)
MCB-60	Unpolished ZrO_2	Uncoated Fe	127
MCB-61	Unpolished ZrO_2	Cu-coated Fe	165
MCB-62	Polished ZrO_2	Uncoated Fe	77
MCB-63	Polished ZrO_2	Cu-coated Fe	11

To study these brazing approaches in more detail, a series of zirconia-to-cast-iron braze joints was made and shear tested at 25 and 400°C. Three different joint arrangements were used:

1. the active-substrate process (AS) using titanium-vapor-coated zirconia, copper-plated cast iron, and Ag-30Cu-10Sn braze alloy;
2. the active-filler-metal process (AF) using uncoated zirconia and cast iron, and Incusil-15 ABA braze alloy; and
3. the same approach as (2) but with copper-coated cast iron (AF-AS).

The results of these tests are given in Table 2. In addition, each of the fractured specimens was examined in a scanning electron microscope so that microstructural features could be correlated with shear test behavior. This analysis produced the following observations.

1. The active-substrate joint tested at 25°C underwent considerable deformation, with fracture occurring in the zirconia beneath the braze interface. The joint tested at 400°C fractured at the zirconia surface apparently by debonding of the titanium coating. Cross-sectional views of the cast-iron bars from these braze joints are shown in Fig. 2. For both 25 and 400°C, fracture occurred in the vicinity of the interface between zirconia and bond zone. At 25°C the fracture path was mainly through the zirconia below the interface as evidenced by the large zirconia fragments still adhering to the bond zone. Also, the filler metal shows signs of a large shear strain. The joint tested at 400°C apparently fractured by debonding at the interface between the zirconia and the original titanium vapor coating. Very little of the zirconia adhered to the bond zone, and the filler metal does not appear to have deformed much.

Table 2. Shear test results for zirconia-to-cast-iron braze joints

Interface	Technique[a]	Test temperature (°C)	Shear strength (MPa)
ZrO_2-Fe	AS	25	188
ZrO_2-Fe	AS	400	91
ZrO_2-Fe	AF	25	126
ZrO_2-Fe	AF	400	20
ZrO_2-Fe	AF-AS	25	165
ZrO_2-Fe	AF-AS	400	140

[a]AS = active-substrate process, AF = active-filler-metal process.

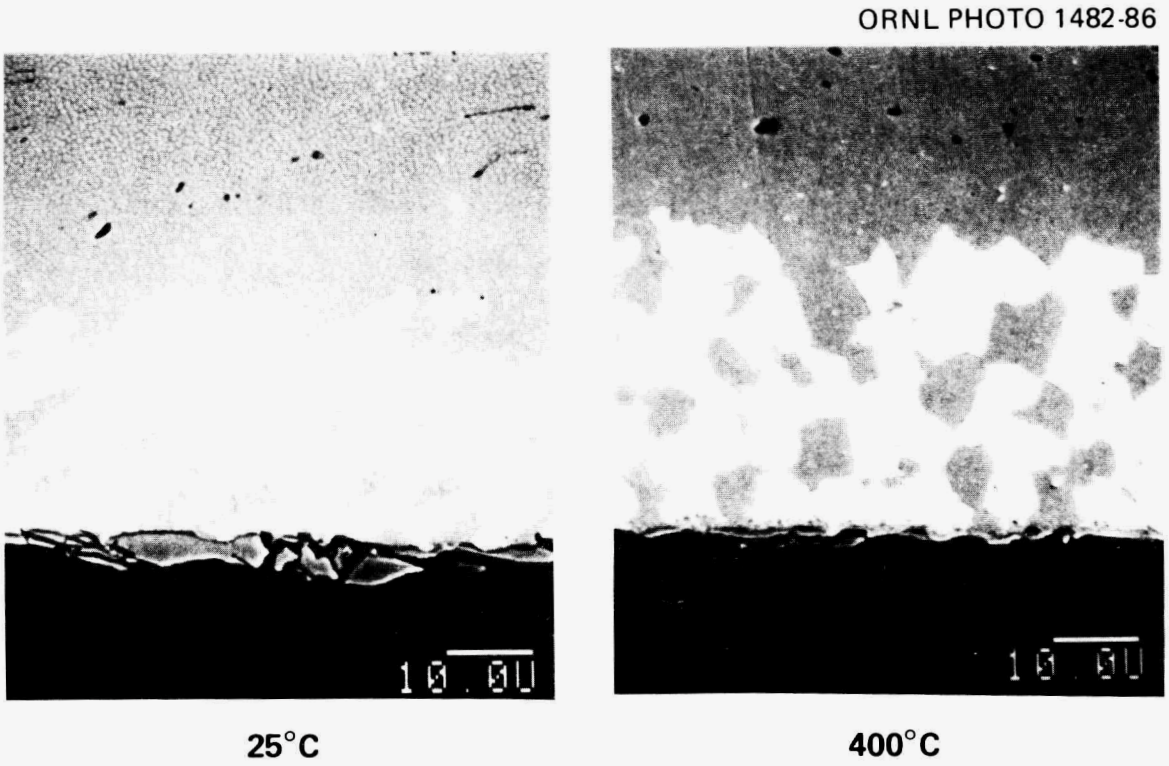

Fig. 2. Electron micrographs of cross sections of zirconia-to-cast-iron bond zones after shear testing at 25 and 400°C. Joints were made by active-substrate brazing.

2. Both active-filler-metal brazes fractured at the braze interface just above the zirconia surface, with the bond zones showing little sign of plastic deformation. The microstructures of these joints are similar and are shown in Fig. 3.

3. Both active-filler-metal joints made with copper-coated cast iron showed signs of plastic deformation in the bond zones. Figure 4 shows that these joints apparently broke at the interface between zirconia and filler metal. However, closer inspection revealed that the specimen tested at 400°C actually broke in the bond zone above the zirconia surface. Also shown in Fig. 4 is that the Incusil filler metal has reacted extensively with the copper coating. Comparison with Fig. 3 indicates that the ratio of silver-rich (light) phase to copper-rich (dark) phase in the bond zone was decreased by using the copper coating. This change in bond zone microstructure may be partly responsible for the better strength of this joint at 400°C.

Based on this analysis, it can be concluded that all three brazing approaches can produce strong (fracture strength ≤ 100 MPa) zirconia-to-cast-iron joints at 25°C, but that joint strength may decrease significantly at 400°C. The active-filler-metal joint made with copper-coated cast iron had the highest strength at 400°C (140 MPa) and was the least affected by increased test temperature. Investigation of the characteristics of these joints is continuing.

ORNL PHOTO 1480-86

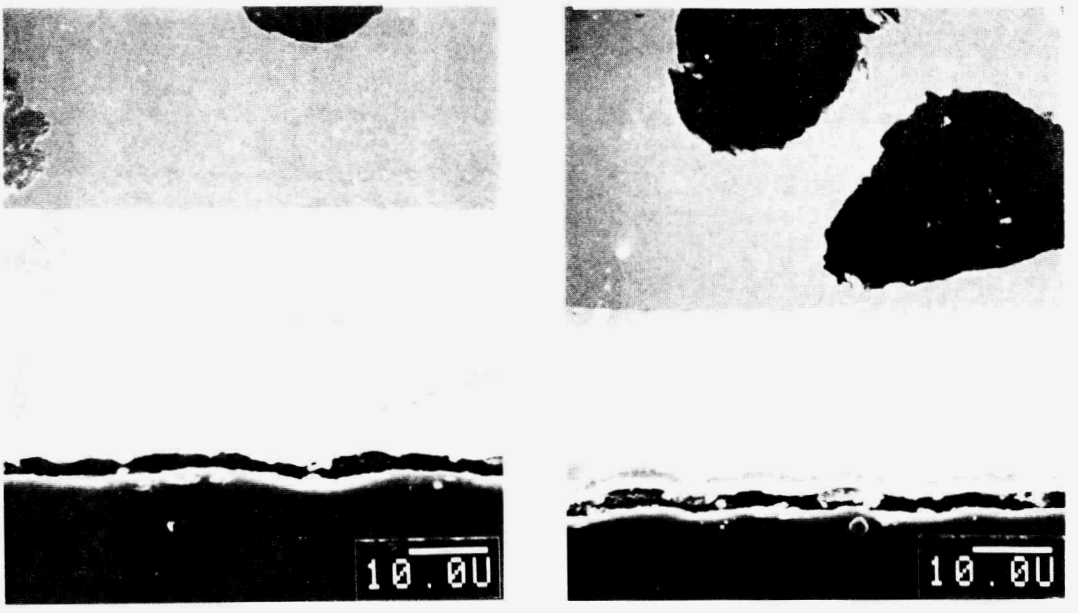

Fig. 3. Electron micrographs of cross sections of zirconia-to-cast-iron bond zones after shear testing at 25 and 400°C. Joints were made by active filler-metal brazing with Incusil-15ABA.

ORNL PHOTO 1478-86

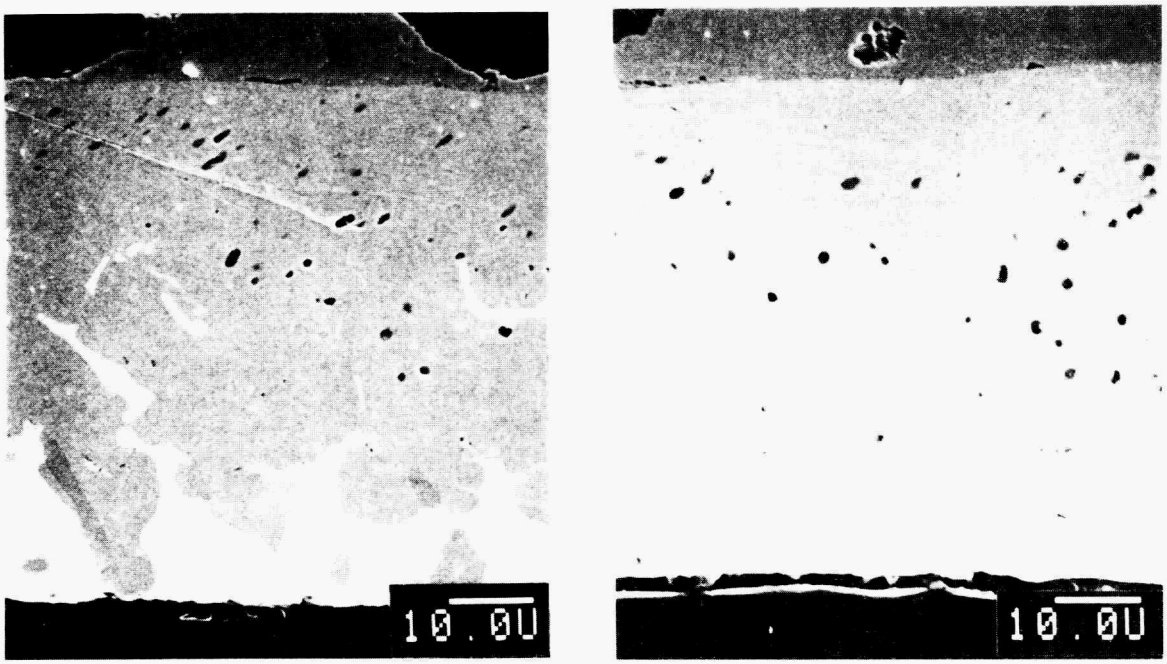

25°C 400°C

Fig. 4. Electron micrographs of cross sections of zirconia-to-cast-iron bond zones after shear testing at 25 and 400°C. Joints were made with Incusil-15ABA and copper-coated cast iron.

Status of milestones

Milestone No. 141104 was completed.

Publications

None.

2.0 MATERIALS DESIGN METHODOLOGY

INTRODUCTION

This portion of the project is identified as project element 2 within the work breakdown structure (WBS). It contains three subelements: (1) Three-Dimensional Modeling, (2) Contact Interfaces, and (3) New Concepts. The subelements include macromodeling and micromodeling of ceramic microstructures, properties of static and dynamic interfaces between ceramics and between ceramics and alloys, and advanced statistical and design approaches for describing mechanical behavior and for employing ceramics in structural design.

The major objectives of research in Materials Design Methodology elements include determining analytical techniques for predicting structural ceramic mechanical behavior from mechanical properties and microstructure, tribological behavior at high temperatures, and improved methods for describing the fracture statistics of structural ceramics. Success in meeting these objectives will provide U.S. companies with methods for optimizing mechanical properties through microstructural control, for predicting and controlling interfacial bonding and minimizing interfacial friction, and for developing a properly descriptive statistical data base for their structural ceramics.

2.2 CONTACT INTERFACES

2.2.1 Static Interfaces

High-Temperature Coating Study to Reduce Contact Stress Damage of Ceramics
J. L. Schienle (Garrett Turbine Engine Company)

Objective/scope

The objective of this research program is to develop coating compositions and procedures that will yield long term adherence and reduce or eliminate contact-stress damage to silicon nitride (Si_3N_4) and silicon carbide (SiC) ceramics. Prior studies [1-3] have determined that Si_3N_4 and SiC ceramics are susceptible to contact-stress damage at ceramic-ceramic and ceramic-metal interfaces in heat engines. Subsequent studies have demonstrated a reduction or elimination of contact-stress damage to these ceramics using plasma-sprayed oxide coatings, but the coating adherence was not adequate for long term use.

This program utilizes an alternate coating method, electron beam physical vapor deposition (EB-PVD), as the coating process because of high control of composition, thickness, and morphology. Three substrate materials were selected for this study: reaction-bonded Si_3N_4 (RBSN), sintered Si_3N_4 (SSN), and sintered SiC (SSC).

The present program score consists of four technical tasks to be conducted over 31 months:

- Task 1 - Coating Adherence and Characteristics Investigation
- Task 2 - Advanced Pretreatment and Coating Studies
- Task 3 - Contact Stress Testing and Friction Measurement
- Task 4 - Post-Contact Strength Measurement

Technical progress

During this reporting period (October 1, 1985 through March 31, 1986), Task 3, Contact Stress Testing and Friction Measurement, was initiated. The emphasis of Task 3 is to establish the baseline flexural strengths and the friction characteristics for uncoated and coated substrates. During testing to establish the friction characteristics, the specimens will be exposed to contact stress conditions. The effect of contact stress on these specimens will be evaluated in Task 4, Post-Contact Strength Measurement.

Experimental procedures

Materials. The substrate materials utilized in this investigation are reaction-bonded silicon nitride (RBSN), sintered silicon nitride (SSN), and sintered silicon carbide (SSC). The RBSN and SSN are RBN104 and Code 2 SSN respectively from the AiResearch Casting Company, Torrance, California, and the SSC is sintered alpha SiC (SASC) from the Carborundum Company, Niagara Falls, New York. Billets of these materials have been cut into 2 x 0.250 x 0.125 inch test bars and longitudinally ground with a 320-grit diamond wheel.

The coating/substrate systems selected for evaluation in Task 3 are shown in Table 1.

Table 1. Task 3 coating/substrate systems.

Substrate	RBSN	SSN	SSC
Pretreatment	CVD alumina CVD AlN	Sol-gel alumina Laser machining	Sol-gel alumina Laser machining
Coating	EB-PVD ZrO_2/20 percent Y_2O_3		

These coating/substrate systems were selected based on Task 2 adherence evaluations. The pretreatments selected yielded the best EB-PVD zirconia coating adherence for their respective substrates[4]. The pretreatments are briefly described below.

CVD alumina coatings approximately 2 micron thick are applied at 920C at Kennametal's Philip M. McKenna Laboratory, Greensburg, Pennsylvania. The specimens are subsequently heat treated in air at 1200C for 2 hours to stabilize the interlayer prior to EB-PVD coating.

CVD AlN coatings approximately 2 to 3 micron thick are deposited at G.A. Technologies, San Diego, California, using a fluidized bed.

Sol-gel alumina coatings approximately 0.5 micron thick are applied by Signal Research Center, Des Plaines, Illinois. The substrates are dipped in alumina sol, air dried, then calcined in air for 2 hours at 1200C.

Laser machining is conducted at GTEC using a 1.2 kw CO_2 laser in a pulsed mode to texturize the substrate surface to form a matrix of cavities.

An EB-PVD coating of zirconia stabilized with 20-percent yttria is utilized for all systems in Table 1. This coating is applied by Temescal, Berkeley, California, at 1800F to a thickness of 75 to 125 microns. A typical coating microstructure resulting from baseline processing procedures is illustrated in Figure 1. After EB-PVD coating, the specimens receive 100-hour/1200C static air heat-treatments to stabilize the coating/substrate interfaces.

Characterization. Flexural testing to establish baseline strengths will be conducted at room temperature, 1000C, and 1375C (static air atmosphere) in four-point bending. Coated substrates will be tested with the coated side of the specimen in tension.

Friction characterization will be conducted using line contact testing, which involves sliding a line contact load across the specimen surface. Figure 2 illustrates the test rig to be used for this task. With this apparatus, a normal force is applied to the specimen through a dead weight load system while a tangential force is applied through displacement of the crosshead. Uncoated specimens will be tested with normal loads of 4.5, 11.4, and 22.7 kg. Prior experience with RBSN and SSC on an earlier contact test rig suggests these loads sufficient to induce contact stress damage to bare surfaces. The applied normal loads for testing coated specimens will be selected based on preliminary contact testing to be conducted under Task 3. All contact tested specimens

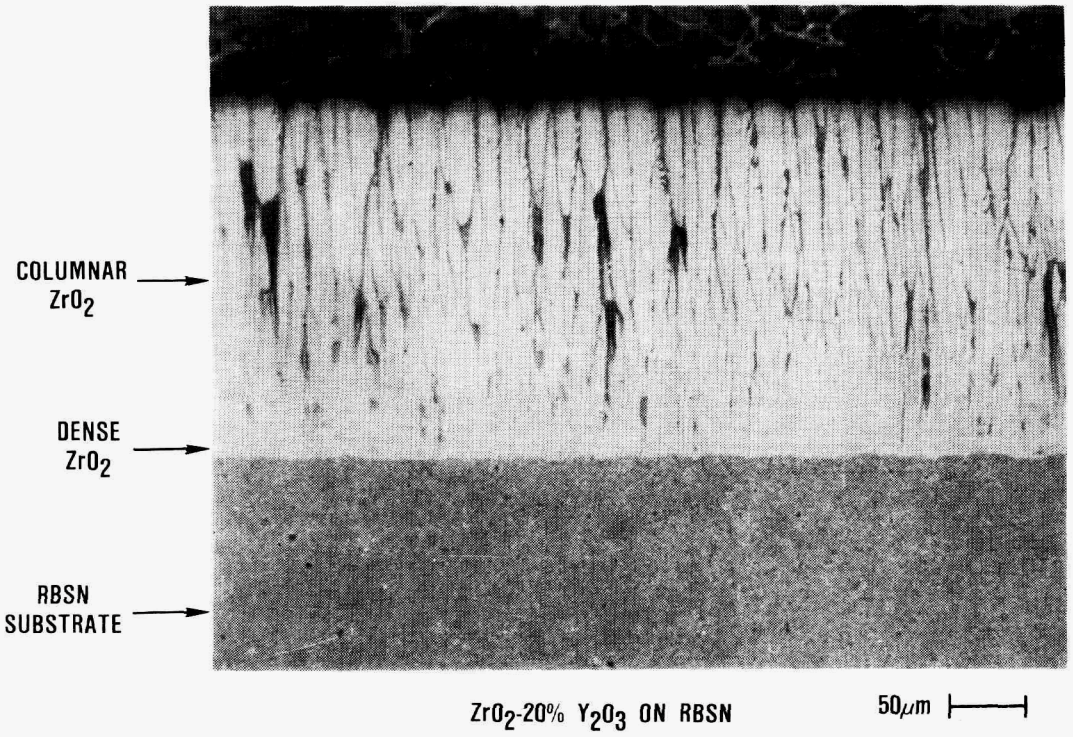

Figure 1. The baseline coating is graded from dense at the interface to columnar.

(except preliminary) will be subsequently flexural tested for strength under Task 4, Post-Contact Strength Measurements, to determine contact damage resistance.

Substrate pretreatment and coating status

Substrate pretreatment and coating is progressing. Substrate pretreatment for Task 3 is nearing completion. EB-PVD zirconia coating is falling behind schedule and delaying the program. Seventy-two of the total 504 specimens to receive EB-PVD coatings have been coated to date. The pretreatment and coating status for each of the six systems shown in Table 1 is discussed in the following paragraphs.

RBSN/CVD Al_2O_3/EB-PVD ZrO_2. One-hundred test bars of RBSN were coated with CVD alumina. Eighty-four of these bars were heat treated in air at 1200C for 2 hours and subsequently sent to Temescal for EB-PVD zirconia coating. Sixteen specimens were retained.

RBSN/CVD AlN/EB-PVD ZrO_2. Eighty-four test bars of RBSN were sent to G.A. Technologies for CVD AlN coating. Forty bars have been coated and subsequently sent to Temescal for EB-PVD zirconia coating. The 44 bars remaining will be coated during the next reporting period.

SSN/Sol-gel Al_2O_3/EB-PVD ZrO_2. One hundred bars of SSN were coated with sol-gel alumina. Eighty-four were sent to Temescal for EB-PVD zirconia coating. Sixteen specimens were retained.

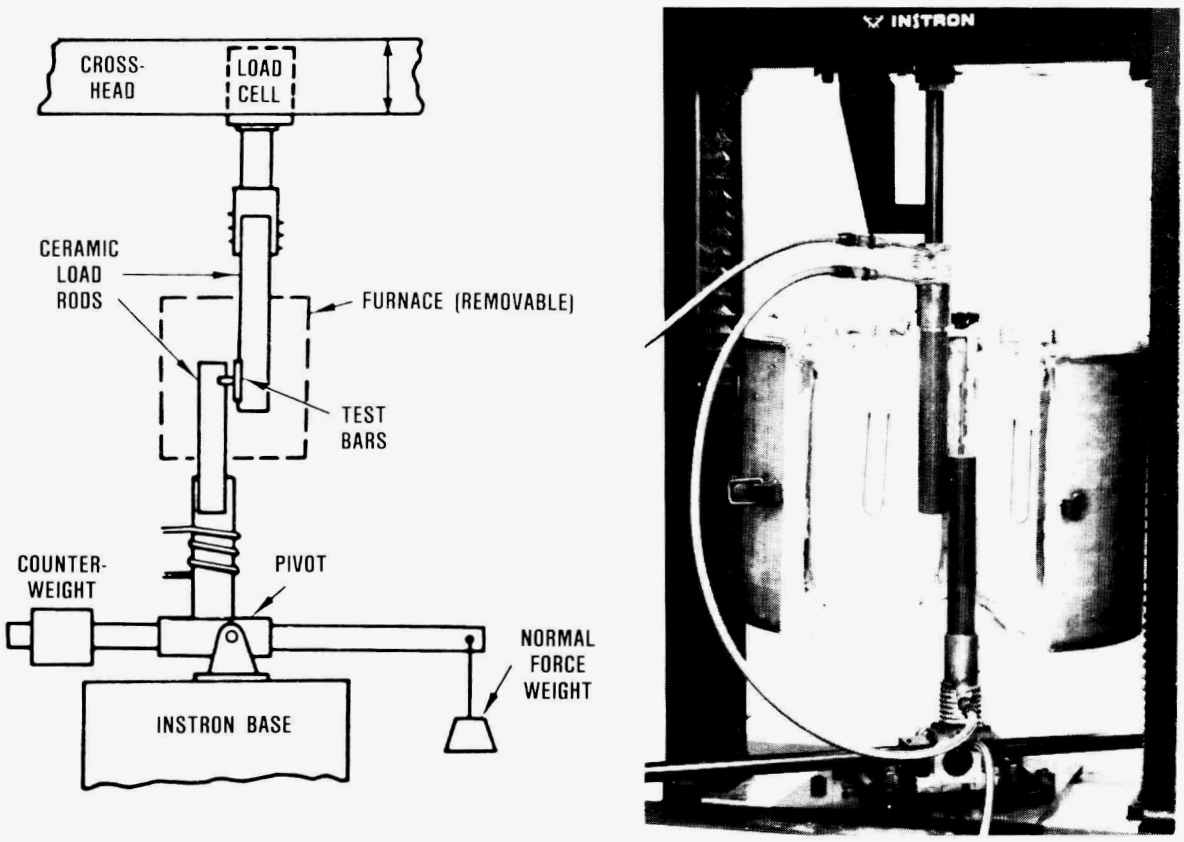

Figure 2. Garrett's line contact rig was used to assess coating adherences.

Laser Machined SSN/EB-PVD ZrO_2. Eighty-four SSN test bars were laser machined (texturized) on one face and subsequently sent to Temescal for EB-PVD zirconia coating. Thirty-six of these specimens have been coated and heat treated to date. Additional substrates were laser machined to evaluate the effect of laser machining on strength.

SSC/Sol-gel Al_2O_3/EB-PVD ZrO_2. One hundred bars of SSC were coated with sol-gel alumina. Eighty-four were sent to Temescal for EB-PVD zirconia coating.

Laser Machined SSC/EB-PVD ZrO_2. Eighty-four SSC test bars were laser machined on one face and subsequently sent to Temescal for EB-PVD zirconia coating. Thirty-six of these specimens have been coated and heat treated to date. Additional substrates were laser machined to evaluate the effect of laser machining on strength.

Results

Strength Testing. Strength testing (flexural) of the as-machined substrates has been completed. The strengths are tabulated in Table 2. These strengths will be used as the baseline for Tasks 3 and 4 of the current program.

Table 2. Average strength (MPa) of as-machined substrates.

(Parentheses indicate number of bars tested)

Temperature	RBSN	SSN	SSC
25C	296.9 ±31.9(10)	591.7 ±66.9(10)	286.2 ±25.5(10)
1000C	360.7 ±17.9(6)	611.0 ±51.0(6)	271.7 ±20.7(6)
1375C	319.3 ±52.4(6)	133.8 ±6.2(6)	295.2 ±11.7(6)

The strength testing of laser machined substrates also has been completed. The results are tabulated in Table 3.

Table 3. Strength testing results of laser-machined substrates.

	SSN		SSC	
Temperature	Strength, MPa	Reduction, %	Strength, MPa	Reduction, %
25C	450.3 ±30.3(8)	23.8	204.8 ±16.6(7)	28.4
1000C	502.8 ±56.6(4)	17.7	224.1 ± 7.6(4)	17.5
1375C	111.0 ± 6.9(4)	17.0	225.2 ±13.1(4)	13.6

The strength reduction resulting from laser machining the surface was significant. However, both SSN and SSC exhibited less strength reduction when tested at elevated temperatures suggesting flaws may blunt or heal during the test (5 minutes hold at temperature). The SSC substrates exhibited more strength reduction at room temperature than SSN. The SSC specimens were damaged at the edges due to spalling which occurred during laser machining (Figure 3). A few specimens were laser machined only over the center section of the bar leaving the edges nontextured by the laser (Figure 4). Subsequently, as shown in Table 4, the strength reduction was not as significant.

Table 4. Strength test results for laser-machined SSC with nontextured edges.

Temperature	Strength, MPa	Reduction, %
25C	220.0 ±9.7(4)	23.1
1000C	241.4 ±2.8 (3)	11.1
1375C	273.1 ±131.1(3)	7.0

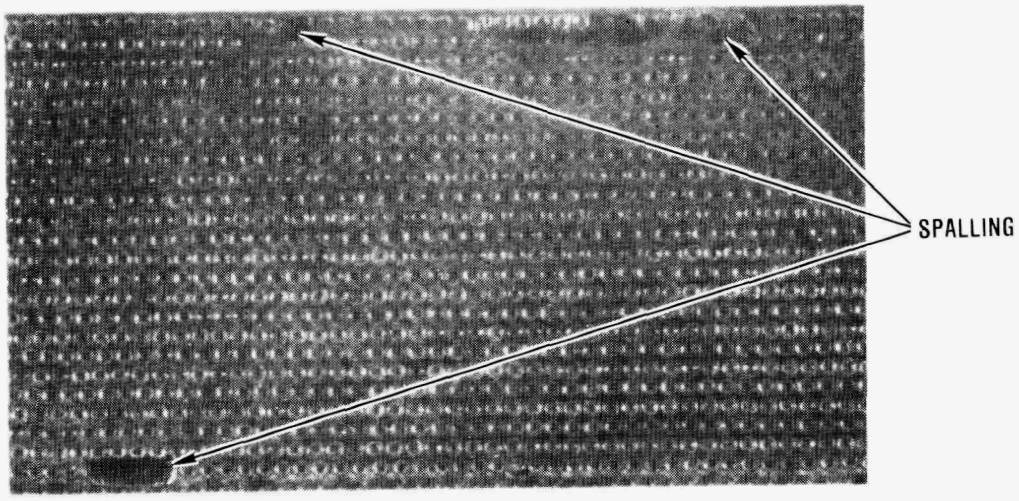

Figure 3. Laser machining of SSC substrates resulted in spalling on edges.

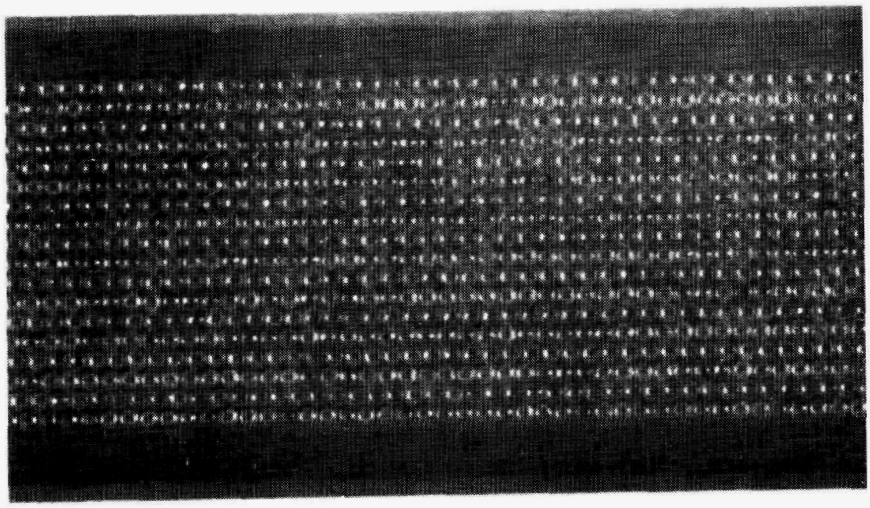

Figure 4. Some specimens were left untreated at the edges to eliminate spalling.

Friction Characterization (Contact Stress Testing). Contact stress testing was initiated on as-machined substrates to establish a baseline for subsequent tests on ZrO_2 coated specimens. The room temperature and 1000C testing has been completed. The 1375C testing is currently in progress. The results will be discussed in the next report.

Summary

- o Substrate pretreatment and coating is progressing. Seventy-two of the total 504 specimens to receive EB-PVD coatings have been coated.
- o Strength testing of as-machined substrates has been completed.
- o Strength test results from laser machined SSN and SSC suggests laser machining significantly reduces substrate strength.
- o Contact testing of as-machined substrates is in progress.

Status of Milestones

- o Tasks 1 and 2 are complete
- o Task 3 is behind schedule due to delays in coating the specimens
- o Task 4 may be delayed due to delays in Task 3

Publications

A paper, "High Temperature Coating Study to Reduce Contact Stress Damage of Ceramics", was presented at the 23rd Automotive Technology Development Contractors Coordination Meeting in Dearborn, Michigan in October 1985. This paper is expected to be published in the proceedings of this meeting.

References

1. D.W. Richerson and K.M. Johansen, "Ceramic Gas Turbine Engine Demonstration Program", Final Report, DARPA Contract N00024-76-C-5352, Garrett Report 21-4410, May 1982.

2. D.W. Richerson, W.D. Carruthers, and L.J. Lindberg, "Contact Stress and Coefficient of Friction Effects on Ceramic Interfaces", Surfaces and Interfaces in Ceramic and Ceramic Metal System, Berkeley, CA, July 29-30, 1980.

3. J.R. Smyth and D.W. Richerson, "High Temperature Dynamic-Contact Behavior of Sintered Alpha Silicon Carbide", Ceramic Engineering and Science Proceedings, Vol. 4, No. 708, 1983, pp. 663-673.

4. J.L. Schienle, "High Temperature Coating Program to Reduce Contact Stress Damage of Ceramics", Semiannual Report, DOE Contract W-7405-ENG-26/ORNL Contract 86X-47992C, Garrett Report 31-5377(4), October 1985.

2.2.2 Dynamic Interfaces

Studies of Dynamic Contact of Ceramics and Alloys for Advanced Heat Engines
K. F. Dufrane and W. A. Glaeser (Battelle Columbus Division)

Objective/Scope

The objective of the study is to develop mathematical models of the friction and wear processes of ceramic interfaces based on experimental data. The supporting experiments are to be conducted at temperatures to 650 C under reciprocating sliding conditions reproducing the loads, speeds, and environment of the ring/cylinder interface of advanced engines. The test specimens are to be carefully characterized before and after testing to provide detailed input to the model. The results are intended to provide the basis for identifying solutions to the tribology problems limiting the development of these engines.

Technical Progress

Apparatus

The apparatus uses specimens of a simple flat-on-flat geometry, which facilitates procurement, finishing, and testing. The apparatus reproduces the important operating conditions of the piston/ring interface of advanced engines. The specimen configuration and loading is shown in Figure 1. The contact surface of the ring specimen is 3.2 x 19 mm. A crown with a 32 mm radius is ground on the ring specimen to insure uniform contact. The ring specimen holders are pivoted at their centers to provide self-alignment. A chamber surrounding the specimens is used to control the atmosphere and contains heating elements to control the temperature. The exhaust from a 4500 watt diesel engine is heated to the operating temperature and passed through the chamber to provide an atmosphere similar to that of actual diesel engine service. A summary of the testing conditions is presented in Table 1.

Materials

Monolithic alpha silicon carbide and three zirconia compounds were selected for the cylinder specimens. The ring specimens consisted of monolithic ceramics (cut from the sides of the cylinder specimens) and plasma-sprayed coatings of metals and ceramics. The compositions of the materials are presented in Table 2.

Table 1. Summary of Testing Conditions

Sliding Contact:	Dual flat-on-flat
"Cylinder" Specimens:	12.7 x 32 x 127 mm
"Ring" Specimens:	3.2 x 19 x 19 mm
"Ring" crown radius:	32 mm
Motion:	Reciprocating, 108 mm stroke
Speed:	500 to 1500 rpm
Load:	to 950 N
Ring Loading:	to 50 N/mm
Atmosphere:	Diesel exhaust or other gases
Measurements:	Friction and wear (after test)

Table 2. Cylinder and Ring Specimens

Material	Abbreviation	Nominal Composition
Magnesia Partially Stabilized Zirconia	MPSZ	3.3 weight % MgO, 3 weight % HfO_2, bal ZrO_2
Yttria Partially Stabilized ized Zirconia	YPSZ	3 mole % Y_2O_3, bal ZrO_2
Alumina Transformation Toughened Zirconia	ATTZ	2 mole % Y_2O_3, 20 weight & Al_2O_3, bal ZrO_2
Sintered Alpha Silicon Carbide	SiC	SiC
Plasma Sprayed Metallic, T400	T400	0.28 Mo, 0.34 Ni, 0.09 Cr, 0.01 Fe 0.02 Si, bal Co
Plasma Sprayed Ceramic M130	M130	0.13 TiO_2, 0.87 Al_2O_3
Plasma Sprayed Metallic, M501	M501	0.3 Mo, 0.12 Cr, 0.025 B, 0.03 Fe 0.0075 C, bal Ni
Plasma Sprayed Intermetallic, P312 M	P312 M	$MoSi_2$

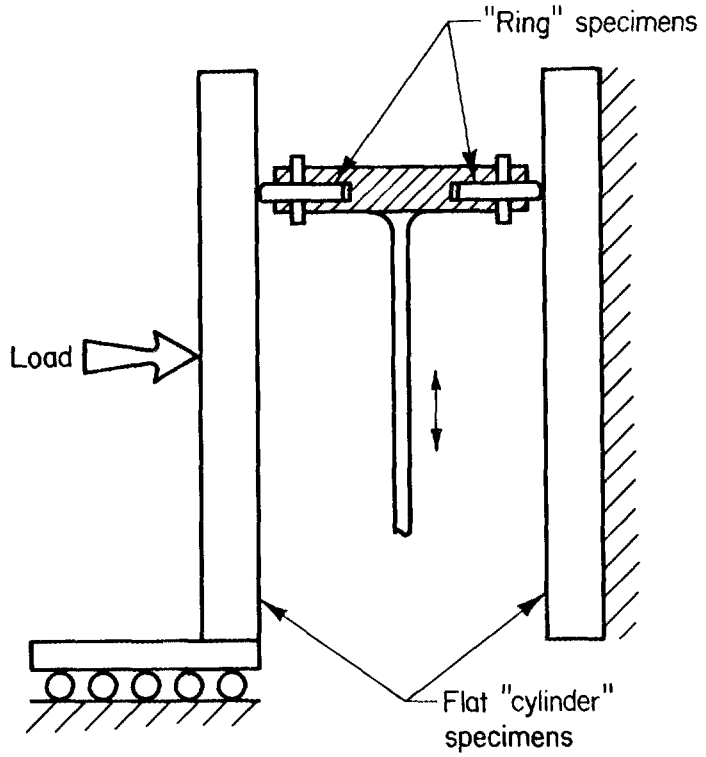

Figure 1. Test specimen configuration and loading.

Experiments with no Lubrication

A series of experiments was run with the plasma-sprayed rings against alpha silicon carbide at 1000 rpm, with diesel exhaust atmosphere, temperatures from 290 to 540 C, and ring loadings from 1.6 to 7.7 N/mm. With the exception of M501, all of the plasma-sprayed coatings spalled off the AISI 401 SS base metal in less than 3 minutes of operation. The coefficients of friction were high, with values from 0.2 to 0.6 typically recorded. The M501 withstood 20 minutes of sliding successfully. However, the wear depth on the rings was 0.15 mm and the coefficient of friction varied between 0.3 and 0.6. Examination of the surfaces revealed that a coating of M501 had transferred to the alpha silicon carbide and the sliding was actually occurring on self-mated M501. The M501 also survived a short period of operating against YPSZ, but the coefficient of friction and wear were similar to that experienced with sliding against alpha silicon carbide. The high wear rates, high coefficients of friction, and frequent coating bonding failures indicated that plasma sprayed rings were unlikely to be able to operate unlubricated for extended periods as rings in advanced heat engines.

Unlubricated self-mated yttria partially stabilized zirconia (YPSZ) also proved incapable of extended service for advanced heat engines. The coefficient of friction was high (to 0.6) and the ring specimens wore 0.05 mm in 3 minutes of operation. The surface of both the cylinder and ring specimens were extensively cracked. The edges of the ring specimens were chipped away in series of stair-step cracks following the original

surface cracks. With the aggressive wear mechanisms and high coefficients of friction observed during the unlubricated sliding experiments, the application of the ceramics studied in unlubricated sliding contact does not appear feasible.

Experiments with Lubrication

The potential benefits of lubrication to the sliding performance of ceramics were examined beginning with an SAE 10 mineral oil at room temperature. The four monolithic ceramics were run self-mated at speeds of 500 to 1000 rpm. The YPSZ, operated at a ring loading of 9 N/mm for 1 hour, produced a coefficient of friction ranging from 0.13 to 0.16. The coefficient of friction was reduced by the presence of mineral oil from the 0.6 measured during dry sliding, but the ring wear depth was a relatively high 0.27 mm during the one hour of operation. The high wear rate was caused by the phenomenon of thermo-elastic instability (TEI) observed throughout the experiment. As shown in Figure 2, the TEI was visible as hot spots and streaks on the cylinder specimens. During sliding, local areas of the surface expand from frictional heating and thereby begin to carry higher portions of the applied load. Depending on the materials properties, sliding speed, and coefficient of friction, if the heat in the local areas is not dissipated fast enough, the local areas continue to expand and thereby carry most of the sliding load. Since the locally protruding areas are subject to wear, the load is transferred to nearby areas heated and expanded by the thermal disturbance. Therefore, the locally heated regions traverse across the width of the mating surfaces. The temperatures developed by TEI can be sufficiently high to emit visible radiation, which was the case for the YPSZ, Figure 2. Because of the rapid local heating to high temperatures, the surface is subject to cracking from thermal shock, Figure 3. The local cracked areas spall, leaving visible shallow pits. The pitted regions enlarge with further running, which appears to be the primary wear mechanism. Superimposed on the cracks and pits are wear grooves apparently caused by debris trapped between the ring and cylinder specimens.

Examination of the worn YPSZ surfaces by scanning electron microscopy (SEM) provided further details of the wear process and cracking. Surface smearing, debris compaction, and microcracking is evident in addition to the major crack pattern in the SEM micrograph shown in Figure 4. The major wear grooves visible in Figure 3 are observable in detail in the SEM micrograph shown in Figure 5. The upper left portion is an area of material removed in a wear groove. The spacing of the cracks is smaller in the groove region. The groove was probably caused by wear debris trapped between the ring and cylinder. Such debris would cause high contact stresses, subsurface lateral fracture, and an intensified thermal shock crack pattern. The cracks in the groove are also wide; apparently debris was released as the edges were being broken down. Smearing is evident in the higher (ungrooved) area. This type of wear causes material removal on a much finer scale than the spalling and major grooving from trapped wear debris. The wear occurs by superficial attrition of a very thin plastically deformed layer. This may be the dominant wear mechanism in the absence of thermal shock. X-ray diffraction analysis comparing the worn and unworn areas showed the crystal structure to be mostly face

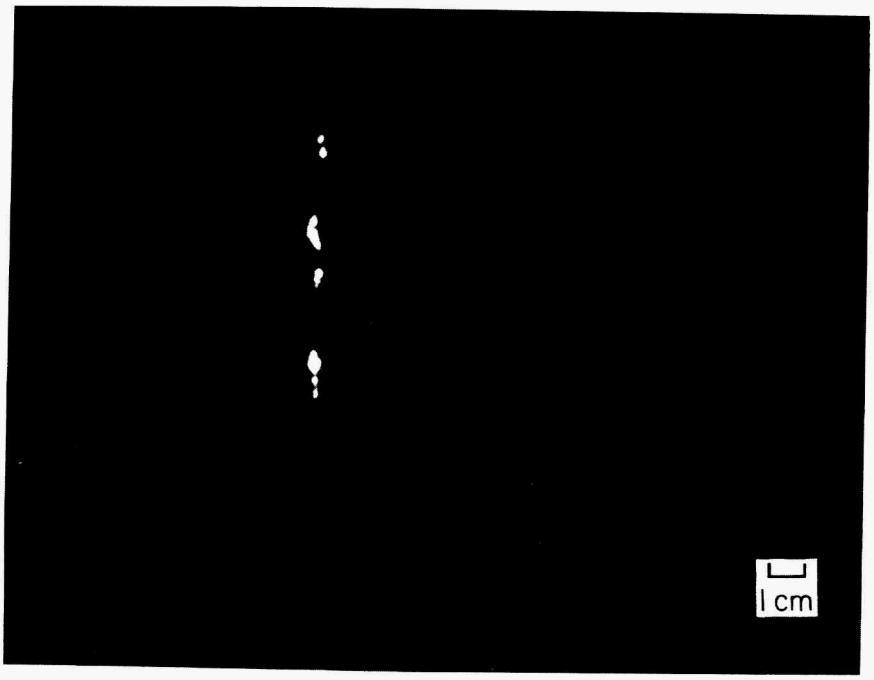

Figure 2. Thermo-elastic instability on self-mated YPSZ with mineral oil lubrication.

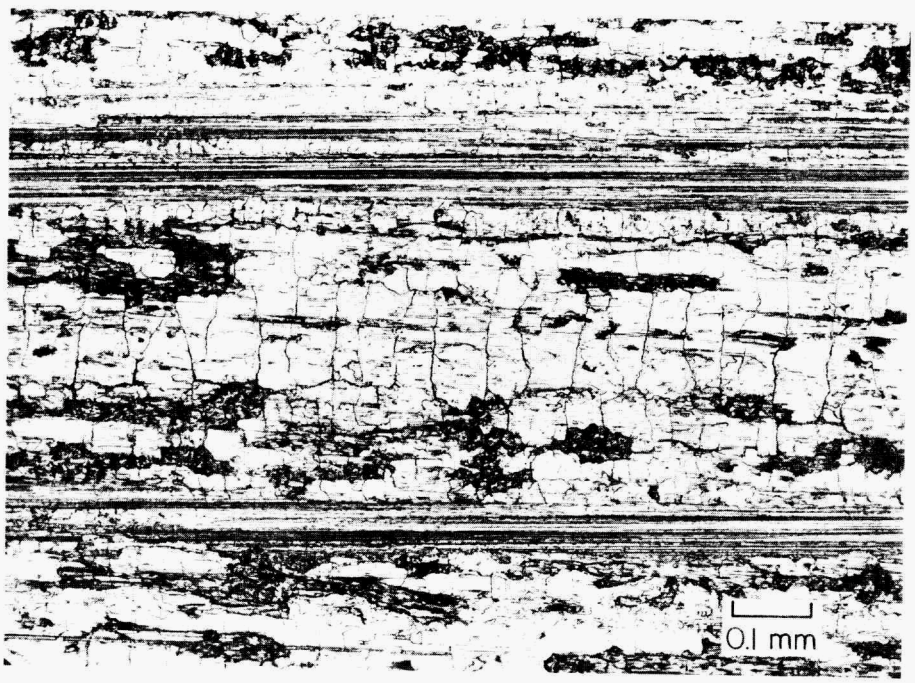

Figure 3. Cracking, spalling, and wear grooves on YPSZ

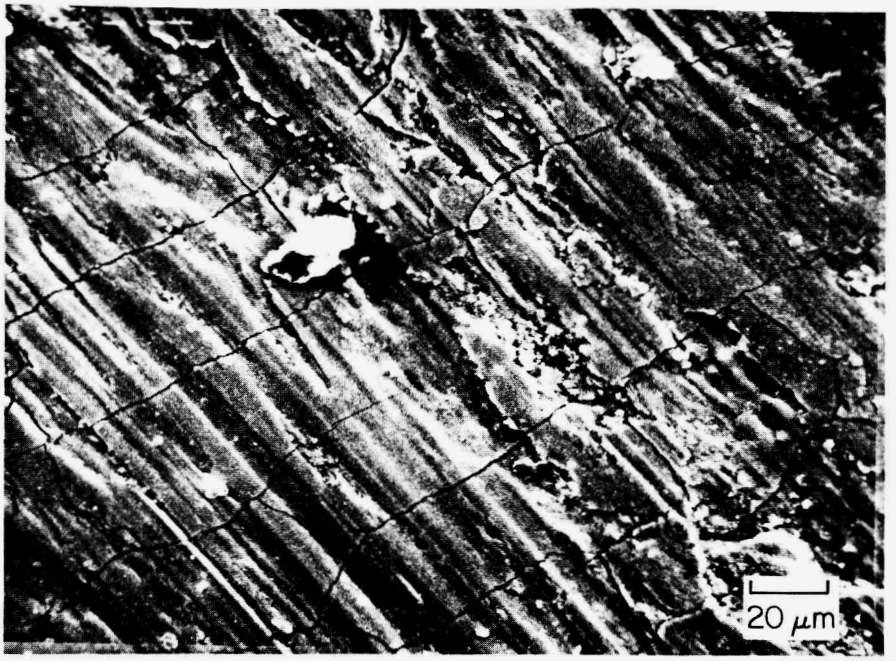

Figure 4. Surface smearing and cracking on YPSZ

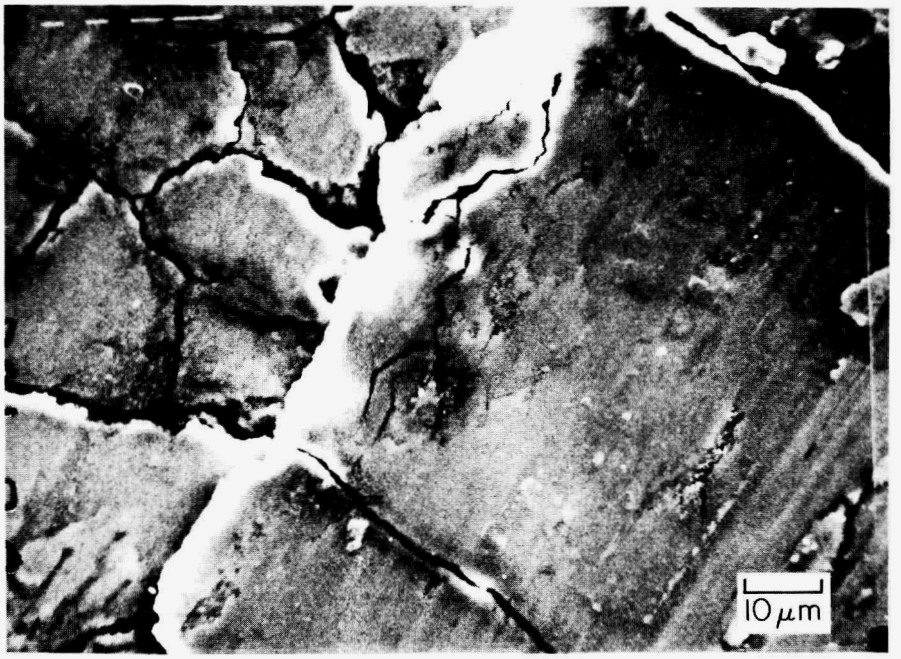

Figure 5. Detail of wear groove on YPSZ

centered cubic. The primary difference caused by wear was a decrease in the small percentage of the monoclinic phase.

Lubrication of self-mated YPSZ with MoS_2 greatly reduced the severity of thermal shock damage, but did not eliminate it entirely. Figure 6 is an SEM micrograph taken on an YPSZ specimen lubricated with MoS_2. The smeared layer was identified to be MoS_2, while the diagonal band was uncovered zirconia. The uncovered band contained thermal-shock cracks, but no spalling was observed.

TEI was also observed in experiments using mineral oil lubrication with self-mated magnesia partially stabilized zirconia (MPSZ) and self-mated alumina transformation toughened zirconia (ATTZ). The MPSZ was the most sensitive of the three zirconias. The coefficient of friction was 0.12 and the ring wear rate was equivalent to that observed with the YPSZ. The surface cracking and spalling were also similar to that observed on the YPSZ.

Similar experiments with alpha silicon carbide resulted in no visible TEI. Since TEI is speed sensitive, the operating speeds were varied from 500 to 1500 rpm with applied ring loads from 12 to 18 N/mm. The coefficient of friction decreased from an initial value of 0.07 to 0.04. The lower values were apparently the result of hydrodynamic lubrication after the ring specimens wore to the correct geometry. The worn surface of one of the ring specimens is shown in Figure 7 with details in Figure 8. No thermal cracks were visible and the surface was becoming polished. The pores were primarily the remains of pits from the original finishing. Surface smearing and fine abrasion is visible in Figure 8. The

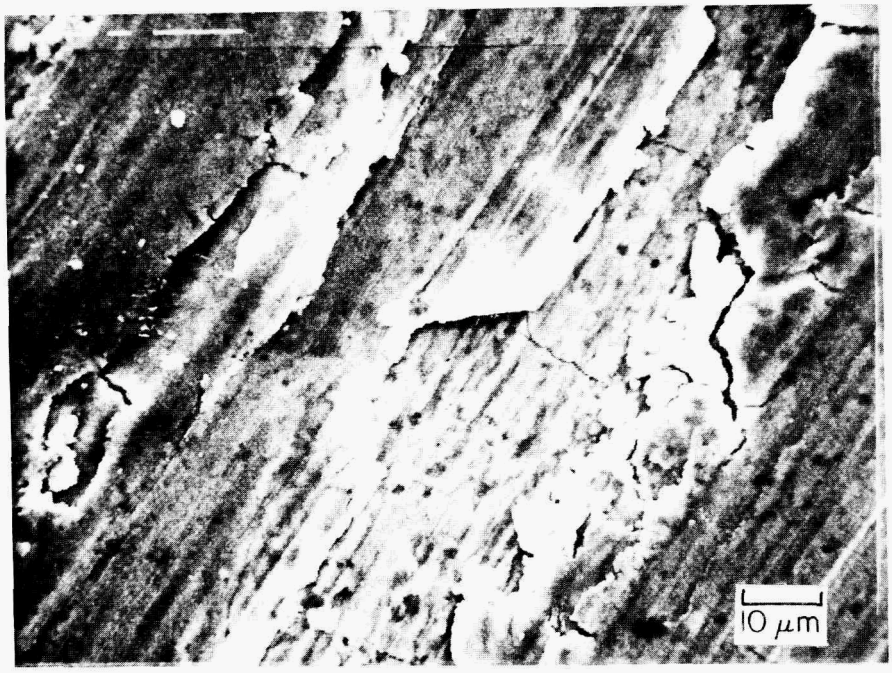

Figure 6. YPSZ wear surface lubricated with MoS_2.

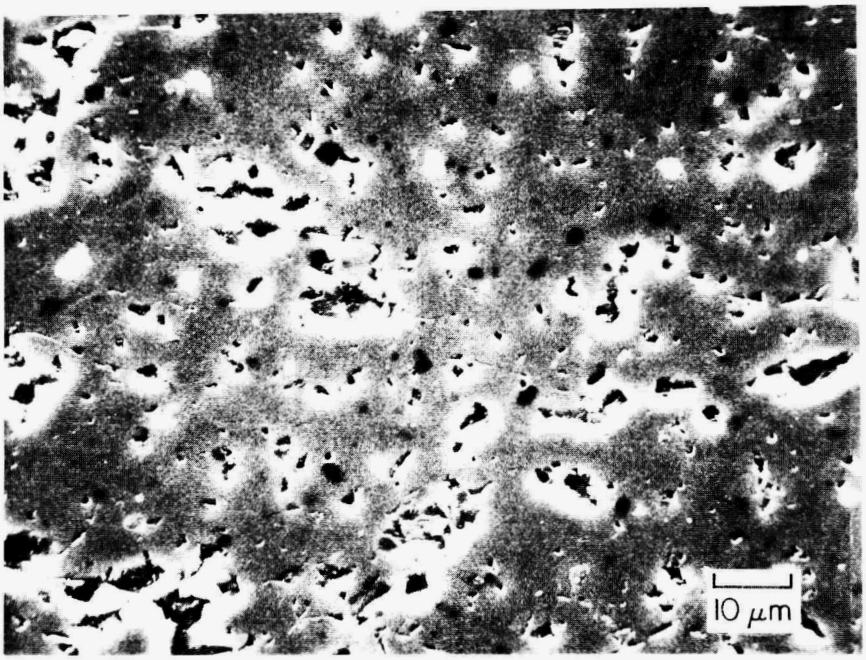

Figure 7. Polished wear surface of SiC

Figure 8. Details of wear process on SiC

abrasion scraches were interrupted in some locations, which suggests an effect of grain orientation on resistance to scratching. The pores were primarily the remains of pits from the original finishing. The ring wear after 4 hours of operation was 0.025 mm. The cylinder specimens were mildly worn in isolated polished areas.

With the marked difference in performance between the zirconias and the alpha silicon carbide, experiments were conducted to explore the effects of ring specimens having much higher thermal conductivity in sliding contact with the zirconias. Hard-chromium-plated mild steel ring specimens were run against the (YPSZ) at room temperature with SAE 10 lubricant. The measured friction coefficient was 0.2 and TEI was observed. Even though the metallic ring specimens had a much high thermal conductivity than the zirconia ring specimens in the previous experiments, the local heat generation on the zirconia cylinder specimens resulted in the formation of visible hot spots. The 0.05 mm chromium layer was worn off the mild steel, and the surface of the zirconia experienced thermal cracking. Similar results were obtained with magnesia partially stabilized zirconia cylinder specimens and chromium-plated ring specimens. As in the self-mated experiments, the magnesia partially stabilized zirconia was more prone to TEI.

Two experiments with silicon carbide ring specimens and magnesia partially stabilized zirconia cylinder specimens produced early failures of the silicon carbide specimens. TEI was observed on the zirconia prior to the ring specimen fractures. The friction coefficient was 0.1, which was lower than measured with the chromium plated ring specimens, but there was no evidence of hydrodynamic lubrication.

Successful sliding performance occurred with silicon carbide cylinder specimens and yttria partially stabilized zirconia ring specimens. The friction coefficient was 0.05 to 0.09 and no TEI was observed. The ring specimens experienced a slight amount of wear, but the wear was apparently to a geometry suitable for forming hydrodynamic lubricant films. The ring specimens were highly polished and free of thermal cracking except near the edge of one specimen. These results suggest that the thermal properties of the cylinder specimen are more important than those of the ring specimen.

Discussion

The experiments under conditions approaching those of advanced engines have shown that the ceramics and coatings studied are not capable of operation in dry sliding contact. High friction and high wear limit the practical application of these materials without lubrication.

In experiments with mineral oil lubrication at room temperature, the coefficients of friction were reduced markedly, but the onset of TEI caused surface cracking and spalling in the monolithic zirconias. Alpha silicon carbide, which did not experience TEI over the speed range of interest, had no surface cracking and developed polished wear areas. Previous studies analyzing TEI showed that a critical speed exists for sliding materials above which nonuniform contact areas of high pressure

and temperature occur and move under the influence of thermal expansion and wear[1,2]. A simplified expression developed for the critical speed is:

$$V_{cr} = \frac{4K^2}{(\mu\alpha E)^2 \pi k z},$$

where

V_{cr} = critical sliding velocity,
K = thermal conductivity,
μ = coefficient of friction,
α = coefficient of thermal expansion,
E = Young's modulus,
k = thermal diffusivity ($K/\rho c$),
z = width of slider,
ρ = density,
c = specific heat.

Using this expression, the critical velocities presented in Table 3 were calculated.

Table 3. Calculated Critical Velocities for Self-Mated Ceramics at Room Temperature

Material	Coefficient of Friction, Measured with SAE 10 Mineral Oil	V_{cr}, cm/s
YPSZ	0.13	8.9
MPSZ	0.12	8.3
ATTZ	0.12	15
SiC	0.07	1100
Si_3N_4	0.12	239
	0.08	538
	(assumed values)	

The average specimen speed at 500 rpm is 180 cm/s and at 1500 rpm is 540 cm/s. As shown in Table 3, the critical speeds for zirconia are well below the ring specimen speed at 500 rpm. The ATTZ, which had the highest calculated critical speed of the three zirconias, was the least prone to TEI. In contrast to the zirconias, the calculated critical speed for SiC is well above the ring specimen sliding speed even at 1500 rpm, which is consistent with no evidence of TEI in the experiments with SiC. For comparison purposes, the critical speeds for Si_3N_4 were calculated for two coefficients of friction. The critical speeds are between those of the zirconias and the SiC. On this basis, Si_3N_4 may also be a candidate

to avoid the surface cracking problems associated with TEI in the practical speed range for advanced engines.

The coefficient of friction is the primary variable that can be modified to effect beneficial increases in the critical speed. However, for the YPSZ, a coefficient of friction of 0.04 increases the critical speed to only 94 cm/s. A value of 0.01 results in a critical speed of 1500 cm/s, which would be in the practical range. Such low coefficients of friction require hydrodynamic lubricant films generated by a viscous fluid between surfaces of the correct geometry. Sliding systems that require the coefficient of friction to be below boundary-lubrication values of 0.1 to avoid TEI are likely to be sensitive to surface damage because of the inevitable disruptions of the hydrodynamic films during starting, stopping, and brief periods of starvation or overload. Therefore, materials with higher critical speeds (influenced strongly by the thermal diffusivity) are likely to be the least susceptible to damage resulting from TEI.

Status of Milestones

The experimental and modeling efforts are proceeding in accordance with the general program milestone schedule.

Publications

1. K. F. Dufrane, W. A. Glaeser, and A. L. Rosenfield, "Studies of Dynamic Contact of Ceramics and Alloys", submitted to the Society of Automotive Engineers, Inc., for publication in the Post-Conference Proceedings of the Twenty-Third Automotive Technology Development Contractors' Coordination Meeting, 1985.

2. K. F. Dufrane, "Sliding Performance of Ceramics for Advanced Heat Engines", submitted to the American Ceramics Society for publication in Ceramic Engineering and Science Proceedings.

References

1. T. A. Dow and R. A. Burton, "The Role of Wear in the Initiation of Thermoelastic Instabilities of Rubbing Contact", Journal of Lubrication Technology, Trans. ASME, Series F, v. 95, n. 1, pp. 71-75, 1973.

2. T. A. Dow and R. D. Stockwell, "Experimental Verification of Thermoelastic Instabilities in Sliding Contact", Journal of Lubrication Technology, Trans. ASME, Series F., v. 99, n. 3, pp. 359-364, 1977.

2.3 NEW CONCEPTS

Advanced Statistics[*]

W. P. Eatherly (Oak Ridge National Laboratory)

Objective/scope

Flaws in brittle materials, including graphite, determine the tensile or flexural strength, and in many cases are bimodal in distribution. Two large bodies of data are available, one on an aerospace graphite (N3M), the other on a structural nuclear graphite (H451). The first data set represents 430 tensile strengths in sets of seven per billet, the second contains some 1200 points in sets of eight and four. No comparable set of data exists on any other brittle ceramic.

The two data sets show a common characteristic, a bimodal strength distribution attributable to omnipresent background flaws of size comparable to the grain size, and so-called disparate flaws introduced during manufacture and of much larger size. The background flaws are indirectly accessible from measurements of sonic attenuation, the disparate flaws are directly accessible by sonic reflection.[1] The background flaw field shows a Weibull behavior when variability in strength due to bulk density is removed, with an n-value of 18 for the high-quality aerospace material and of 7 for the more modest quality nuclear material.

We review the current status of the larger data base on H451 graphite as an indication of the behavior of at least one type of brittle material. The data[2] available to us comprises a study of three production runs, representing 14, 56, and 28 cylindrical billets. From the central axis of each billet, 12 specimens were extracted, 8 axial and 4 transverse, with stress volumes defined by diameters 6.35 mm and lengths 23 mm. We include here the axial specimen analysis only, with results which are nearly identical for the transverse specimens.

Technical progress

We assume in this section the reader's familiarity with the general statistical principles involved. For those not concerned, the results are summarized in the concluding section below.

The results of a provisional variance analysis for the three lots of graphite are given in the first part of Table 1. The two statistical parameters[3] characterizing the sample distributions are s_W^2 and $\hat{\theta}$:

$$E(s_W^2) = \sigma_W^2 \ , \qquad E(\hat{\theta}) = \theta = \sigma_b^2/\sigma_W^2 \ ,$$

---

[*]These studies supported jointly by the Ceramic Technology for Advanced Heat Engines Project and the HTGR Technology Program.

where s_W^2 is the within-billet variance and s_B^2 is the between-billet variance for the sample, σ_W^2 and σ_B^2 the same for the population. The degrees of freedom for the mean sum of squares for σ_W^2 is ν_2 and for the remainder of the partitioned sum (Scheffé's MS_A) is ν_1. Also given are the mean strengths m for the lots.

Two tests for homogeneity were considered, the Bartlett test in its χ^2 form and the Foster Q-test.[4] The latter test was rejected because of its lack of sensitivity to large values of s_I^2 unless these are far off the expected χ^2-distribution. This flaw appears inherent to the Q-test. The criterion for homogeneity in the Bartlett test is that the observed statistic K be less than the upper αth critical point for the χ^2 distribution, and in the Foster test that the observed statistic Q be less than the αth critical point of the q-distribution. The reader is referred to ref. 4 for the forms of K and Q. We elected to use $\alpha = 0.85$ for the critical point. Clearly, the complete data sets do not satisfy either criterion for graphite lots 472 and 478, and that for lot 482 does so only marginally.

Two tests were also utilized to determine normality of the distribution of within-billet strengths, these being more critical than the between-billet values. The first was the Komolgorov-Smirnov single statistic test (applied at the 80% level); the second, the correlated third-fourth moment test. The results of the former are also given in Table 1 under the heading "K-S test." The moment tests were unsatisfactory and will be discussed later.

Anticipating bimodality into well-separated peaks as indicated from the sonic results, the disparate flaw strengths were isolated by rejection of low-lying outliers. Data "rejection" was accomplished on the basis of Nair and Studentized Range tests,[5] the one to test for low-lying outliers and the other for kurtosis. We also used the common restriction for small data sets: if the within-billet data subset required removal of more than one datum, the entire subset was rejected. The choice of risk (α) for these criteria is somewhat arbitrary, since the underlying distribution of flaws must be continuous and the dichotomization into disparate and background flaws is itself arbitrary. The choices $\alpha = 0.05$ for the Nair and 0.10 for the Range test were sufficient to obtain variance homogeneity. The number of "rejected" data points and subsets are given in Table 2.

The results of the variance analysis and the homogeneity tests are given in the second part of Table 3 for the truncated distributions. Partially filled cells (i.e., billets for which less than eight specimens were available) were treated as "filled" by leaving the mean and variance unchanged but increasing the degrees of freedom arbitrarily. By t-test on the means and F-test on θ, the three lots are different.

The rejected data, to the extent they contained low outliers whether isolated or from rejected subsets, were now taken to represent specimens with disparate flaws. For brevity, we consider only the collective results from all three lots. For the specimen volume employed, the probability of occurrence of a disparate flaw is 3.4% (26 flawed specimens from a total population of 774). Binomial analysis indicated a slight correlation effect, that is, a tendency to find multiple disparates within a billet.

Table 1. One-way variance analyses and homogeneity tests before and after truncation

		Full distributions			Truncated distributions		
	Lot:	472	478	482	472	478	482
m, MPa		12.2	13.6	11.1	12.2	13.8	10.8
psi		1779	1979	1615	1771	2013	1570
s_W, MPa		1.42	1.70	1.57	1.07	1.46	1.43
psi		207	247	228	156	213	208
$\hat{\theta}$		3.29	1.62	1.98	5.52	2.30	2.51
ν_1		13	55	27	12	51	26
ν_2		98	392	196	91	364	189
K		37.5	108.7	37.6	15.0	68.0	28.9
χ^2 (ν_1)		22.4	73.3	40.1	21.0	68.7	38.9
Q		0.127	0.027	0.049	0.099	0.025	0.050
$q(n_1,n_2)$		0.103	0.024	0.049	0.112	0.027	0.050
K-S Test		0.894	1.176	1.139	0.670	0.759	0.907

Table 2. Rejection of data to achieve homogeneity

Lot	Single datum (outlier)	Entire billet, 8 data	
		(outliers)	(range)
472	3	0	1
478	7	3	1
482	3	0	1

Table 3. Parameterization of disparates

Distance, mean below billet mean	5.3 MPa (768 psi)
Standard deviation	0.92 MPa (133 psi)
Correlation coefficient	0.9931

The strengths of the 26 disparate specimens were normally distributed, a not entirely surprising result in that they were identified by their distance from the normally distributed billet means. The parameters are given in Table 3. The moment correlation coefficient R is that for

strength deficiency versus argument of the cumulative normal distribution function using the formula $\Phi = (8i - 3)/(8n + 5)$ for the sample cumulative. Here, R has no statistical significance but is presented only to indicate the excellent linearity of the cumulative plot. In fact, as mentioned above, this and all other distributions in the analysis were tested for goodness-of-fit by the Kolmogorov-Smirnov test at $\gamma = 0.85$. All truncated distributions for both the individual strengths and the billet means satisfied this condition.

The distributions were slightly platykurtic to begin with, and, although truncation removed the skewness, it also increased the kurtosis. For purposes of establishing tolerance limits, however, this will lead to a conservative prediction. The platykurtic nature of the distributions cannot obviously be removed by outlier truncation and thus the correlated moment tests are not usable.

Conclusions

We may now summarize our results by stating that the distribution of strengths for a production lot may be characterized by three normal distributions. The numerical values for the parameters involved will, of course, be affected by the specimen stress volume. The three distributions are those for (1) the billet mean strength with inherent variability given by the standard deviation (see the second part of Table 1)

$$s_b = \sqrt{\hat{\theta}}\, s_W \ ;$$

(2) the variability within a billet given by the standard deviation s_W (Table 1); and (3) an additional distribution due to disparate flaws with mean lying 5.3 MPa (768 psi) below the billet mean, standard deviation 0.92 MPa (133 psi), and occurring for 3.4% of the specimens (Table 3). One obviously does not reject high-strength billets because of disparates. Rather, the low-strength billets must be rejected at a higher tolerance level.

Unfortunately, the specimens used here were destroyed before this analysis was performed. It is now impossible to verify that the specimens identified here as outliers did indeed contain large disparate flaws, but any other explanation would be forced. If our experience with aerospace graphites can be used as a guide, we would expect that about 70% or more of the outlier fracture surfaces would contain an identifiable disparate flaw.[6]

Modeling the statistics

It is relatively rare in statistics that a situation exists where the statistical distribution is known *ab initio* and nonconformance of the data to the statistic can be attributed to a faulty experiment. Obvious and somewhat trivial examples of known distributions arise in throwing dice or drawing cards. The overwhelming practical situation is that a data base comes into existence, an underlying distribution is hypothesized, and goodness-of-fit tests are employed to reach a decision as to whether the

choice of underlying distribution is appropriate.* Quite clearly, additional data or new types of experiments may prove the initial choice of underlying distribution to be inappropriate or incomplete. Only when massive numbers of data points exist and only when they are taken under a variety of conditions can we begin to say with confidence that the underlying distribution functions are known. We wish now to consider what inferences can be drawn from the above data set.

The background flaw field

We first appeal to another data set[7] beyond that treated by the variance analysis. In a carefully constructed experiment, Kennedy sought to establish the Weibull character of the H451 tensile strengths. For this purpose a density correction is required.

Over a number of commercial graphites spanning the range of fine-grained specialty materials to extremely coarse-grained electrode stock, there has been shown to exist a strong correlation between strength and density for specimens within a given billet. This is normally expressed in the form of a Knudsen equation, viz,

$$\sigma = \sigma_0 \exp \alpha(\rho - \rho_0) ,$$

where σ_0 is the ultimate strength at density ρ_0 and σ is the strength at density ρ. If one is concerned with establishing the Weibull character of the strength, then the variability due to density must first be removed.

The establishment of Weibull statistics in their usual formulation requires the validation of two relations. The first is the relationship between variance σ^2 and mean μ at any volume, given by the coefficient of variation (COV)

$$\text{COV} = \frac{\sigma}{\mu} = \frac{\Gamma(1 + \frac{2}{m}) - \Gamma^2(1 + \frac{1}{m})}{\Gamma(1 + \frac{1}{m})} ,$$

where m is the Weibull exponent. The second relationship is

$$\frac{\mu(V_2)}{\mu(V_2)} = \left(\frac{V_2}{V_1}\right)^{1/m}$$

and defines the shift of mean value with volume V, the "weakest-link" effect. (We assume that the background flaws affect the specimen through stress volume rather than area.) It is the COV relationship which is clearly sensitive to the density correlation through the total variance σ^2 rather than the desired variance due to Weibull effects alone. Upon correction, Kennedy demonstrated that both these relations are satisfied with $m \cong 7$.

---

*Our only other alternative would be to use a Bayesian methodology.

This result raises two questions: In the variance analysis and its bimodality, we assumed normal distributions; how can this be valid if even one of the modes is Weibull? If disparates truly exist, why do not they mask the Weibull? We answer the first question positively in that the density correlation, if not removed by correction to a reference density, will mask the Weibull. Unfortunately, this cannot be demonstrated conclusively for our large data set since specimen densities were not measured. We answer the second question positively in that over some three volume decades in which the volume effects were sought, the specimens were smaller or comparable to those used in the large data set. Hence, the chances of finding a disparate flaw were small or negligible.

We thus accept the conclusion that the underlying distribution for the background flaws is Weibull with exponent about 7 unless further data implies otherwise.

The disparate flaws

To establish the distribution for the disparate flaws, we have no recourse except hypotheses — no specific relevant data exist. We shall construct a model based on two assumptions:

1. Defining a base cell volume τ as sufficient to contain either one disparate flaw or none. Then the number of disparate flaws contained in an arbitrary larger volume V is binomially distributed over τ.
2. If the arbitrary volume V contains N volumes τ, then the largest flaw on the average will be the lowest (first) order statistic for an N-fold sampling of a normal distribution. (At this point we continue to assume that the normal distributions found from on the variance analysis of the large data base are valid.)

We will not concern ourselves with the mathematics but will proceed directly to the conclusions, and these are almost totally dominated by assumption 1. As the stress volume of the specimen increases, the number of specimens containing no flaws rapidly decreases, and we increasingly sample only the disparate mode. The large data base represents specimens of stress volume 728 mm^3. If we increase the volume by a factor of 20 (say 17.2-mm diam by 68.4-mm length), then the fraction of specimens containing one or more disparate flaws increases from 3.4% to about 51%. Taking our large data base to have a mean tensile strength of 12.4 MPa (1800 psi), if no disparate flaw existed, the result of increasing the specimen size twentyfold with disparates reduces the mean strength to 9.6 MPa (1390 psi). Of this reduction, 96% is due to the increased number of specimens with disparate flaws, and only about 4% due to the fact that some of the specimens contained more than one flaw.

These results are, of course, easily generalized since they are a product distribution of the binomial and order statistics. We are led to the conclusion that the existence of a bimodal distribution with this type of model leads to extremely rapid strength reductions as the uniaxial stress volume increases. We do not as yet have the data base to test this model.

While the above results are extremely tentative and arise from two large data bases on graphite, we suggest similar models will apply to brittle ceramics in general.

References

1. H. S. Starrett and R. J. Edwards, "The Detection of Threshold Size Flaws in GraphNOL N3M Graphite by Ultrasonic Pulse Echo," p. 512 in *15th Biennial Conference on Carbon, Extended Abstracts and Program*, June 22–23, 1981, Philadelphia, co-sponsored by The American Carbon Society and The University of Pennsylvania, The University of Pennsylvania, Philadelphia, June 1981.

2. G. B. Engle and R. J. Price, *The Strength Testing of Production Grade H451 Graphite*, GA-A14269, General Atomic Company, San Diego, 1977.

3. H. Scheffé, *Analysis of Variance*, Wiley, New York, 1964.

4. Irving W. Burr, *Applied Statistical Methods*, Academic Press, New York, 1974.

5. M. G. Natrella, *Experimental Statistics*, NBS Handbook 91 Corrected, National Bureau of Standards, Washington, D.C., 1966.

6. H. S. Starrett and R. J. Edwards, "Effect of Flaw Size on the Tensile Strain-to-Failure of GraphNOL N3M Graphite," p. 510 in *15th Biennial Conference on Carbon, Extended Abstracts and Program*, June 22–23, 1981, Philadelphia, The University of Pennsylvania, Philadelphia, June 1981.

7. C. R. Kennedy, Oak Ridge National Laboratory, unpublished data.

Status of milestones

None.

Publications

None.

Advanced Statistical Concepts of Fracture in Brittle Materials

C. A. Johnson and W. T. Tucker (General Electric Corporate R&D)

OBJECTIVE/SCOPE

The design and application of reliable load-bearing structural components from ceramic materials requires a detailed understanding of the statistical nature of fracture in brittle materials. The overall objective of this program is to advance the current understanding of fracture statistics, especially in the following four areas:

- Optimum testing plans and data analysis techniques.
- Confidence and tolerance bounds on predictions that use the Weibull distribution function.
- Consequences of time dependent crack growth on the evolution of initial flaw distributions.
- Strength distributions in multiaxial stress fields.

The studies are being carried out largely by analytical and computer simulation techniques. Actual fracture data are then used as appropriate to confirm and demonstrate the resulting data analysis techniques.

TECHNICAL PROGRESS

During this reporting period, two milestones were completed and two others initiated. Results on the completed milestones will be emphasized in this report. The first milestone involved development of generalized methods to estimate statistical parameters (such as the Weibull modulus) from positions of fracture origins. The second milestone involved a survey of available literature pertaining to confidence and tolerance bounds on estimates of non-normal distributions, in particular, the Weibull distribution. Results of the survey are included herein as an annotated bibliography of 19 of the more useful references on this topic.

I. Analysis of Fracture Origin Positions

As discussed in the previous Semi-annual report (1), information about the variability in strength can be derived from variability in fracture origin positions of test specimens that contain stress gradients. For a "random" distribution of defects, the most likely position of fracture initiation in a structure with a macroscopic stress gradient is the position of maximum stress. Because the most severe flaw (in terms of size, shape, orientation and position) may not be present in that location, failure may instead originate at a position stressed at lower than the maximum stress. When the material has a very small variability in strength and flaw size, there will be little variability in fracture origin positions, and the origins will tend to occur at or near positions of maximum stress. When the material has a larger variability in strength and flaw size, there will be greater variability in fracture origin positions, and the origins will occur more often in locations stressed far below the maximum stress.

The probability of an origin occurring in any given location can be predicted if the strength distribution is known for that material. Conversely, if the positions of the fracture origins are measured in a number of nominally identical test specimens or components, then information can be derived about the strength distribution. The objective of this effort was to develop practical methods to use fracture origin position data for the estimation of statistical parameters of the strength distribution.

The two-parameter Weibull distribution is an attractive choice for derivation of relationships pertaining to fracture origin positions. For the Weibull distribution, we have shown by derivation and demonstrated by simulation (as described below) that fracture origin data is independent of strength data. Therefore, an overall estimate of Weibull modulus using both types of data has less uncertainty than an estimate from the strength data alone. It is believed that the Weibull distribution is the only distribution where the strengths and origin positions are statistically independent.

In the previous semi-annual report, the distribution of fracture origin positions was described for rectangular three-point bend specimens with volume distributed defects where the strengths were consistent with the Weibull two-parameter distribution. The distribution of positions was illustrated both graphically (Fig. 3 of Ref. 1) and in equation form (Eqn. 1 of Ref. 1). It can be seen from either description that the distribution of origin positions is a sensitive function of the Weibull modulus, m.

Descriptions of the distribution of origin positions have since been derived for other bending geometries. The following three equations describe the distribution of origin positions for: (1) Four-point bend specimens with rectangular cross sections and volume distributed defects; (2) Four-point bend specimens with rectangular cross sections and surface distributed defects; (3) Three-point bend specimens with circular cross sections and surface distributed defects.

$$F = 1 - R^{m+1} + \left|\frac{1 - a/b}{1 + ma/b}\right| R^{m+1} \ln R^{m+1} \qquad (1)$$

$$F = 1 - R^{m+1} + \left|\frac{wa(m+1)}{bD}\right| R^{m+1} + \left|\frac{h(1 - a/b)}{D}\right| R^{m+1} \ln R^{m+1} \qquad (2)$$

$$F = \left|\int_0^{\cos^{-1}R} \cos^m\theta d\theta - R^{m+1}\int_0^{\cos^{-1}R} \sec\theta d\theta\right| \Big/ \int_0^{\pi/2} \cos^m\theta d\theta \qquad (3)$$

where R is a stress ratio (ratio of stress at a position of interest divided by the maximum stress in the beam); F is the fraction of origins expected to occur at or above a prescribed R value; m is the Weibull modulus; a is the inner span length; b is the outer span length; h is the specimen height; w is the specimen width; and

$$D = b(h + w)(1 + am/b)\left|1 + \frac{mw}{h + w}\right| .$$

Eqns. 1 and 2 can be reduced and simplified to describe three-point bending by setting the inner span length to zero. When this is done, Eqn. 1 correctly reduces to Eqn. 1 of Ref. 1.

The assumptions used to derive Eqns. 1-3 include: (1) The two-parameter Weibull distribution correctly describes the strength (and flaw size) distribution; (2) The material is uniform and homogeneous throughout; (3) The beam formula correctly describes the complete stress state of bend specimens (i.e., no parasitic stresses); (4) The longitudinal stress along the beam length is a satisfactory approximation of the maximum principal stress; and (5) The failure criteria of the material depends only on the maximum principal stress (no shear sensitivity, etc.).

Very little experimental fracture data are available that include accurate measurements of fracture origin positions. One set that is available consists of 45 cylindrical Pyrex glass rods (5mm diameter) that were tested in three point bending on a 2.0 inch span at room temperature (2).

To insure that failure occurred from only one flaw distribution, the specimens were uniformly abraded by tumbling for two hours in a slurry containing 220 grit SiC abrasive powder. After loading to failure, the fracture origin was located on each half of each specimen, and the position of each origin was measured in terms of distance from the nearest load point and angle from the point of maximum tensile stress. The relative stress at each origin was easily calculated from the angle and distance. The relative stress for each specimen was then assigned as the average of the measurements from the two halves.

The resulting data are included on Fig. 1 where F is plotted versus relative stress, similar to Fig. 3 of Ref. 1. The curves in Fig. 1 were calculated using Eqn. 3. The data points fall reasonably well on one of the family of curves with a Weibull modulus of approximately 22.

The Weibull modulus was also estimated by analysis of the fracture strengths. Fig. 2 is a conventional plot of transformed probability versus log strength. Strengths from a Weibull distribution should tend to fall on a straight line with a slope equal to the Weibull modulus, m. Linear regression of the 45 glass rod strengths yielded an estimate of 12.5 for the Weibull modulus.

It is clear that a discrepancy exists between the two estimates. The discrepancy may be due to any of several possible causes including: sampling fluctuations; incorrect assumption concerning stress state, flaw type and/or failure model; non-Weibull strength distribution; inhomogeneous Weibull distribution, or measurement errors. There is too little data to positively identify the source or sources of the discrepancy. No single cause seems to be responsible.

In order to further demonstrate and confirm the techniques of fracture origin position analysis, effort is currently underway to measure both strength and origin positions in a series of rectangular three and four-point bend specimens of sintered SiC fabricated in three different specimen sizes according to MIL STD 1942(MR).

An important aspect of fracture origin analysis is the independence of the origin and the strength data. If the data are independent, then 10 specimens generate the equivalent information of 20 measurements. In turn, estimates of parameters such as the Weibull modulus will have statistical properties (such as confidence bounds on the estimate) that are characteristic of 20 measurements. Independence of the fracture origin data has been demonstrated using probability intervals of the estimated m ($\hat{m}$) and by studies of correlation coefficients on estimates of m.

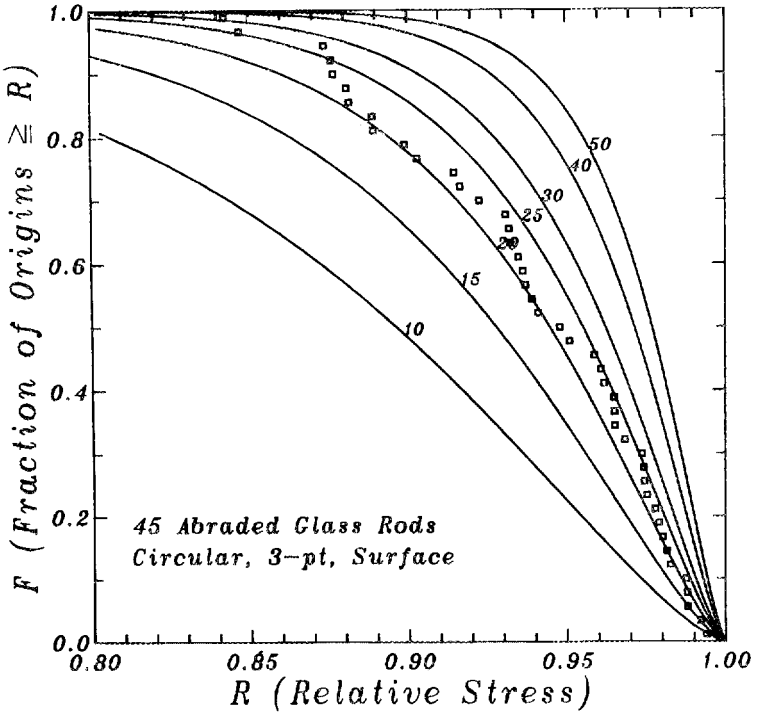

Figure 1. F versus R plot for three point bending of cylindrical rods with surface defects; includes fracture origin data from 45 glass rods.

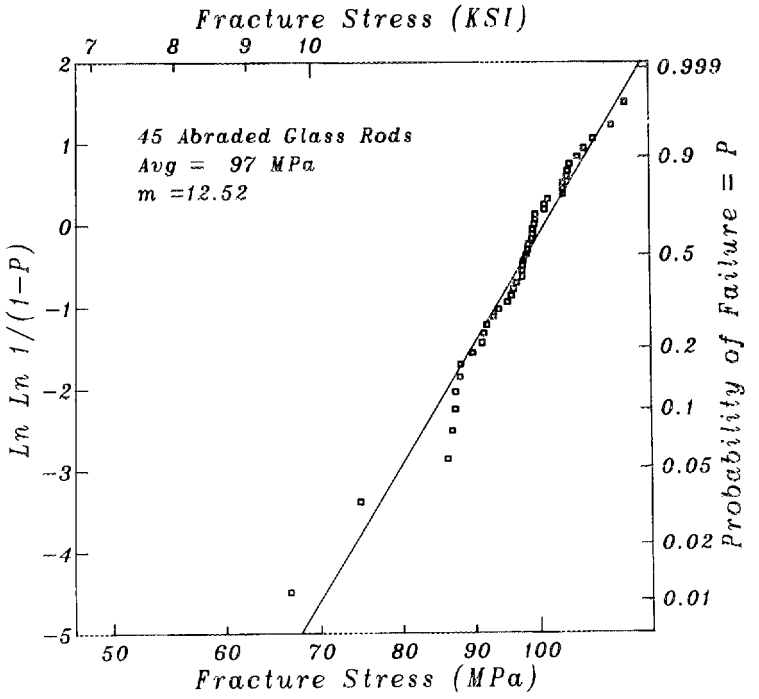

Figure 2. Conventional plot of transformed probability versus log strength with strength data from 45 glass rods.

Both methods use computer simulation to choose random specimens from an infinite population of computer-generated specimens, where the infinite population has a Weibull strength distribution with a specified m and σ_0. Each random specimen chosen has a fracture strength and an origin position. By choosing several random specimens, m can be estimated for that group using both strength and origin position techniques. The process can be repeated many times to gain information on the statistical properties of the different methods of estimating m (different estimators).

Figs. 3, 4 and 5 present the results of part of the study on probability intervals on estimates of m. Fig. 3 describes the variability of m when estimated by linear regression of strengths using the relationship P = (n-.5)/N to estimate the probability of failure from the ranking numbers. Fig. 4 is similar but represents non-linear regression of fracture origin positions on plots of F versus R such as Fig. 1. Fig. 5 then represents the behavior when the results of the two previous methods are averaged.

First consider Fig. 3. It can be shown that the ratio of the estimated m divided by the true m is independent of the value of the true m for many estimators (including this one) that use strengths. This invariant ratio is plotted versus the number of specimens in a group on Fig. 3. Included on the plot are various solid lines representing the behavior of specific percentiles of behavior. For instance, if 50 specimens were tested to failure, the estimate of m would be expected to be below approximately 0.7 times the true m one percent of the time; and below approximately 1.35 times the true m 99 percent of the time. Therefore the estimate should fall between 0.7 and 1.35 times the true m 98 percent of the time. The small data points included on Fig. 3 represent the actual positions of the various percentile behaviors as determined by the simulation. The simulation involved generation and analysis of approximately two million random specimens (including 5000 groups of 2 specimens, 5000 groups of 3, etc). The solid curves are drawn using cubic splines with fixed knots to smooth the data. The dashed line represents the average behavior.

Fig. 4 is similar to Fig. 3 except that the estimator was one that uses fracture origin positions and the invariant variable plotted on the vertical axis is slightly different. It can be shown that the invariant ratio of m's for estimators that use origin position data is the ratio of the estimated m plus one divided by the true m plus one.

Fig. 5 uses an estimator that simply involves averaging the resulting m values of the previous two estimators for each group of specimens considered in the simulation.

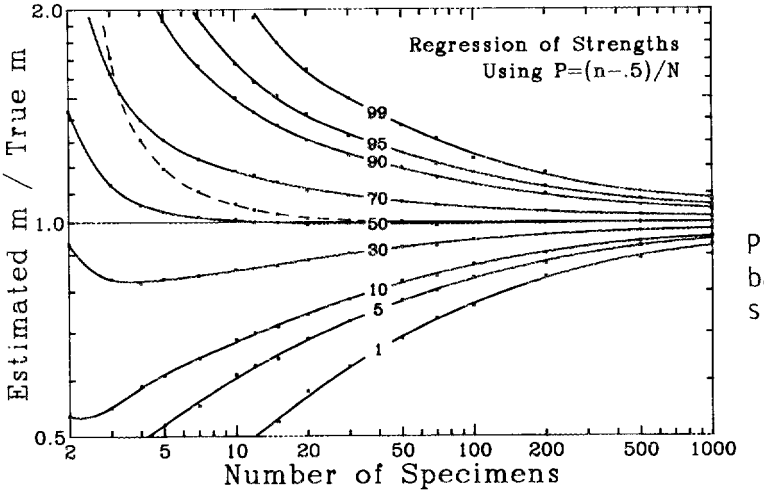

Figure 3.

Probability contours based on observed strengths.

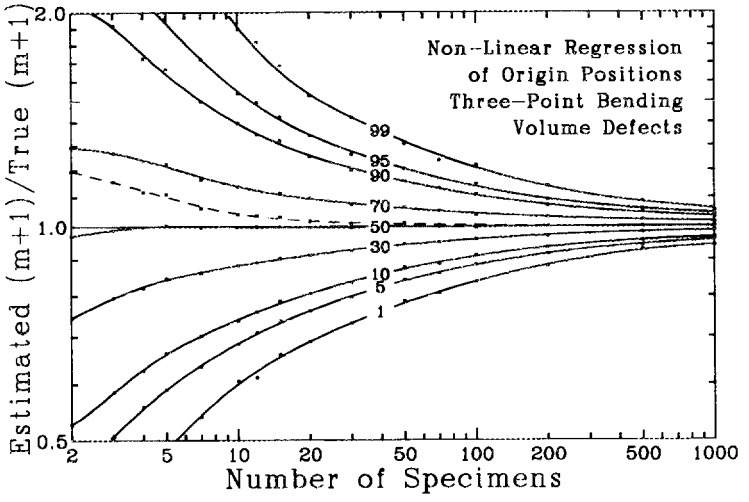

Figure 4.

Probability contours based on observed origins.

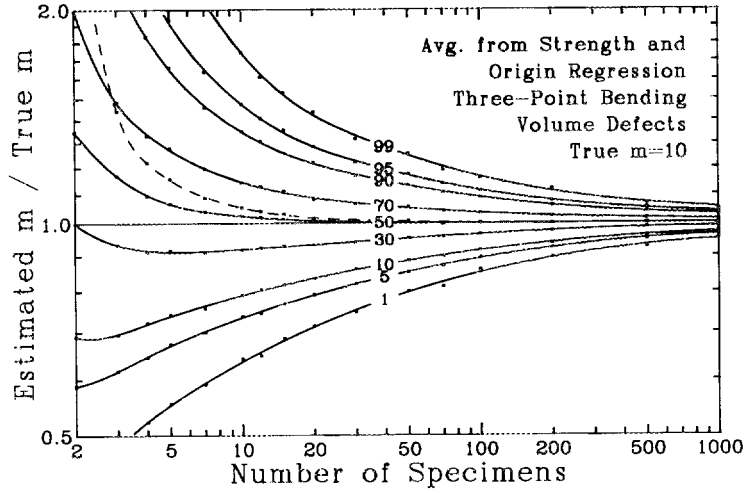

Figure 5.

Combined probability contours.

Because of the different forms of the invariant ratios for the two estimators, there is no ratio of m's that is independent of the true m. Therefore, the $\hat{m}/m$ ratio is plotted on Fig. 5, but the curves are only strictly applicable when the true m is 10 (which is the case for the simulation that generated Fig. 5).

Several comments can be made in comparing Figs. 3-5. The separation between the extreme percentile behaviors (the size of the envelope) is a measure of the statistical efficiency of the estimators. A more efficient estimator has less uncertainty in the estimate and a smaller separation for a given number of tested specimens. The envelope sizes of Fig. 3 and 4 are approximately equal. (Actually, the envelope size from origin regression is slightly smaller than that for strength regression suggesting that there is more information tied up in the origins than in the strengths.) The envelope size of Fig. 5, however, is significantly smaller than that of either strengths or origins alone. This behavior is evidence of at least partial independence of the information contained in the two types of data. If the data were not independent, the envelope size of the combined estimator would be no smaller than that for each individual estimator. If the data were perfectly independent, the size of the envelope of Fig. 5 should be approximately 0.7 times the size of that in either Fig. 3 or 4. The factor of 0.7 is approximately the reduction of envelope size that seen in Figs. 3-5.

Another approach to demonstrate independence is illustrated in Figs. 6 and 7. For each data point in Fig. 6, 10 specimens were chosen from a population with a true m of 10. The m value of this group was determined by two estimators, regression of the strengths and maximum likelihood of the strengths. Then the two estimates of m were used to define the position of one data point on Fig. 6. This process was repeated 200 times on Fig. 6 revealing a visible diagonal trend. The diagonal trend is evidence of the non-independence of these two estimators. Both use the same strength data, therefore, when one estimator yields an abnormally high estimate of m, the other estimator using the same raw data tends to also yield an abnormally high estimate of m. Conversely, when one estimate is low, the other also tends to be low, thus generating the diagonal trend on Fig. 6.

A similar simulation procedure was used to generate Fig. 7, except that the second estimator was non-linear regression of the origin position data. In this case, there is no visible trend. The lack of any apparent correlation in the two estimates of m as shown on Fig. 7 is evidence of independence of the strength and origin position data.

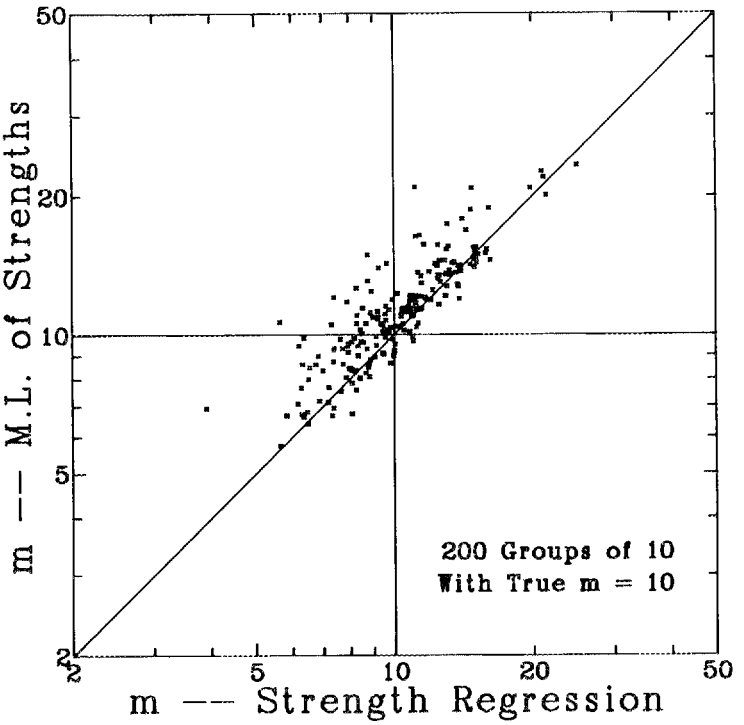

Figure 6. Scatter plot: strength versus strength

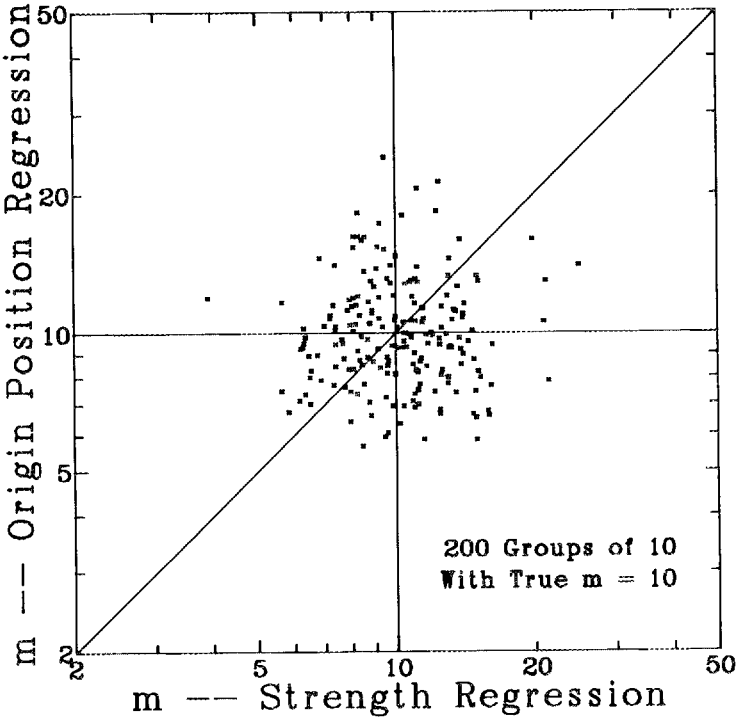

Figure 7. Scatter plot: origin versus strength

Quantitative evaluation of correlation coefficients has been done for the case of 5000 points on both Figs. 6 and 7. The resulting correlation coefficient for strength regression vs strength maximum likelihood was 0.88 showing a very high correlation between the two estimates. The correlation coefficient for strength regression vs origin position regression was approximately 0.001 showing that the strength data is highly independent of the origin position data.

II. BIBLIOGRAPHY OF STATISTICAL CONFIDENCE PROCEDURES FOR LIFE DATA

One of the milestones of the first year of the contract was the preparation of an annotated bibliography of confidence and tolerance limits for non-normal distributions, in particular, the Weibull distribution. This bibliography emphasizes those methods developed for the Weibull distribution. However, the books referenced include procedures for many other distributions and give further references as well. Special attention is given to those methods that give exact limits and bounds for the Weibull distribution. The "statistical" literature has been primarily researched in preparing the bibliography and this is reflected in the references presented.

Before giving the bibliography, certain connotational and terminological differences between the statistics' and materials' fields should be pointed out. The statistical term, life, refers to strength or stress at failure in material work; that is, an observed lifetime is analogous to the measured stress at failure. Also the statistical connotation regression model or procedure in life data analyses is analogous to the modeling of a volume or area dependency in material applications. Furthermore, in the case of the Weibull (and similar distributions) the material form for the (cumulative) hazard, $V(\sigma/\sigma_0)^m$, is called the proportional hazards model in the statistical literature. And if a lifetime or strength is transformed by taking the logarithm, then the model is called (in statistical applications) the accelerated failure or log-linear model.

Accelerated testing in statistical applications is accomplished by testing in a more severe environment than the operating environment. The aim is to produce observed failures so that a meaningful analysis results. In step-stress testing this is done in graduated stages or steps. Similar phenomenon occur in material applications when subcritical crack growth occurs. Thus "time" for a materials' person is analogous to "stress" for a statistician in the context of accelerated testing.

One final topic is of interest. In the statistical literature tests with various types of censoring are considered. The two major types are time censoring called Type I censoring and failure censoring called Type II censoring. In Type I censoring the test is terminated at a predetermined time and thus the number of failed units is random. In Type II censoring the test is terminated when a particular number of units have failed and thus the failure times are random. (For further reading see the Nelson and Mann et al books.) Unfortunately, time censoring is more common in practice and failure censoring more common in in the literature, since it is more tractable.

While many tests of materials are conducted without censoring (for example, all units fail from surface defects and are tested until they fail), Type I censoring can occur. Indeed, a specimen that has both surface and volume defects and can fail from either will experience Type I censoring. If a surface defect produces failure then the volume defects have been censored and if a volume defect produces failure then the surface defects have been censored. In order to properly analyze such data one must be able to distinguish between surface and volume defects.

A. Books

Many of the procedures are by now well known and are given in book form. We suggest that the interested reader consult more than one of the referenced books.

1. Kalbfleisch, J. D. and R. L. Prentice (1980), The Statistical Analysis of Failure Time Data, John Wiley & Sons, New York.

   While special attention is given to biomedical problems and asymptotic maximum likelihood and nonparametric procedures the book gives a thorough treatment of regression methods. Also the generalized F distribution is covered. This is a general form that includes as special cases the log-normal, Weibull, log-logistic, reciprocal Weibull, and generalized gamma distributions and is useful in inference procedures.

2. Lawless, J. F. (1982), Statistical Models and Methods for Lifetime Data, John wiley & Sons, New York.

   The book gives a good coverage of the major life distributions including the Weibull. Exact methods are given based on a conditional approach developed by the author that include tolerance procedures. Also

mention is made of exact methods developed by Mann, Mann & Fertig, McCool, and Thoman et al, as well as certain approximate methods. Regression models, maximum likelihood estimation, and nonparametric and distribution free methods are also covered.

3. Mann, N. R., R. E. Schafer, and N. D. Singpurwalla (1974), Methods for Statistical Analysis of Reliability and Life Data, John Wiley & Sons, New York.

   This book has become somewhat of a "bible" of the field. Good coverage of the major life distributions including the Weibull is given. Also exact methods based on work by Mann and others that cover tolerance procedures are given. Furthermore, some coverage of accelerated methods and Bayesian methods in reliability is given.

4. Nelson, W. (1982), Applied Life Data Analysis, John Wiley & Sons, New York.

   This book gives an excellent treatment in an applied vein. Good coverage of the major life distributions including the Weibull is given. Exact confidence methods based on the Mann et al work are covered as well as many approximate methods. Excellent coverage of plotting methods (some of which have been developed by the author) are given. Also a chapter is presented that surveys related topics including accelerated testing and reliability.

B. Seminal Papers

These papers involve exact and/or efficient procedures for the Weibull distribution. They represent only a small portion of the work in this area and thus the interested reader should also consult the references given in these citations.

5. Bain, L. J. (1972), "Inferences Based on Censored Sampling from the Weibull or Extreme-Value Distribution," Technometrics, 14, 693-702.

   Bain presents an unbiased linear estimator based on the first r of n extreme-value order statistics which is studied further in the Mann et al book.

6. Bain, L. J. and C. E. Antle (1967) "Estimation of Parameters in the Weibull Distribution," Technometrics, 9, 621-27.

This is one of the earlier works on parameter estimation. It also gives references to earlier works and introduces new, simple estimators and studies invariance properties of these and maximum likelihood estimators.

7. Lawless, J. F. (1972), "Confidence Interval Estimation for the Parameters of the Weibull Distribution," Utilitas Mathematica, 2, 71-87.

   This is the first in a series of papers by Lawless concerning exact methods for the Weibull allowing for censoring in which he introduces his conditional approach.

8. Lawless, J. F. (1973), "On the Estimation of Safe Life When the Underlying Life Distribution Is Weibull," Technometrics, 15, 857-65.

   This paper is a continuation of the author's work with a conditional approach in which he obtains an estimate of the the smallest observation from a future sample based on an observed sample.

9. Lawless, J. F. (1975), "Construction of Tolerance Bounds for the Extreme-Value and Weibull Distributions," Technometrics, 17, 255-61.

   This paper gives a culmination of procedures developed by Lawless based on a conditional approach. A method of finding confidence bounds on the percentiles of the two-parameter Weibull or extreme-value distributions is given. The procedures allow a comparison with approximate bounds based on an F approximation and also on approximate maximum likelihood estimates. The approximate F method is given in the Mann et al book and Lawless concludes "the method ... appears to have much to recommend it."

10. Mann, N. R. (1970), "Estimators and Exact Confidence Bounds for Weibull Parameters Based on a Few Ordered Observations," Technometrics, 12, 345-61.

    This is the first of a number of papers by Mann (and others) in which exact methods based on the use of order statistics are developed. These methods allow for censoring.

11. Mann, N. R. and K. W. Fertig (1973), "Tables for Obtaining Confidence Bounds and Tolerance Bounds Based on Best Linear Invariant Estimates of Parameters of the Extreme-Value Distribution," Technometrics, 15, 87-101.

These tables allow use of the Mann procedures.

12. Mann, N. R., K. W. Fertig, and E. M. Scheuer (1971), "Confidence and Tolerance Bounds and a New Goodness-of-Fit Test for Two-Parameter Weibull or Extreme-Value Distributions with Tables for Censored Samples of Size 3(1)25," Aerospace Research Laboratories Report ARL 71-0077, Office of Aerospace Research, U.S. Air Force, Wright-Patterson Air Force Base, Ohio.

Exact confidence and tolerance bounds are developed and tables given for their use. Also see the Mann et al and Nelson books for further references to this work.

13. Thoman, D. R., L. J. Bain, and C. E. Antle (1969), "Inferences on the Parameters of the Weibull Distribution," Technometrics, 11, 445-60.

This paper possibly gives the first exact methods for the Weibull distribution. However, the methods do not allow for censoring. Tables are given for use of the method.

14. Thoman, D. R., L. J. Bain, and C. E. Antle (1970), "Maximum Likelihood Estimation, Exact Confidence Intervals for Reliability, and Tolerance Limits in the Weibull Distribution," Technometrics, 12, 363-71.

As the title indicates, exact reliability and tolerance limits are presented. Also tables are given for use of the method. Again this work gives possibly the first exact methods and does not allow for censoring.

15. Weibull, W. (1939), "A Statistical Theory of the Strength of Materials," The Royal Swedish Institute for Engineering Research, Proceedings, 151, Stockholm.

This is the seminal work for the Weibull distribution. While some writers have minimized Weibull's work he gives a much better presentation on statistical grounds than do many later writers in the materials area. Weibull makes a clear and understanding distinction between the (cumulative) hazard function which he labels the risk of rupture and the

probability of rupture. Unfortunately, many later writers are not as careful as Weibull and this has led to theoretical difficulties and some lack of understanding of the fundamental problem.

C. Miscellaneous Citations

This section covers a number of references to related work in accelerated testing due to its possible usefulness in situations of subcritical crack growth and optimum experimental design.

16. Meeker, W. Q., Jr. (1984), "A Comparison of Accelerated Life Test Plans for Weibull and Lognormal Distributions and Type I Censoring," Technometrics, 26, 157-71.

    Optimum accelerated test plans have some practical deficiencies. Meeker offers compromise plans that sacrifice some precision but give information to detect departures from the assumed model and are more robust to departures if they occur.

17. Nelson, W. (1974), "A Survey of Methods for Planning and Analyzing Accelerated Tests," IEEE Trans. Electr. Insul., EI-9, 12-18.

    As the title the paper gives a survey of methods of accelerated testing and analysis up to 1974.

18. Nelson, W. (1980), "Accelerated Life Testing -- Step-Stress Models and Data Analyses," IEEE Trans. Reliab., R-29, 103-08.

    The paper gives a clear presentation of the elements of a step-stress model. While the specific model may not be appropriate for subcritical crack growth, the methodology is indicative of that required in analyzing subcritical crack growth.

19. Nelson, W. and W. Q. Meeker, Jr. (1978), "Theory for Optimum Accelerated Censored Life Tests for Weibull and Extreme-Value Distributions," Technometrics, 20, 171-77

    The authors give asymptotically optimum test plans for simultaneous testing with Type I censoring for the Weibull distribution. They also review other literature.

STATUS OF MILESTONES

On schedule.

PUBLICATIONS

1. C.A. Johnson and W.T. Tucker, "Advanced Statistical Concepts of Fracture in Brittle Materials," submitted for publication to the proceedings of the 23rd Automotive Technology Development Contractors' Coordination Meeting, October 1985, Dearborn, Michigan.

2. C.A. Johnson and W.T. Tucker, "Estimation of Weibull Modulus from Fracture Origin Positions," in preparation.

REFERENCES

1. C.A. Johnson and W.T. Tucker, "Advanced Statistical Concepts of Fracture in Brittle Materials," Ceramic Technology for Advanced Heat Engines Project, Semi-annual Progress Report for Period April-September 1985.

2. C.A. Johnson and S. Prochazka, "Investigation of Ceramics for High Temperature Turbine Components," Final Report, Contract N62269-76-C-0243, 1977.

3.0 DATA BASE AND LIFE PREDICTION

INTRODUCTION

This portion of the project is identified as project element 3 within the work breakdown structure (WBS). It contains five subelements, including (1) Structural Qualification, (2) Time-Dependent Behavior, (3) Environmental Effects, (4) Fracture Mechanics, and (5) Nondestructive Evaluation (NDE) Development. Research conducted during this period includes activities in subelements (1), (2), and (3). Work in the Structural Qualification subelement includes proof testing, correlations with NDE results and microstructure, and application to components. Work in the Time-Dependent Behavior subelement includes studies of fatigue and creep in structural ceramics at high temperatures. Research in the Environmental Effects subelement includes study of the long-term effects of oxidation, corrosion, and erosion on the mechanical properties and microstructures of structural ceramics.

The research content of the Data Base and Life Prediction project element includes (1) experimental life testing and microstructural analysis of Si_3N_4 and SiC ceramics, (2) time-temperature strength dependence of Si_3N_4 ceramics, and (3) static fatigue behavior of PSZ ceramics.

Major objectives of research in the Data Base and Life Prediction project element are understanding and application of predictive models for structural ceramic mechanical reliability, measurement techniques for long-term mechanical property behavior in structural ceramics, and physical understanding of time-dependent mechanical failure. Success in meeting these objectives will provide U.S. companies with the tools needed for accurately predicting the mechanical reliability of ceramic heat engine components, including the effects of applied stress, time, temperature, and atmosphere on the critical ceramic properties.

3.1 STRUCTURAL QUALIFICATION

Microstructural Analysis of Corrosive Reactions in Structural Ceramics

N. J. Tighe and R. M. Hu (National Bureau of Standards, Gaithersburg, Md.)

Objective/Scope

The objective of the program is to identify the failure causing defects and to determine mechanisms of defect interaction with the environmental testing conditions. Test specimens from fracture mechanics tests in the NBS laboratory and in other laboratories that have DOE/NASA research funding will be used to identify patterns of failure that correspond to strength variations between billets of the same ceramic.

Technical progress

Scanning and transmission electron microscopy studies are being used to identify microstructural elements and to characterize microstructural changes with respect to deformation mechanisms and corrosion behavior in silicon carbide and silicon nitride ceramics. Of particular interest are the ceramics that are proposed for use in heat engines and heat exchangers. Considerable work has been done at NBS to evaluate the reliability of these materials under specific chemical and thermal stress applications by testing them under environmental conditions that simulate corrosive service conditions. Oxidation and chemical attack at high temperature were found to contribute to strength degradation and premature failure. When the ceramics are stressed at high temperatures the microstructure is affected and discrete changes occur in the grains, the phase boundaries and in the second phases.

Thin foil specimens were prepared from transverse and parallel cross-sections of the bend bars in order to identify microstructural changes as a function of distance from the tensile and compression surfaces. Commercially prepared samples of sintered alpha SiC, and hot-pressed Si_3N_4 doped with MgO, Y_2O_3, and BN were tested and examined.

Pieces from salt corroded SiC samples were received from NASA for examination. Before examining these samples it was necessary to develop suitable thin foil specimen preparation techniques which would retain the reaction product that formed a thick scale on the samples. Therefore, coupons and thin disk specimens were prepared from an NBS set of sintered alpha SiC billets that had been used in deformation tests. These samples were heated with $NaCO_3$ at temperatures up to 1000°C for 5, 15 and 30 min. and 48 h in order to correspond to the NASA tests. The microstructural characterization was carried out using analytical scanning transmission electron microscopy and scanning electron microscopy.

Earlier examinations of the SiC showed that micron-sized fibrous inclusions of graphite influenced the high temperature mechanical properties. The BN additions to yttria doped Si_3N_4 also formed with a fibrous morphology but the effects of these fibers on the high temperature properties have not been assessed. However the BN additions apparently contribute to increased room temperature toughness. High temperature exposure produced an initial strengthening in both silicon carbide and silicon nitride samples because some surface defects were healed by the formation of a silica scale. Prolonged exposures allowed deep penetration of the oxides along grain boundaries, cavitation along boundaries, reaction with internal inclusions and eventual degradation of strength. They also were used to clarify the behavior differences between the ceramics with amorphous grain boundary phases and those with crystalline grain boundary phases.

In the case of the salt reactions, the electron microscopy results show that severe corrosion occurred in the silicon carbide specimens after a few minutes exposure to $NaCO_3$. The salt reacted aggressively with graphite inclusions, dissolved silicon carbide grains and enlarged the surface pores. Examination of the reacted samples by scanning electron microscopy showed a severely cracked surface layer of silica that had deep pits extending into the SiC matrix as shown in Fig. 1A. The pits seen in Fig. 1 can be associated with cracks and pits that are present in the original billet as shown in Fig. 1B. The reaction product was removed with an HF solution and the underlying SiC grains were found to have been etched by the sodium salt. The severity of the etching was related to the time of exposure but some etching was observed in the 5 min. samples. The severe attack on the grains is evident in the micrographs in Fig. 2 which shows the SiC samples which were reacted at $1000^{o}C$ for 1 and 48 h.

Thin foil samples have been made from the as-received and the reacted specimens. The samples were dimpled before ion thinning. Some disks were reacted with the sodium salt and other disks were made from previously reacted samples. The reaction product was found to be amorphous silica containing some sodium. Areas containing both the reaction product and the SiC matrix have been observed. The preparation of thin sections from transverse sections has been started. After specimen preparation and observation techniques are established, we will be able to examine the NASA samples.

A billet of hot-pressed silicon nitride that contained yttria, alumina and approximately 20% boron nitride was sectioned and examined by analytical scanning transmission electron microscopy. The boron nitride inclusions were found to have a fibrous morphology that was similar to that found in the alpha silicon carbide. The fiber bundles linked over several grain diameters and appeared to be well-sintered to the silicon nitride and to the yttrium aluminate grains. Although the boron nitride additions could contribute to the toughness, it is expected that the thermal, mechanical and corrosion stresses will cause strength degradation because the boron nitride is unstable in oxidizing atmospheres. These fibers may behave in a manner similar to that observed of the carbon fibers in the silicon carbide.

Status of milestones

Characterization of corrosion reactions in SiC and Si_3N_4. The reaction product formed during heating of SiC coated with $NaCO_3$ at 1000°C characterized using SEM and STEM as amorphous sodium/silica film at the ceramic interface. After cross sectional samples are examined by STEM we will be able to address the associating specific microstructural elements with changes in reactions process.

Element analysis. Sodium was located in the reaction film using X-ray mapping techniques. Sodium is mobile in the electron beam so that precise locations may have to be determined in the STEM. The scanning electron microscope has developed serious vacuum problems which limits use of the windowless detector. We have some STEM samples ready for analysis.

A series of standard ceramic samples that are single crystal oxides and carbides and specially prepared oxide glasses have been developed in the group by B.J. Hockey in collaboration with D. Blackburn of the Glass and Composites Group. These standards are being used for semi-quantitative analysis procedures.

Publications

Paper "Creep Deformation in Si_3N_4 and SiC Ceramics" was prepared for publication in the Materials Research Journal.

Paper "Microstructures of SiC and Si_3N_4 with Fibrous Inclusions" submitted to the Electron Microscopy Society of America for August meeting presentation.

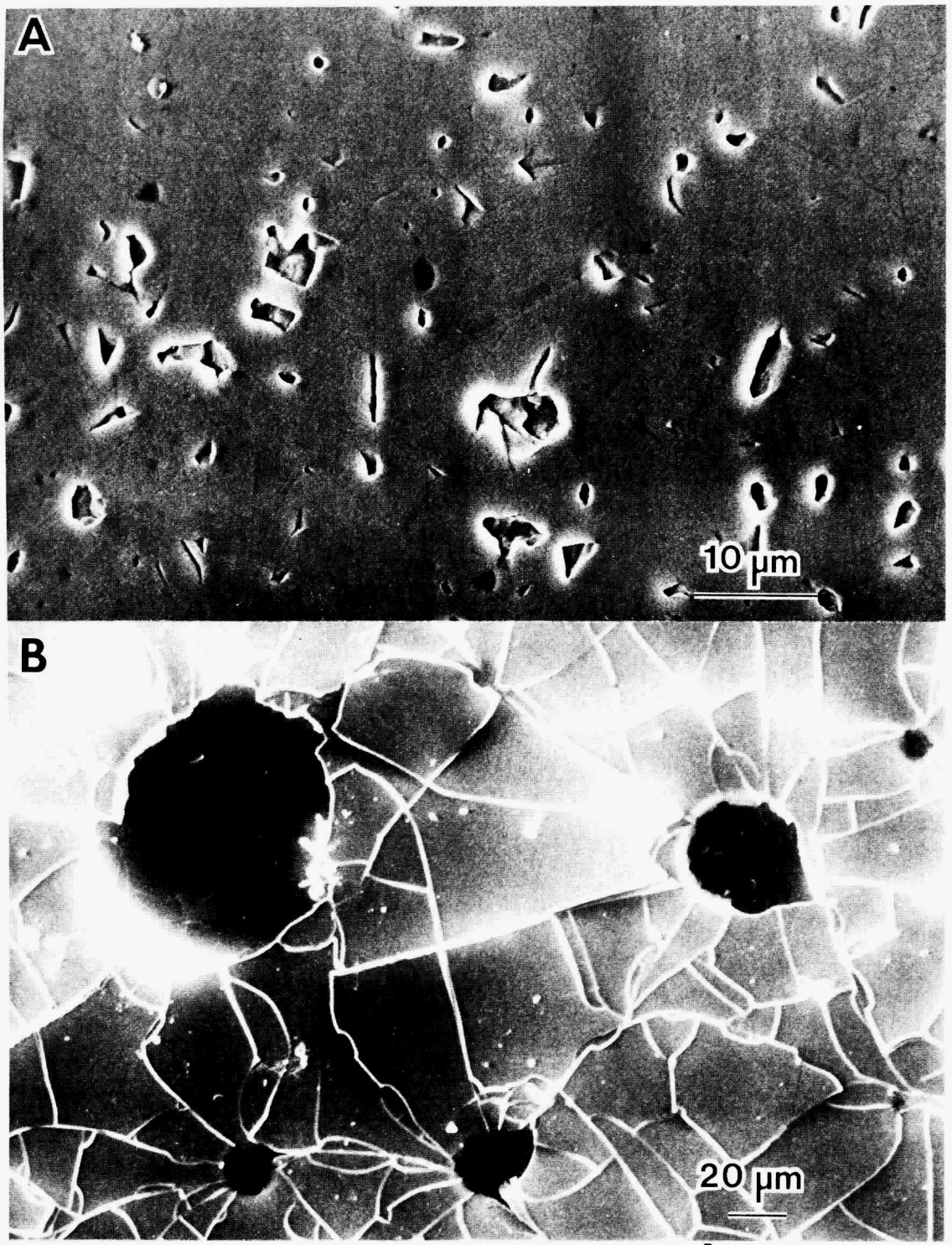

Fig. 1. Sintered alpha SiC after heating 48h at 1000°C.
(A) Showing thermal etching on polished surface.
(B) Reaction product formed with $NaCO_3$ on polished surface.

Fig. 2. Sintered SiC specimens reacted with $NaCO_3$ at 1000°C for (A) 1 h and (B) 48 h. Reaction product removed by HF.

Physical Properties of Structural Ceramics

R. K. Williams, R. S. Graves, and M. A. Janney (Oak Ridge National Laboratory)

Objective/scope

The structural ceramics presently considered for use in advanced heat engine applications usually contain more than one phase and several components. The thermal conductivities of these materials are low relative to metals, and this, along with thermal expansion plus fracture strength and toughness, is a prime factor in determining suitability of a given ceramic for a particular advanced engine component. The purpose of this research is to develop an improved understanding of the factors which determine the thermal conductivities of these complex structural materials at high temperatures.

Technical progress

A study of the effect of grain size on the thermal conductivity, λ, of alumina has been completed. This work was undertaken because thermal conductivity helps to determine the magnitude of thermal stresses, and recent theoretical work[1] indicates that the variation with grain size should be larger than had previously been predicted. This is significant because grain size, and therefore thermal conductivity, can be controlled by altering processing conditions.

The new theory, which was developed by P. G. Klemens and his student, R. Brito Orta,[2] involves a reconsideration of the role played by long wavelength longitudinal phonons. The result is that the contribution of these excitations to the thermal conductivity is larger than had been thought and might typically be about 20% of the total at ambient temperatures. This contribution also varies more rapidly with temperature, not as T^{-1}, and should be sensitive to grain size. The more rapid temperature variation is seen experimentally; the sensitivity to grain size arises because the excitations have long wavelengths, which are comparable to typical ceramic grain sizes. Alumina was chosen as a model material because it can be obtained in high purity and because the densification and grain growth behavior is understood. Theoretical calculations for alumina were performed by Brito Orta.[2]

After milling for 8 hours in isopropanol, the alumina powder was densified by hot pressing for one hour at 1450°C with a pressure of 34 MPa. Baikowski grade CR10 alumina (5-9's) was the starting material, and sintering aids were not used. After densification, samples were annealed in air at 1500, 1550, 1600, 1650, 1700, and 1800°C for 1 hour. Densities of these 15-mm-diameter, 7-mm-high samples varied from 99.5 to 96.9% of theoretical; the lowest density was for a sample annealed at 1800°C. The grain sizes were obtained by thermally etching polished sections in air at 1400°C for 1 hour. Both longitudinal and transverse sections were examined, and a scanning electron microscope was used for the samples annealed at temperatures up to 1600°C. Grain sizes were determined from photomicrographs by using the linear intercept method.

Thermal conductivity samples, 6.35 mm in diameter and 5 mm long, were machined from the larger, hot pressed alumina discs. The steady state measurements were made by a comparative method that has an estimated uncertainty of about ±2% (ref. 3). Three data points, at nominally 30, 60, and 90°C, were obtained on each sample and the values were corrected to theoretical density via Maxell's equation.[4] The results were then smoothed by assuming that λ^{-1} varies linearly with temperature.

The results are shown in Fig. 1. The theoretical values[2] contain one adjustable parameter and were therefore normalized to the experimental result for an average grain size of 1 μm. The experimental results show the trend predicted theoretically, but, in this grain size range, the effect (~11%) is somewhat smaller than predicted (~14%). Another point of interest is that the thermal conductivity values for these dense, high purity alumina samples are 5 to 10% lower than literature data[5] for polycrystalline alumina.

From a practical point of view, the importance of these results is in demonstrating a new method for changing the thermal conductivity. When lower conductivity is desired, this effect has an additional advantage because it supplements the reduction caused by substituting foreign atoms in the lattice. The reason for this is that foreign atom scattering is most effective for short wavelength phonons, while the grain size effect reduces the contribution from long wavelengths.

Status of milestones

On schedule.

Publications

None.

References

1. P. G. Klemens, *Int. J. Thermophys.* **2**, 55-62 (1980).

2. R. A. Brito Orta, "The Contribution of Longitudinal Phonons to the Lattice Thermal Conductivity," PhD thesis, University of Connecticut, 1982.

3. R. K. Williams, R. K. Nanstad, R. S. Graves, and R. G. Berggren, *J. Nucl. Mater.* **115**, 211-15 (1983).

4. R. A. Crane, R. I. Vachon, and M. S. Khader, "Thermal Conductivity of Granular Materials – A Review", pp. 109-23 in *Proceedings of the Seventh Symposium on Thermophysical Properties*, ed. A. Cezairliyan, American Society of Mechnical Engineers, New York, 1977.

5. Y. S. Touloukian, R. W. Powell, C. Y. Ho, and P. G. Klemens, p. 119 in "Thermal Conductivity, Nonmetallic Solids," vol. 2 of *Thermophysical Properties of Matter*, I.F.I./Plenum, New York-Washington, 1970.

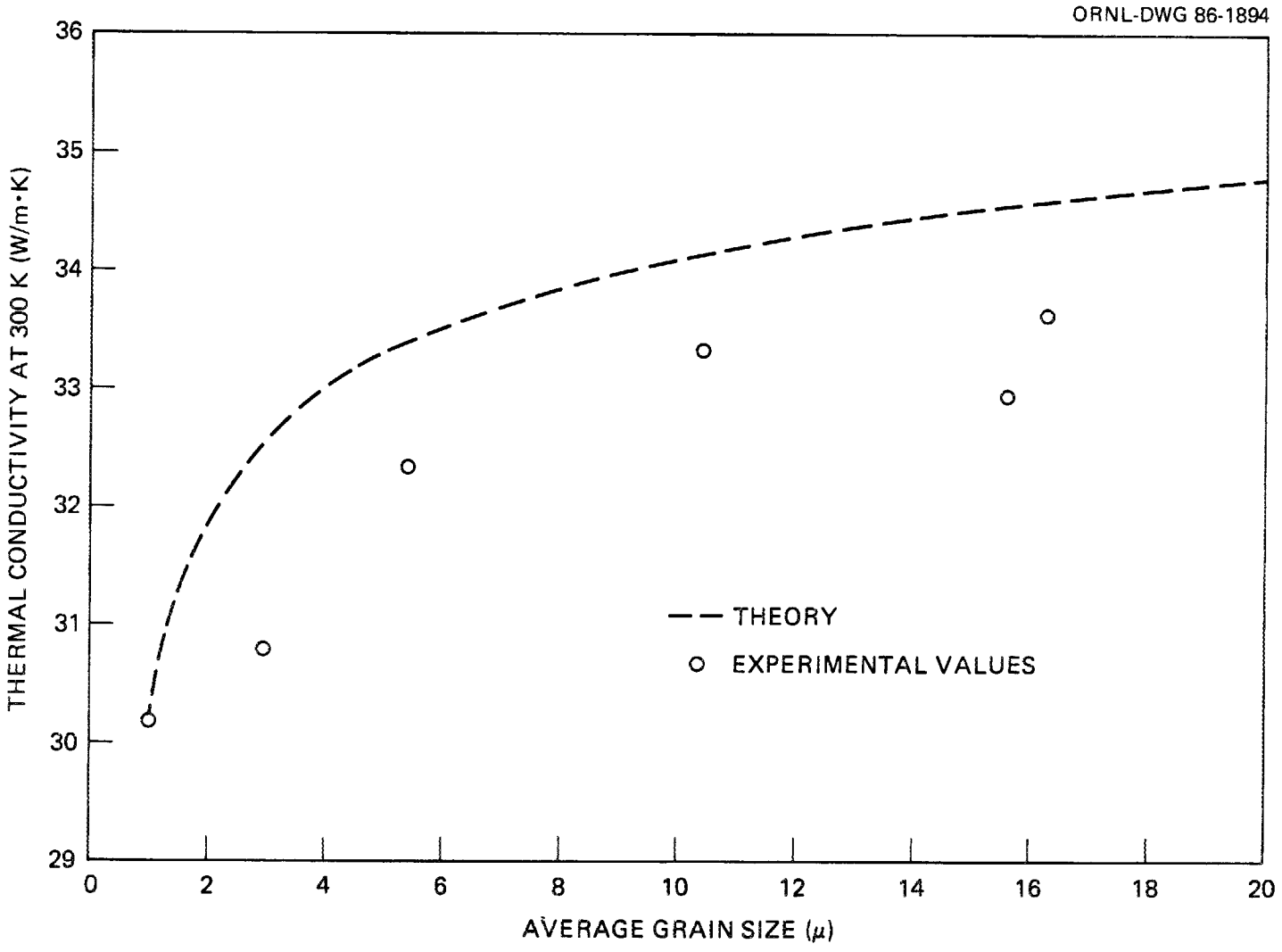

Fig. 1. Effect of grain size on the thermal conductivity of fully dense, high purity Al_2O_3. The theoretical curve is from ref. 2.

3.2 TIME-DEPENDENT BEHAVIOR

Characterization of Transformation-Toughened Ceramics
J. J. Swab (Army Materials Technology Laboratory)

Objective/Scope:

Because of their unusual combination of properties, transformation toughened zirconias (TTZ) are leading candidates for cylinder liners, piston caps, head plates, valve seats and other components for the adiabetic diesel engine. These materials are age-hardened ceramic alloy systems and as such, they are likely to be susceptible to overaging and loss of strength after long times at high temperatures (i.e., close to the age-hardening temperatures). The possibility of overaging with its likely negative impact on materials performance was identified as a critical area of ignorance in the preliminary technology assessment on ceramics for diesel engines previously prepared by AMMRC. Accordingly, a task was initiated to a) define the extent and magnitude of the overaging (if any) and b) develop toughened ceramic alloy systems which would not be susceptible to overaging at temperatures which may be encountered in advanced diesel engines (1000C-1200C).

Technical Progress:

During this period, six of the eight zirconias to be examined have been obtained and machined into bend bars. One of the materials will be received within the next two months and the final one will not be received because the manufacturer has informed me that his company can not supply me with the material.

Four of the materials are currently in various stages of evaluation. The other two have just been received from the machinist and no data is available. To date, the Hitachi zirconia has exhibited the best room temperature as-received strength, 1189MPa. See the attached table. (All strengths listed are characteristic strengths of the bend bars) However, there is a large scatter in the data over the 20 specimen range from a low of 277MPa to a high of 1453MPa. This material is now undergoing heat treatments of 100 and 500 hours at 1000C, to determine the affects of overaging on its strength.

Tests on the other zirconias have revealed that as expected, overaging reduces the material strength. The Kyocera material showed a strength loss of 40% after 100 hours at 1000C and 60% after 500 hours at 1000C when compared to the as-received strength. The AC Sparkplug zirconia exhibited strength losses of 10 and 11% while the Toshiba zirconia exhibited losses of only 7 and 9%. Both of the latter materials were subjected to heat treatments identical to the Kyocera material.

The Kyocera, Toshiba and AC Sparkplug zirconias are now undergoing post heat treatment characterization. This includes X-ray phase and chemical analysis, microstructural evaluation and microhardness.

At this time, fracture toughness evaluation of these zirconias has been put on hold. The reason for this is the controversy which surrounds the various test techniques and the data that is obtained from them. I am currently collaborating with other members of MTL to determine which test technique will be best suited for this program.

Status of Milestones:

Construction of three heat treatment furnaces has been completed.

Initiation of machining of the TTZ materials into bend bars has been started.

The final draft of the in-house technical report, authored by Lise Schioler, on the work done for the last three years has been edited and correstions are now being made.

Publications:

None

ZIRCONIA DATA TABLE

PROPERTY		MATERIAL / UNITS	KY	AC	TOSH	HIT
DENSITY:	COMPANY LISTING	g/cc	5.9	NDA	6.05	6.08
	AS-RECEIVED		5.853	5.840	5.880	6.038
	50 HRS @ 200C					
	100 HRS @ 1000C		5.803	5.853	5.884	
	500 HRS @ 1000C		5.772	5.863	5.877	
SONIC MOE:	COMPANY LISTING	GPa	206	NDA	180	209
	AS-RECEIVED		201	204	200	213
	50 HRS @ 200C					
	100 HRS @ 1000C		203	206	200	
	500 HRS @ 1000C		205	208	200	
MOR:	COMPANY LISTING	MPa	980a	NDA	900a	1000
(4-PT BEND)	AS-RECEIVED		750	753	630	1189
	50 HRS @ 200C					
	100 HRS @ 1000C		454	675	589	
	500 HRS @ 1000C		312	669	571	

KY - KYOCERA Z201
AC - AC SPARKPLUG
TOSH - TOSHIBA "TASZIC"
HIT - HITACHI

NDA - NO DATA AVAILABLE
a - BELIEVED TO BE 3-PT BEND RESULTS

Fracture Behavior of Toughened Ceramics

P. F. Becher and W. H. Warwick (Oak Ridge National Laboratory)

Objective/scope

Because of their excellent toughness, oxide ceramics such as partially stabilized zirconia (PSZ), dispersion-toughened alumina (DTA), and whisker-reinforced ceramics are prime candidates for many diesel engine components. The enhanced toughness of the PSZ and DTA materials is thought to be due to a stress-induced transformation (of the dispersed tetragonal ZrO_2 phase), which requires additional energy in order for catastrophic fracture to occur. However, these materials are still susceptible to strength degradation by slow crack growth. Also, there is limited evidence that at temperatures above 700°C, time-dependent aging effects can reduce the concentration of the phase involved in the transformation process leading to significant losses in toughness and strength. Again it is essential that mechanisms responsible for both the slow crack growth and aging behavior be well understood. Similarly the toughening behavior in whisker-reinforced ceramics and their high-temperature performance must be evaluated in order to develop materials for particular applications.

In response to these needs, studies have been initiated to examine toughening and fatigue properties of transformation-toughened and whisker-reinforced materials. Particular emphasis has been placed on understanding the effect of microstructure on processes responsible for time-dependent variations in toughness and high-temperature strength. In addition, fundamental insight into the slow crack growth behavior associated with these materials is being obtained.

Technical progress

SiC-whisker-reinforced ceramics

Thermal expansion data were obtained for hot pressed, fully dense SiC-whisker-reinforced composites having alumina as the matrix and for samples of General Electric Lucalox alumina and Carborundum sintered α-SiC. The SiC whiskers were predominately alpha phase SiC. The thermal expansion runs consisted of heating and cooling at a rate of 5°C/min in air employing a National Bureau of Standards (NBS) sapphire reference sample in a dual rod dilatometer.* The thermal expansion specimens for the SiC-whisker-reinforced ceramics were fabricated so that the axis of expansion was perpendicular to the axis of hot pressing in the original billet. As seen in Fig. 1, the extent of expansion due to heating in the alumina-based composites decreases with increasing SiC content as expected because the α-SiC has a lower mean linear thermal expansion coefficient than that of alumina (4.8×10^{-6}/°C and 8.2×10^{-6}/°C respectively) over the temperature range 22 to 1100°C. The mean linear thermal expansion coefficients for various alumina-based composites thus exhibit decreasing values with increase in SiC whisker content (Table 1).

*Dilatronic System, Theta Industries, Inc., Port Washington, N.Y.

Table 1. Linear thermal expansion coefficients ($\bar{\alpha}$) for various alumina–silicon carbide compositions

Material	Mean value of $\bar{\alpha}$, 10^{-6}/°C (22–1100°C)
Lucalox alumina	8.22
Alumina–10 vol % SiC whiskers	7.87
–20 vol % SiC whiskers	7.35
–30 vol % SiC whiskers	6.70
–60 vol % SiC whiskers	5.82
Sintered α-SiC	4.75

Studies of the interrupted static fatigue behavior at elevated temperatures in air of alumina–20 vol % SiC whiskers were initiated to examine the influence of oxidation and slow crack growth effects on the high-temperature strength. Also, recent results obtained by A. Chokshi of the University of Southern California show that the creep resistance in four-point flexure of the ORNL hot pressed alumina containing 20 vol % SiC whiskers is much greater than that of earlier samples (Al_2O_3–18 vol % SiC whiskers) supplied by ARCO.[1] For example, at 1600°C with an applied four-point flexure stress of 100 MPa, the creep strain rates were approximately 1×10^{-5}/s and approximately 4×10^{-7}/s, respectively for the ARCO and ORNL composites.

Partially stabilized zirconia

As discussed in previous reports, PSZ ceramics can exhibit quite high fracture toughness values to temperatures of at least 500°C. Recent studies demonstrate the practical aspects of this quite dramatically. The flexure strengths of as-polished bars with several 9.1-kg Vickers indents in the maximum tensile stress region of the bar (to introduce very large indents and associated cracks) were compared with the strengths of as-polished bars. In this way one can determine the real damage resistance of materials (i.e., how much the strength changes with additional surface damage). For example, highly polished and annealed single crystal alumina can exhibit four-point flexure strengths of approximately 650 MPa, but this is reduced to approximately 240 MPa with only the introduction of a 200-g Vickers indent in the tensile surface! This reflects the low critical fracture toughness (K_{IC} ~1.8 MPa $\sqrt{m}$) of the single crystal. Fine grained (≤5 μm) dense alumina (K_{IC} ~3.5 MPa $\sqrt{m}$) exhibits a loss in flexure strength from

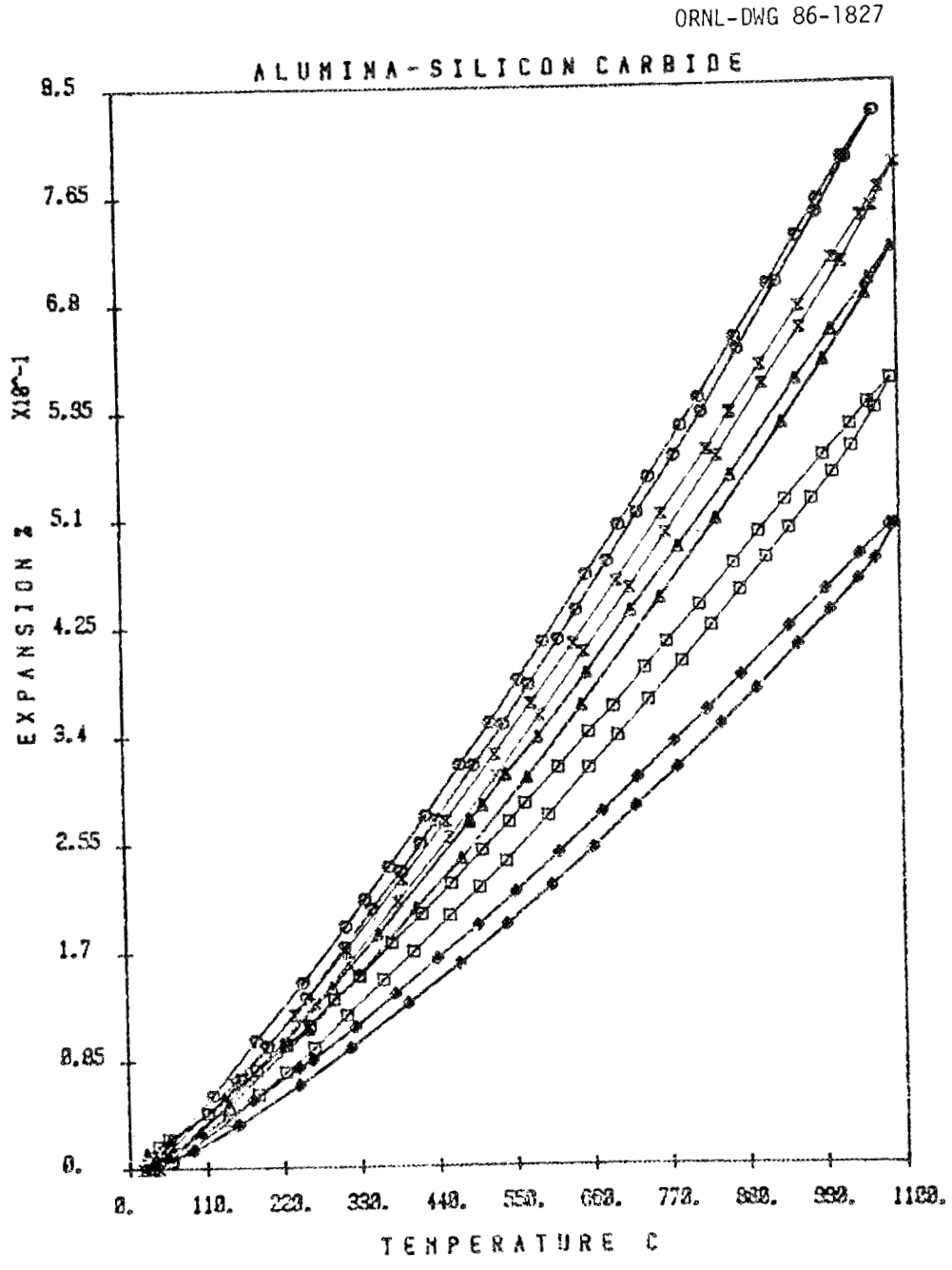

Fig. 1. Linear thermal expansion behavior of various alumina–silicon carbide compositions. Each sample was heated and cooled at 5°C/min in air, and its expansion was referenced against a National Bureau of Standards sapphire standard specimen that was run simultaneously. Samples consisted of the following: Lucalox (O), alumina–20 vol % SiC whiskers (X), alumina–30 vol % SiC whiskers (Δ), alumina–60 vol % SiC whiskers (□), and sintered α-SiC (◇).

500 MPa to 210 MPa when a 9.1-kg Vickers indent is used. Both materials exhibit large losses in strength because they have low toughness. Thus the flexure strengths are very sensitive to the cracks introduced by the Vickers indents.

Toughened PSZ ceramics on the other hand exhibit little loss in flexure strength with the introduction of large Vickers indents and associated cracks. A PSZ ceramic with K_{IC} of 17.5 MPa $\sqrt{m}$ still exhibited a fracture strength of 665 MPa or more when a series of 20-kg Vickers indents were introduced into the tensile surface.

As seen in Fig. 2, the flexure strength of other PSZ ceramics ($K_{IC} \geq 12$ MPa $\sqrt{m}$) are essentially the same whether the polished tensile surface contains 9.1-kg Vickers indents or not. This lack of significant strength degradation with additional surface damage is a result of the high fracture toughness. This is reflected by the significant strength loss (~two-fold reduction) incurred by indenting the tensile surface for strengths obtained at 800°C or more where transformation toughening does not occur and K_{IC} is low (~3 MPa $\sqrt{m}$), Fig. 3. In the temperature range below 800°C, where transformation toughening occurs, K_{IC} is at least 8 MPa $\sqrt{m}$, the flexure strengths are not degraded by the surface damage produced by the Vickers indents.

Status of milestones

None.

Publications

None.

Reference

1. A. H. Chokshi, University of Southern California, personal communication, 1986.

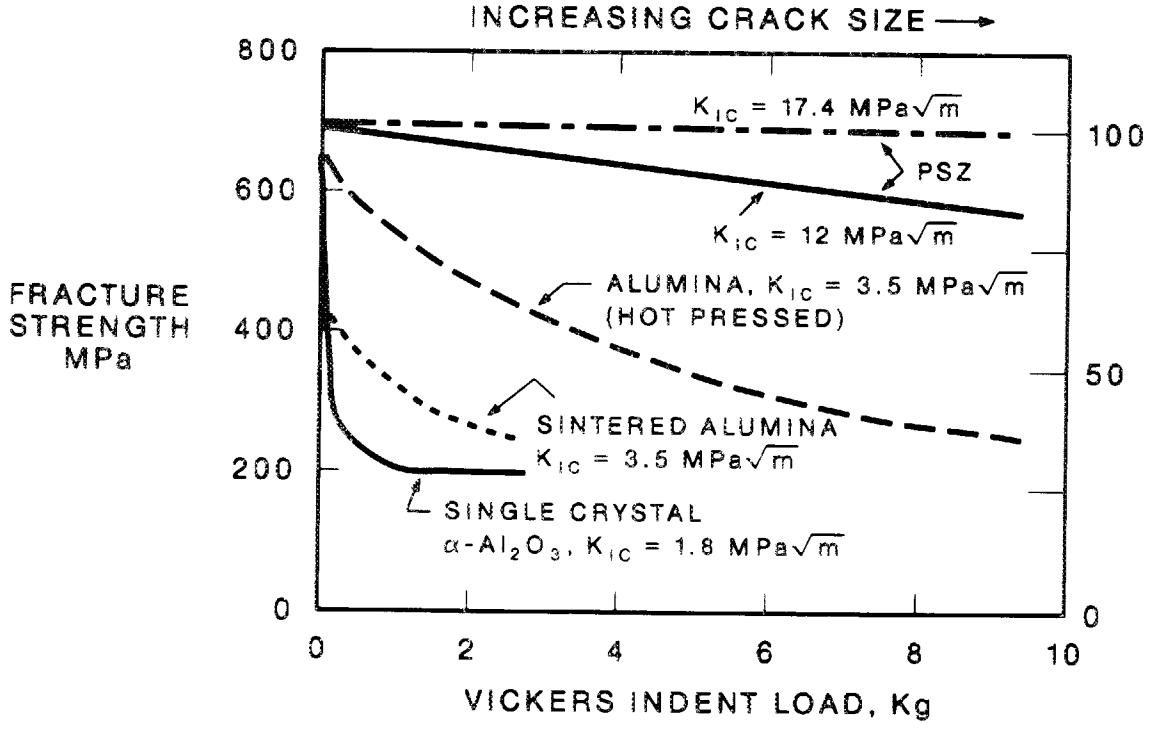

Fig. 2. Toughened ceramics retain high fracture strengths even when subjected to surface damage. The benefit of transformation toughening in PSZ ceramics is indicated by minimal loss in fracture strength when the crack size introduced by Vickers indentation is increased. Conventional ceramics exhibit continuous loss in fracture strength when larger surface cracks are introduced by Vickers indentation.

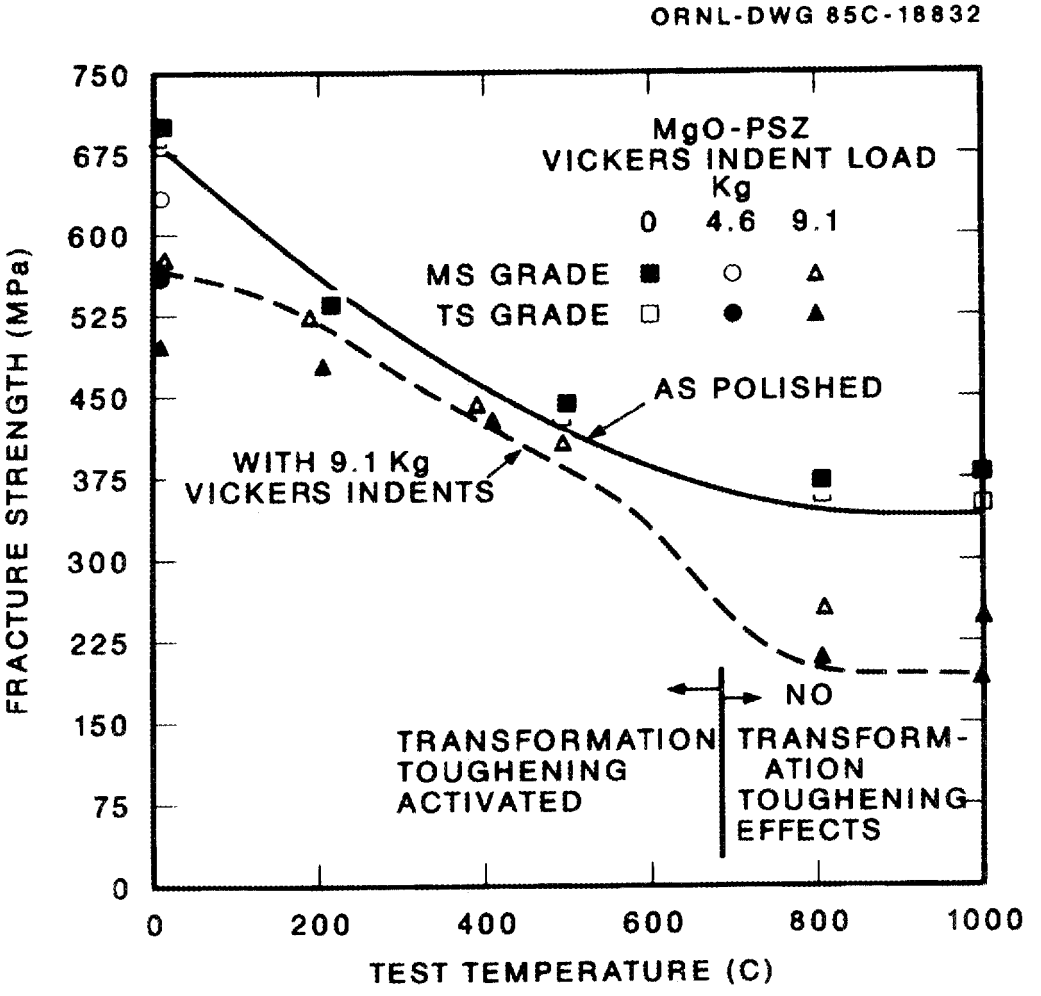

Fig. 3. The fracture strengths of partially stabilized ZrO_2 ceramics are quite insensitive to surface damage. At 500°C or less, the four-point flexure strengths of MS and TS Grades of PSZ (K_{IC} ≥12 MPa $\sqrt{m}$ at 22°C) are not substantially lowered when high-load (4.6 and 9.1 kg) Vickers indents are introduced in the tensile surfaces. In this temperature range, the PSZ ceramics exhibit transformation toughening (K_{IC} ≥8 MPa $\sqrt{m}$ at ≤500°C). At 800°C and higher, the strengths are lowered approximately two-fold consistent with the absence of transformation toughening (K_{IC} ~3 MPa $\sqrt{m}$).

Cyclic Fatigue of Toughened Ceramics

K. C. Liu and C. R. Brinkman (Oak Ridge National Laboratory)

Objective/scope

The objective of this task activity is to develop, design, fabricate, and demonstrate the capability of performing tension-tension dynamic fatigue testing on a uniaxially loaded ceramic specimen at elevated temperatures.

Three areas of research have been identified as the main thrust of this task: (1) design, fabrication, and demonstration of a load train column that truly aligns with the line of specimen loading; (2) development of a simple specimen grip that can effectively link the load train and test specimen without complicating the specimen geometry and, hence, minimize the cost of the test specimen; and (3) design and analysis of a specimen for tensile cyclic fatigue testing.

Technical progress

Room-temperature fatigue testing of aluminum oxide

Material and specimens. Commercially available Al_2O_3 was used as a model brittle material for the purpose of demonstration and evaluation of room-temperature test capabilities of the dynamic fatigue loading grips developed recently. This material was procured in the form of rods from Coors Porcelain Company in two grades with 96 and 99.8% nominal purity, respectively.

Uniform gage tensile specimens were fabricated with 1/4-in. (6.3-mm) gage diameter and 1-in. (25.4-mm) gage length as shown in Fig. 1. Specimens with 5/8-in.-diam (16-mm) shanks were made from 3/4-in. (19.1-mm) rods and those with 0.394-in.-diam (10-mm) shanks from 5/8-in. (16-mm) rods. The basic geometry and dimensions were the same in the gage section. The use of two sizes was for trial testing to determine the optimal design of the shank and buttonhead. Substantial savings in both material and machining costs can be realized if the specimens can be made from smaller rods.

Specimens were ground circumferentially to the final dimensions except the reduced gage section. All circumferential marks in the gage section were removed at the final grinding along the axis to a surface finish of about 16 rms or better. They were then radiographed and inspected with liquid fluorescent penetrant for internal and surface defects. Deeper axial marks were then removed by hand polishing with diamond paste. Specimens were photographed as shown in Fig. 1 with the fluorescent penetrant illuminated by ultraviolet light for defect identifications and reference after testing.

Tests were performed in a tension-tension cyclic fatigue mode with an R-ratio of 0.075 by using a servocontrolled electrohydraulic testing machine in load control. Strain control is possible if necessary. Strains were measured by strain gages for a limited number of specimens, and a mechanical extensometer was used in other tests. Noncontact optical strain extensometry is being investigated for future test applications in high-temperature environments. Other experimental details were discussed in the previous progress report.

YP-1325

Fig. 1. Aluminum oxide fatigue specimens highlighted by fluorescent penetrant with ultraviolet light.

Tests conducted on 96% pure alumina (Coors AD-96). Seven tests were carried out successfully to completion, excluding specimen 9 which ruptured at the root of the buttonhead. Good specimen alignment was observed from cyclic loading of strain-gaged specimens, indicating that the self-aligning grip system was working well. Test results are summarized in Table 1 and plotted in Fig. 2. Specimens 3 and 9 were tested in pure tension and were assumed to have failed in a single cycle. The tensile strength of specimen 9 would have been higher if it had not failed prematurely, i.e., buttonhead root failure. Fatigue testing was completed via multiple step loading for specimens 2 and 7. In the case of specimen 2, it was obvious that the first cyclic load was too low to result in failure in a reasonable time period. Therefore, the stress was increased from 20.37 ksi (140 MPa) to 30.56 ksi (211 MPa) in the second step loading, which resulted in failure of the specimen in 4,445 cycles. Interestingly, specimen 6, which was cycled to 30.56 ksi (211 MPa) continually throughout the test, failed at 4,025 cycles, about the same as the fatigue lifetime of specimen 2. However, the test on specimen 7, whose loading conditions were intended to duplicate the 30.56-ksi (211-MPa) cyclic tests in loading step 2, outperformed both specimens 2 and 6 by a factor of about six to the point where the test was discontinued. Subsequently, the cyclic load was increased to 35.7 ksi (246 MPa) and the specimen failed at 450 cycles.

A fatigue lifetime curve drawn visually through the data as shown in Fig. 2 strongly suggests the existence of endurance limit. The reasons for the high cycle fatigue life of specimen 7 are unknown. However, the test results appear to indicate that a series of cyclic step loads below a critical value has little or no detrimental effect on subsequent fatigue life. This observation is only weakly supported by test results obtained from specimen 2.

The material supplier's published data as indicated in Fig. 2 were used as references for comparison with the ORNL data. A direct comparison can not be made for the tensile strength because Coors' tensile strength reported as 28 ksi (193 MPa) was obtained from the average value of lateral compression tests using cylindrical specimens that were in a strict sense under a biaxial stress state. However, an indirect comparison shows that the ORNL tensile strength data of 46 ksi (317 MPa) falls only moderately below the flexural strength of 52 ksi (359 MPa) reported by Coors.

The fracture surface of specimen 3 was examined by scanning electron microscopy (SEM). The surface morphology shown in Fig. 3 suggests that the tensile failure was initiated from a surface defect denoted by an arrow in Fig. 3(*a*). More detailed features of the surface defect are shown in Fig. 3(*b*). The size and shape of internal porosity are not uniform, but the pores are distributed relatively evenly. The mode of the tensile fracture was transgranular failure.

Figures 4(*a*) and (*b*) are fractographs of specimen 6, which failed by cyclic fatigue. The topological morphology suggests that the fatigue failure might have initiated from the subsurface indicated by an open arrow in Fig. 4(*a*). A close-up view of the area is shown in Fig. 4(*b*). The grain boundary structure and failure mode observed in the lower half of Fig. 4(*b*) and that observed in Fig. 3(*b*) are very similar. No cracking is visible along the grain boundaries, which are only vaguely discernable. In contrast, the grain boundary structure shown in the upper half of Fig. 4(*b*) is well defined, and grain boundary cracks are clearly visible. Some of the fracture failure appeared to be intergranular in nature.

Table 1. Results of tensile and cyclic fatigue tests of Coors aluminum oxide at room temperature

Specimen	Load level	Loading stress (ksi)	(MPa)	Number of cycles	Cycles to failure
		96% Purity			
3	1	46.04	317		1
9[a]	1	>43.29	298		1
5	1	41.35	285		4
6	1	30.56	211		4,025
2	1	20.37	140	30,124	
	2	30.56	211		4,445
7	1	25.47	176	52,830	
	2	30.56	211	24,310	
	3	35.7	246		450
4	1	29.03	200		30,482
8	1	29.54	204		699,982
		99.8% Purity			
20	1	39.73	274		1
18	1	43.8	302		1
17	1	38.3	264		42
13	1	34.63	239		9,179
11	1	33.1	228		2,935
12	1	30.05	207		115,418
14	1	29.54	204		399,861

[a]Fracture failure occurred at the root of specimen buttonhead.

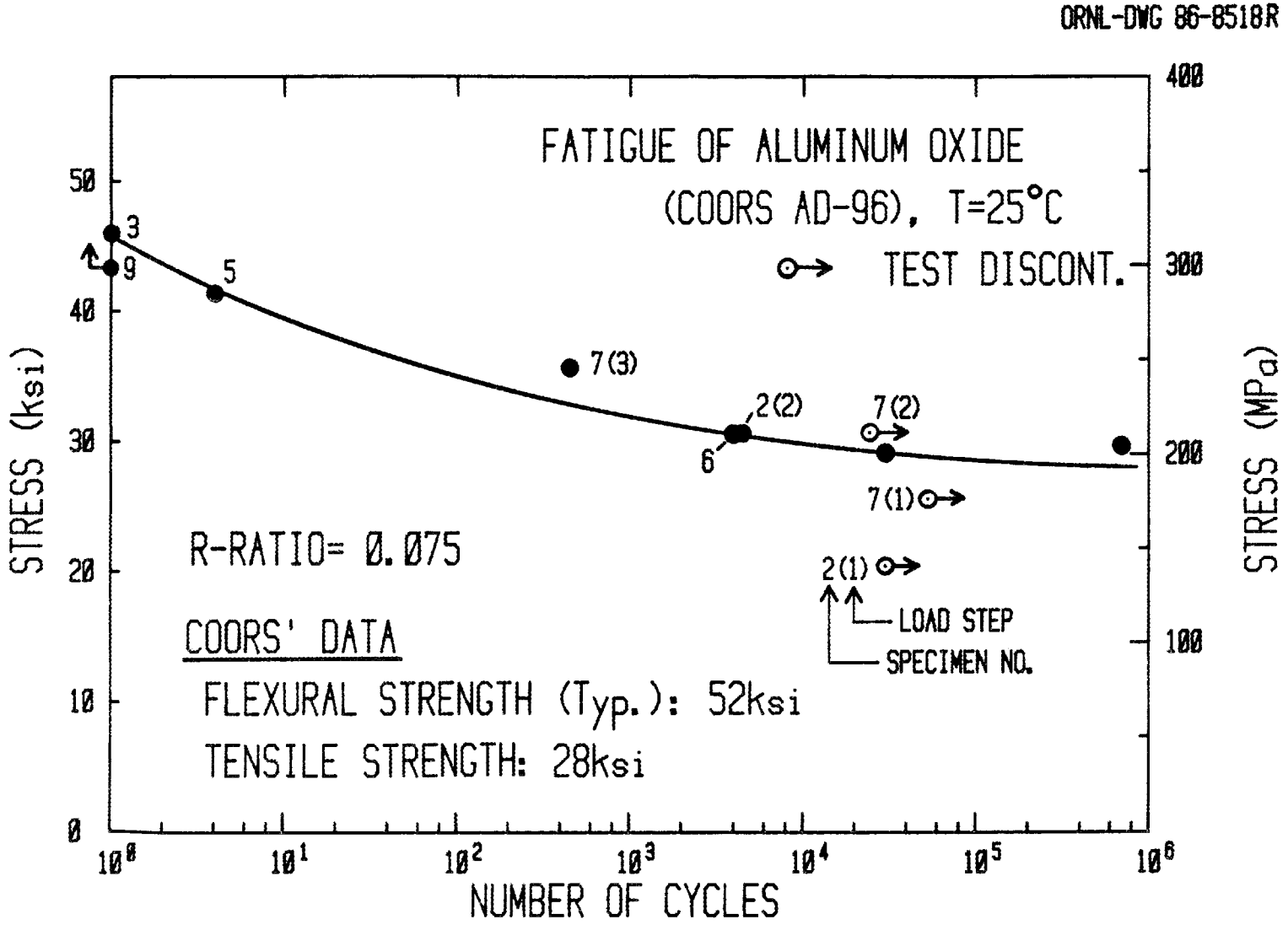

Fig. 2. Fatigue behavior of Al_2O_3 (Coors AD-96) tested at room temperature.

M22731

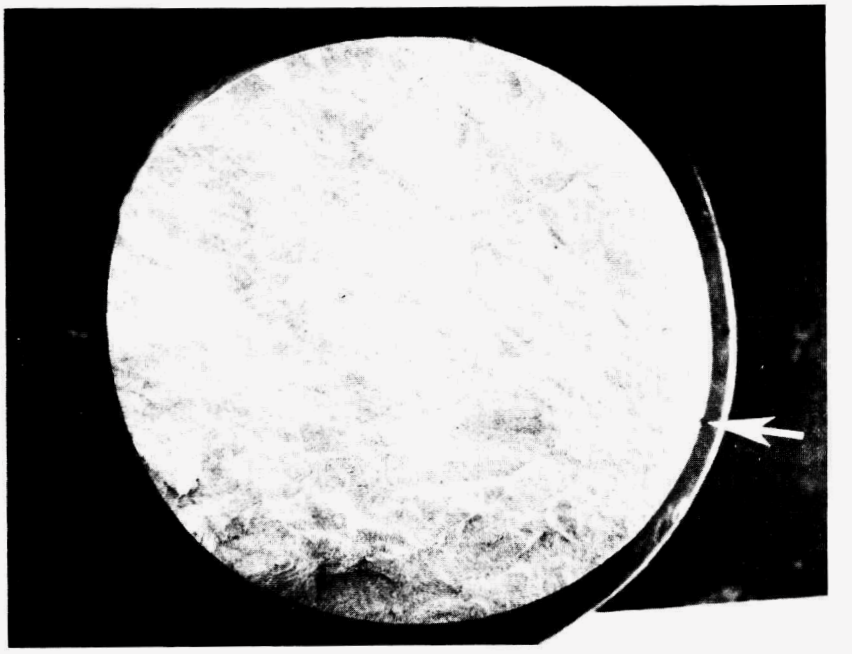

(*a*) 1 mm

M22734

(*b*) 50 μm

Fig. 3. Fractographs of specimen 3 tested in pure tension.

M22735

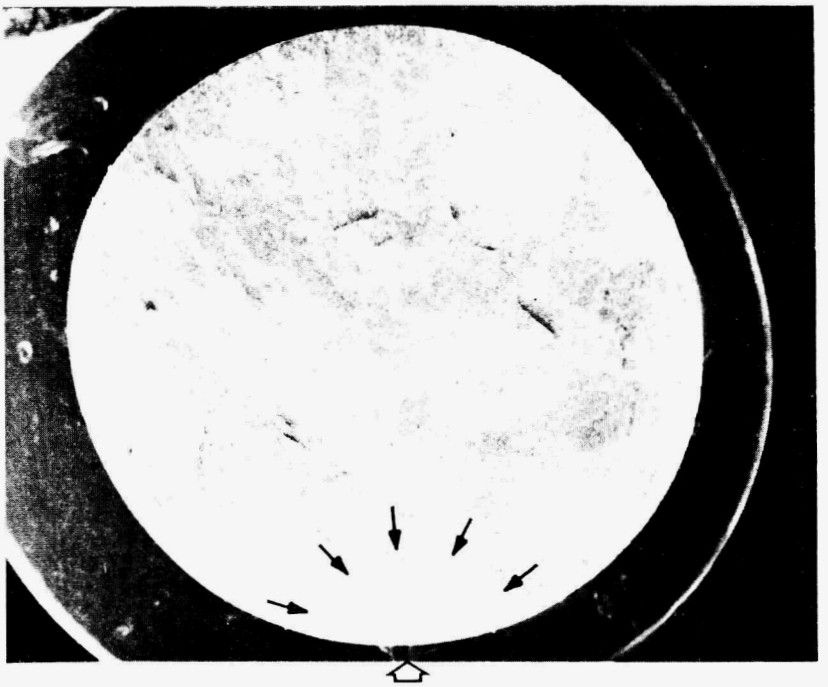

(*a*) 1 mm

M22737

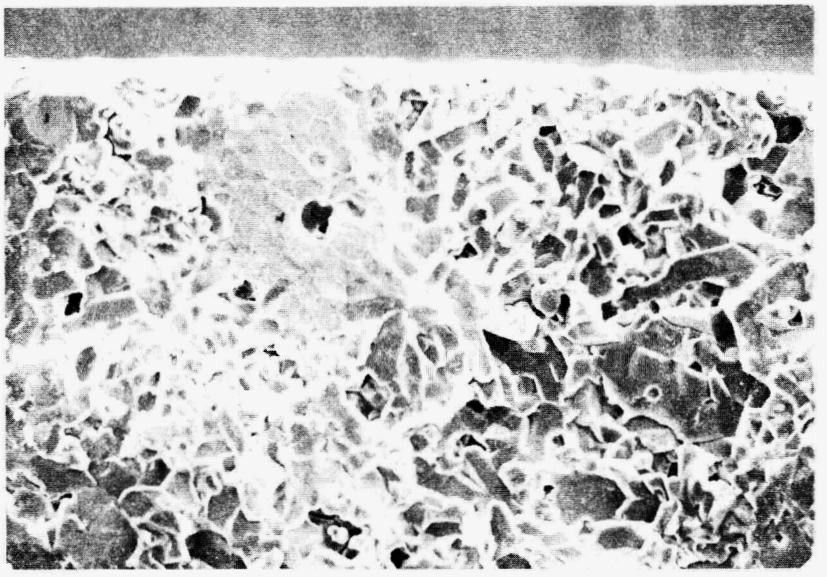

(*b*) 50 μm

Fig. 4. Fractographs of specimen 6 tested in tension-tension cyclic fatigue.

Tests Conducted on 99.8% Pure Alumina (Coors AD-998). A matrix consisting of seven fatigue tests was performed for AD-998 Al_2O_3. Test conditions and results are tabulated in Table 1. To facilitate comparison, all data including those of AD-96 are plotted in the same diagram (Fig. 5). The fatigue lifetime curve of AD-998 was determined by a visual method also because the nonlinear curve fitting capability was not available. The fatigue properties are about the same for both materials in the high cycle range with a slight indication of AD-998 having a higher fatigue life. In contrast, the tensile strength of AD-998 was about 10 to 14% lower than that of AD-96. An exceptionally high fatigue performance is seen for spec-imen 13, and perhaps for specimen 7 also; both data points fall high above the average fatigue lifetime curve of the respective material. Reasons will not be known until SEM studies are complete.

Data scatter is common in results from multiple fatigue experiments. Therefore, data are often treated statistically to characterize fatigue behavior. Fatigue experiments on brittle materials are more difficult to analyze because the materials contain many defects that can cause premature failure. Taken in this light, the amount of data scatter observed in Fig. 5 is about the same as that observed in data obtained from carefully conducted tests on metallic specimens. Furthermore, the consistency of test results appears to suggest that the self-aligning dynamic grips are reliable and that meaningful fatigue data can be generated for advanced structural ceramics.

It is worthwhile to note that the fatigue behavior of Al_2O_3 in the log-log plot of stress and number of cycles to failure (N_f) is similar in form to that observed for most metal alloys. The latter is usually represented by a two-term power-law equation as a function of elastic and plastic strains. The low-cycle range is governed by the plastic strain and the high-cycle range by the elastic strain. However, the same mathematical formulation is not appropriate in describing the fatigue behavior of Al_2O_3, because the fatigue failure of most ceramics at room temperature occurs in the elastic range. An equation of the form $\sigma = AN_f^a + B$ will be used to fit the data upon completion of test activity at room temperature.

High-temperature testing system

The final design of a load train column assembly for high-temperature testing has been completed. An isometric cutaway view of the assembly is shown in Fig. 6. The lower pull rod assembly is not shown in the figure. A ceramic rod (3) is used as an extension of the water-cooled metal pull rod. The buttonhead specimen (5) is held concentrically to a bushing (2) with a tapered split collar (1). Snug fitting is essential between the inner diameter of the bushing (2) and the extension rod (3) in order to make concentric load transfer via the horizontal pin (4). Fixtures 1 through 4 used inside the heating zone will be made of high-performance silicon carbide or silicon nitride.

A high-temperature furnace capable of heating the specimen to 1500°C, as shown schematically in Fig. 6, has been designed and is being ordered.

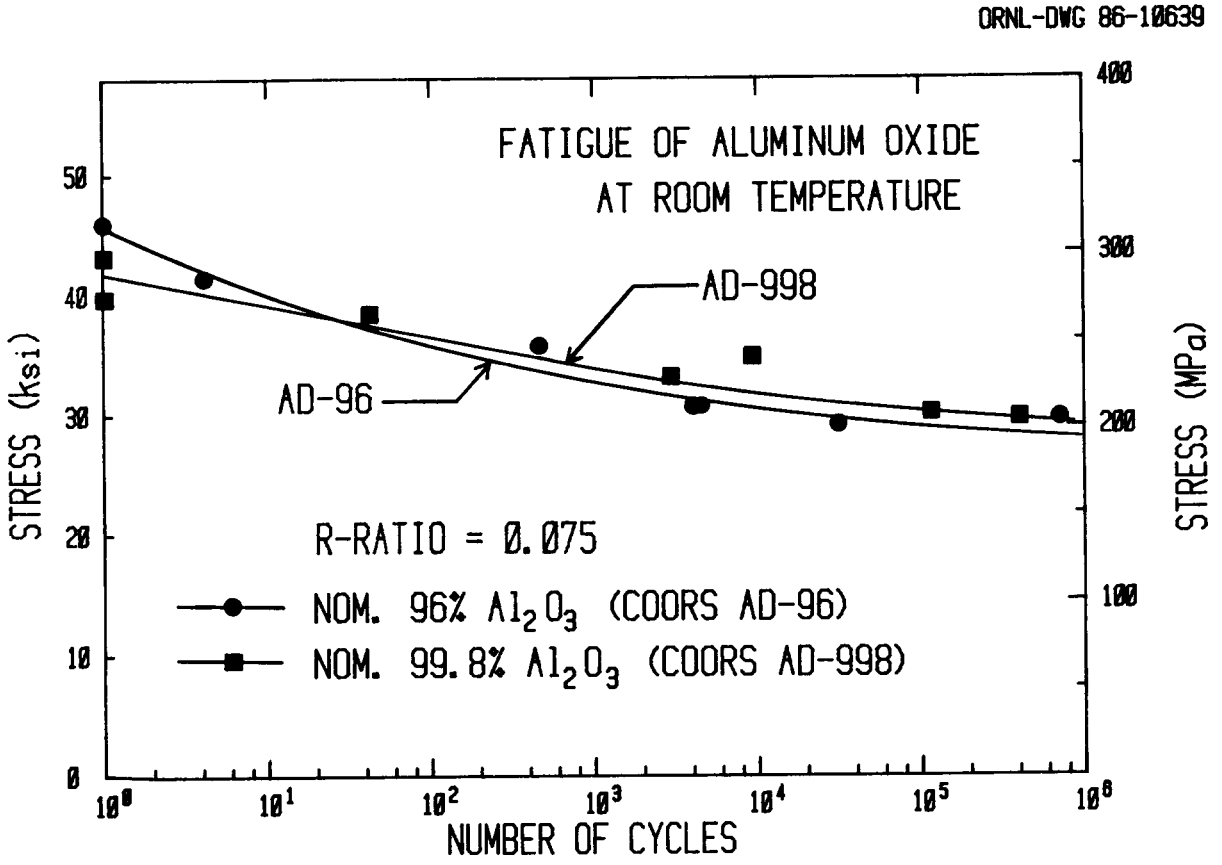

Fig. 5. Comparison between fatigue behavior of Al_2O_3 with 96% purity and that of Al_2O_3 with 99.8% purity, tested at room temperature.

ORNL-DWG 86-10640

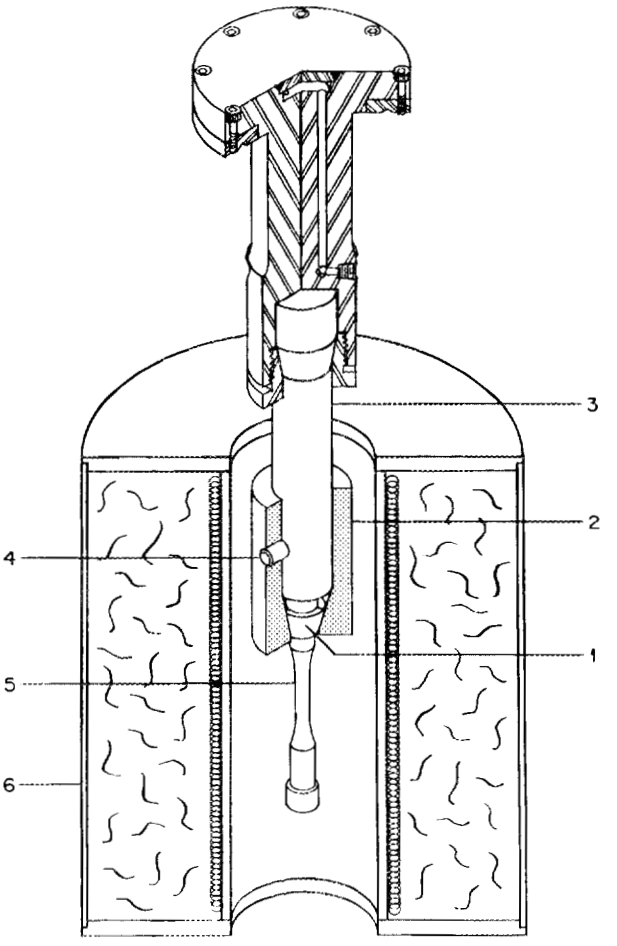

Fig. 6. Schematic diagram of apparatus for tensile fatigue testing of structural ceramics at high temperature.

Important findings and observations

Aluminum oxide specimens have been successfully tested in cyclic tension with results suggesting that the existence of fatigue endurance limit is highly probable for this material at room temperature. The results further suggest that the self-aligning grip system is reliable and that meaningful fatigue data can be generated.

Status of milestones

Milestone 321402 was completed as scheduled (evaluation of room-temperature test capabilities of dynamic loading grips and design of elevated-temperature heating systems).

Publications

A paper titled "Tensile Cyclic Fatigue of Structural Ceramics," by K. C. Liu and C. R. Brinkman, was presented to the 23rd Automotive Technology Development Contractors' Coordination Meeting on October 23, 1985, at Dearborn, Michigan. The final manuscript has been submitted for publication in the conference proceedings.

3.3 ENVIRONMENTAL EFFECTS

Static Behavior of Toughened Ceramics

M. K. Ferber, T. Hine, and G. Zeigler (University of Illinois)

Objective/Scope

The objective of this program is to study the long-term mechanical stability of toughened ceramics for diesel engine applications. The work is divided into the two tasks. The first involves the measurement of the time-dependent strength behavior of ceramic bend-bar samples as a function of temperature and applied stress using the Interrupted Fatigue (I.F.) method. Although a variety of candidate engine materials will be examined, current studies are focusing upon commercially available partially stabilized zirconia (PSZ). In the second task, the microstructures of selected I.F. specimens will be characterized using SEM and TEM. In addition, x-ray diffraction and dilatometry studies will be conducted to examine changes in the transformation behavior of the PSZ ceramics resulting from the high-temperature exposure.

Technical Progress

(a) Procedure

Two commercial Mg-PSZ ceramics* designated TS PSZ (thermal shock grade) and MS PSZ (maximum strength grade/1983) were chosen for initial testing since both are prime candidates for use as prototype diesel engine components.[1] Both 1983 and 1984 vintages of the TS PSZ (designated TS (83) and TS (84)) were examined. Starting materials were obtained in the form of either circular discs 100 mm in diameter and 7.6 mm thick or rectangular plates (101.6 x 101.6 x 6.35 mm). Rectangular bend specimens (25.4 X 2.82 X 2.5 mm) were then machined from these shapes for subsequent mechanical property studies. The tensile surface of each sample was polished to a 0.25 μm finish and the edges beveled using a 6 μm diamond wheel.

The fatigue behavior was determined using an interrupted fatigue (I.F.) technique in which the four-point bend strength S_f was measured as a function of time (τ), temperature (T), and applied stress (σ_a). This method has several advantages over conventional static fatigue[a] testing. First, since time is a controllable quantity, problems associated with an unpredictable fatigue life (as in the case of static fatigue) are avoided. In the present study, this feature allowed for periodic examination of test specimens so that changes in both phase composition and transformation characteristics could be ascertained. A second advantage is that processes responsible for both strength degradation and strength enhancement can be readily distinguished.[2]

*Manufactured by Nilcra Ceramics, USA Office, Glendale Heights, Illinois.

I.F. studies involving both materials were conducted at temperatures of 500, 800, and 1000°C for exposure times ranging from 1 to 1008 h. The baseline data were established using specimens subjected to a zero stress level. Subsequent tests were then performed with σ_a equal to 60% of the fast fracture strength (i.e. 60% of S_f value measured at the same T for τ = 1 h and σ_a = 0). For each test condition, S_f was determined at temperature by fracturing three or more samples. All testing was conducted in a specially designed Flexure Test System (F.T.S.) capable of holding up to three bend samples.* The general layout and operation of the F.T.S. is discussed elsewhere.[3]

Several techniques were used to characterize both the as-received and tested I.F. samples. For example, the microstructures were examined using both standard ceramographic methods, TEM, and SEM. The latter technique allowed for characterization of fracture surfaces. The volume fractions of the cubic (c), tetragonal (t), and monoclinic (m) phases were also determined from x-ray diffraction and Raman spectroscopy studies. The expansion-contraction characteristics of selected I.F. samples were measured using a standard pushrod dilatometer. The resulting data (percent elongation versus temperature) were used to examine changes in the (t)-(m) transformation characteristics arising from the high-temperature exposure.

(b) As-Received Materials

The microstructures of the TS and MS PSZ ceramics generally consisted of 30-50 μm grains containing fine (<0.1 X 0.4 μm) (t) precipitates. An x-ray analysis of the polished surfaces of the as-received materials gave (m) volume fractions (V_f^m) of 0.16 and 0.9, respectively. The calculations were based on equations given in Ref. 4. Unfortunately the volume fractions for the (c) and (t) phases (V_f^c and V_f^t) could not be determined using this technique because of overlapping of the cubic (111) tetragonal (101) peaks. However, additional Raman spectrographic studies provided independent estimates of the V_f^t/V_f^m ratios. These numbers were then used in conjunction with the x-ray data to yield the approximate phase analysis:

$$\text{TS PSZ:}\quad V_f^c = 0.64;\ V_f^t = 0.20;\ V_f^m = 0.16$$

$$\text{MS PSZ:}\quad V_f^c = 0.65;\ V_f^t = 0.26;\ V_f^m = 0.09$$

These results agree favorably with those reported by the vendor and determined in independent investigations.[5]

Results from the I.F. measurements for the TS(83) PSZ are shown in Fig. 1(a) and (b). At 500°C (σ_a = 248 MPa) the strength did not change appreciably for exposure times up to 1008 h (Fig. 1(a)). However, when the T was raised to 800°C (σ_a = 207 MPa), S_f increased significantly for

*The F.T.S. design is based on a similar system originally developed by S. M. Wiederhorn and N. J. Tighe of the National Bureau of Standards.

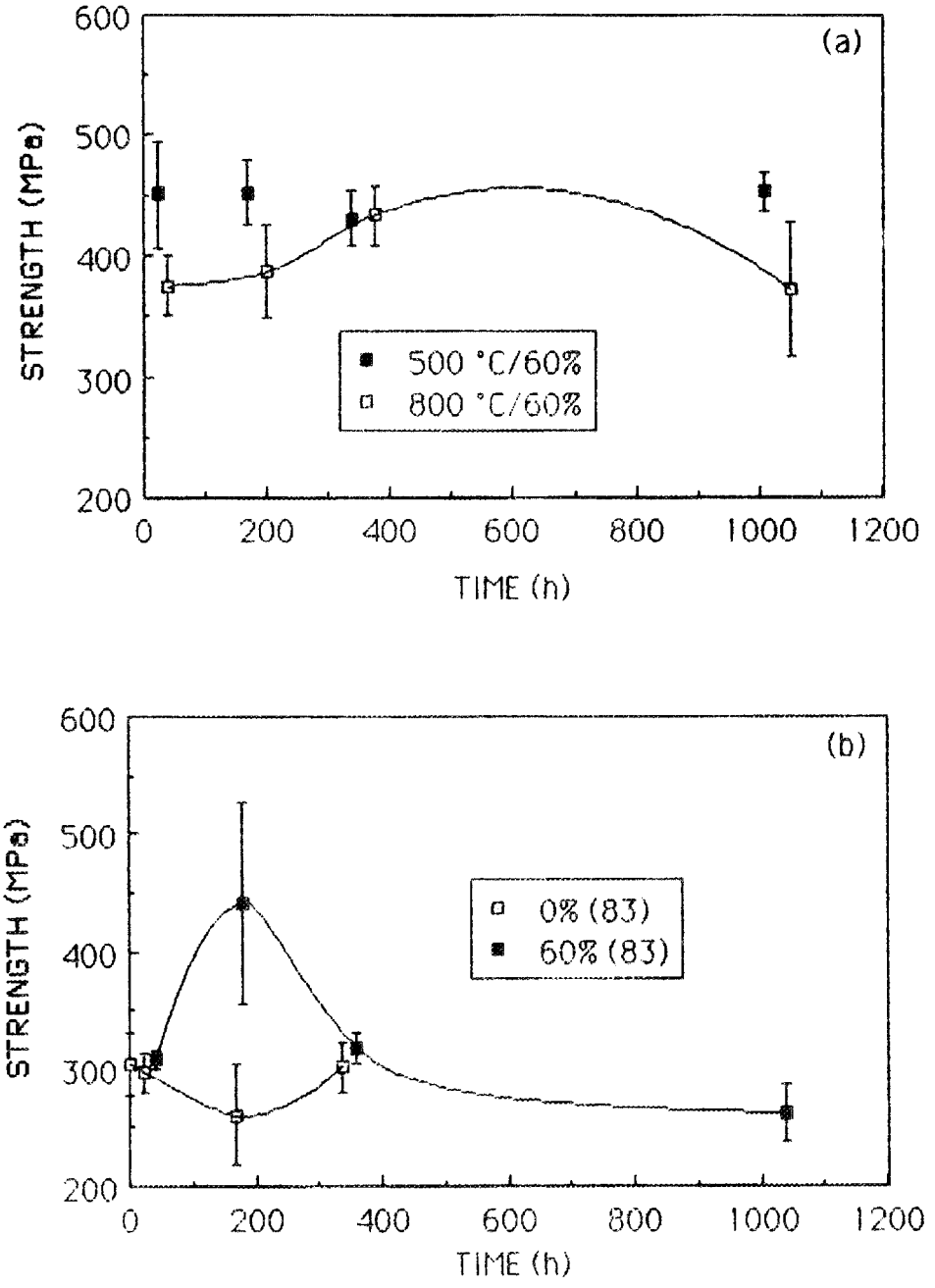

Figure 1. Strength behavior obtained for TS(83) PSZ at 500°C (a) was insensitive to time while data obtained at 800°C (a) and 1000°C (b) gave evidence of an applied stress dependence.

t< 200 h and then decreased to 373 +/- 56 MPa for τ = 1008 h. Therefore S_f measured at 800°C exhibited a definite maximum with increasing exposure time.

Similar behavior was observed when the TS(83) samples were stressed (σ_a = 172 MPa) at 1000°C (Fig. 1(b)). In this case the average strength after 1008 h was only 85% of it's initial short-term value (τ = 24 h). A few I.F. measurements at 1000°C were also conducted using σ_a = 241 MPa. In this case all samples fractured prematurely within ~5h (300 s). When no stress was applied, the strength did not change significantly, at least to 360 h, the extent of present data. These results suggest that for T $\geq$ 800°C, the applied stress level can have a dramatic affect upon the long-term mechanical behavior.

The reproducibility of the I.F. data was examined by testing a second group of TS(84) samples at 1000°C. The general trends (Fig. 2) were very similar to those for the 1983 vintage specimens. The only apparent difference was that the maximum in the TS(84) curve for the stressed samples occurred at a slightly longer exposure time. This discrepancy may have been due to differences in the short term (τ = 0.5 h) strength: 304 +/- 26 MPa for TS(83) and 375 +/- 20 MPa for TS(84).

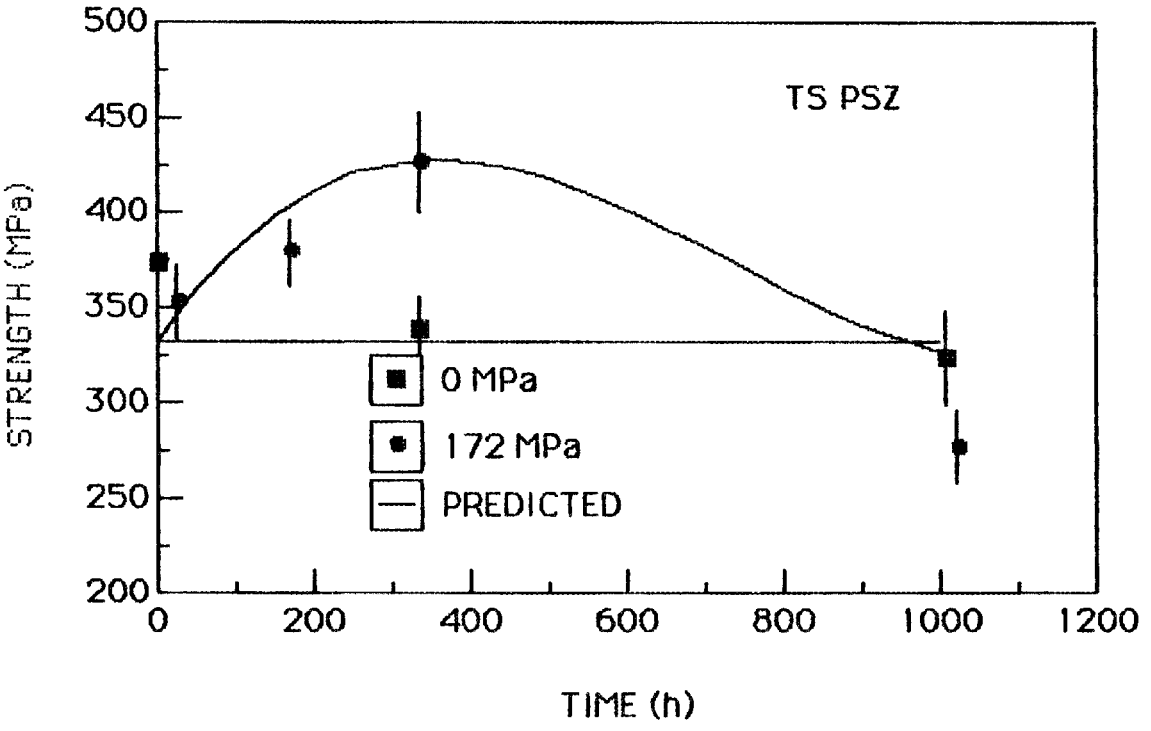

Figure 2. I.F. behavior for TS(84) PSZ was similar to that of TS(83) materials. Note the solid lines in this figure are model predictions.

The I.F. data for the MS PSZ samples tested at 800 and 1000°C are illustrated in Figs. 3(a) and (b), respectively. At 800°C, the strength at both the 0% and 60% stress levels exhibited a short-term increase and then was relatively independent of time. The extent of this increase in S_f was only marginally dependent upon the stress level; the strength being slightly greater for the stressed samples (σ_a = 207 MPa) at all values of τ. The I.F. data at 1000°C (Fig. 3(b)) revealed a modest strength maximum at $\tau \approx 200$ h for both the stressed and unstressed samples. At longer exposure times, S_f for the 0% stress level dropped well below the starting strength.

X-ray analyses of the polished surfaces of fractured MS and TS specimens were used to determine the volume fraction of (m). Results for tests conducted at 1000°C are summarized in Fig. 4(a) and (b). In general V_f^m increased significantly with increasing exposure time. Furthermore, the data for the TS(83) material suggest that the magnitude of V_f^m for a given τ was significantly greater when a stress was applied. However, the stress dependency for (m) formation in the TS(84) and MS PSZ ceramics was minimal. The reasons for these differences are unclear.

The fact that V_f^m values often exceeded the V_f^t for the as-received ceramics indicates that both the (c) and (t) phases were involved in the (m) formation. Recent aging studies conducted at 1100°C[6-9] have shown that at least two types of reactions can lead to the generation of the (m) phase. The first is the eutectoid decomposition of the MgO-stabilized (c) matrix;

$$Mg\text{-}ZrO_2\ (c) \rightarrow ZrO_2\ (m) + MgO. \qquad (1)$$

This reaction generally initiates along grain boundaries and then slowly consumes the (c) phase within grain interiors. The resulting (m) phase has a typical grain size of 1-5 μm.[8,9] The thermal expansion anisotropy associated with these (m) grains can promote extensive microcracking upon cooling. This microcracking is also facilitated by thermal expansion differences between the (m) grains and surrounding matrix.

The second type of reaction involves the formation of an ordered anion vacancy δ-phase ($Mg_2Zr_5O_{12}$) within the region between adjacent (t) precipitates.[5-8] The δ-phase nucleates at the (t)-(c) interface and then grows into the (c) matrix due to short-range diffusion of Mg. The interfacial strains which accompany this δ-phase reaction can destroy the precipitate coherency and thus promote the (t) to (m) transition upon cooling. This results in an increase in the M_s temperature. The presence of these destabilized precipitates at relatively low concentration levels can lead to improved thermal shock resistance without significantly sacrificing strength and toughness.[6-8]

SEM and optical examinations of the polished (tensile) surfaces of several fractured TS(83) samples (tested at 1000°C) gave additional evidence for the eutectoid decomposition reaction. As shown in Fig. 5, extensive formation of the (m) phase occurred in the specimen exposed for 1008 h at the 60% stress level. The (m) grain size was in the 1-5 μm range in agreement with previous studies.[5-7] Numerous microcracks were also observed particularly in regions containing a high density of (m) grains. In general, the concentration of this (m) phase diminished as the

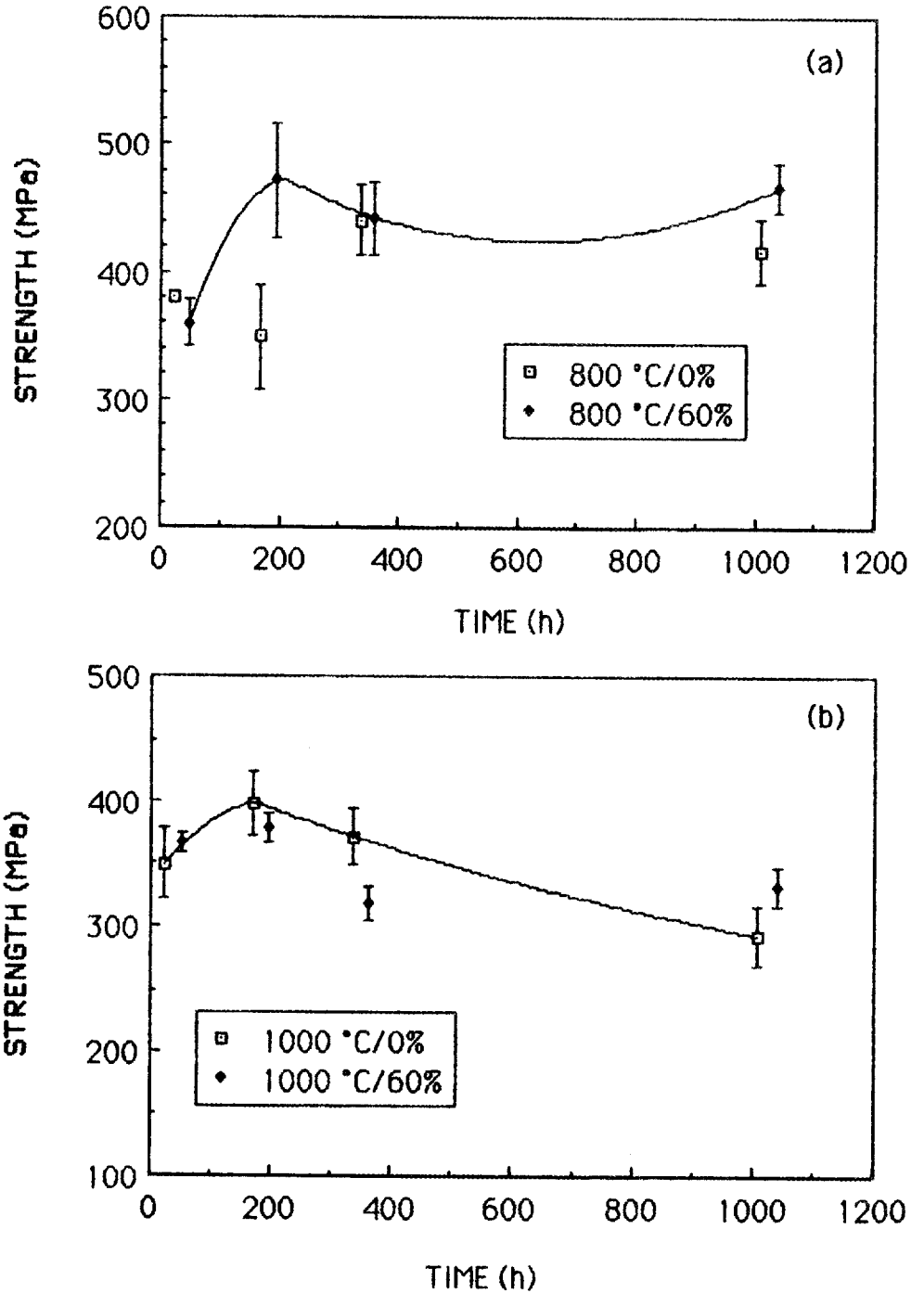

Figure 3. The stress dependency of fracture strength for MS PSZ at both 800°C (a) and 1000°C (b) was less pronounced.

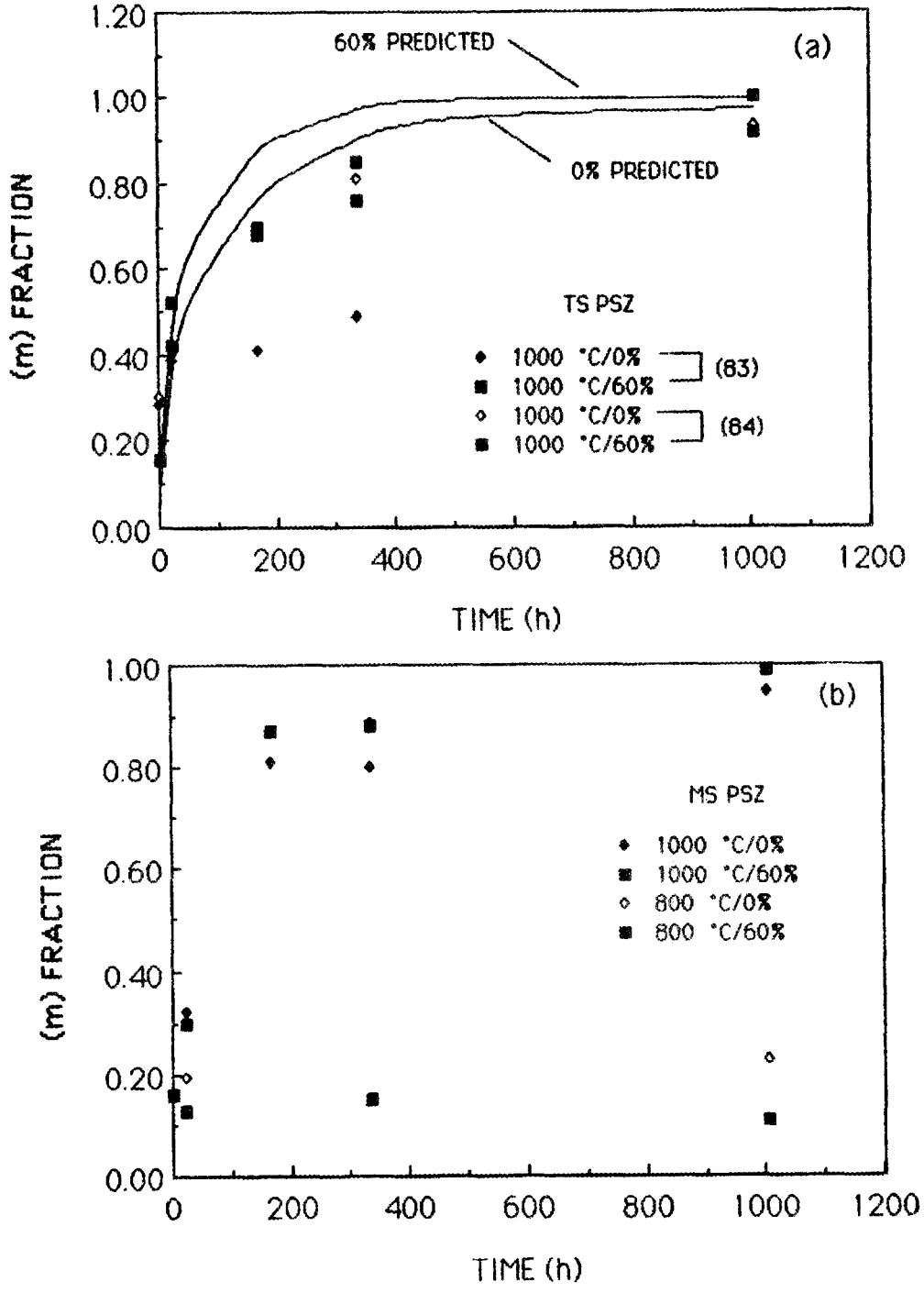

Figure 4. The volume fraction of (m) phase generated in both the TS and MS PSZ ceramics ((a) and (b), respectively) increased significantly with time for samples tested at 1000°C. The rate of (m) formation of the TS(83) materials was also dependent upon applied stress. Note the solid lines in this figure are model predictions.

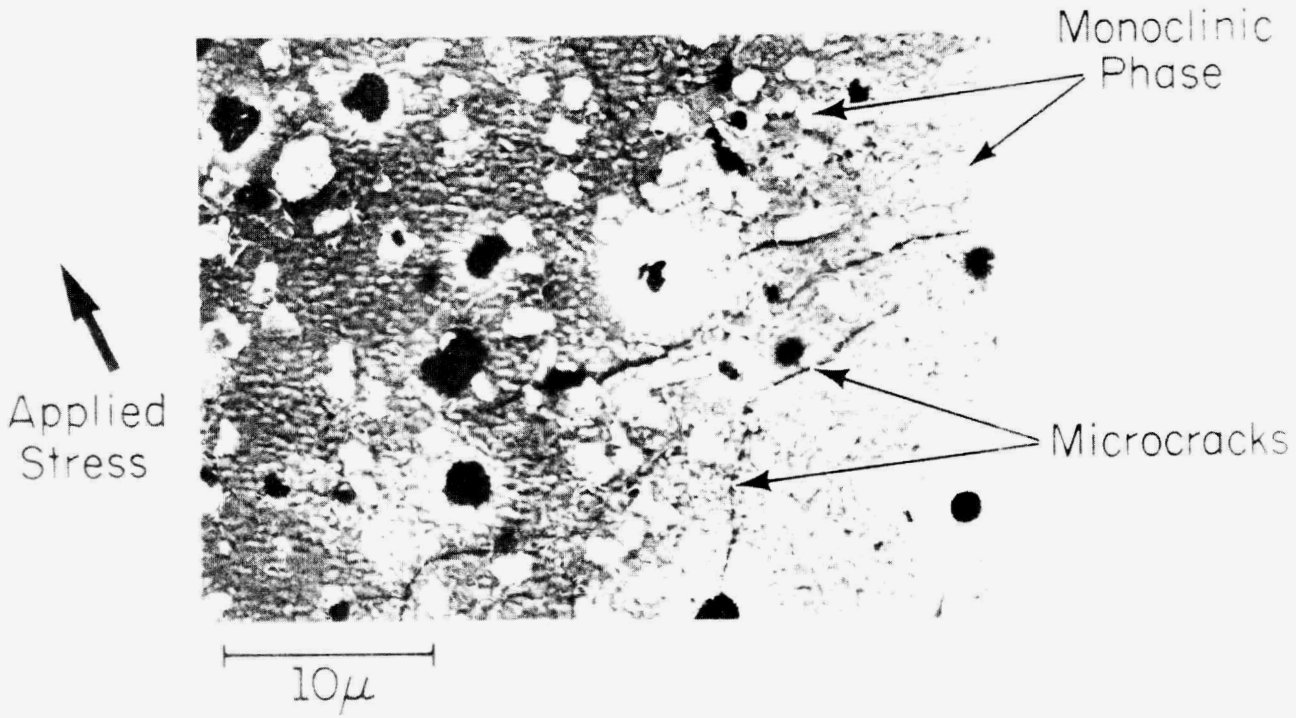

Figure 5. SEM studies gave evidence of eutectoid decomposition of the (c) phase in TS samples exposed at 1000°C for 1008 h.

exposure time decreased. In addition, no microcracking was observed for $\tau \leq 168$ h. The optical observations involving polished (and etched) tensile surfaces clearly illustrated the formation of the decomposition phase in the grain boundary regions. The optical micrographs are currently being used to calculate the rate of generation of the (m) phase. The results will be discussed next reporting period.

TEM studies involving samples of TS(83) tested under stress at 1000°C for 1008 h, also indicated the presence of a highly strained (m) decomposition product. In addition, the decomposition behavior in the tensile region of the flexure bar did not appear to be significantly different than that in the compressive region.

(c) Modeling Effort

Based on results of previous microstructural, x-ray, and thermal expansion studies it is clear that several processes could be responsible for the strength-time behavior for the TS(83) and (84) PSZ tested at 1000°C. For example, the initial strengthening of the stressed samples may have resulted from the preferential generation of compressive stresses along the flexure bar tensile surfaces due to stress dependency of the eutectoid decomposition reaction. The fact S_f only increased when S_a was nonzero suggests that the rate of (m) formation was a function of the applied stress level. Limited evidence for this stress dependency was provided by the x-ray data for the TS(83) samples.

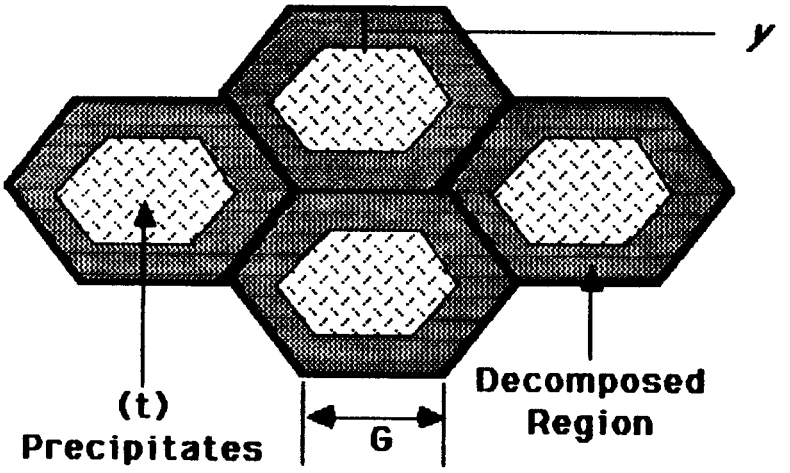

Figure 6. A simple grain structure was assumed for the modeling effort.

In order to model this process, the kinetic aspects of the decomposition reaction must first be established. Assuming that Fig. 6 adequately represents the reaction geometry one may write

$$y = (1-(1-\alpha)^{1/3})G/1.15, \quad (2)$$

where α is the volume fraction of reacted material, G is the length of a grain edge and y is the reaction distance into the grain interior. For a diffusion controlled process, $y^2 = k\tau$, where k is the rate constant. The stress dependency of the (m) formation is introduced into the model by assuming

$$k = k_o \exp(bS_a/RT), \quad (3)$$

where k_o and b are the appropriate kinetic parameters.

The time-dependent residual strain e_t generated within the flexure specimen as a result of the decomposition reaction can be expressed as

$$e_t \approx \alpha\, \varepsilon, \quad (4)$$

where $\varepsilon(\approx 1.8\%)$ is the linear strain arising from the formation of the (m) phase. This information is then used in conjunction with established thermo-elastic solutions[10] to predict the residual stress distributions. Next, assuming a given flaw size, the applied stress intensity K_{IA} is calculated from both the residual and applied stress (S_a) distributions utilizing a method outlined by Geen.[11] Finally S_a is adjusted until $K_{IA} = K_{IC}$ (i.e., $S_f = S_a$).

The application of the above procedure to the TS(84) strength data obtained in the present study led to estimates of k_o and b of 0.54 $\mu m^2/h$ and 33.5 J/(mole-MPa), respectively. The subsequent residual stress calculations (Fig. 7) revealed the formation of substantial surface compressive stresses at intermediate exposure times. The ultimate drop in the residual stress magnitude at τ = 1008 h is a consequence of the saturation condition: $\alpha \to 1$. The resulting I.F. predictions for the TS material (solid lines in Fig. 2) were in excellent agreement with the experimental data. The actual calculations were based on a flaw size of 50 μm and K_{IC} of 4 MPa $(m)^{1/2}$.

The values obtained for α could also be related to the volume fraction of (m) phase measured in the x-ray studies for the TS PSZ by assuming $\alpha \approx V_f^m$. The predicted stress dependencies of V_f^m (solid lines in Fig. 4(a)) were in considerable disagreement with those observed experimentally. This discrepancy may have been due to fact that the assumption $\alpha \approx V_f^m$ neglected the contribution from the time-dependent precipitate destabilization process. To eliminate this problem in future studies, α will be measured directly from optical micrographs in which the decomposition phase can be clearly distinguished.

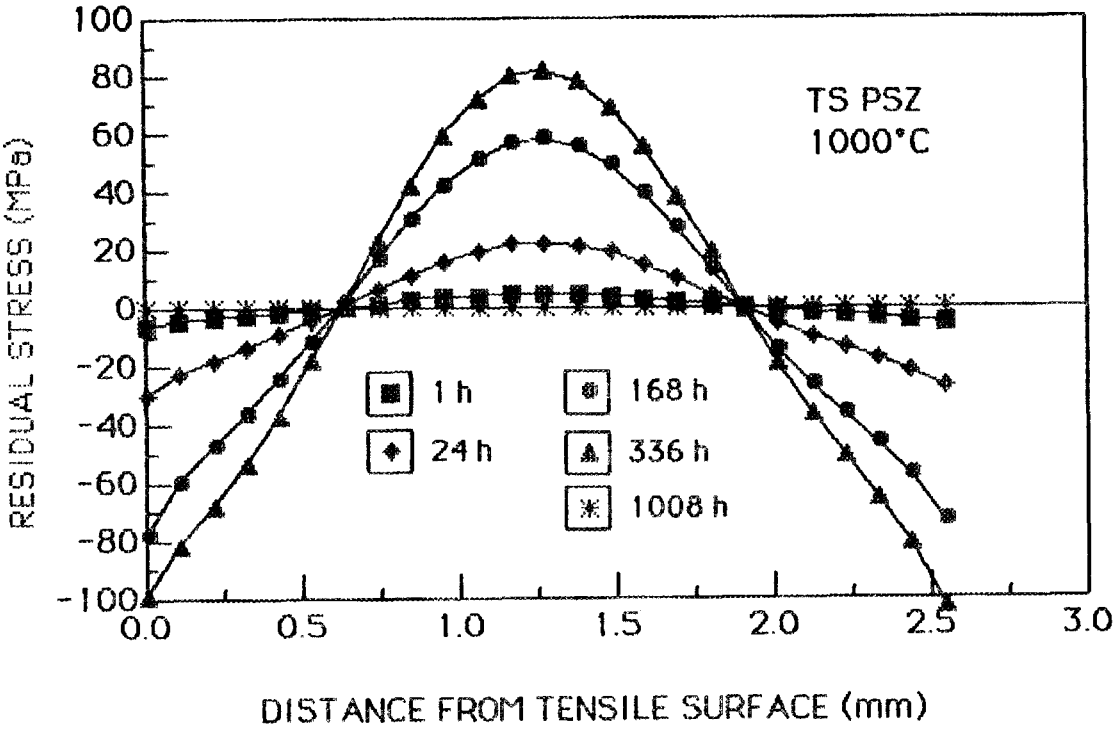

Figure 7. Model predictions indicated the generation of substantial residual stresses within stressed TS flexure specimens.

The decomposition model is subject to several limitations, First, the stress parameter b in the Eq. 3 ignores the influence of residual stresses. Recent calculations have shown that if this additional dependency is included, the value of b is significantly lower. However the general strength predictions are not altered. A second limitation is that the model does not account for other effects which include:

(1) reductions in S_f due to microcrack formation at long exposure times,
(2) time-dependent variations in K_{IC} arising from alterations in microstructure and phase assemblage, and
(3) strength changes resulting from non-linear creep.

Current research is aimed at addressing these possible mechanisms.

Status of Milestones

No milestones for this reporting period.

Publications

A paper entitled, "Characterization of the Mechanisms Responsible for Time-Dependent Strength Variations in Partially Stabilized Zirconia Ceramics," was prepared for presentation in the Second International Symposium on CERAMIC MATERIALS AND COMPONENTS FOR ENGINES to be held in Lubeck-Travemunde, Federal Republic of Germany on April 14-17, 1986.

References

1. R. Kamo and W. Bryzik, "Cummins/TACOM Advanced Adiabadic Engine," pp. 121-134 in *Proceedings of the Twenty-First Automotive Technology Development Contractors' Coordination Meeting* P-138, Society of Automotive Engineers, Warrendale, PA, March 1984.

2. S. M. Wiederhorn, "A Probabilistic Framework for Structural Ceramics," pp. 197-226 in *Fracture Mechanics of Ceramics*, Vol 5., eds. R. C. Bradt, A. G. Evans, D. P. H. Hasselman, and F. F. Lange. Plenum, New York, 1983.

3. M. K. Ferber and T. Hine, "Time Dependent Mechanical Behavior of Partially Stabilized Zirconia for Diesel Engine Applications" to be published in the proceedings of the 23rd Automotive Technology Development Contractor's Coordination Meeting held in Dearborn, Michigan on October 23, 1985.

4. D. L. Porter and A. H. Heuer, "Microstructural Development in MgO-Partially Stabilized Zirconia (Mg-PSZ)," *J. Am. Ceram. Soc.*, **62** (5-6), pp. 298-305 (1979).

5. D. C. Larsen and J. W. Adams, "Long-Term Stability and Properties of Partially Stabilized Zirconia," pp. 399-407 in *Proceedings of the Twenty-Second Automotive Technology Development Contractors' Coordination Meeting* P-155, Society of Automotive Engineers, Warrendale, PA, March 1985.

6. R. Hannink and M. Swain, "Magnesia-Partially Stabilized Zirconia: The Influence of Heat Treatment on Thermomechanical Properties," *J. Aust. Ceram. Soc.* **18** (2), pp. 53-62 (1983).

7. R. Hannink and R. Garvie, "Sub-eutectoid Aged Mg-PSZ Alloy with Enhanced Thermal Upshock Resistance," *J. Mater. Sci.* **17**, pp. 1637-43 (1982).

8. R. Hannink, "Microstructural Development of Sub-eutectoid Aged Mg-ZrO_2 Alloys," *J. Mater. Sci.* **18**, pp. 457-70 (1982).

9. M. V. Swain, R. C. Garvie, R. H. J. Hannink, "Influence of Thermal Decomposition on the Mechanical Properties of Magnesia-Stabilized Cubic Zirconia," *J. Am. Ceram. Soc.* **66** (5), pp. 358-362 (1983).

10. S. P. Timoshenko and J. N. Goodier, Theory of Elasticity, pp. 433-43, McGraw-Hill Book Company, New York, 1951.

11. D. J. Green, "Compressive Surface Strengthening of Brittle Materials by a Residual Stress Distribution," *J. Am. Ceram. Soc.* **66** (11), pp. 807-10 (1983).

Environmental Effects in Toughened Ceramics

Norman L. Hecht (University of Dayton)

Objective/scope

The University of Dayton has continued its study of "The Effect of Environment Upon Mechanical Behavior of Structural Ceramics for Application in the DOE Ceramic Technology for Advanced Heat Engines Program." This study was initiated in January 1985 through a subcontract with Martin Marietta Energy Systems Inc. The primary goal of this program is to determine the effect of environment upon toughening and strength in commercially available transformation toughened ceramics [(partially stabilized ZrO_2 (PSZ) and dispersion toughened Al_2O_3(DTA)]. Emphasis is focused on understanding the mechanism(s) responsible for environmentally induced strength degradation in the temperature range of 25°C to 1050°C. It is anticipated that the information and insight obtained from this program can be used to determine the long-term applicability of toughened ceramics as diesel engine components.

Dynamic fatigue methods (4 point bend strength measurements as a function of stressing rate) are being used in a three-phase program to investigate strength and slow crack growth in environments containing controlled amounts of water vapor. Similar tests are also being conducted in inert atmospheres (nitrogen) to distinguish intrinsic effects from environmentally induced effects.

In the first phase of the program all commercially available materials were investigated for evaluation. In this phase of the program, manufacturers' data and preliminary characterization studies conducted at the University of Dayton were utilized to screen candidate PSZ and DTA materials. From the eight candidate materials screened, four were selected for further study in the second phase of the program. A mini-matrix test plan was developed for the evaluation of the four candidate materials. The results of these mini-matrix test programs will be utilized to select the two finalist candidate materials to be more intensively evaluated by a detailed matrix test plan. A description of the activities pursued and the results obtained are presented in this semiannual report.

Work plan

As described in our last semiannual report, the work scope consisted of three major tasks. A description of these tasks is outlined in Table 1. Eight commercial transformation toughened ceramics (see Table 2) were identified for screening and initial evaluation as outlined in Task I. The elements to be employed in the preliminary screening analysis conducted in Task I are described in Table 3. The mini-matrix test plan developed for evaluating the four candidate materials under Task II is outlined in Table 4. The detailed matrix test plan to be used for the thorough evaluation of the two finalist materials is presented in Table 5.

Table 1. Work Scope.

TASK I	TASK II	TASK III
Evaluation of Potential Candidate Transformation Toughened Ceramics (TTC) • Identification of TTC Suppliers • Screening Evaluation of Potential Candidate TTC Materials • Analysis of TTC Screening Data	Investigation of the Selected Candidate Materials • Finalize Candidate Selection for Matrix Testing Plan (two temperatures, two atmospheres, and two stressing rates) • Conduct Candidate Matrix Test Program	Detailed Investigation of the Two Finalist TTC Materials • Selection of the Two Finalist Materials • Finalization of an Expanded Matrix Testing Plan • Implementation of Testing Plan

Table 2. Transformation Toughened Ceramic Materials Identified for Evaluation.

Material Supplier	Material Designation	Material Description
Ceramatec Inc.	ZTA-XS121	ZrO_2 Dispersion Toughened Al_2O_3
Kyocera Int'l.	DTA-AZ301	Dispersion Toughened Al_2O_3 (19% ZrO_2)
Nilcra Ceramic (USA) Inc.	MS-PSZ	3 wt. % MgO Stabilized ZrO_2 (heat treated for high strength)
Nilcra Ceramic (USA) Inc.	TS-PSZ	3 wt. % MgO Stabilized ZrO_2 (heat treated for high thermal shock resistance)
Ceramatec Inc.	YTZP-XS241	~5 wt. % Y_2O_3 Stabilized ZrO_2 (with 10% Al_2O_3 addition)
NGK Locke Inc.	Z191	5 wt. % Y_2O_3 Stabilized ZrO_2
Kyocera Int'l.	PSZ-Z201	5.4 wt. % Y_2O_3 Stabilized ZrO_2
Ceramatec Inc.	CTZP	CeO_2 Stabilized ZrO_2 (with 10% Al_2O_3 addition)

Table 3. Elements of the Preliminary Screening Analysis (Task I).

- Visual Inspection (low power microscope)
- Surface Finish Measurement
- SEM/EDAX
- High Power Optical Microscopy
- Density
- Vickers Hardness
- Coefficient of Thermal Expansion Measurement
- Modulus of Rupture (MOR) Testing (in N_2 at room temperature and at 1050°C)
- XRD (as-received, after MOR_{RT}, and MOR_{1050})
- Fracture Toughness (controlled surface flaw and micro-indent technique)

Table 4. Matrix Test Plan (Task II).

Temperature (°C)	Environment	Stress Rates σ_1	σ_2	σ_3	σ_4
25	Dry Nitrogen	B			B*
250	Dry Nitrogen	X			X
250	90% N_2, 10% H_2O	X			X
1050	Dry Nitrogen	X			X
1050	90% N_2, 10% H_2O	X			X

*B = baseline screening measurement; X = matrix measurement

σ_1 = 0.5 MPa/s (74 psi/s)
σ_2 = 2.6 MPa/s (370 psi/s)
σ_3 = 26 MPa/s (3700 psi/s)
σ_4 = 77 MPa/s (11060 psi/s)

Table 5. Full Matrix Test Plan.

Temperature	Environment	Stress Rates $\dot{\sigma}_1$	$\dot{\sigma}_2$	$\dot{\sigma}_3$	$\dot{\sigma}_4$
T_2	Atm_1	x	x	x	x
	Atm_2	x	x	x	x
T_3	Atm_1	x	x	x	x
	Atm_2	x	x	x	x
T_4	Atm_1	x	x	x	x
	Atm_2	x	x	x	x

KEY:

Variable values to be investigated in the evaluation program.

Test Variable	Proposed Variable Levels
Stress Rate:	*Stress rate/crosshead speed
σ_1	0.5 MPa/s (74 psi/s) - .0025 cm/min (.001 in/min)
σ_2	2.6 MPa/s (370 psi/s) - .0125 cm/min (.005 in/min)
σ_3	26 MPa/s (3700 psi/s) - .125 cm/min (.05 in/min)
σ_4	77 MPa/s (11060 psi/s) - .375 cm/min (.15 in/min)
Temperature	
T_1	25°C (77°F)
T_2	250°C (482°F)
T_3	800°C (1472°F)
T_4	1050°C (1922°F)
Environmental Conditions	
Atm_1	Dry Nitrogen
Atm_2	90% Nitrogen/10% Water

*Stress rates are approximate values based on average room temperature elastic modulus data for the designated crosshead speeds.

Technical progress

Results

Summary of Task I results. The results obtained from the studies conducted under Task I were described in detail in our first semiannual report. The results obtained in Task I are summarized in Table 6 and in Figure 1. Task I was completed with the selection of the four candidate materials to be studied further, NGK Locke Z191, Ceramatec CTZP, Nilcra MS-PSZ, and Kyocera AZ301.

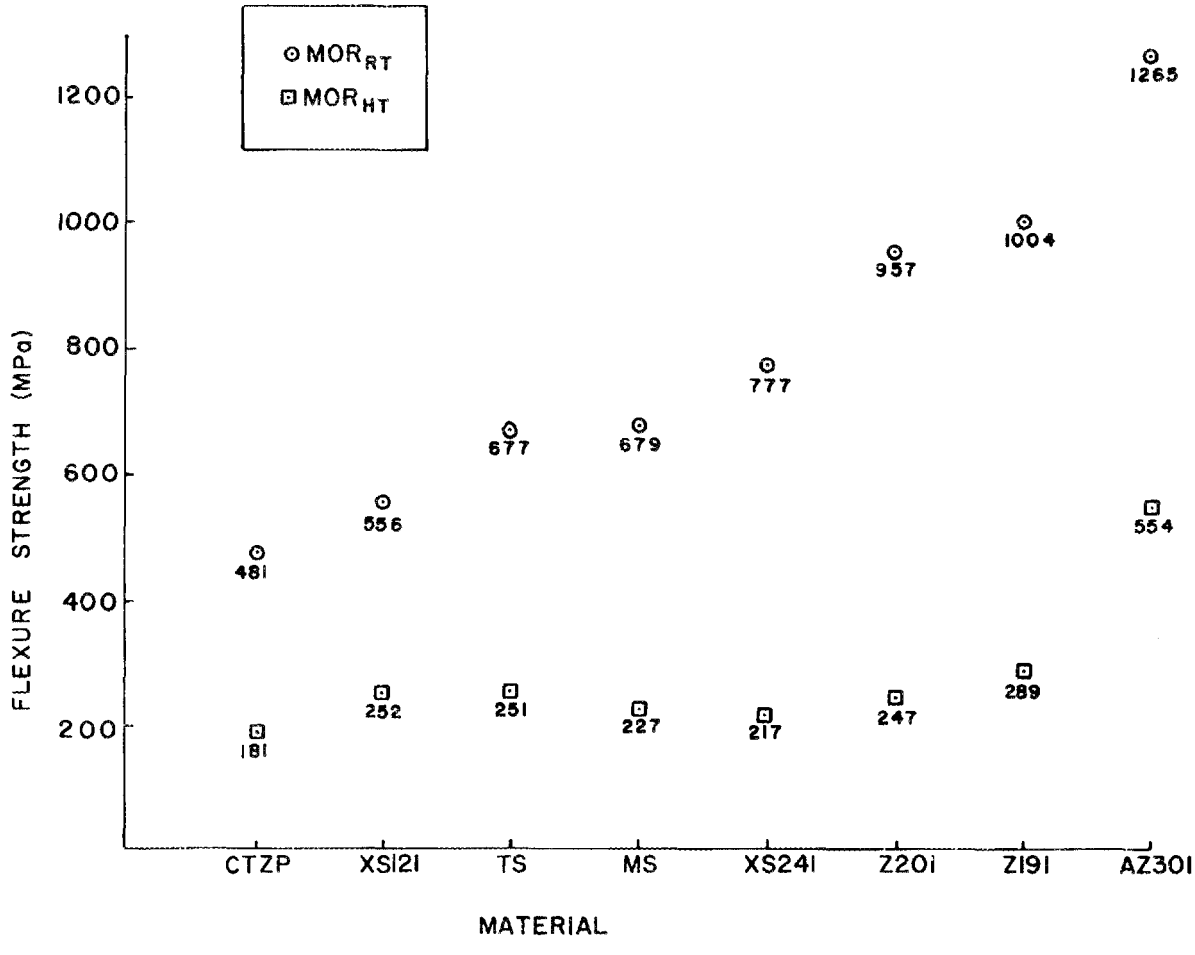

Figure 1. MOR test results from the screening analysis (Task I).

Table 6. Summary of Screening Evaluations for TTC Materials.

Material Designation	Nilcra MS-PSZ	Nilcra TS-PSZ	Kyocera DTA-AZ301	Kyocera PSZ-Z201
Chemistry (Components)	ZrO_2 MgO	ZrO_2 MgO	Al_2O_3 ZrO_2 SiO_2 -Trace	ZrO_2 Y_2O_3
Crystal Structure				
% Monoclinic As-Received	23	33	28	3
% Monoclinic After MOR_{1050}	88	69	21	0
Density (g/cc)	5.7	5.7	4.2	5.9
Hardness (kg/mm^2)	1099	1025	1939	1282
Fracture Toughness ($MPa\sqrt{m}$)				
By Controlled Flaw	-	-	4.6	5.4
By Micro Indent	7.6	6.0	11.1	8.8
MOR-MPa (Std. Dev. %)				
Fast Fracture RT	679(6)	677(3)	1265(11)	957(5)
At 1050°C	225(4)	251(-)	554(24)	247(21)
Major Microstructural Features	Porous coarse grained (30-60 μ) material.	Porous coarse grained (30-60 μ) material.	Dense two phase material with oblong Al_2O_3 grains 4 x 14 μ and ZrO_2 grains ≈ .4 μ.	Dense fine grained material (0.2-0.5μ avg. ≈ .3μ).
Average Sample Surface Finish Measurements (μ in)	10 (4-15)	9 (4-12)	2.8 (2-4)	6.1 (4-8)
Coefficient of Thermal Expansion (x 10^{-6}/°C)	10.3	9.5	8.4	11.0

(Table 6 concluded on the following page.)

Material Designation	NGK Z191	Ceramatec ZTA-XS121	Ceramatec YTZP-XS241	Ceramatec CTZP
Chemistry (Components)	ZrO_2, Y_2O_3 SiO_2 Al_2O_3 } Trace	Al_2O_3, ZrO_2 SiO_2 K_2O/CaO-Trace	ZrO_2 Y_2O_3 Al_2O_3	ZrO_2, SiO_2 Al_2O_3, CeO_2 K_2O/CaO-Trace
Crystal Structure				
% Monoclinic As-Received	7	30	11	1
% Monoclinic After MOR_{1050}	0	24	8	0
Density (g/cc)	5.9	4.4	5.4	5.7
Hardness (kg/mm^2)	1292	1172	1120	864
Fracture Toughness ($MPa\sqrt{m}$)				
By Controlled Flaw	6.8	2.8	4.8	-
By Micro Indent	7.4	6.9	6.6	7.0
MOR-MPa (Std. Dev. %)				
Fast Fracture RT	1004(16)	556(4)	777(19)	481(4)
At 1050°C	296(6)	252(-)	217(-)	186(13)
Major Microstructural Features	Dense fine grained matl. (0.3μ)	Fine grained two-phase matl. (0.3-2.5μ avg. ≈ 1.5μ). Uniform distribution of pores (0.2-1.5μ).	Fine grained two-phase matl. (0.4-1.5μ). Uniform distribution of pores (0.5-5μ).	Fine grained two-phase matl. (1-3μ). Uniform distribution of pores.
Average Sample Surface Finish Measurements (μ in)	6.9 (4-16)	3.1 (2-10)	8 (6-10)	3.1 (2-6)
Coefficient of Thermal Expansion ($\times 10^{-6}/°C$)	10.1	9.4*	9.9	10.7

*Phase change @ 625°C.

Results obtained in Task II. NGK Z191 was the first material to be evaluated in the mini-matrix test plan under Task II. Testing of the Z191 material was initiated at 1050°C in 10% water vapor using both fast and slow loading rates. However, at the slow loading test conditions, permanent plastic deformation was observed in all the samples tested. The occurrence of plastic deformation in Z191 prompted the decision to further evaluate two or three samples of all of the other candidate systems except the TS materials at 1050°C using the slow loading rate. As a result of these additional MOR tests, it was found that the Kyocera Z201 material also undergoes plastic deformation at the stated test conditions. However, none of the other materials displayed plastic deformation. The degree of deformation observed in the Z201 material was not as severe as that observed in the Z191 material (see Figure 2). Subsequent testing also

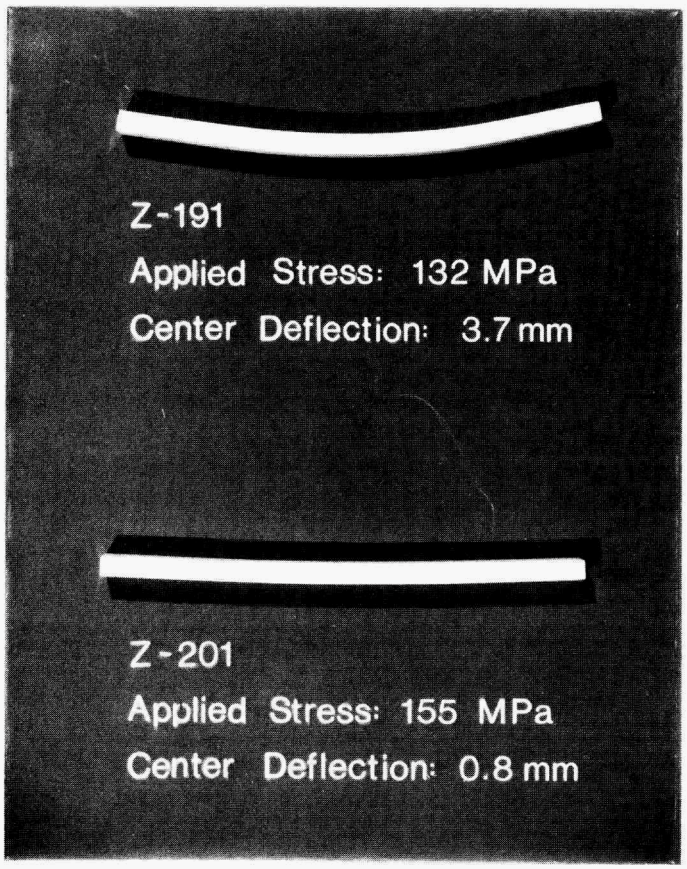

Figure 2. Comparison of Z191 and Z201 materials after MOR_{1050} slow fracture.

showed that plastic deformation occurs in both the Z191 and Z201 materials when they were tested at the slow loading rate at 1050°C in a dry nitrogen atmosphere. A summary of all the Modulus of Rupture (MOR) test results obtained to date in the mini-matrix test plan, as well as the additional modulus of rupture test results of the other candidate materials at 1050°C, are presented in Table 7.

Table 7. Summary of MOR Test Results.

Temp (°C)	ATM	Loading Rate (MPa/sec)	Material							
			AZ301	Z191	Z201	241	MS	TS	121	CTZP
25	Dry N_2	0.5	1103	1014	775	761	621	583	567	472
25	Dry N_2	77	1265	1004	957	777	679	677	556	481
250	Dry N_2	77	897	900	689	X	540	X	X	523
250	Dry N_2	0.5	X	X	X	X	X	X	X	X
250	10% H_2O	77	1036	827	?	X	525	X	X	433
250	10% H_2O	0.5	892	862	?	X	448	X	X	341
800	Dry N_2	77	?	460	?	X	299	X	X	216
800	Dry N_2	0.5	X	447	X	X	X	X	X	X
800	10% H_2O	77	?	325	?	X	282	X	X	202
800	10% H_2O	0.5	?	261	?	X	270	X	X	218
1050	Dry N_2	77	?	319	?	X	?	X	X	?
1050	Dry N_2	0.5	?	120	175	X	248	X	X	191
1050	10% H_2O	77	554	296	247	217	225	251	252	186
1050	10% H_2O	0.5	620	115	173	248	254	X	251	154

X - not to be tested as part of the mini-matrix

? - to be tested

The Z191 material has been evaluated at all of the matrix test conditions, as well as at the 800°C test temperature. In addition, it was decided to also investigate the Kyocera Z201 material further because of the less severe plastic deformation as compared to the 191 material. However, further testing of both the Z201 and AZ301 materials has been limited because of the delay by the manufacturer in supplying the needed test samples. As shown in Table 7, testing of the MS and CTZP materials are almost completed. A graphic display of all the modulus of rupture test results are presented in Figures 3 through 6.

The modulus of rupture test specimens were also evaluated by x-ray diffraction analysis (XRD) and scanning electron microscopy (SEM). A summary of the XRD results are presented in Table 8. The SEM micrographs of the fractured MOR samples showed little difference between the microstructure observed in the as-received material and the microstructure observed in the samples tested at the different mini-matrix test conditions. However, it is observed that the Z191 and Z201 samples which failed by plastic deformation have smooth fracture surfaces. Specimens which failed in the more conventional manner display a much coarser fracture surface.

Aging studies. The extended exposure of the transformation toughened ceramic samples to water vapor at low and moderate temperatures (aging) is also being investigated in this study. Several different aging treatments

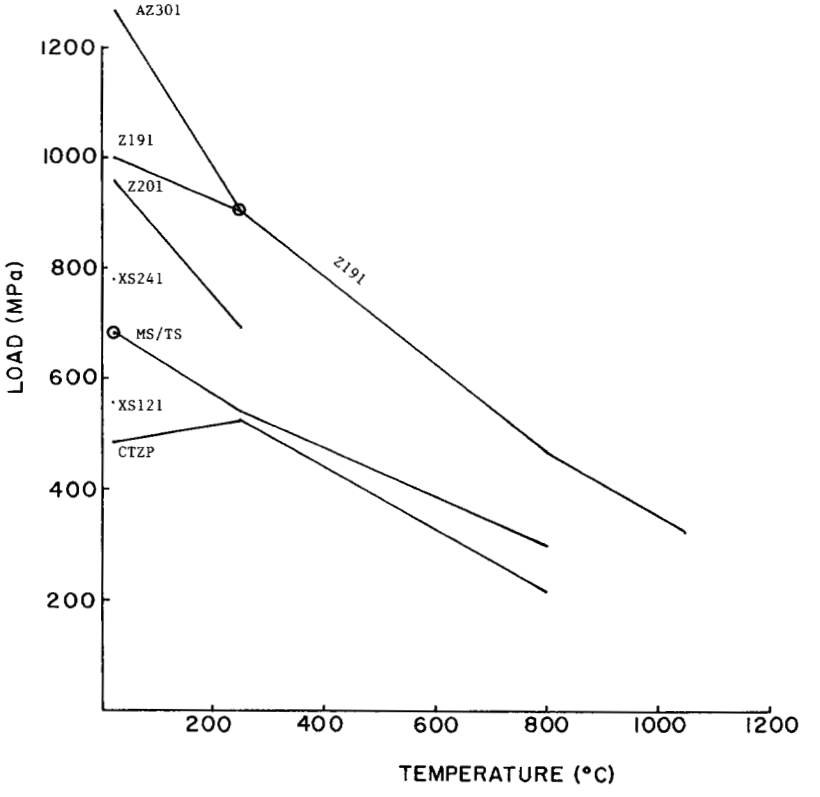

Figure 3. Summary of MOR data in Dry N_2 at fast loading rates.

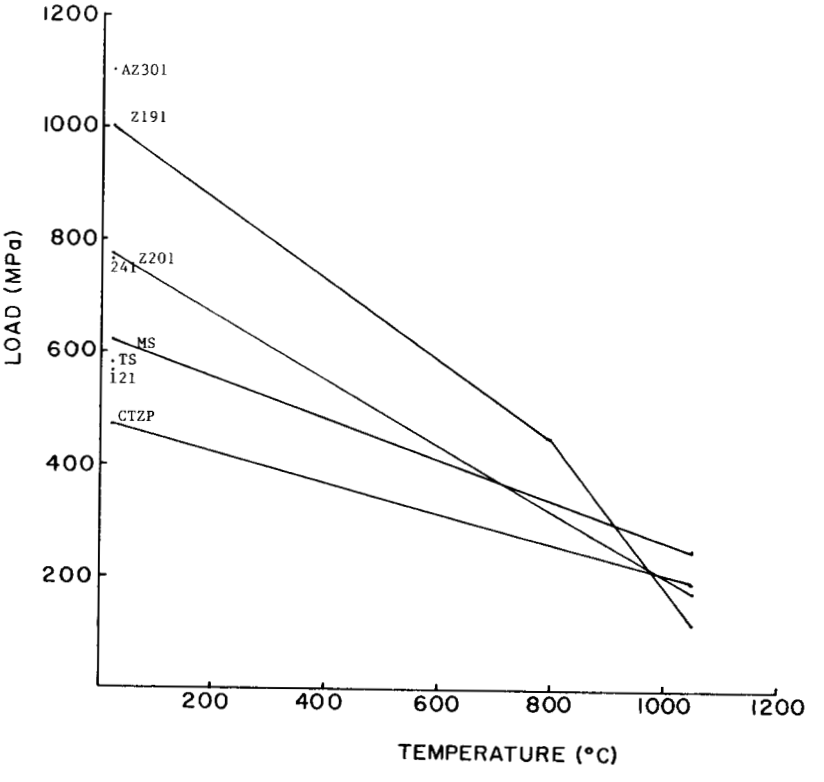

Figure 4. Summary of MOR data in Dry N_2 at slow loading rates.

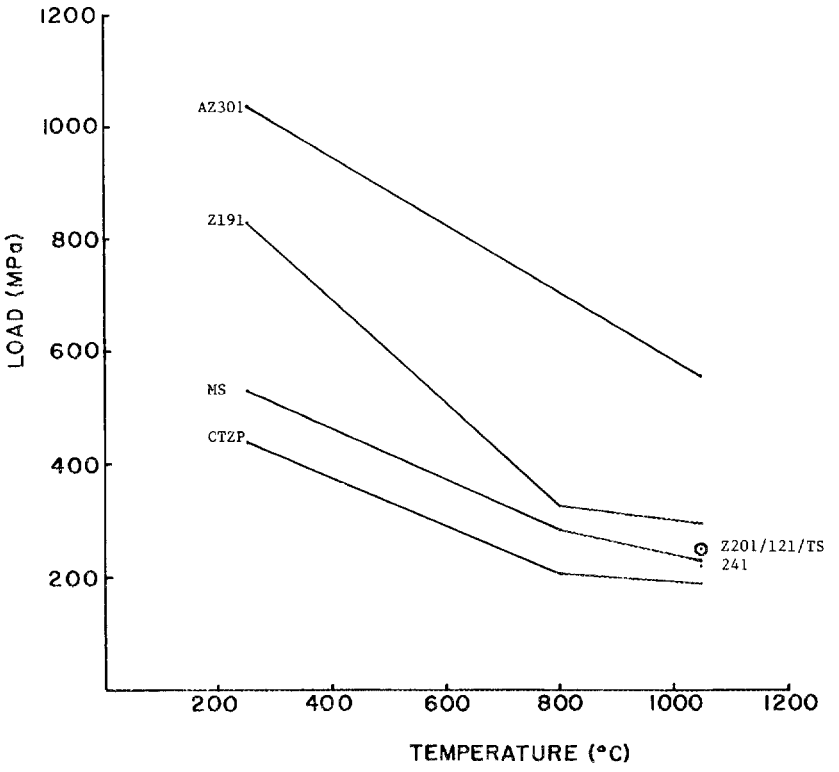

Figure 5. Summary of MOR data in 10% H_2O at fast loading rates.

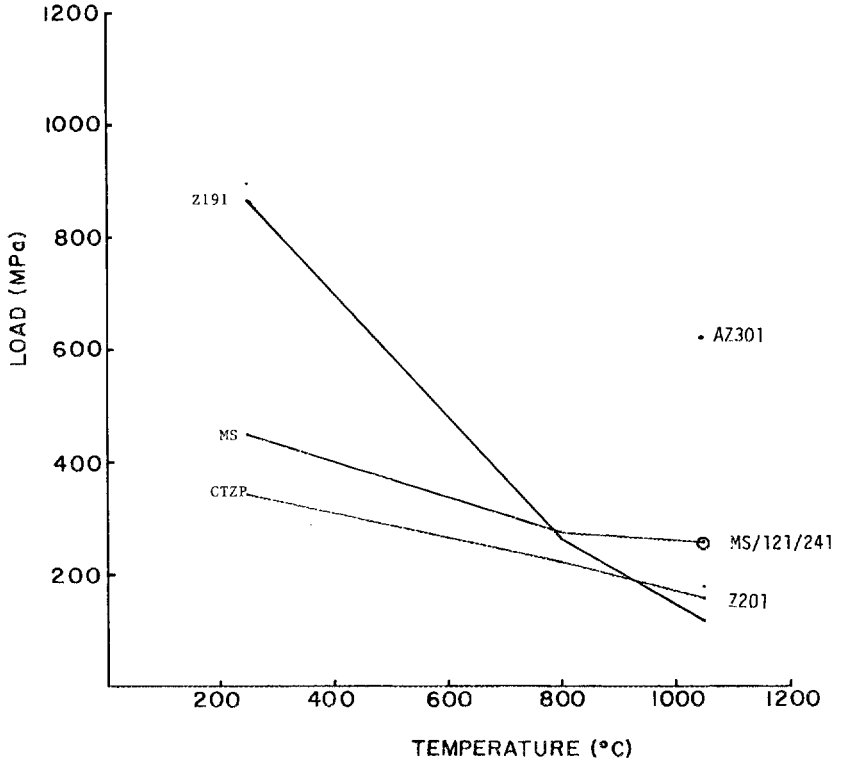

Figure 6. Summary of MOR data in 10% H_2O at slow loading rates.

Table 8. Summary of XRD Data for Materials Evaluated.

Material/ Condition	Z191		CTZP		MS-PSZ		Z201		AZ301*	
	% Mono	Major Phase	% Mono	Major Phase	% Mono	Major Phase	% Mono	Major Phase	% Mono	Major Phase
As-Received	?	T	1	T	23	T	3	T	28	T
After MOR 250 Dry N_2 (FF)	?	T	0	T	21	T	0	T	?	-
After MOR 250 10% H_2O (FF/SF)	7/8	T	0/0	T	24/25	T	?	-	?	-
After MOR 800 Dry N_2 (FF)	4	T	0	T	17	T	?	-	?	-
After MOR 800 10% H_2O (FF/SF)	0/15	T	0/0	T	21/21	T	?	-	?	-
After MOR 1050 Dry N_2 (FF)	0	T	0	T	77	M	0	T	?	-
After MOR 1050 10% H_2O (FF/SF)	0/0	T	0/0	T	88/50	M	0/0	T	21/17	T

* - Al_2O_3 is the major phase
? - to be tested
FF - fast loading rate
SF - slow loading rate
Mono - monoclinic
T - tetragonal
M - monoclinic

have been employed in studying the candidate transformation toughened ceramics. A compilation of the aging treatments employed in our studies is presented in Table 9. The results of the XRD analysis of the aged samples are summarized in Table 10. The modulus of rupture test restuls of the aged samples are summarized in Table 11.

Selected aged samples are also being studied by infrared spectroscopy, and the ATR FT-IR spectra obtained are being compared with the spectra obtained for the as-received transformation toughened ceramics. Attenuated total reflection (ATR) techniques have been widely used to study the surfaces of solid state inorganic materials. A number of papers have reported that the combination of ATR with FT-IR provides a tool that has excellent sensitivity to a wide spectral region. The primary objective for using ATR FT-IR to study transformation toughened ceramics is to better understand the mechanism involved in the phase transformations at the

Table 9. Aging Treatments.

Material	Initial Aging	Advanced Aging
Z191	25 hrs. @ 300°C	120 hrs. @ 250°C
AZ301	25 hrs. @ 300°C	---
Z201	25 hrs. @ 300°C	120 hrs. @ 250°C
CTZP	25 hrs. @ 300°C	120 hrs. @ 150°C/120 hrs. @ 250°C
XS121	25 hrs. @ 300°C	120 hrs. @ 250°C
XS241	25 hrs. @ 300°C	120 and 240 hrs. @ 250°C
MS-PSZ	200 hrs. @ 800°C	120 hrs. @ 250°C
TS-PSZ	200 hrs. @ 800°C	120 hrs. @ 250°C

Table 10. XRD Analysis of Aged Samples.

Material	% Monoclinic As-Received (MP)*	% Monoclinic Initial Aging (MP)*	% Monoclinic Advanced Aging (MP)*
Z191	7 (t)	10 (t)	9 (t)
AZ301	28 (t)	27 (t)	-
Z201	3 (t)	4 (t)	4 (t)
CTZP	1 (t)	0 (t)	0 (t)
XS121	30 (t)	60 (m)	64 (m)
XS241	11(7-21) (t)	42 (c)	46 (c)
MS-PSZ	23 (t)	33 (t)	32 (t)
TS-PSZ	33 (t)	41 (t)	43 (t)

*MP - major zirconia phase

Table 11. MOR Test Results of Aged Samples.

Material	MOR As-Received (MPa)	MOR After Initial Aging (MPa)	MOR After Advanced Aging (MPa)
Z191	1004	957	-
AZ301	1265	1206	-
Z201	957	791	-
CTZP	481	481	492 (@150°C)
XS121	556	556	645 (120 hrs. @ 250°C)
XS241	777	729	519 (120 hrs. @ 250°C)
MS-PSZ	679	674	-
TS-PSZ	608	677	662 (120 hrs. @ 250°C)

polycrystalline surface which have been accelerated by the presence of moisture during aging of the specimens at relatively low temperatures.

A single beam multiple internal reflection attachment is being used with a KRS-5 crystal plate. IR spectra were obtained using a Nicolet DBX Model 20 with 2000 to 4000 scans. The spectral range extended from 4000 to 400 cm^{-1}, and most of the experimental work was focused on crystalline phase transformations of zirconia in the region of 800 to 400 cm^{-1}.

The ATR FT-IR spectra were obtained for specimens in the as-received condition and aged at selected temperatures. The samples studied by infrared spectroscopy are described in Table 12. A summary of the IR

Table 12. Specimens Studied by ATR FT-IR.

		Aging Treatment				
Material	As-Received	150°C, 120 hrs.	250°C, 120 hrs.	250°C, 240 hrs.	800°C, 200 hrs.	1050°C, MOR
Z201	X		X			
XS241	X		X	X		
CTZP	X	X	X			
MS-PSZ	X		X		X	X

absorption bands detected for each of the candidate materials investigated is presented in Table 13. Typical spectra obtained for each of the different aged materials analyzed are presented in Figures 7 through 10.

Table 13. ATR FT-IR Absorption Bands of Specimens Studied.

Specimen	Absorption Bands (in cm^{-1})
PSZ-Z201	
As-Received	780 (sh); 710 (w,sh); 640; 568
Aged (250°C, 120 hrs.)	780 (sh); 647; 568
XS-241	
As-Received	762 (sh); 640 (s); 562 (sh); 522 (s)
Aged (250°C, 120 hrs.)	762 (br,sh); 640 (br); 562 (sh); 531 (s); 478 (w,sh)
Aged (250°C, 240 hrs.)	762 (br,sh); 709 (br,sh); 665 (v,br); 640 (sh); 562 (s,sh); 531 (s); 478 (m); 422 (w)
CTZP	
As-Received	776 (w,br); 638 (sh); 630 (s); 519 (s)
Aged (150°C, 120 hrs.)	776 (w,br); 644 (s); 632 (sh); 540 (sh); 527 (s); 465 (w); 452 (w); 418 (w)
Aged (250°C, 120 hrs.)	776 (w); 632 (s); 540 (sh); 527 (s); 465 (w); 452 (w); 418 (w)
MS-PSZ	
As-Received	~673 (v,br); 572 (s)
Aged (250°C, 120 hrs.)	~673 (v,br); 572 (s); 475 (sh)
Aged (800°C, 200 hrs.)	709 (sh); ~615 (v,br); 562 (m); 475 (s,sh)
After MOR_{1050} testing (w/10% H_2O)	709 (w); 692 (m); 606 (m); 562 (m); 475 (s); 456 (sh)

sh: shoulder
br: broad
v: very
s: strong
m: medium
w: weak

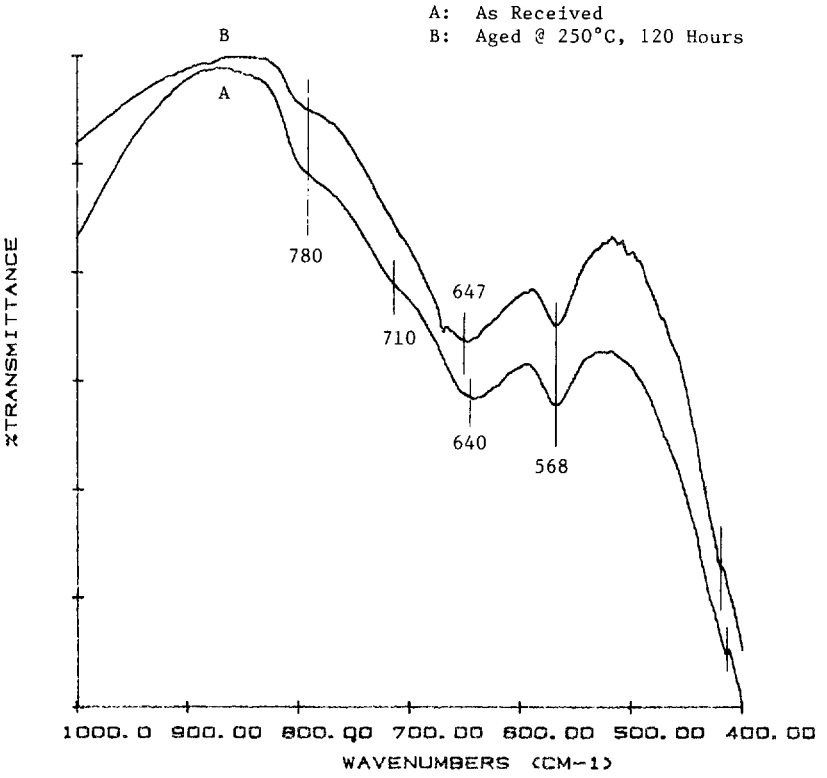

Figure 7. ATR FT-IR spectra for Z201.

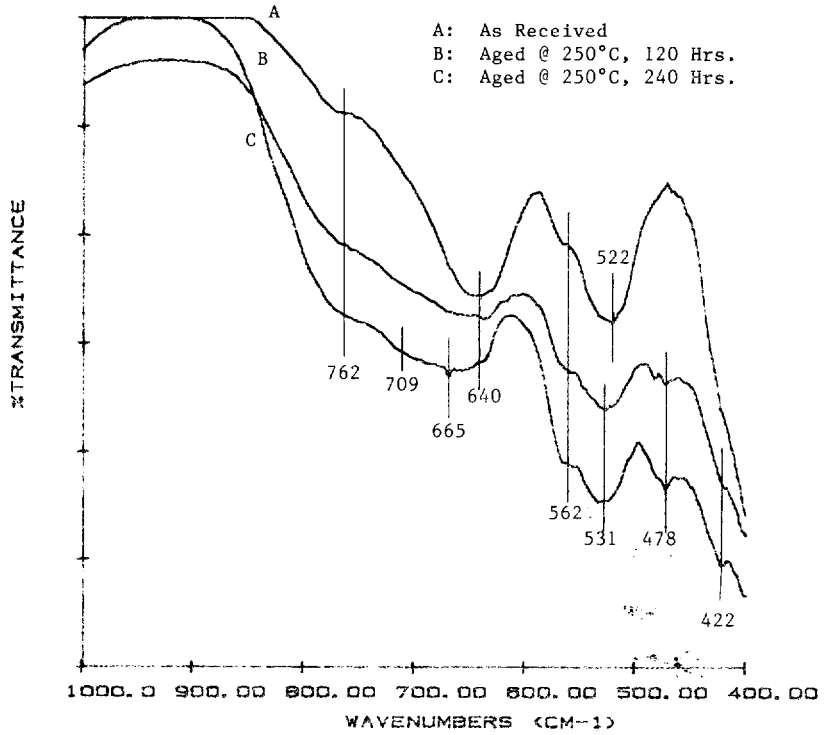

Figure 8. ATR FT-IR spectra for XS241.

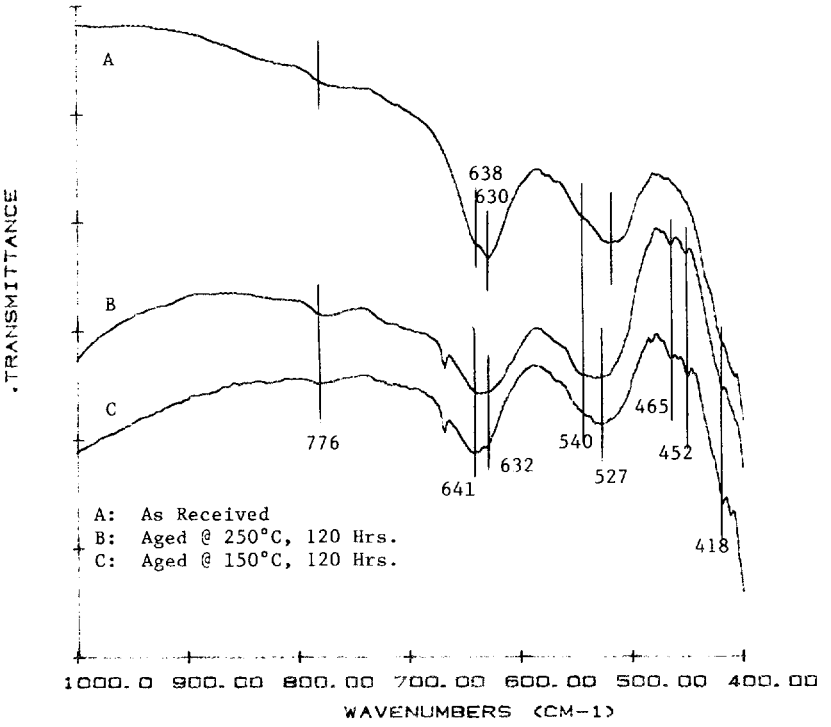

Figure 9. ATR FT-IR spectra for CTZP.

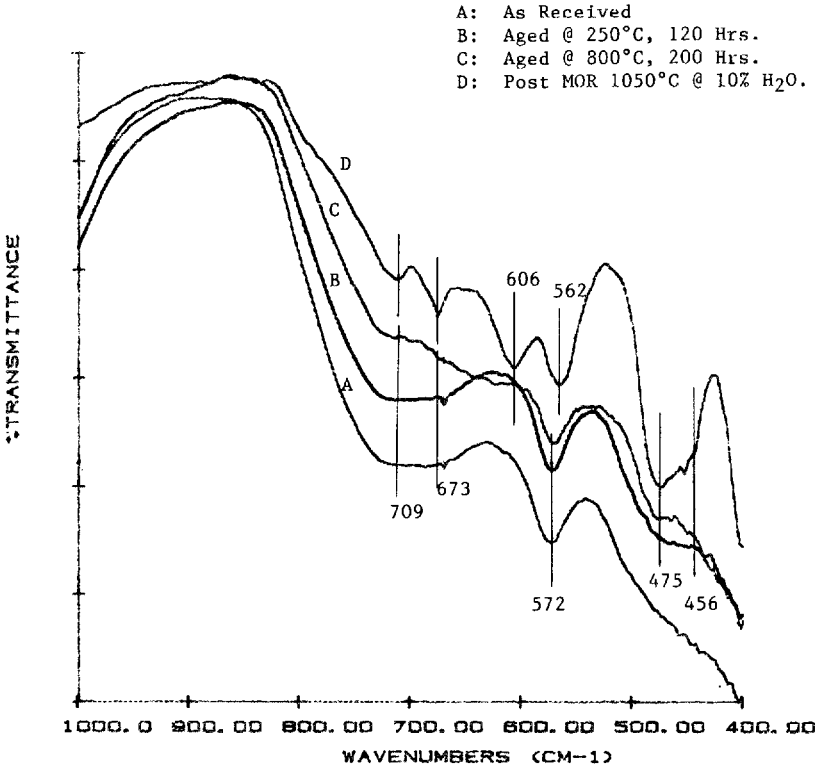

Figure 10. ATR FT-IR spectra forMS-PSZ.

In addition to the ATR FT-IR analysis, samples of MS-PSZ and XS241 materials in the as-received and aged condition were evaluated by x-ray photoelectron spectroscopy (XPS). The results obtained for the four samples analyzed by high resolution XPS scans are presented in Table 14.

Table 14. Approximate Atom % Surface Composition of Samples XS241 and MS-PSZ Zirconia by XPS.

Sample	$O(H_2O)$	O(-OH)	$O(O^{=})$	Zr	Y	Mg
TZP-XS241						
As-Received	9.3	39.7	26.7	22.9	1.3	-
As-Aged	5.9	33.6	33.0	25.2	1.9	-
MS-PSZ						
As-Received	9.6	47.1	18.8	20.7	-	3.8
As-Aged	4.4	32.4	31.0	26.2	-	6.1

Raman spectroscopy studies.

Introduction. The primary objective of the work during this semi-annual period was to develop measurement and analysis techniques which will provide quantitative assessments of the concentrations of the phases in samples of partially stabilized zirconia (PSZ). There are two basic approaches to achieving this objective; namely, (1) to develop a highly dependable set of standards for the observed phases which is then fitted to the sample spectrum to give the absolute concentrations, and (2) to measure only the relative concentrations within each sample.

The first approach is most difficult to achieve with backscattering Raman spectroscopy from solid surfaces, especially of polycrystalline materials. The intensity of the Raman scattering from a crystal is proportional to the length L of the scattering volume that is being observed times the square of the Raman scattering tensor R.[1] Single crystal zirconium oxide is transparent to visible light. In polycrystalline form, however, the material becomes opaque or at least translucent. This comes from the multiple reflections and refractions of the incident light by the boundaries or interfaces between the individual crystalline grains. The high refractive index of 2.2 of this material[2] contributes significantly to this result. Thus, the penetration depth or scattering length will depend on the grain size, the packing or density of the grains, and the nature of the grain boundaries. Furthermore, in PSZ there are three phases; namely, monoclinic, tetragonal, and cubic, which can be present. The Raman tensors of these symmetries are different as well as being dependent on crystalline orientation and incident light polarization for the non-cubic phases.

Added to the above complications are the variations that can occur from sample to sample, due to surface preparation and surface history.

The character of the surface illuminated by the laser light determines how much of the light actually penetrates into the bulk of the sample. This, in turn, determines the intensity of the Raman light. The fraction of this light which escapes the sample in the direction of the collecting lens determines the actual observed Raman signal. Basically, the observed signal is seen as a "crystalline" Raman spectrum superimposed on some sort of broad background spectrum. The central problem in comparing two different samples is the identification and measurement of this background spectrum, especially relative to the crystalline spectrum.

The PSZ material offers a further challenge in that one of the three phases, namely cubic, appears in a highly disordered or nearly amorphous state,[3] and therefore, produces a broad spectrum that comes from the one phonon density of states. Nevertheless if the grain sizes of the monoclinic and tetragonal phases are sufficiently small such that the measurement is an integration over a large number of grains which presumably have random orientation, then the observed spectrum should be analyzable in terms of the absolute concentrations of the three phases.

To accomplish this feat, standard samples having only one phase are needed. Then the concentrations would be determined by fitting the three standard spectra to the unknown spectrum using nonlinear regression analysis. The current impediments to this approach are the lack of good 100% samples of the cubic phase and a satisfactory means for accounting for the differences in surface history and preparation.

Measurements. The second approach and the one used in this report, that of relative concentrations, is much simpler to accomplish. The scheme which has been commonly used [4,5] to compute the monoclinic fraction x(m) is given by

$$x(m) = I(m)/[I(m) + I(t)]$$

where I(m) and I(t) are, respectively, the Raman intensities of a monoclinic line and a tetragonal line. The best approach to spectral intensity measurements is to record the spectrum with sufficient resolution to resolve the desired spectral feature and then integrate that feature. An example of a sample which shows both monoclinic and tetragonal spectra is given in Figure 11. The monoclinic phase resulted from the aging process. The spectrum of the as-received material is close to 100% tetragonal.

We chose the tetragonal line at 146 cm^{-1} and the monoclinic pair at 178 and 188 cm^{-1} for this analysis. These selections were made on the basis that (1) the lines were close together which simplifies the recording and analysis of the spectra, (2) there were clearly no interferences with any other features, (3) the lines were very similar in shape and width, and (4) their peak intensities in samples having only one phase were quite similar which ensured good sensitivity to changes over the full range of x(m). The widths of these lines are about 12 cm^{-1} which is adequately resolved with a 200 μm slit (≈3 cm^{-1}). Since the monoclinic feature is an unresolved doublet, one-half of the measured total area of this feature relative to the tetragonal value was used in the calculation of x(m). Thus, we now have

$$x(m) = \int I(m)/[\int I(m) + 2\int I(t)]$$

where $\int I(m)$ and $\int I(t)$ are, respectively, the integrated intensities of the monoclinic and tegragonal features.

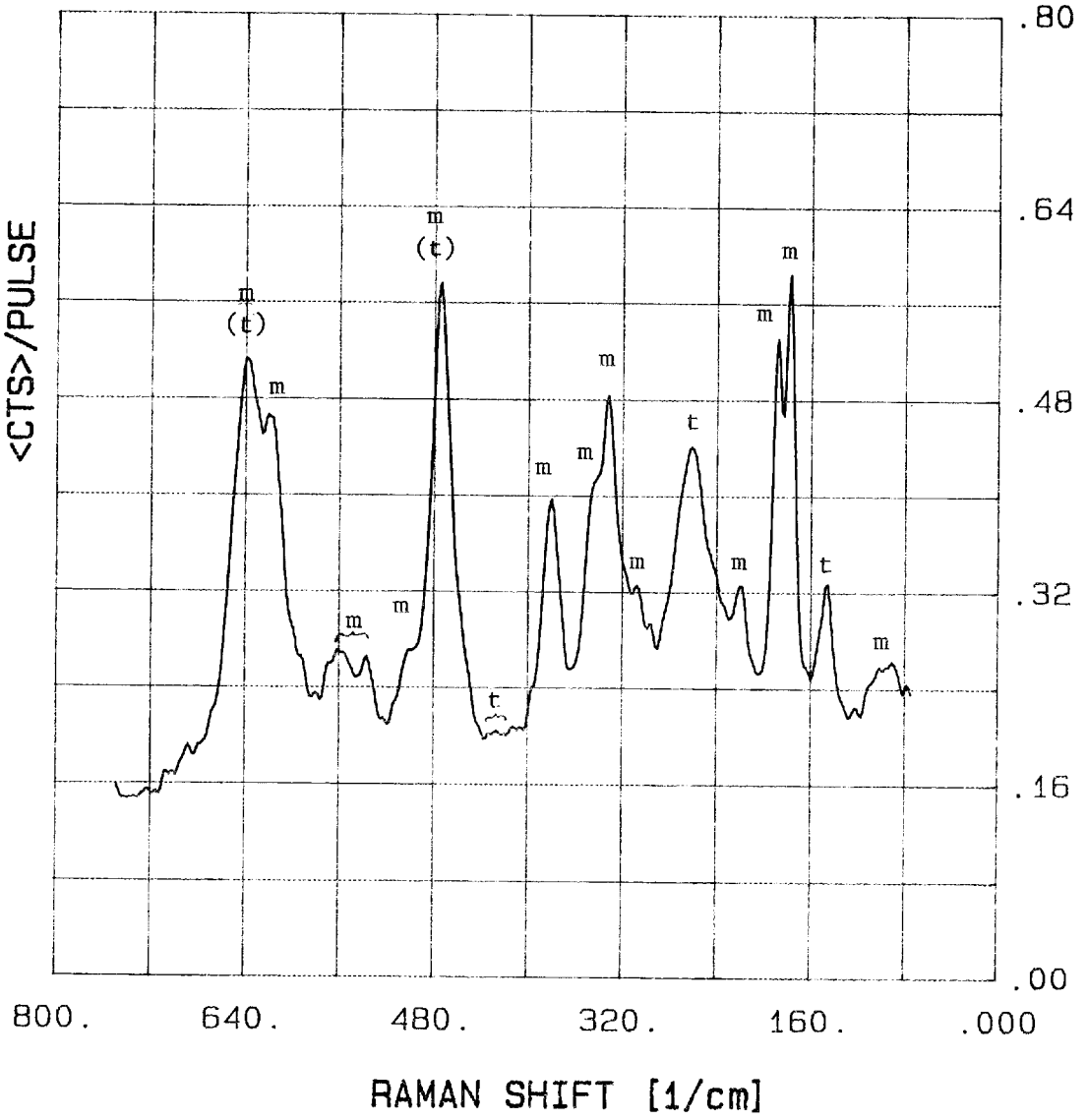

Figure 11. The Raman spectrum of sample No. 44 of Ceramatec TZP-XS241 after aging 240 hours at 250°C. The lines belonging to the monoclinic and tetragonal phases of zirconia are, respectively, denoted by "m" and "t". The letter enclosed in parentheses indicates that phase is only weakly present.

Measurements were carried out on eight samples which had been fractured. The spectrum between 120 and 210 cm^{-1} was recorded twice on each sample. One scan was taken at 5 mm from the unstressed end with the second scan taken at the very edge of the fractured end on the tension side. The laser beam was focused by a 100 mm focal length, cylindrical lens to form a line about 20 μm wide and 2 mm long. On the fractured end, the line was oriented parallel to the local direction of the broken edge and positioned to be within about 20 μm of the edge.

The average laser power incident on the sample was less than 5 mW. The ability to record high quality Raman spectra of these samples at such a low power level completely circumvents the heating problems that have been experienced with zirconia materials. This heating problem comes from the rather low thermal conductivity of the material. The use of a cylindrical focusing lens further reduces the heating effect by spreading the light over a long dimension. This type of illumination provides the additional advantage of integrating the contributions from many grains without sacrificing the capability for achieving good spatial resolution at the fractured edge. A spectrum typical of the type used for these data showing 65% monoclinic phase is given in Figure 12.

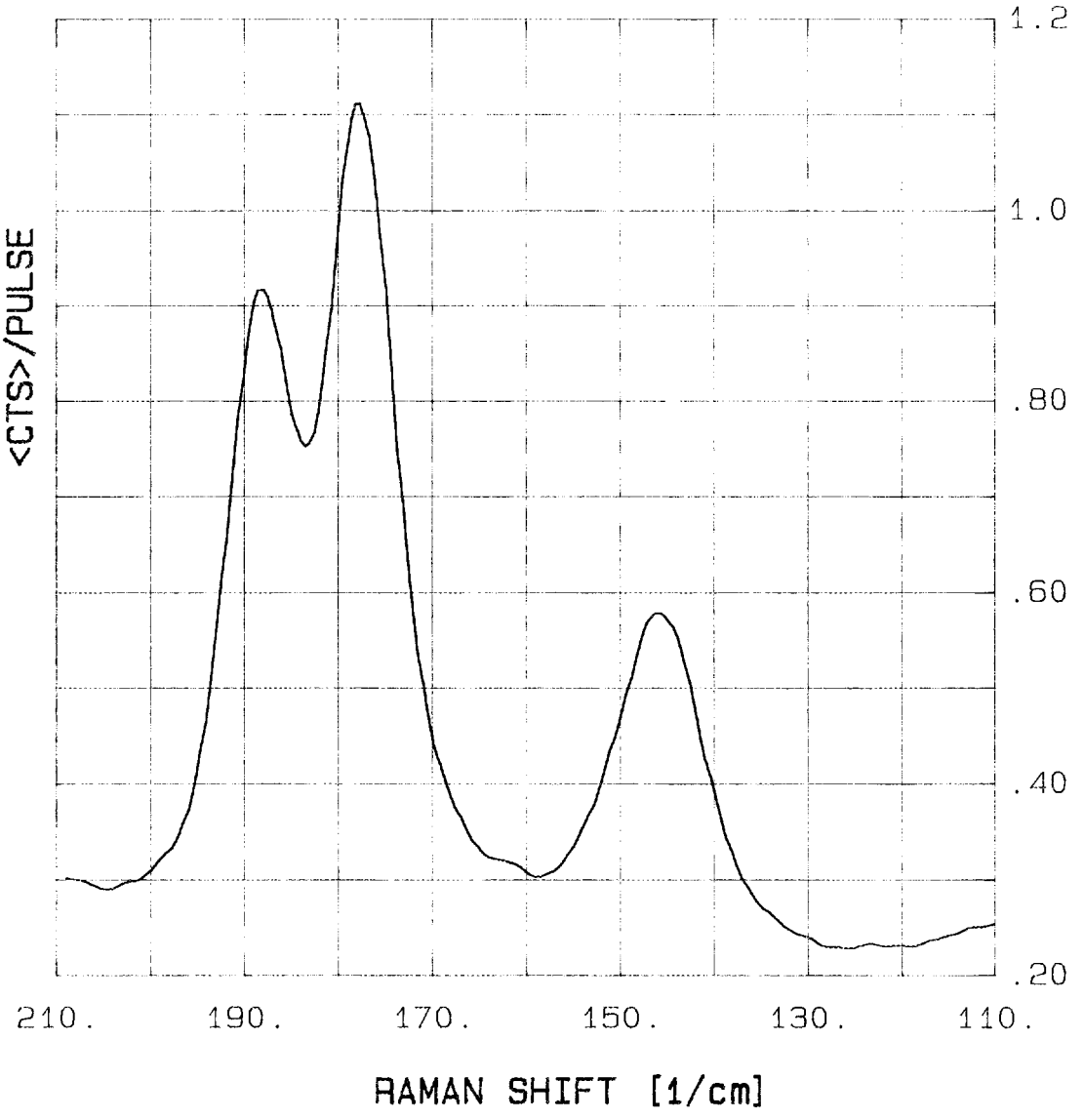

Figure 12. The Raman spectrum of 146 cm^{-1} tetragonal line and the 178-188 cm^{-1} monoclinic line pair of the unstressed end of sample No. 17 of Ceramatec ZTA-XS121 zirconia.

The software developed for this data analysis provides the following processing sequence.

1. The intensity coordinate is coorected to account for the maximum signal limit imposed by grated detection (count saturation).
2. The spectrum is smoothed to remove the random noise component.
3. A background spectrum is selected interactively and subtracted.
4. The peaks in the resulting spectrum can then be integrated between selected points.
5. The results of the analysis are presented in tabular form. Peak height in counts per laser pulse, peak wavenumber position in cm^{-1}, full width at half maximum in cm^{-1}, and the monoclinic fraction x(m) are printed.
6. A plot function is provided for plotting the smoothed, background-subtracted spectrum.

A good example of the effect of fracture on the monoclinic fraction is seen by comparing the spectrum given in Figure 13 to that given in Figure 14 taken on sample No. 10 of Nilcra TS-PSZ. The monoclinic fraction changes from 16% at the unstressed end to 63% at the fractured edge. The results of these measurements are presented in Table 15. The minimum detectable percentage of one phase depends mainly on intensity of the Raman line being measured. For the lines chosen here, a two percent fraction is about at the threshold for measurement of that phase. Furthermore, with almost every sample, it was observed that the Raman intensities were all noticably reduced at the fractured edge compared to the unstressed spectra. This strongly suggests that fracturing causes significant changes in the material that either reduces the effective penetration depth or increases the fraction of cubic phase as was described in the Introduction.

Summary. Measurement and analysis procedures have been developed and applied to a range of fractured samples to quantitatively assess the degree of phase transformation induced by fracturing. The data shows that Raman spectra are quite sensitive to these transformations, and therefore, provides a good diagnostic tool for evaluating these ceramic materials. During the remainder of the current program, this technique will be used to support the mechanical and enviornmental studies on these materials.

A strong effort will be made to establish procedures for determining the fraction of the cubic phase. High spatial resolution (~1 μm) studies using the Raman microprobe will also be carried out on selected samples in the vicinity of cracks or fractures to determine the spatial extent of the fracture-induced transformations. Our goal will be to generate spatial profiles of a given phase.

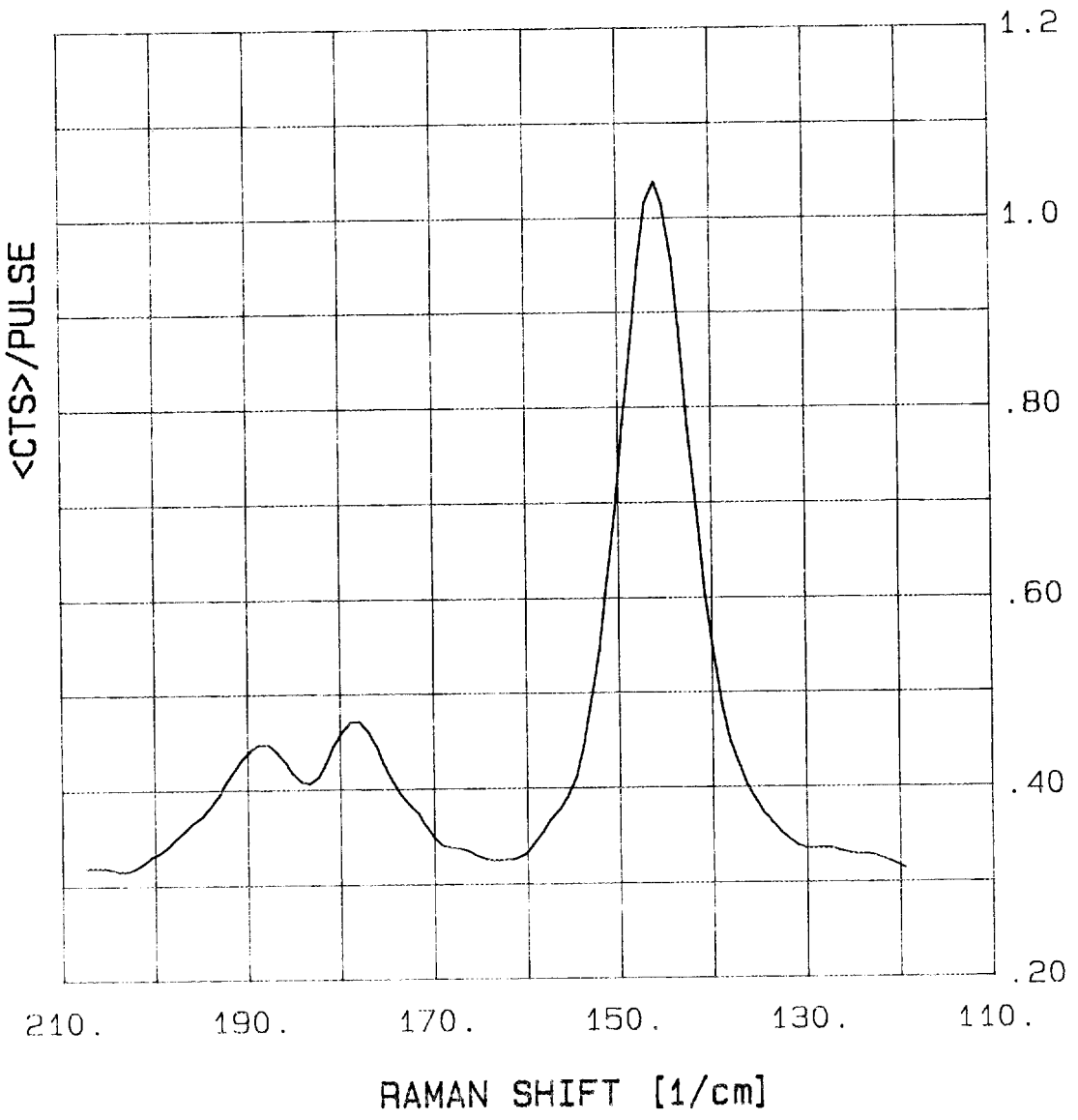

Figure 13. The Raman spectrum of the 146 cm^{-1} tetragonal line and the 178-188 cm^{-1} monoclinic line pair of the unstressed end of Sample No. 10 of Nilcra TS-PSZ zirconia.

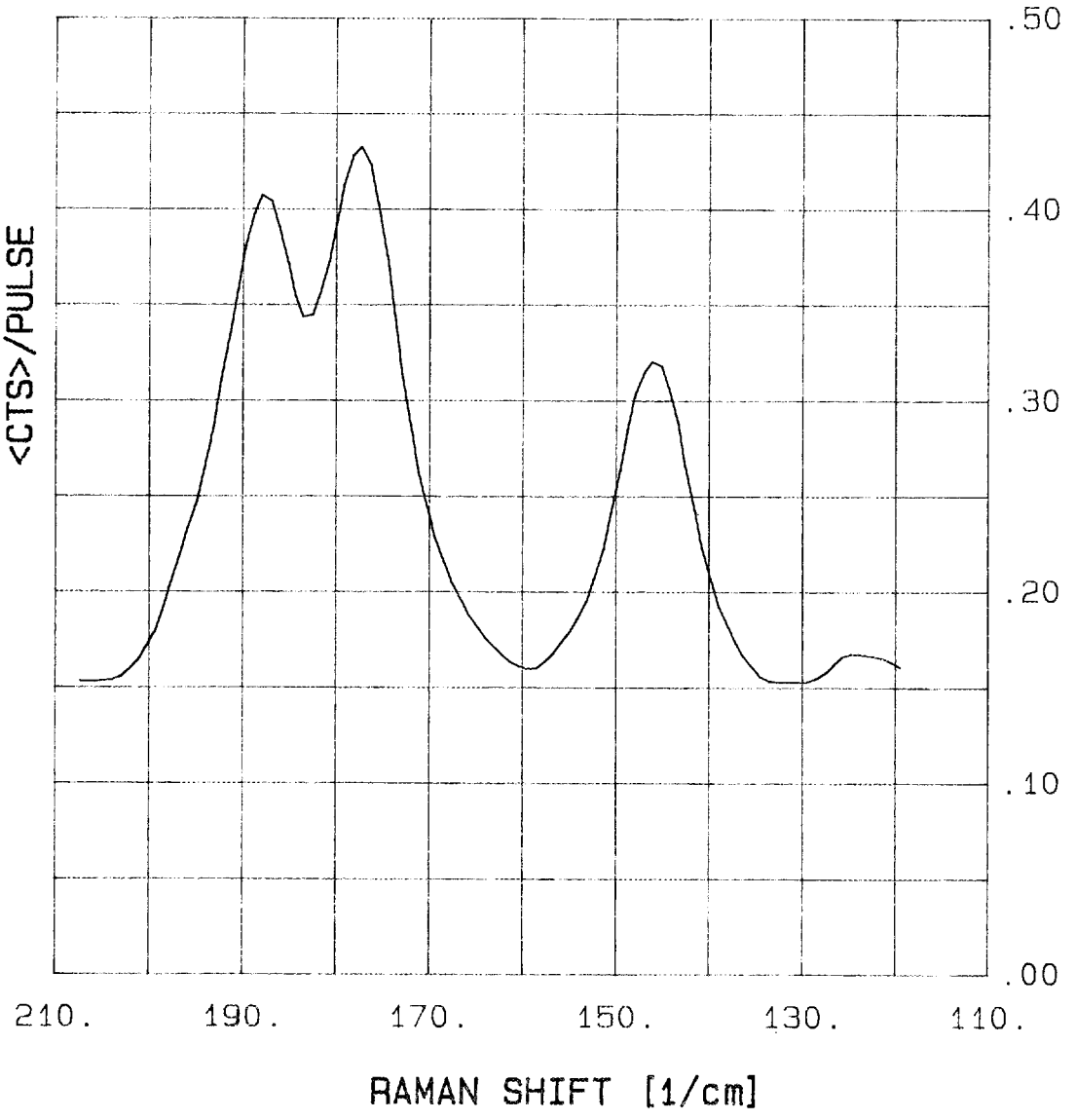

Figure 14. The Raman spectrum of the 146 cm^{-1} tetragonal line and the 178-188 cm^{-1} monoclinic line pair of the fractured edge on the tension side of sample No. 10 of Nilcra TS-PSZ zirconia.

Table 15. The Zirconium Monoclinic Fraction x(m) = 1 - x(t) in Fractured Samples of Transformation-Toughened Ceramics Relative to the Tetragonal Fraction x(t).

Material	Sample Number	Monoclinic Fraction x(m) Unstressed End (Percent)	Monoclinic Fraction x(m) Fractured Edge (Percent)
Ceramatec TZP-XS241	10	10	21
Ceramatec ZTA-SX121	17	65	68
Ceramatec CTZP	13	0	17
Nilcra TS-PSZ	10	16	63
Nilcra MS-PSZ	10	3	12
NGK-Locke Z191	10	0	0
Kyocera DTA-AZ301	10	42	55
Kyocera PSZ-Z201	10	0	0

Statistical analysis of MOR data. A Weibull analysis was performed on available MOR data for the DTA-AZ301, PSZ-201, CTZP, MS-PSZ, and Z191 materials. Maximum likelihood estimates of the Weibull parameters were obtained for each combination of material, environment, temperature, and loading rate which contained at least four MOR test results. This analysis assumes that MOR can be modeled by the Weibull distribution function

$$F(s) = 1 - \exp[-(S/So)^m]$$

where F(s) is the probability that a specimen will have a MOR less than S, So is the scale parameter (characteristic value), and m is the Weibull modulus (shape parameter). Approximately 63% of the population of breaking strengths will have MOR's less than So. Larger values of m imply less scatter in the distribution of MOR values. (The coefficient of variation is approximately equal to 1/m.) For ceramic materials, m is typically in the range of 10 to 20.

Table 16 presents the estimates of the Weibull module ($\hat{m}$) for each combination for which four or more MOR values were available for the five materials. Nine specimens of DTA-AZ301 were tested at 0.5 MPa/s in dry N_2 at 25°C. All other individual test sets contained either four or five MOR values. To indicate the potential scatter in maximum likelihood, estimates of $\hat{m}$, 90% confidence bounds from a sample of size five are given by the interval (0.36 $\hat{m}$, 1.46 $\hat{m}$). For example, if $\hat{m}$ = 15, there

Table 16. Maximum Likelihood Estimates of Weibull Moduli (m).

Atmosphere	Temperature (°C)	Loading Rate (MPa/s)	AZ301	Z201	CTZP	MS-PSZ	Z191
Dry N_2	25	77	18.8	28.7	34.0	25.8	9.4
		0.5	9.9*	15.3	84.5	22.5	13.9
		Composite**	11.2	18.8	43.0	24.3	10.9
	250	77		7.7	10.2	11.3	
		0.5					
		Composite**					
	800	77					
		0.5					
		Composite**					
	1050	77					
		0.5			11.6	23.2	
		Composite**					
10% H_2O	25	77					
		0.5					
		Composite**					
	250	77			14.5	21.7	
		0.5			5.0	14.3	
		Composite**			6.6	17.5	
	800	77					
		0.5					
		Composite**					
	1050	77	5.3		10.9	32.4	17.0
		0.5	6.4		5.9	28.0	11.9
		Composite**	5.7		7.5	26.5	14.2

*Sample size = 9. All other individual loading rate sample sizes were 4 or 5.

**Composite estimates were calculated from pooled loading rate data sets after normalizing by the loading rate scale parameters.

is 90% confidence that the interval (5.4, 21.9) will contain the true value of m.

The maximum likelihood estimates of the scale parameters ($\hat{So}$) are presented in Table 17. The values are representative of the middle (the 63rd percentile) of the distribution of breaking strengths. The 90% confidence limits on So depend on the estimate of the Weibull modulus and the sample size. For a sample size of five, the 90% confidence limits for

Table 17. Maximum Likelihood Estimates of Weibull Scale Parameters (So).

Atmosphere	Temperature (°C)	Loading Rate (MPa/s)	DTA-AZ301	PSZ-Z201	CTZP	MS-PSZ	Z191
Dry N_2	25	77	1311	978	489	694	1062
		0.5	1160*	859	475	637	1052
	250	77		736	551	566	
		0.5					
	800	77					
		0.5					
	1050	77					
		0.5			201	253	
10% H_2O	25	77					
		0.5					
	250	77			449	538	
		0.5			371	467	
	800	77					
		0.5					
	1050	77	602		195	230	304
		0.5	670		167	259	120

*Sample size = 9. All other sample sizes were 4 or 5.

selected m values are given by:

$\hat{m}$	Lower Confidence Limit	Upper Confidence Limit
5	0.801 $\hat{So}$	1.283 $\hat{So}$
10	0.899 $\hat{So}$	1.133 $\hat{So}$
20	0.946 $\hat{So}$	1.064 $\hat{So}$
30	0.964 $\hat{So}$	1.042 $\hat{So}$

For example, for a sample size of five, if $\hat{m}$ = 10, there is 90% confidence that the scale parameter will be estimated with 10 to 13%. The uncertainty in the estimate of So is comparable to that in the estimate of the mean (or median) of a population.

To obtain better estimates of the Weibull moduli, data from the two loading rates were pooled and all other experimental conditions were fixed. This procedure is based on the assumption that the Weibull modulus is independent on loading rate. Since the scale parameters are expected to depend on loading rate (a fundamental assumption of delayed failure theory in ceramics), the MOR values are normalized by dividing the respective

estimate of So. The composite maximum likelihood estimates of the Weibull moduli of the normalized data are also presented in Table 16. This technique presents a composite estimate of m, but confidence bounds for such an estimate are not known.

Finally, the appropriateness of the Weibull model was considered. Samples of size five are not sufficient to demonstrate the adequacy of a probability model, but they may indicate a large departure from an assumed model. No such departures were detected. The pooled data rate (of normalized values) were also analyzed, and no significant departures from a Weibull distribution were detected. As an example, Figure 15 presents the equivalent of a Weibull plot of 14 normalized MOR values from the DTA-AZ301, dry N_2,25°C tests. This is the largest available data set. Deviations from a straight line would indicate the lack of a Weibull fit. The deviations from linear observed in Figure 15 are not significant for a sample size of 14.

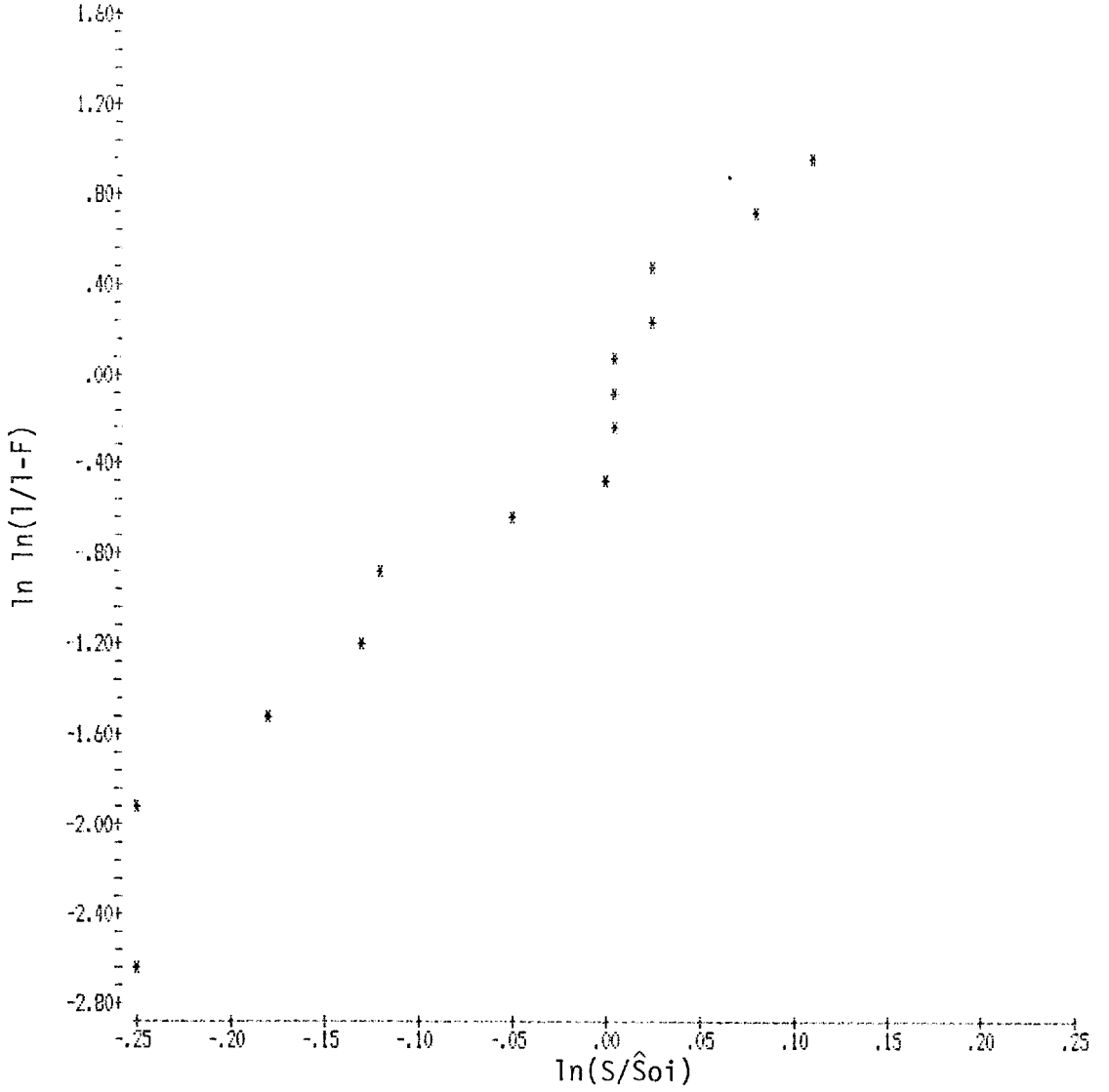

Figure 15. Weibull plot for normalized MOR DTA-AZ301, dry N_2, 25°C.

Table 18 presents estimates of the Weibull parameters from the specimens which were aged for 25 hours at 300°C. Due to the unknown effect of the aging process, these data have been separated from those of the unaged specimens.

Table 18. Maximum Likelihood Estimates of Weibull Modulus (m) and Scale (So) Parameters Aged Specimens, Dry N_2, 25°C 77 MPa/s.

	m	So
DTA-AZ301	13.7	1254
PSZ-Z201	8.0	840
CTZP	28.3	491
MS-PSZ	54.2	681
Z191	6.2	1024

Sample = 5 for all five data sets.

An analysis to quantify the effect of stress rate on MOR was started, but results are not yet available. Since MOR did not increase with stress rate for some of the data sets, the usual methods of analysis may not be appropriate for these data. Larger data sets and more stress rates for the selected materials are also necessary for a more meaningful analysis.

Analysis of modulus of rupture and x-ray diffraction results. The MOR data displayed in Figures 3 through 6 clearly demonstrate the rapid decline in bend strength with increasing temperature. Except for the AZ301 material, the transformation toughened ceramics have an average bend strength of about 200 MPa at 1050°C and between 200 and 300 MPa at 800°C, even though their bend strengths range from 480 to 1000 MPa at room temperature. The AZ301 material has a room temperature bend strength in excess of 1200 MPa and an average bend strength of almost 600 MPa at 1050°C. The transformation toughened ceramics tend to display a linear decrease in bend strength with increasing temperature. The MOR measurements made in dry N_2 tended to be higher than those made in N_2 with 10% H_2O. In addition, the MOR measurements made using the rapid loading rate tended to be higher than the measurements made using the slow loading rate. Although the rapid decline in strength with increasing temperature is of considerable concern, it should be recognized that fully stabilized ZrO_2 has an average reported bend strength of 245 MPa at room temperature which drops to an average value of 145 MPa at 1000°C. Even at 1000°C, the transformation toughened ceramics tend to have a bend strength about 40% higher than fully stabilized ZrO_2.

A matter of greater concern is the plastic or permanent deformation observed in the two Y_2O_3 stabilized ZrO_2 materials (Z191 and Z201) when slow loaded at 1050°C. However, the plastic deformation observed is consistent with the creep behavior reported by Larsen,[6] et al. for Z191 at 1000°C. The very fine particle size ~0.3 μ and the presence of SiO_2 in the Z191 material is thought to account for the deformation behavior observed. It is believed that this deformation or creep is due to grain boundary sliding and plastic flow.

The XRD data (Table 8) suggests that only the MS and TS materials are subject to alteration of the ZrO_2 crystal structure during the MOR testing. However, the results of the Raman data suggest that the crystal structure of the ZrO_2 is altered for most of the specimens at the very surface of the tensile fracture surface (≈ the first 20 μ). It is believed that the large crystal change observed by XRD in the MS and TS materials is due to the temperature effects (1050°C) more than the mechanical effects due to fracture. The lack of crystal change in the Z201 and Z191 materials (Y_2O_3 stabilized) is not readily explainable and will require more study.

Analysis of aging studies. As shown in Table 10, the aging treatment does not always alter the ZrO_2 crystal structure nor as shown in Table 11 does it always alter the bend strength of the aged material. The XS121, XS241, MS-PSZ, and TS-PSZ materials all underwent significant increases in the percent monoclinic phase as a result of aging treatments. Significant decreases in bend strength due to aging was only observed in the Z201 and the XS241 materials (see Table 11). Reduction in bend strength due to aging was the most pronounced in the XS241 material aged for 120 hours at 250°C (≈35% reduction). It should also be noted that the aging treatment resulted in an increase in the bend strengths measured for XS121 and TS-PSZ materials. The cause of this strength increase is not readily apparent and will be studied further.

The XPS analysis of the MS-PSZ and the XS241 materials (see Table 14) before and after aging showed that hydroxyl and water atoms did not increase at the surface of the aged material but rather tended to decrease after aging. The results of the IR studies further reinforces this finding of the XPS analysis. In the hydroxyl or water molecule vibrational regions of ≈3500 and ≈1600 cm^{-1}, there was no significant difference in IR spectra of the as-received and the aged specimens.

In Figure 7, the spectra Z201 shows little difference between the as-received and the aged specimens. The absorption bands observed at 640 and 568 cm^{-1} are attributed to the tetragonal phase of zirconia. However, in Figure 8, for the XS241 spectra (B and C) for the aged specimens, shows a number of differences when compared with that of the as-received specimen (A). The absorption band at 640 cm^{-1} in spectrum (A) decreased in intensity and a broad shoulder at 709 cm^{-1} appeared as the specimen was aged at 250°C for 120 hours and 240°C. At the same time, a new band at 478 and 442 cm^{-1} increased as aging time was increased. The x-ray diffraction data for these specimens also showed an increase in the monoclinic phase as the specimen was aged. These new absorption bands are thought to be attributed to the formation of the monoclinic phase in zirconia.

Figure 9 presents the ATR FT-IR spectra for CTZP specimens in the as-received and aged conditions at 150°C and 250°C for 120 hours, respectively.

The absorption band at 519 cm^{-1} in spectrum (A) shifted to a higher wavenumber with a lowered intensity for both aged specimens. The bands at 630 cm^{-1} and the shoulder at 638 cm^{-1} of the as-received specimen in spectrum (A) were reversed compared to the intensities in the spectra for (B) and (C). A broad band at 776 cm^{-1} of the spectrum (B) was more pronounced as compared with the spectra of (A) and (C), and very weak bands at 465, 452, and 418 cm^{-1} were shown in spectra (B) and (C). However, these spectral differences identified for the CTZP specimens are relatively negligible, and there is little difference between the aged and unaged specimens. These findings are also confirmed by the XRD data.

Figure 10 presents the IR spectra for selected MS-PSZ specimens. The spectra (A), (B), (C), and (D) were obtained for MS-PSZ samples in the as-received condition, aged at 250°C for 120 hours, aged at 800°C for 200 hours, and after MOR testing at 1050°C in 10% H_2O, respectively. A gradual change of the tetragonal phase (A) to the monoclinic phase (D) can be seen at ≈700 cm^{-1} and 475 cm^{-1}. These results are in good agreement with the results of the XRD analysis. The XRD data showed that the major crystal phase for the as-received specimen was tetragonal with 23% monoclinic and 88% monoclinic for the specimen tested at 1050°C in 10% H_2O.

The results of our aging studies are in general agreement with the results reported in the literature for similar studies.[7-13] Although we have been unable to identify the specific mechanisms responsible for the premature surface transformation of tetragonal phase to the monoclinic phase during aging, we have developed a basic description for the process.

The aging process is somewhat complex and depends upon the specific stabilization agent, the quantity (mole/percent) of stabilizer employed, the particle size (which is a function of processing treatment), the amount of moisture present, and the aging temperature.

The complex relationship between the various material parameters and aging effects has been described in the work of Sato,[7,8,9] et al., in the investigation of Y_2O_3 stabilized ZrO_2. The results of his work show that grain size and mole/percent of Y_2O_3 are the dominating factors effecting the amount of transition to the monoclinic phase as a function of aging temperature.

The lower the amount of Y_2O_3 stabilizer and the larger the grain size the lower the aging (critical) temperature necessary to generate significant quantities of transformation. In all cases, the transformation peaked between 200°C and 300°C for most of the materials evaluated.

Aging in water compared to aging in air resulted in a much greater degree of transformation at a much lower critical temperature. It also appears that the higher the moisture content present, the more accelerated the transformation process. The studies by Sato, et al., have also shown that the addition of 5 and 10% Al_2O_3 to the Y_2O_3 stabilized ZrO_2 will inhibit premature transformation due to aging.

Based on the data reviewed, it is definitely apparent that the aging of transformation toughened ceramics in moisture laden environments will promote premature phase transformation on the surface. Although some aging conditions will promote a reduction in strength, the mechanisms involved and the specific relationships between material properties, aging parameters, and strength are not well established. However, it would appear that by controlling particle size and stabilization content,

it may be possible to inhibit, if not completely eliminate, premature phase transformation. A better understanding of the specific mechanism involved in this process would facilitate efforts to prevent phase transformation and strength degradation.

Future plans

During the next several months, the following activities are planned:

1) Complete the mini-matrix test plan in fulfillment of the requirements for Task II.
2) Select the two finalist materials for Task III.
3) Initiate the matrix test plan for the two finalist materials.
4) Continue the aging studies: (a) using the IR equipment try to monitor the aging process in selected samples and (b) investigate the effect of thermal aging in the absence of H_2O on selected transformation toughened materials.

Status of milestones

Milestone 331402 was completed June 30, 1985. Milestone 331403 has not been completed due to delay in receiving the required test samples. Expected date of completion is April 30, 1986.

References

1. R. Loudon, "The Raman Effect in Crystals," *Advan. Phys.* 13, 423 (1964).

2. CRC Handbook of Chemistry and Physcis, edited by R. C. Weast, 65th Edition, B-161, 1984-85.

3. A. Feinberg and C. H. Perry, "Structural Disorder and Phase Transitions in ZrO_2-Y_2O_3 System," *J. Phys. Chem. Solids* 42, 513, 1981.

4. D. R. Clarke and F. Adar, "Measurement of the Crystallographically Transformed Zone Produced by Fracture in Ceramics Containing Tetragonal Zirconia," *J. Am. Ceram. Soc.* 65, 284, 1982.

5. C. H. Perry and D. W. Liu, "Phase Characterization of Partially Stabilized Zirconia by Raman Spectroscopy," *J. Am. Ceram. Soc.* 68, C-184, 1985

6. D. C. Larsen and J. W. Adams, "Long-Term Stability and Properties of Zirconia Ceramics for Heavy Duty Diesel Engine Components," DOE/NASA/0305-1, NASA CR-174943, September 1985, NASA Lewis Research Center, Cleveland, Ohio.

7. T. Sato, S. Ohtaki, and M. Shimada , "Transformation of Yttria Partially Stabilized Zirconia by Low-Temperature Annealing in Air," *J. Mat. Sci.* 20, 1466-1470, 1985.

8. T. Sato and M. Shimada , "Transformation of Yttria-Doped Tetragonal ZrO_2 Polycrystals by Annealing in Water," *J. Am. Ceram. Soc.* 68[6], 356-359, 1985.

9. T. Sato and M. Shimada , "Crystalline Phase Change in Yttria-Partially-Stabilized Zirconia by Low-Temperature Annealing, Communications of the American Ceramic Society, October 1984, C-212.

10. R. L. K. Matsumoto, "Strength Recovery in Degraded Yttria-Doped Tetragonal Zirconia Polycrystals," *J. Am. Ceram. Soc.* 68[8], C-213, 1985.

11. T. Sato and M. Shimada, "Transformation of Ceria-Doped Tetragonal Zirconia Polycrystals by Annealing in Water," *Am. Ceram. Soc. Bull.* 64[10], 1382-1384, 1985.

12. Y. Murase and E. Kato, "Role of Water Vapor in Crystallite Growth and Tetragonal-Monoclinic Phase Transformation of ZrO_2," *J. Am. Ceram. Soc.* 66[3], 196-200, 1983.

13. K. Kobayashi, H. Kuwajima, and T. Masaki, "Phase Change and Mechanical Properties of ZrO_2-Y_2O_3 Solid Electrolytic After Aging," *Solid State Ionics 3/4*, 489-493, 1981.

3.4 FRACTURE MECHANICS

3.4.1 Fracture Mechanics

Improved Methods for Measuring the Fracture Resistance of Structural Ceramics

R. C. Bradt and A. S. Kobayashi (University of Washington)

Objective/Scope

The long-term goals of this study are to develop and demonstrate a technique comprising a single measurement, or a technique comprising a set of correlative measurements for structural ceramics, including monolithic and composite materials, which will allow the reliable and accurate determination of their resistance to fracture (crack propagation) over the temperature range from 25°C to 1400°C.

Technical Progress

Using the chevron-notch method, additional room temperature data has been generated for monolithic Si_3N_4 (GTE A2Y6) and SiC (Hexaloy) materials that were started during the last reporting period. The two composites that were received for preliminary evaluation include an Al_2O_3 matrix / 25 vol% SiC whisker composite and an Al_2O_3 matrix / 7.5 vol% SiC whisker composite. Both were obtained from ARCO Metals Co.

The computer program used previously only for the calculation of fracture toughness has been expanded to include capabilities for plotting of J_R, G_R and K_R curves, and also the determination of the work of fracture from the digitized load-displacement data, taken directly from the test machine.

Some of the initial room temperature, monolithic data has been reduced and is shown in Table I. The work of fracture, as calculated by the computer program (CHEVRP), is compared with the K_{IC} values and the respective standard deviations. The test data of the Al_2O_3 matrix / 25 vol% SiC whisker and the Al_2O_3 matrix / 7.5 vol% SiC whisker chevron notched bend specimens presented in Table II have been analysed using the computer program described above.

The "ANSYS" finite element numerical model, consisting of eight noded (3 DOF/node) bricks with 1000 degrees of freedom in the solution, is being modified to use a finer mesh. When compared with the Bluhm slice model and the Sakai modified slice model, the 3-D method has been consistently stiffer. This modification will test the validity of the current 3-D analysis by considering the effect of mesh size on stiffness. Progress of this task has been somewhat limited by main frame computer time availability. This problem is being rectified by the implementation of an in-house, dedicated computer.

The high temperature test furnace has been installed and tested to 1200°C. Larger heating elements and improved sealing will be necessary to obtain the goal of 1400°C. These items are in progress.

Status of Milestones

Progress on milestones is satisfactory with the exception of the ceramic composite materials. It is evident that although preliminary composite test specimens have been received and tested, the receipt of the complete series of specimens for that portion of the program will be slightly delayed.

Problems Encountered

No serious problems have been encountered during this period.

Publications

The paper on laser interferometry is being finalized during this report period:

Fracture Toughness Testing of Ceramics Using a Laser Interferometric Strain Gage, (ACerS. PCRM at Irvine)

Two papers are being written.

1. Fracture Arrest in a Ceramic-Ceramic Composite
2. A 3-D Finite Element Analysis of the Chevron Notched 3-Point Bend Specimen

References

1. J.I. Bluhm , "Slice Synthesis of a Three Dimensional Work of Fracture Specimen", *Eng. Fract. Mech.* 7, 593-604, (1977).

2. M. Sakai, et al., "Numerical Fracture Analysis of Chevron Notched Specimens: I, Shear Correction Factor, k", *J. Amer. Ceram. Soc.* 66(5), 371-375, (1983).

3. M. Sakai, et al., "Numerical Fracture Analysis of Chevron Notched Specimens: II, Stability Condition for Crack Growth", *J. Amer. Ceram. Soc.* 66(5), 376-379, (1983).

4. M. Sakai and R. C. Bradt, "Graphical Methods for Determining the Nonlinear Fracture Parameters of Silica and Graphite Refractory Composites", in: *Proceedings of the Fourth International Symposium on the Fracture Mechanics of Ceramics*, V.P.I. (1985).

Table I
Fracture Testing
(Chevron Notched 3 Point Bend)

a/W	K_{IC} (MPa $m^{\frac{1}{2}}$)	WOF (J/m^2)
	Si_3N_4 (GTE A2Y6)	
0.38	7.99	86.5
0.36	7.80	91.1
0.37	7.99	84.3
0.35	7.01	75.9
Mean	7.70 ± 0.47	84.5 ± 6.36
	SiC (Hexaloy)	
0.33	3.31	10.4
0.34	2.43	8.89
0.34	3.08	8.32
0.32	2.91	10.0
0.30	4.34	12.9
0.29	3.83	11.3
0.29	3.06	10.7
Mean	3.28 ± 0.63	10.4 ± 1.52

Table II
Fracture Testing
ARCO Al_2O_3/SiC COMPOSITES
(Chevron Notched 3 Point Bend)

a/W	K_{IC} (MPa $m^{\frac{1}{2}}$)	WOF (J/m^2)
	A4AS	
0.47	4.93	21.3
0.45	5.22	24.1
0.49	4.87	21.1
0.44	4.07	21.1
0.34	4.87	26.7
0.33	4.87	24.2
0.38	4.30	21.3
0.36	4.71	25.6
0.35	4.52	27.4
Mean	4.71 ± 0.35	23.6 ± 2.54
	SA25	
0.43	5.98	43.3
0.39	5.38	36.3
0.29	6.75	38.6
0.34	6.11	45.5
0.32	6.63	50.8
0.25	5.08	42.4
0.34	5.56	41.0
0.36	5.77	37.8
0.33	6.39	43.1
0.35	5.75	36.9
0.36	6.09	*
0.38	5.87	*
0.37	5.91	*
Mean	5.94 ± 0.47	41.6 ± 4.24

*No WOF due to incomplete data record

Testing and Evaluation of Advanced Ceramics at High Temperature in Uniaxial Tension

J. Sankar and V. S. Avva (North Carolina A & T State University)

Objectives/Scope

The purpose of this effort will be to test and evaluate advanced ceramic materials at temperatures up to 1500°C in uniaxial tension. Testing may include fast fracture strength, stepped static fatigue strength, and cyclic fatigue strength, along with analysis of fracture surfaces by scanning electron microscopy. This effort will comprise the following tasks:

Task 1. Specifications for Testing Machine and Controls + (Procurement)
Task 2. Identification of Test Material (s) + (Procurement of Specimens)
Task 3. Identification of Test Specimen Configuration
Task 4. Specifications for Testing Grips and Extensometer + (Procurement)
Task 5. Specifications for Testing Furnance and Controls + (Procurement)
Task 6. Development of Test Plan
Task 7. High Temperature Tensile Testing
Task 8. Reporting (Periodic)
Task 9. Final Report

It is anticipated that this two (2) year program will help in understanding the behavior of ceramic materials at very high temperatures in uniaxial tension.

Technical Progress

During the past six (6) months attentions were given simultaneously to all Tasks 1-5 with special attentions to Tasks 3 and 4. The MTS 880 Automated Materials Testing Machine ordered under Task 1 is now at A & T. Presently calibration and familiarizing of the machine is underway. As reported previously GTE Silicon Nitride SNW-1000 is selected as the candidate material for the program.

During the reporting period much attention was focused on coming up with the proper test specimen configuration. Various specimen configurations were investigated during the reporting period and quotations were received from GTE for fabricating GTE Silicon Nitride SNW-1000 button head circular cross-sectional tensile samples. Unfortunately the samples design which was reported previously has to be slightly changed now to overcome some difficulties which are anticipated from this previous design. Discussion with Ken Liu, who used similar desigh for Alumninum Oxide samples at ORNL revealed that the shank area which was 10 mm (.39") in diameter prematurely cracked under gripping pressure during testing.

Attached is the final drawing for the SNW-1000 Silicon Nitride Tensile Test Specimen. In the new sketch the shank diameter had been changed to 12 mm (.47") from the previous 10 mm (.39") and the shank-button head joint radius of curvature to 3 mm R (.12 R) from 4 mm R (.16 R). With all other previous parameters remaining the same, this has resulted in a longer length in the neck section thereby increasing the overall length to 152 mm (6"). Other specimen dimensions, tolerances and the surface finish requirements are given in the figure. Ordering of the samples from GTE is presently underway.

As far as the test grips are concerned (Task 4), a grip similar to the hydraulic self-aligning grip system suggested by K. C. Liu of ORNL for his program "Tensile Cyclic Fatigue of Structural Ceramics" is selected. These grips which are fabricated through the Tennessee Tool and Engineering Inc., Oak Ridge are already now at A & T and being mounted on the MTS 880 system.

Status of Milestone

Tasks 1-4 are complete. Specifications for the high temperature holders are being worked out now. Furnace specifications are also being modified to accomodate the new specimen and load train design.

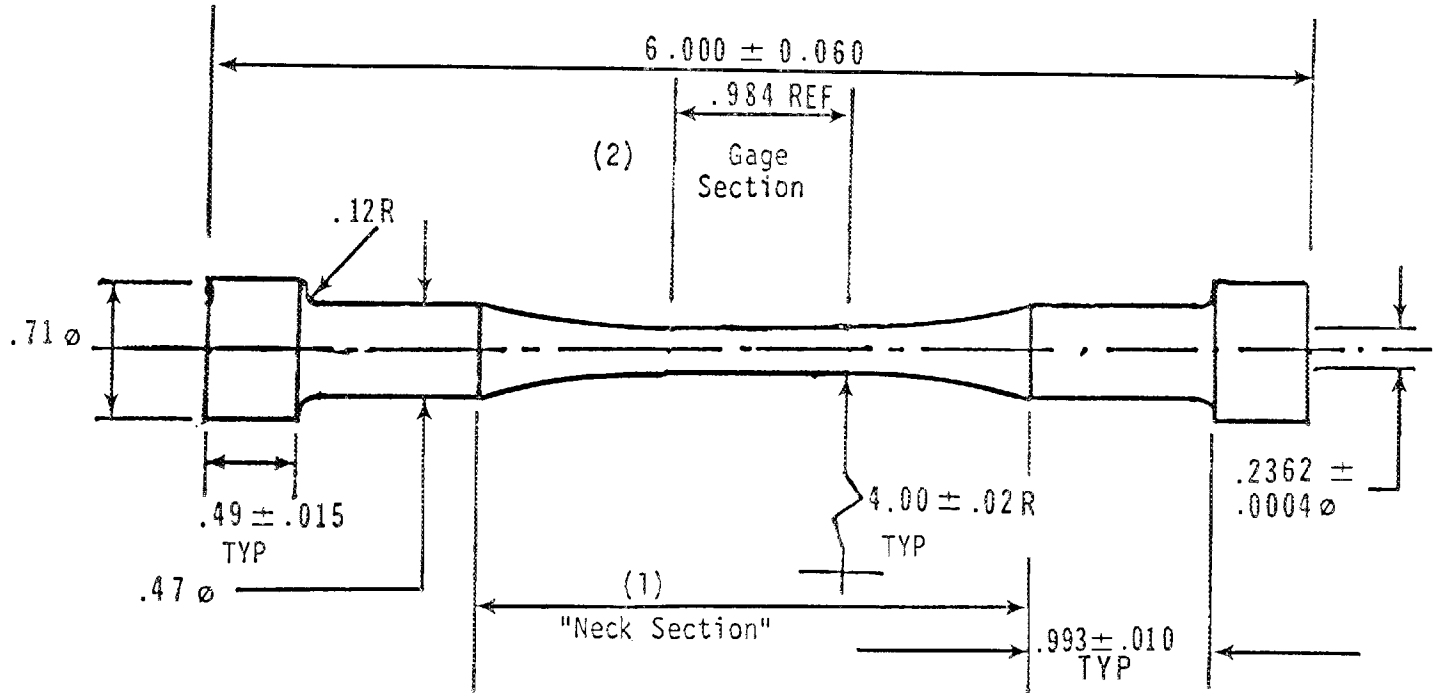

NOTES:

(1) "Neck Section" to be ground and lapped to 8 to 12 μ-IN finish (minimum) after firing. Lapping operation must remove .003 inches minimum of material stock.
(2) "Gage Section"O.D to be round within .0004 in.
(3) Break sharp edges. (.005-.015)
(4) Handle carefully. Each specimen to be packed individually in protective packaging.
(5) All dimensions in inches.

Figure 1. SNW-1000 Tensile Test Specimen Geometry.

Standard Tensile Test Development

S. M. Wiederhorn, Leon Chuck and Tze-jer Chang
(National Bureau of Standards)

Objective/Scope

This project is concerned with the development of test equipment and test procedures for measuring the strength and creep resistance of ceramic materials at elevated temperatures. The goal of the project is to assist in the development of a reliable data base that can be used for structural design of heat engines for vehicular applications.

The mechanical strength of ceramic materials is usually measured in a flexural test configuration because of the ease of conducting such tests on these materials. Flexural tests are also relatively inexpensive to run, requiring a minimum of effort in the way of specimen preparation and test facility construction. Specimens consisting of small rectangular parallel pipeds are prepared by simple grinding and polishing operations, and testing is usually conducted with a simple compressive load train.

Despite the usefulness of flexural testing as a general means of characterizing strength, the technique is not capable of providing critical engineering data for structural design. At low temperatures the technique measures strength on a limited volume, which is usually not sufficient for the extreme value statistics required for lifetime prediction on this materials. At elevated temperatures creep occurs in ceramics and as a consequence the stress distribution within the test specimen changes with time, precluding an accurate analysis of the creep and creep rupture process. Crucial for purposes of design, such analyses require testing in pure states of stress: both compression and tension are required. Whereas compressive testing is relatively simple, tensile testing is not, and there is a pressing need for a relatively inexpensive tensile test that can be used routinely to obtain strength and creep data.

In this program an inexpensive technique of measuring the creep and strength of ceramics at elevated temperatures is being developed and will be used to characterize the mechanical behavior of structural ceramics at elevated temperatures. The test method will be inexpensive, using self aligning test fixtures, and simple grinding techniques for specimen preparation. Creep data obtained with this technique will be compared with data obtained from other tensile test techniques, and with data obtained by flexure and compressive creep studies.

Technical progress

An experimental loading fixture and test specimen has been developed which is of a unique design. Shaped like a clothespin, the test fixture permits experiments to be conducted in compressive

loading, which is of advantage at elevated temperature. The equipment is capable of studying creep in structural ceramics to a temperature of 1500°C and, has been used at a temperature as high as 1380°C. A schematic diagram, and photographs of the test fixture are show in figure 1. As can be seen the test fixture consists of two levers, the lower one resting against the flat surface of a ram that is attached to a load cell via a push rod that exits the bottom of the furnace. The upper lever is of a split design to avoid bending forces about the broad face of the simple dog bone shaped specimen used with this fixture. Load reversal is accomplished by a roller bearing that is located between the two levers. The roller bearing is half-way between the point of load application and the tensile specimen, so that the load on the specimen is of the same magnitude as the external applied load. The shoulders of the test specimens are rounded to permit self alignment along an axis perpendicular to the narrow face of the specimen.

Specimens are made by simple grinding operations. A block of material with two of the dimensions equal to the height and width of the test specimens is reduced in cross-section using a shaped grinding wheel, which leaves the cross-section of the block identical to that of the cross-section of the test specimen. A thin diamond cutting blade is then used to cut specimens from the block. Using a special fixture to hold each specimen, the shoulders are then rounded for self alignment. Following this procedure, an initial batch of 35 test specimens were made in the NBS grinding shop. The estimated cost of these specimens was approximately $60 each, which makes them only three times as expensive as flexural test bars from the same material. The price per specimen is, however, much less than other specimens that have been used the past creep studies. If this experimental configuration works out well, additional specimens will be made from the other materials used in the project.

Initial tests are being conducted at 1300°C, on a commercial grade of sintered siliconized, silicon carbide (KX-01). The test temperature is sufficiently high that the silicon behaves as a soft metal. Consequently, specimens creep at a reasonable rate for this study, 10^{-10} sec^{-1} to 10^{-6} sec^{-1}. To obtain accurate measurements of the creep rate, displacement measurements were made directly on the gauge section of the specimens. A high resolution telescope with a working distance of approximately 10 cm was constructed to view the specimen surface. The gauge section was marked with a set of alpha silicon carbide flags that were glued onto the specimen gauge section. At elevated temperatures, the flags sintered to the gauge section and hence were firmly attached to the specimen, figure 2. To enhance visibility of the flags, platinum wires were attached to each flag. The surface of the flags were marked with linear indentations so that the position of the wires could be monitored during creep with the telescope. A high-intensity, fiber optics tungsten lamp was used for illumination, and a blue-green filter was used to screen the background radiation from the furnace. Using this system, the displacement during creep could be measured to an accuracy of approximately 2 micrometers, at 1300°C.

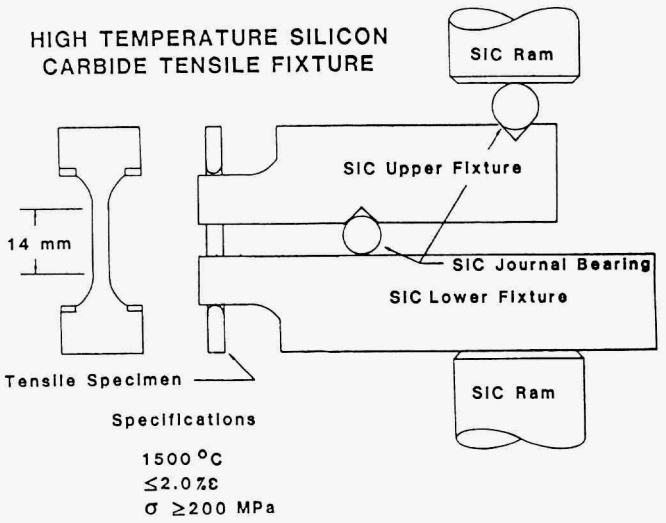

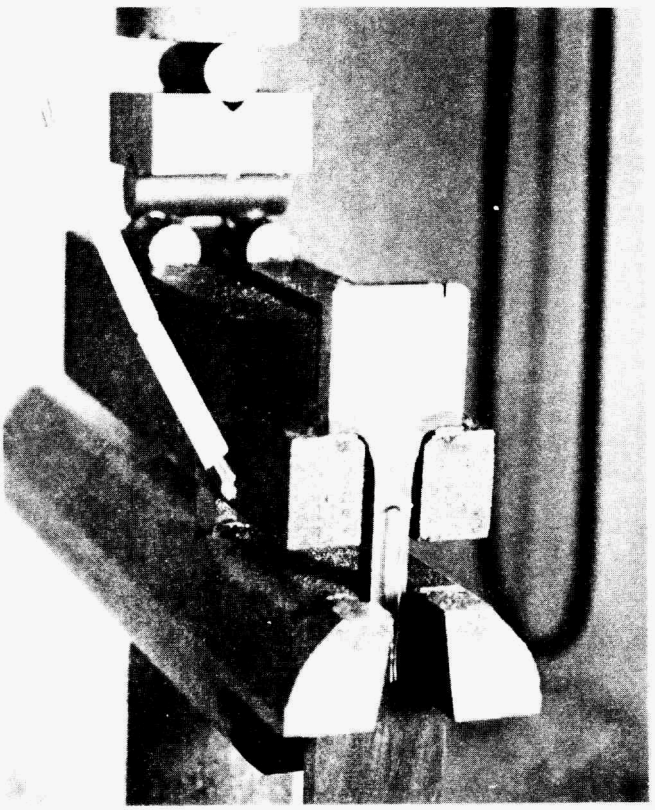

Figure 1. Clothespin Design test fixture: (a) Schematic of fixture and test specimen; (b) photograph of test fixture mounted in furnace. Specimen is mounted to the fixture and flags are attached to the gauge section of the specimen. The location of the thermocouple which is used to measure the temperature of the specimen is also apparent on the figure.

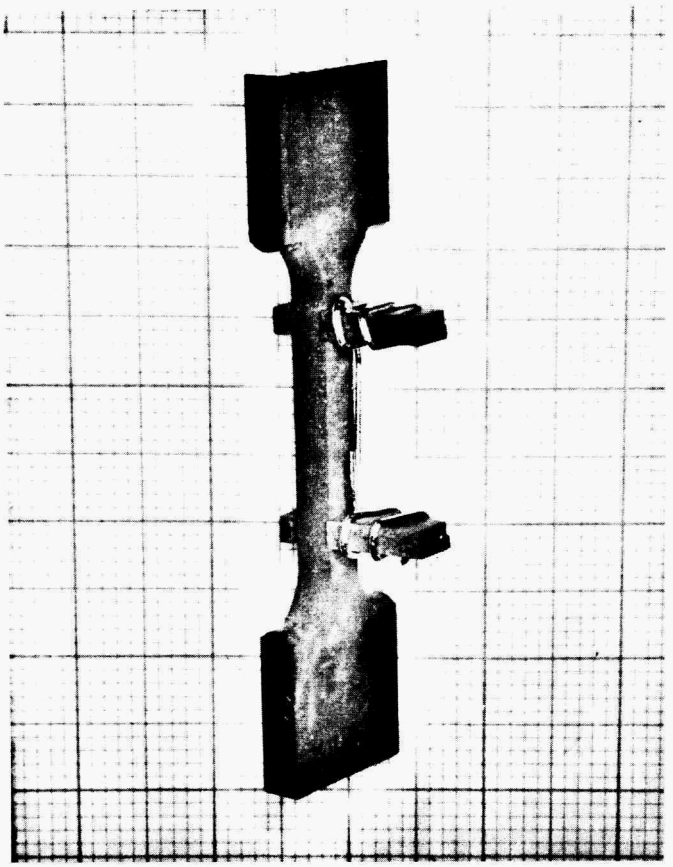

Figure 2. Photograph of the alpha silicon carbide flags that are used to measure the displacement of the gauge of the specimen during deformation. The linear indentations in the platinum wires are not visible in this figure.

Creep tests on siliconized, silicon carbide specimens prepared by the NBS grinding shop are being carried out at 1300°C at applied stresses ranging from 75 to 200 MPa, for periods of the order of 200 hours. The system is capable of determining displacements to an accuracy of approximately 2 micrometers which permits creep rates as low as 10^{-10} sec^{-1} to be measured. In the eight tensile tests conducted to date, the test fixture has performed well. However, two of the fixtures have broken, suggesting the need for a stronger grade of silicon carbide for higher stresses. Studies suggest that steady state creep occurs in siliconized, silicon carbide at approximately 20 hours after load application, figure 3. This result contrasts with bending creep studies on this material, in which transient creep was observed for periods of time ranging up to hundreds of hours. Because the characterization of creep in complex loading is important to the development of engineering criteria for structural design, one of the first investigations to be conducted will be directed towards the resolution of this difference in creep behavior.

Since bending leads to parasitic stresses, which are not a result of the applied tensile stress, a full evaluation of the accuracy and reproducibility of the tensile creep test being developed requires a determination of the bending that occurs during the test. To evaluate the amount of bending, an apparatus was constructed for us by Professor K. Jakus of the University of Massachusetts. The equipment is similar in design to that of a Talysurf Profilometer, but is capable of measuring surface displacement over much longer distances (~5 cm). The stylus used to contact the surface is a sapphire sphere which reduces wear during contact. The equipment is controlled by a computer so that the curvature of the specimen can be calculated directly from the displacement data. The curvature is used to calculate the strain due to bending. Preliminary investigations suggest that strain in bending is approximately 10 percent of that in tension. Once the construction of the equipment has been completed, it will be used to monitor bending of tensile specimens from this and other laboratories.

Status of Milestones

Test technique development: To date all milestones have been met or are on target. The clothespin design test fixture has been constructed and is operational. The construction of a second test fixture using a more standard pin and clevis fixture has been started, and should be completed by 9/86. If agreement is obtained between these two techniques, the construction of a third type of test fixture (powder grip design) will be canceled.

Comparison of Creep data obtained in tensile testing with that obtained in compression and bending: This portion of the program is ahead of schedule. Creep data has already been obtained in bending; compressive creep equipment is being constructed. Data collection on this portion of the program will be completed as of 9/86. Two lectures on this subject will be presented at the Annual Meeting of the American Ceramic Society in May. In collaboration with T.-J. Chuang who is supported by the Fossil Energy program of the Department of Energy, a

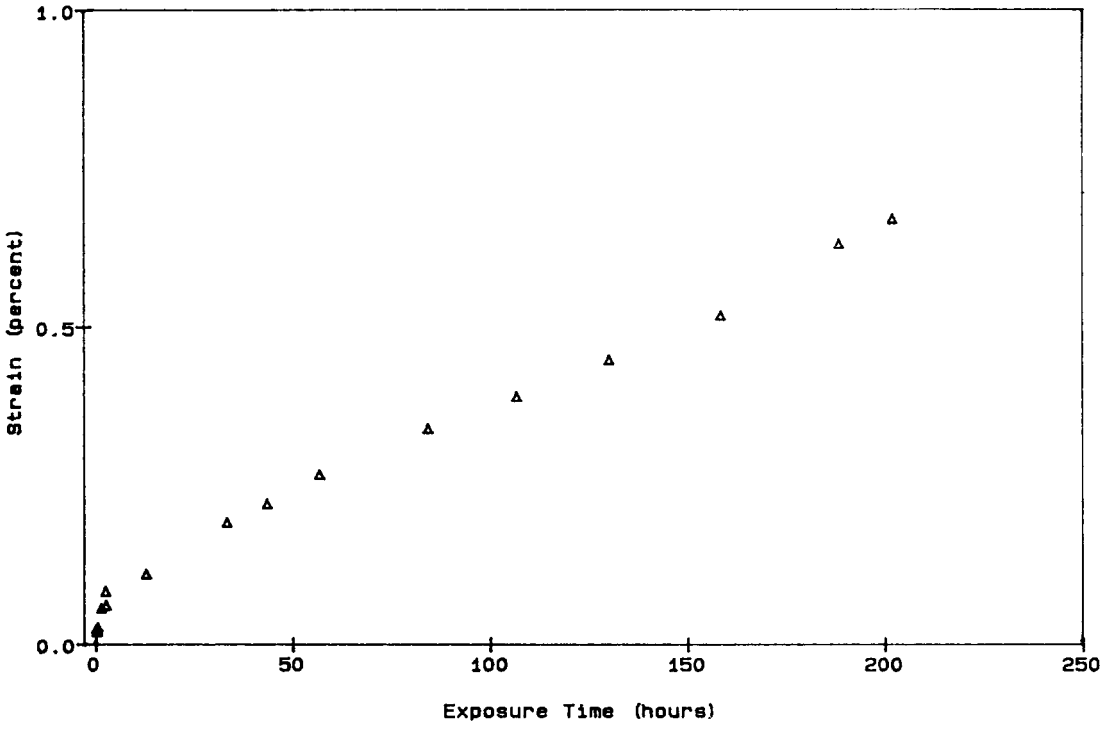

Figure 3. Creep data obtained on siliconized, silicon carbide (KX-01), at 1300°C and a load of 100 MPa. Transient creep in this specimen lasts for only 20 hours.

transient stress analysis of creep in bending has been completed. This analysis will be used to explain our creep data. A paper on this subject will be written by 12/86.

Interlaboratory comparison of tensile test method: Although the milestones for this portion of the program lie in the future, a comparison is being made between our data and that collected at Pennsylvania State University on the same material. We view this comparison as a prelude to a interlaboratory comparison on tensile test techniques for ceramic materials at elevated temperatures.

Publications

"Design Criteria for High Temperature Structural Applications" S.M. Wiederhorn and E.R. Fuller, Jr. Proceedings of the Second International Symposium "Ceramic Materials and Components for Engines," Lübeck-Travemünde, Federal Republic of Germany, April 14-17, 1986.

3.5 NONDESTRUCTIVE EVALUATION DEVELOPMENT

Nondestructive Examination
R. W. McClung (Oak Ridge National Laboratory)

Objective/scope

The purpose of this program is to conduct nondestructive evaluation (NDE) development directed at identifying approaches for quantitative determination of conditions (including both properties and flaws) in ceramics that affect the structural performance. Those materials that have been seriously considered for application in advanced heat engines are all brittle materials whose fracture is affected by structural features with dimensions on the order of the dimensions of their microstructure. This work seeks to characterize those features by using high-frequency ultrasonics and radiography to detect, size, and locate critical flaws and to measure nondestructively the elastic properties of the host material.

Technical progress

Ultrasonics – W. A. Simpson, Jr.

We have received a high-speed ultrasonic peak detector that was ordered to permit recording of small flaws in ceramics. This unit is capable of responding to the single occurrence of one-half cycle of a 100-MHz signal. Upon receipt of the detector, we scanned a partially stabilized zirconia standard that had previously been shown to contain numerous voids about 25 μm in diameter. Using an external 120-MHz, 20-dB-gain preamplifier to boost the total gain of the system, we found that the scattering from such flaws could easily drive the peak detector to full-scale output even when the repetition rate of the ultrasonic pulser was reduced to a value that would permit only a single occurrence to be acquired.

Because the peak detector is a digital instrument with internal digitization of the acquired signal, we modified our system scan controller to permit the detector output to be interfaced to our minicomputer. The system presently digitizes the ultrasonic signal amplitude but has an upper frequency limit of about 20 MHz. With the integration of the new detector, we can generate ultrasonic gray-scale C-scans at frequencies from 1 to 100 MHz.

As an initial test of the new system, we used a 50-MHz center-frequency transducer to scan three zirconia modulus of rupture (MOR) bars that we had previously examined with a conventional 20-MHz ultrasonic system and for which we reported the detection of eight flaws having amplitudes equivalent to or larger than a 250-μm (0.01-in.) manufactured flaw. All eight of these flaws were detected and recorded with the new system (in fact, all eight yielded signals sufficiently large to saturate the detector) and scores of smaller indications as well. In particular, two of the bars were found to have clusters of 20 to 50 indications (all but two of which were smaller than the signal from a 250-μm discontinuity) within a 0.4-cm^2 area.

Figure 1 shows the results obtained on three zirconia bars. The figure is plotted in gray scale so that the full range of scattering amplitudes can be depicted. The black specks are caused by scattering from discrete sources within each bar and represent discontinuities in the local acoustic properties of the ceramic. These discontinuities all lie at a depth of about 1.5 mm; additional scans would be necessary to fully cover the volume of each bar.

These samples were scanned with both 25- and 50-MHz broad-band transducers, and the results were virtually identical. This is not surprising, because the relatively large grain size in this material causes severe scattering losses and limits the maximum frequency to about 35 MHz.

A second sample, fabricated on another program and containing a 125-μm (0.005-in.) manufactured discontinuity in silicon, was available for study. A scan of this sample indicated that the flaw could easily be detected and recorded, driving the peak detector to full-scale output with a gain reserve of about 16 dB.

The next sample examined was a small piece of partially stabilized zirconia that contained a number of naturally occurring indications whose frequency-dependent scattering characteristics were previously reported to imply a diameter of about 25 μm. With maximum gain of the system, these indications were recorded at about 75% of the full-scale output of the peak detector. With a scan index of 25 μm, all indications were repeatedly and reliably detected and recorded.

Several pieces of monolithic silicon nitride were also available for evaluation, and preliminary examination indicated that there was little bulk scattering loss from these specimens up to the 100-MHz limit of our system. Accordingly, a 645-mm^2 (1-$in.^2$) area was scanned with a 50-MHz broad-band transducer whose −20-dB upper-frequency limit exceeds 80 MHz. Figures 2 and 3 show the results. In Fig. 2, the data are presented in gray scale, and numerous indications can be seen as well as a periodic variation in the background brightness, which is probably caused by density variations in the ceramic. The light streak at the right of the figure is a surface feature.

Figure 3 shows the same data plotted in a manner such that only those features whose scattering amplitude exceeds a threshold are plotted. This shows only the flaws; the threshold is 6 dB below the full-scale output of the peak detector, so the indications shown in the figure have relatively large amplitudes. As before, the backscattering spectra from some of the smallest of these indications imply a diameter of about 25 μm.

We have also received on loan three silicon nitride standards from GTE Products Corp. These samples (I, II, and III) contain manufactured flaws consisting of, respectively, numerous 100- to 200-μm voids; three "cracks" 200 μm thick by 1.5 mm^2; and cylindrical voids 100 μm in diameter by 1.5 mm long. Because of the relatively large size of these flaws, a 25-MHz center-frequency transducer was found to be sufficient. Figures 4 through 6 show the constant gain results on the three samples. In Figs. 5 and 6, several indications in addition to the intended flaws were detected, and there is apparently only a single manufactured defect in sample III. Figure 7 shows the data from sample II in pseudo three-dimensional form, which generally provides better amplitude discrimination than even a gray-scale presentation.

ORNL-DWG 86-10214

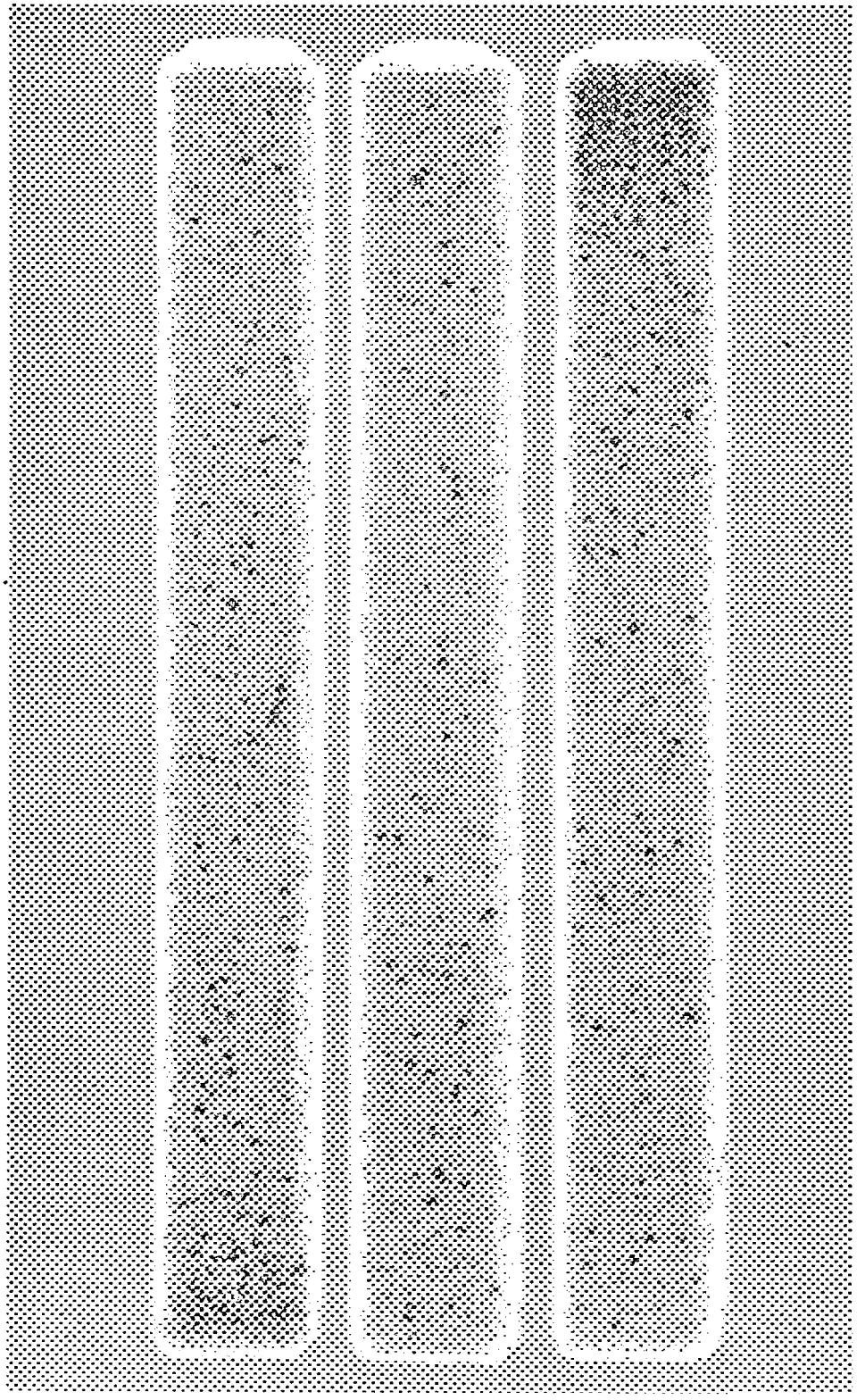

Fig. 1. Zirconia modulus of rupture (MOR) bars, showing numerous ultrasonic indications.

ORNL-DWG 86-10216

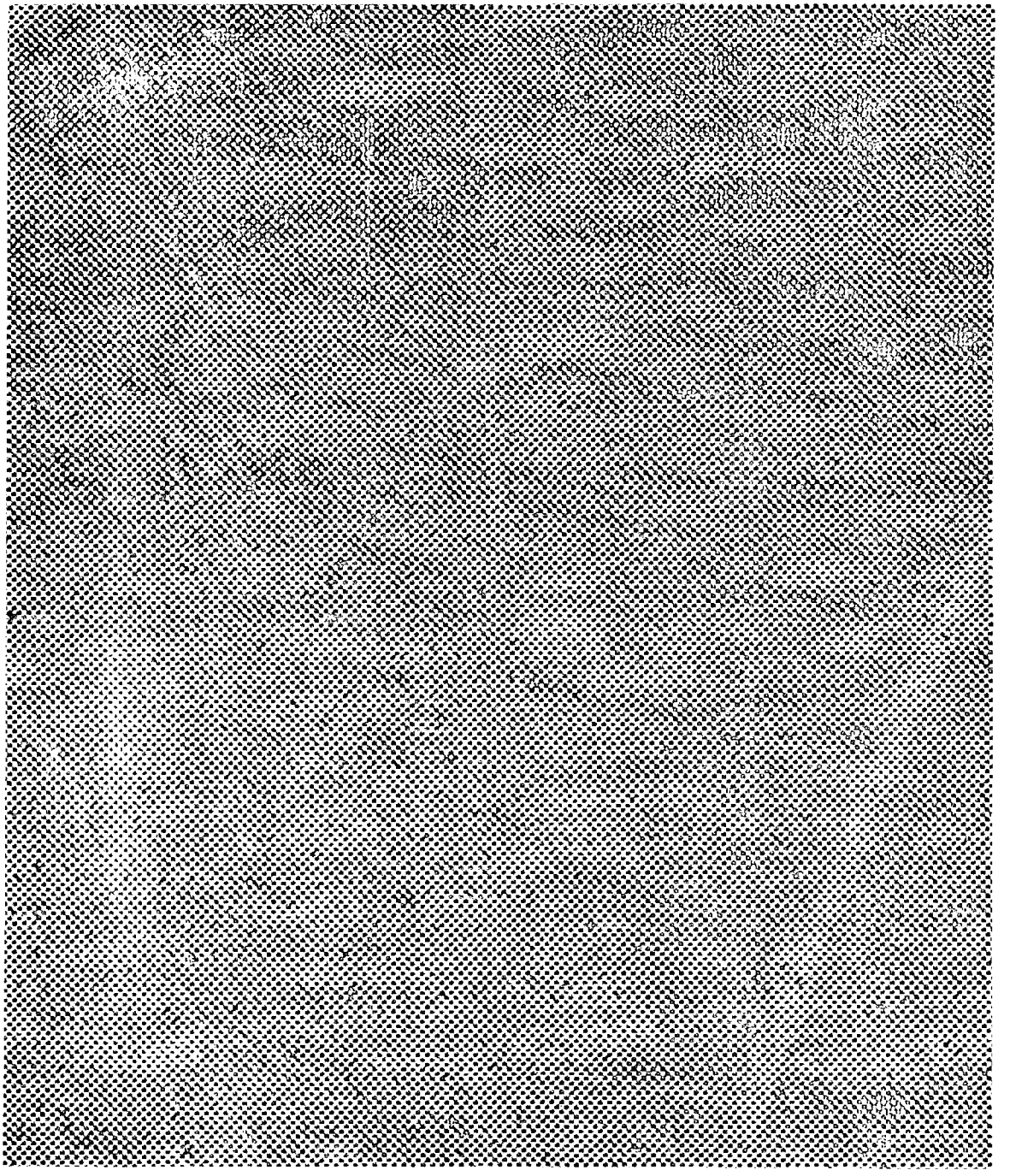

Fig. 2. Gray-scale presentation of scattering from 645 mm² (1 in.²) of monolithic silicon nitride, showing numberous indications.

ORNL-DWG 86-10218

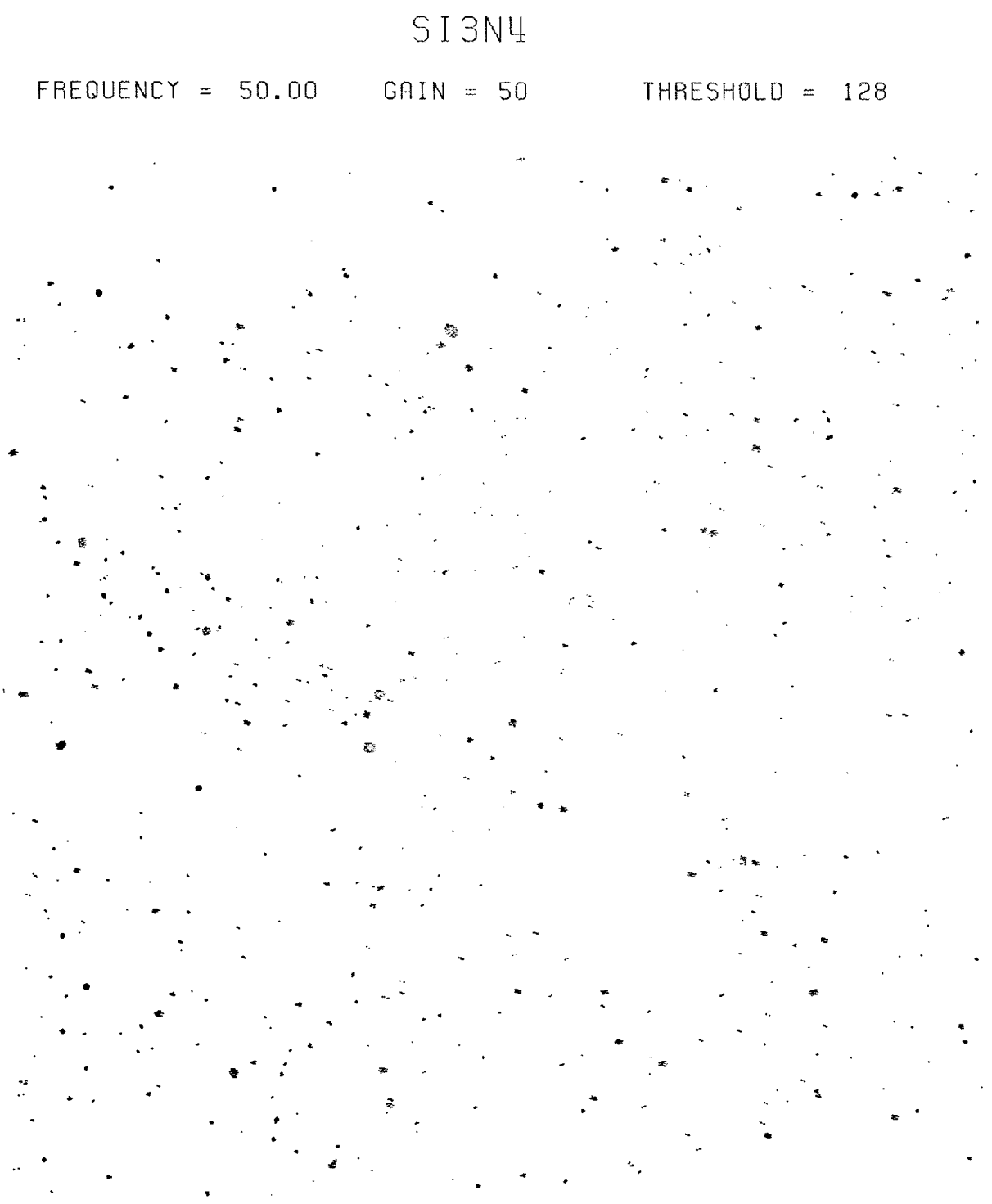

Fig. 3. Distribution of ultrasonic indications in 645 mm² (1 in.²) of silicon nitride.

ORNL-DWG 86-10208

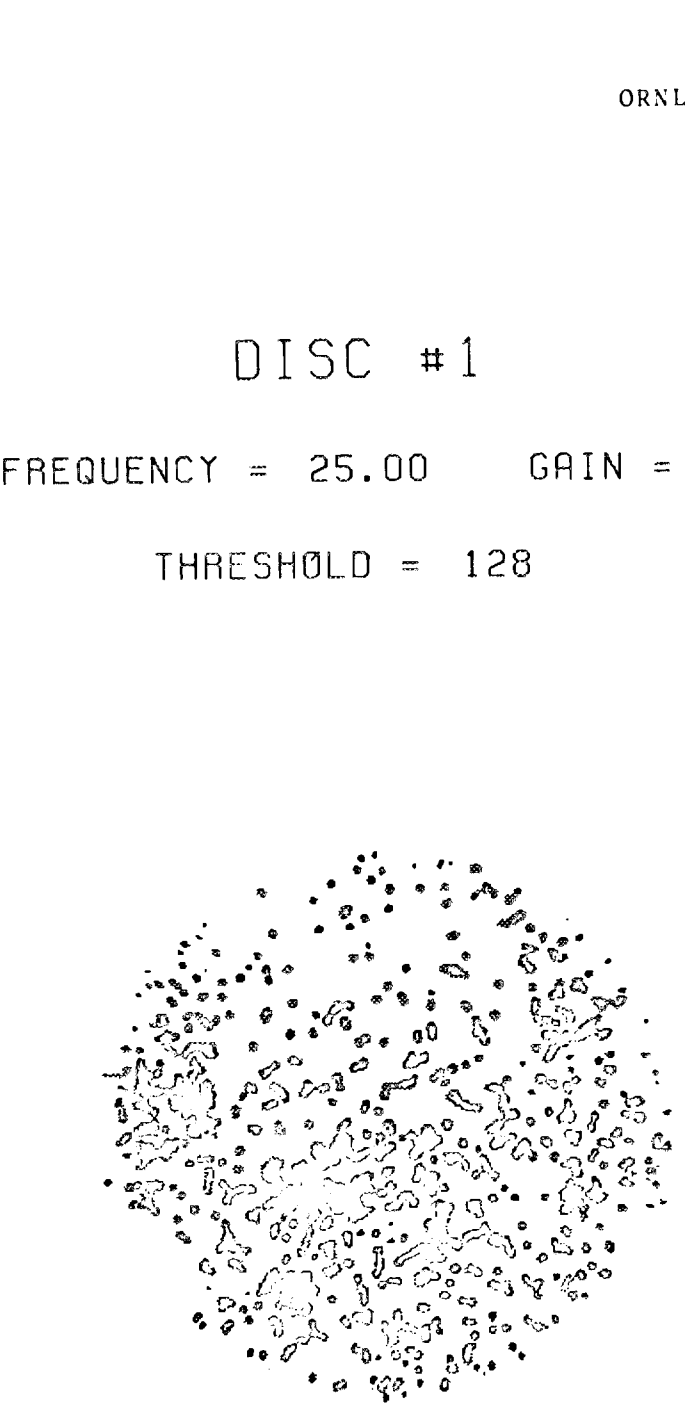

Fig. 4. Detection of 100- to 200-μm voids in silicon nitride.

ORNL-DWG 86-10209

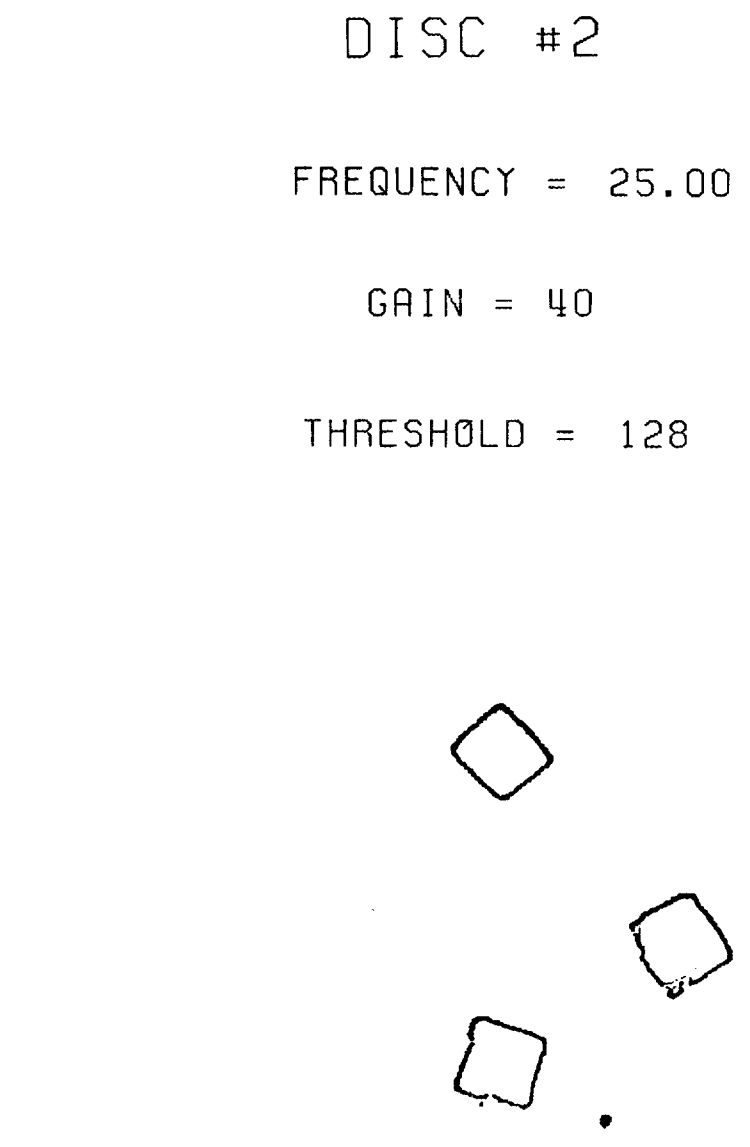

Fig. 5. Detection of three "cracks" in silicon nitride.

ORNL-DWG 86-10210

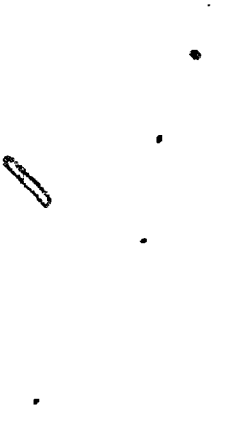

Fig. 6. Detection of a 100-μm-diam cylindrical void in silicon nitride.

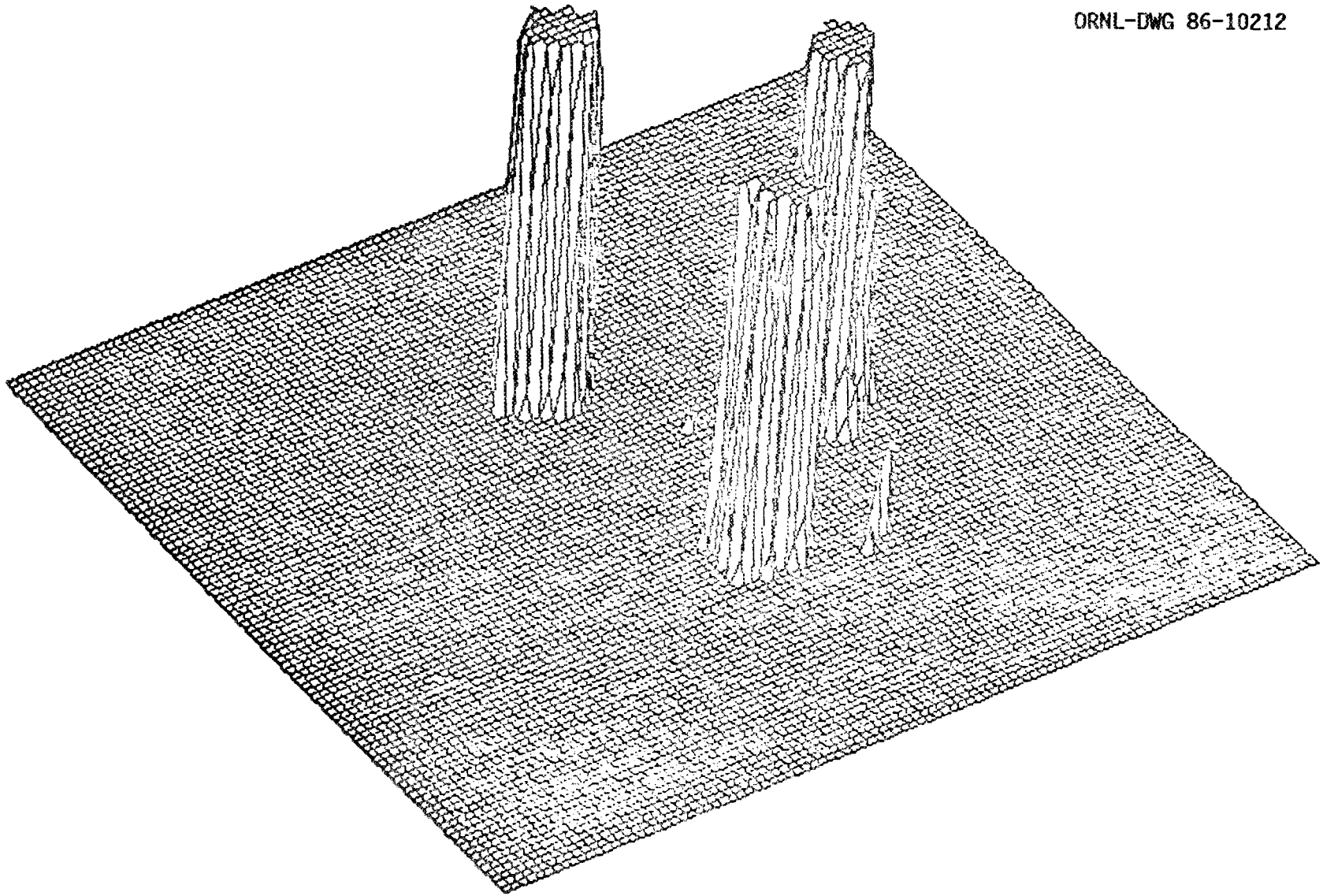

Fig. 7. Pseudo three-dimensional view of crack standards in silicon nitride.

Because the detectability of a flaw is dependent on the wavelength of the ultrasonic energy and focal spot size of the transducer, we are ordering higher-frequency (75–100-MHz) units for evaluation. They should provide some improvement, because it is clear that we are now limited by transducer characteristics rather than by the ultrasonic instrumentation.

Three composite ceramic specimens consisting of silicon carbide whiskers in alumina have been obtained. Two of them have clumps of whiskers about 100 and 200 μm in diameter, respectively, as determined by scanning electron microscopy analysis of a fracture surface. The third sample appears to be relatively homogeneous. We previously were able to examine briefly a similar specimen and found the elastic behavior to approximate that of monolithic ceramics, because the whisker diameter is much smaller than the ultrasonic wavelength (~100 μm).

The samples are being radiographed, following which we will begin ultrasonic studies.

Radiography – B. E. Foster

A third silicon nitride MOR bar was obtained with no apparent discontinuities. We attempted to place 50-μm-diam holes with 50-μm depths. However, we only obtained holes 5 and 8 μm deep. We were successful in placing 100-μm-diam holes with depths of 30 and 70 μm and 75 μm-diam holes with depths of 22 and 37 μm.

Three of the four holes were imaged with a radiographic technique. We now have hole standards with calculated equivalent penetrameter sensitivities from 0.5 to 3% and simulated spherical voids with approximate diameters of 20 to 180 μm.

The three MOR bars (radiographic hole standards) containing flat-bottom holes with diameters of 75, 100, 125, and 250 μm and depths from 10 to 70 μm were taken to Ridge, Inc., Tucker, Georgia. The purpose was to evaluate the achievable sensitivity of microfocus projection and tomography equipment. However, we experienced problems that were diagnosed as being internal to the X-ray tube. Suspected were a misaligned filament, astigmator coils, and a halo focal spot (a second focal spot, but larger in diameter). After the equipment problems are resolved, we will attempt the evaluation again.

We requested and received the short-term loan of three silicon nitride "standards" from GTE Products Corp. in Belmont, California. The sample identity and characterization of the intentional internal defects were as follows:

Sample	Thickness, mm (in.)	Diameter, mm (in.)	Defects
I	4.2 (0.167)	17.3 (0.691)	Voids 0.1–0.2 mm (0.004–0.008 in.)
II	5.6 (0.226)	17.3 (0.691)	Cracks 0.2 mm thick by 1.5 mm long (0.008 by 0.062 in.)
III	5.0 (0.198)	17.3 (0.691)	Cylindrical voids 0.1 mm diam by 1.5 mm long (0.004 in. by 0.062 in.)

The samples were first radiographed (X-ray beam parallel to sample axis) with an X-ray energy of 48 kVcp and 25 mA. The exposure time was varied to accommodate the different sample thicknesses with the following observations:

Sample I – Many irregularly shaped voids (0.1–0.2 mm in diameter).
Sample II – Three rectangular voids (1.5–2 mm per side); no indications of cracks.
Sample III – A single void (0.1 mm wide by 1.5 mm long).

Photographic reproductions of the radiographs of the three samples are shown in Fig. 8 with an enlargement of approximately 2.5 times. The radiographs were printed directly instead of making negatives and then printing, resulting in the image reversal (the voids are the white areas in the photographs).

We then radiographed the samples with the X-ray beam passing through the diameter (the 17.3-mm thickness) with an energy of 95 kVcp and 10 mA, and we obtained the following results:

Sample I – The voids were shown to be located in a central plane (0.1 mm wide) across the diameter of the sample.
Sample II – The three voids were shown to be located in a central plane, cracklike in appearance with widths less than 0.1 mm and lengths of 1.5 to 2 mm.
Sample III – The void was shown to be located in a central plane, cylindrical with a diameter of 0.1 mm.

Status of milestones

No milestones were completed during this period.

Publications

None.

YP2589

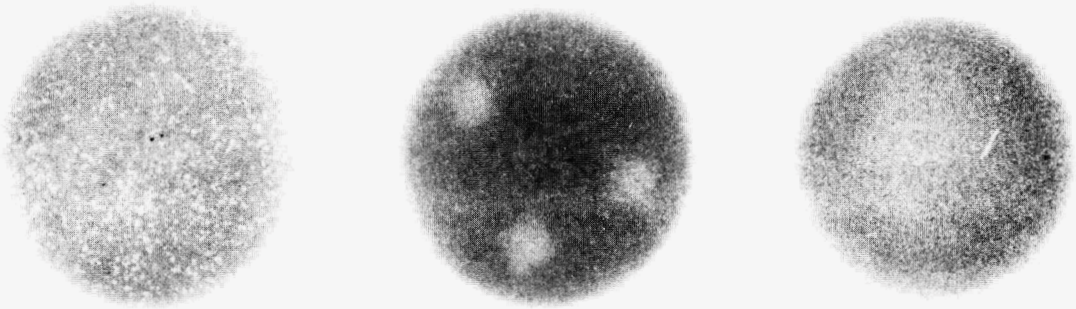

I II III

Fig. 8. Photographic reversal of radiographs of three silicon nitride "standards".

Computed Tomography - W. A. Ellingson and E. Segal (Argonne National Laboratory)

Objective/scope

The purpose of this program is to develop x-ray computed tomographic (CT) imaging for application to structural ceramic materials. This technique has the potential for mapping density distributions, detecting and sizing high- and low-density inclusions, and detecting cracks in green-state and densified ceramics. CT imaging is capable of interrogating the full volume of a component, and is noncontacting. It is also relatively insensitive to part shape and thus can be used to inspect components with complex shapes, such as turbocharger rotors or turbine blades.[1,2]

Technical progress

Efforts during the current reporting period included extensive analytical and experimental work on beam-hardening corrections for a medical x-ray CT scanner. CT scans were made of green-state Si_3N_4 as well as several other materials in order to develop the necessary information for calibration.

This is the first report submitted on this project, and so before the detailed results of this work are discussed, a few general comments will be made about the CT technique. It is not possible here, however, to give more than a brief overview of how CT scanners work. More complete discussions of the method may be found in Refs. 3-5.

Brief background on CT scanner operation

Computed tomography is the reconstruction by digital computer of a tomographic plane ("slice") of an object. In computed tomography, the intensity of a collimated x-ray beam passing through a test object is measured by an array of detectors located on the other side of the object. Figure 1 illustrates the translate-rotate method used in first- and second-generation CT scanners. After each translation, which generates a projection data set, the source-detector pair is rotated about the object (or conversely, the object is rotated slightly and moved through the beam again). When the object has been scanned/rotated through, typically, 180 degrees, the individual projection data sets are "summed" with a computer to generate a highly accurate reconstructed cross-sectional image of that slice of the object. The x-ray source and detector array can then be raised or lowered to a different location on the object and another slice scanned. Because the reconstructed image is processed by a computer, enhancement techniques can be used to accentuate various parts of the image.

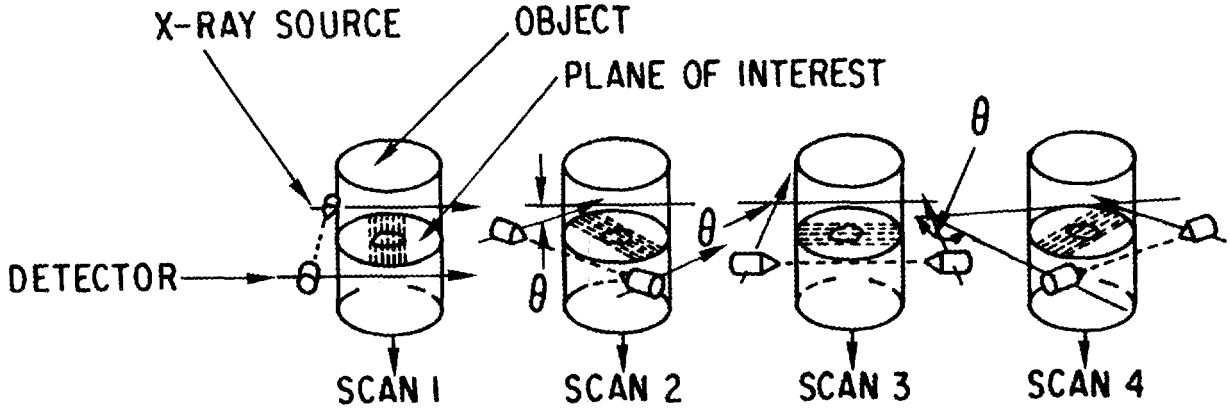

Figure 1. Schematic diagram of the computerized transaxial scanning procedure used to obtain transmission-profile data. The source and detector move synchronously at each θ position. Four θ positions are shown.

A tomographic system exposes only a small cross-sectional slice of the test object at any given time, thus eliminating the superposition of features that occurs when a three-dimensional object is portrayed in two-dimensional imagery -- one of the main sources of ambiguity in conventional film radiography. The result of such superpositioning is that defects often cannot be characterized or located with precision.

The numerous design considerations for CT systems include range of specimen sizes, densities, and weights; throughput; resolution requirements; and cost. Figure 2 shows a diagram of several CT scanner configurations that are available. Figure 2(A) shows a first-generation CT scanner, which uses a single detector. The data are accumulated by translating the source-detector (S-D) pair, then rotating the object or the S-D pair through N angular positions, as shown in Fig. 1. The second-generation CT scanner in Fig. 2(B) differs from a first-generation scanner primarily in the substitution of a detector array for the single detector. This greatly decreases data acquisition time. Figure 2(C) is a diagram of a third-generation CT scanner. This differs from the second-generation machine in that the detector array forms an arc, so that rotation is the only motion required. Figure 2(D) shows a fourth-generation CT scanner, which has stationary detectors arrayed in a complete circle. This allows rotation of the x-ray source alone, and further increases the speed of data acquisition.

Figure 3 shows a simplified diagram of a typical state-of-the-art medical CT scanner. The two major components are the gantry, which contains the x-ray head and detectors, and the translating table, which positions the object in the gantry. Either a monochromatic isotope source (e.g., ^{60}Co, ^{192}Ir, ^{241}Am) or a polychromatic x-ray source can be used. With a monochromatic isotope source, no beam-hardening corrections are necessary. The determination of appropriate corrections for polychromatic x-ray sources is the focus of the present project.

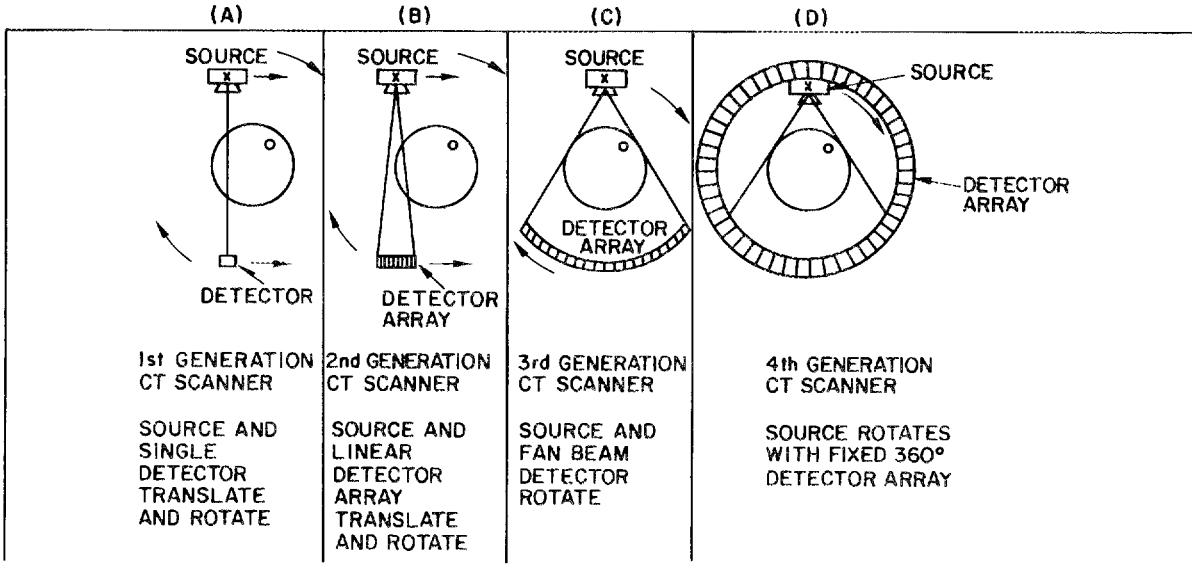

Figure 2. Source-detector configurations used in CT scanners.

Beam-hardening problem for ceramics

The reconstructive imaging process used in CT scanners is based on the assumption that the process is linear; i.e., the measured attenuation is proportional to the linear attenuation coefficient, μ, of the radiation, and the dimensions of the scanned object. Any real nonlinearity in the imaging process will introduce artifacts (streaks or rings) into the resulting images. Nonlinearity is avoided when a monoenergetic radiation source is used. However, in most medical CT scanners, the source is a polychromatic x-ray tube with a wide range of photon energies. In this case, the value of μ depends on the energy of the x-ray photons as

$$\mu = \mu(E) \quad . \tag{1}$$

Therefore, the total μ value measured by the system is given by

$$\mu = \int_{E_o}^{E_v} \mu(E)\, dE \quad , \tag{2}$$

and the photon attenuation is proportional not only to the penetration length of the radiation in the object, but also to the energy of the beam. Since the linear attenuation coefficient is higher for lower-energy photons, these are successively filtered out as the x-ray beam passes into the material, leaving only high-energy photons; hence the term "beam hardening."

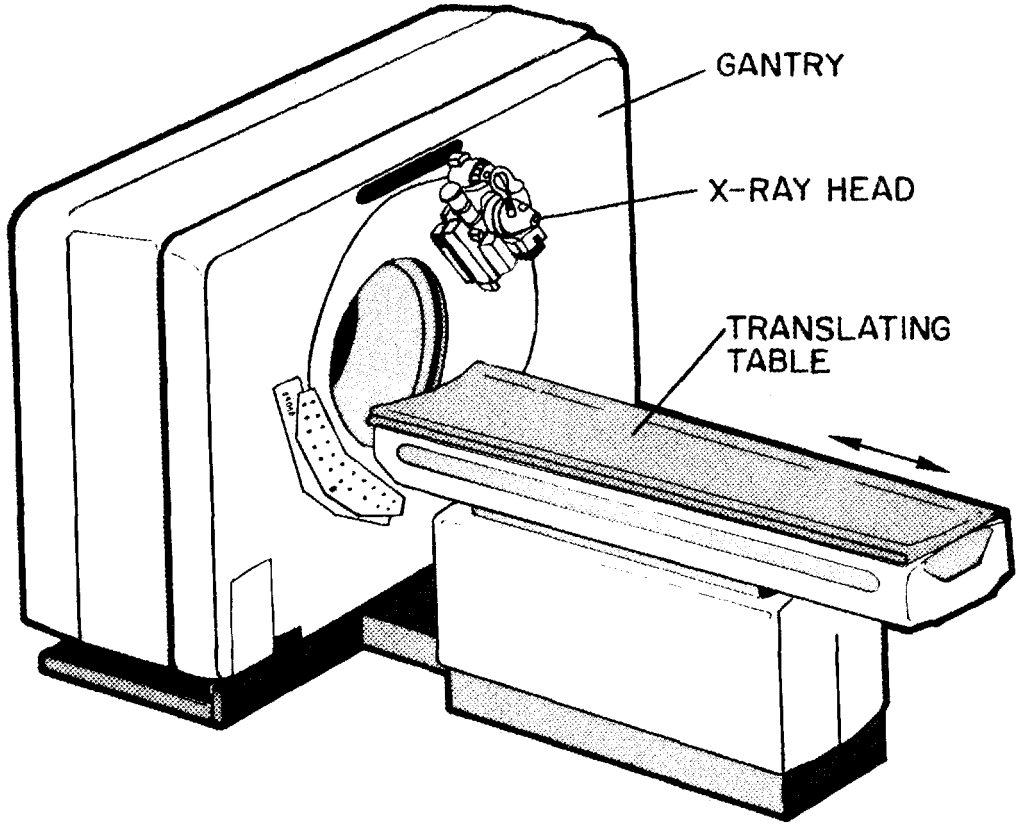

Figure 3. Schematic diagram of typical state-of-the-art medical CT scanner.

The photon energy spectrum of medical CT scanners usually ranges from about 20 to 140 keV (Fig. 4). The attenuation coefficient for ceramics decreases by more than an order of magnitude over this energy range, as shown in Fig. 5 for Si_3N_4. Hence, the beam-hardening effect is a severe problem for inspecting ceramic components.

Effect of specimen size on beam hardening in Si_3N_4

A series of nine Si_3N_4 ceramic blocks, prepared for this program by Babcock & Wilcox (Lynchburg, VA), were used to test the effect of specimen size on beam hardening. The specimens were prepared by cold pressing to 6000 psi followed by isostatic compaction. Table 1 shows the dimensions and features of the Si_3N_4 blocks.

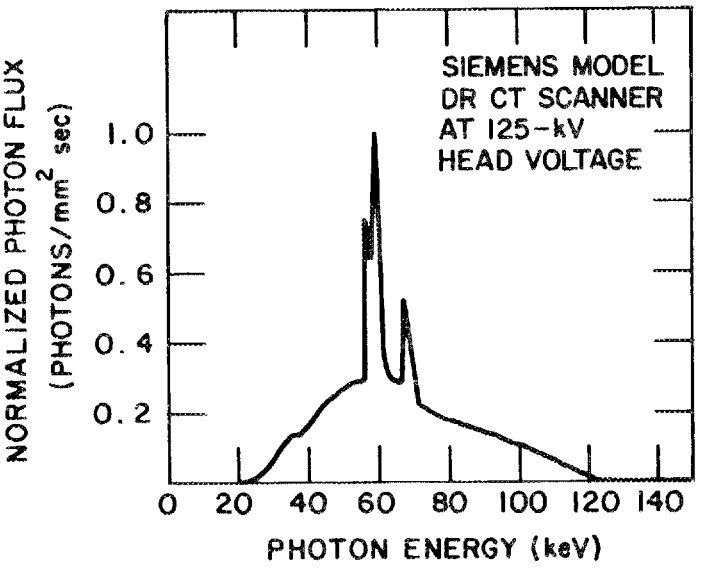

Figure 4. Typical photon energy spectrum of x-rays generated by a Siemens Model DR CT scanner with an applied voltage of 125 kV.

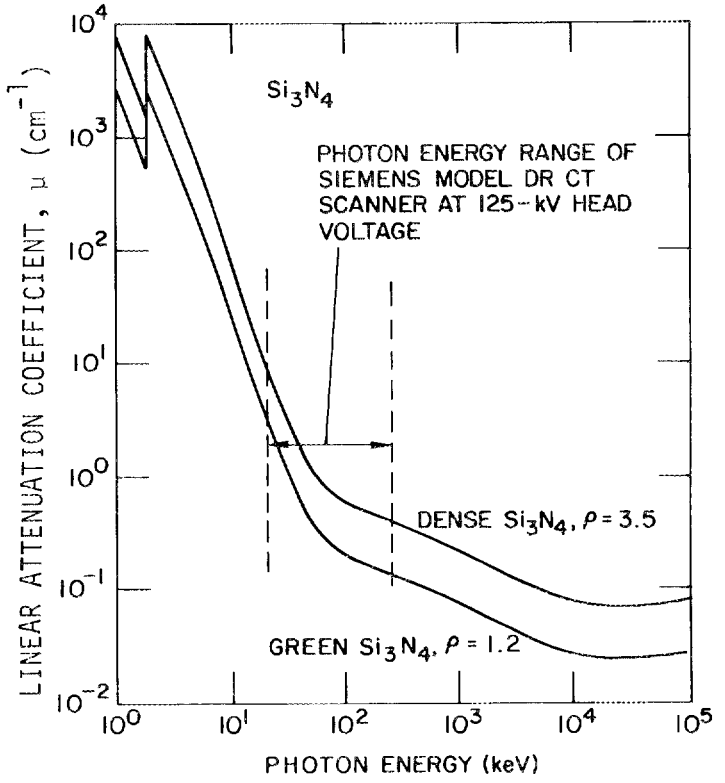

Figure 5. Linear attenuation coefficient μ as a function of photon energy for dense and green-state Si_3N_4.

Table 1. Si_3N_4 Specimens Tested with the Siemens Model DR CT Scanner

Sample No.				
Babcock & Wilcox	CT Scan Identification	Dimensions (mm)	Density (g/cm^3)	Remarks
1	1	18x13x6	1.967	
2	4	18x13x6	1.967	
3	7	18x13x6	1.967	partially sintered
4	2	48x38x26	1.995	
5	5	48x38x26	1.995	
6	8	48x38x26	1.995	partially sintered
7	3	57x43x31	1.967	
8	6	57x43x31	1.967	
9	9	57x43x31	1.995	partially sintered

Each image of Fig. 6 shows a 2-mm-thick CT slice for one of the samples listed in Table 1. The superimposed density traces show computed density values in Hounsfield units (HUs) as a function of spatial position across the block. The relative attenuation A_r, in HUs, is given by

$$A_r = \frac{\mu - \mu_{H_2O}}{\mu_{H_2O}} \cdot K \quad , \tag{3}$$

where K = 1000. In a homogeneous medium, the HU value should be proportional to the local density of the material. However, all the slices of Fig. 6 show a parabolic-type HU distribution. This effect, known as "cupping," is caused not by higher densities near the edges of the blocks, but by the higher attenuation of the low-energy part of the x-ray photon spectrum. Thus, the low-energy photons are absorbed by the edges of the block. Since the HU value is proportional to the absorption, it is higher at the edges. Beam hardening is also responsible for the higher HU values observed for the small test block (Fig. 6a), since the small block absorbs low-energy photons more efficiently.

In order to obtain an idea of the relative effect of Si_3N_4 specimen thickness on attenuation for the energy spectrum of the CT scanner used here, an analytical study was done for 3 specimen thicknesses. Figure 7 shows the effect of specimen thickness on the output energy spectra for green-state and densified Si_3N_4. Attenuation increases significantly with specimen thickness for photon energies below 60 keV. For example, in the green material, the attenuation at 50 keV increases by ~65% as thickness increases from 1 to 2.5 cm, and the attenuation increases by ~25% as thickness increases from 2.5 to 5 cm.

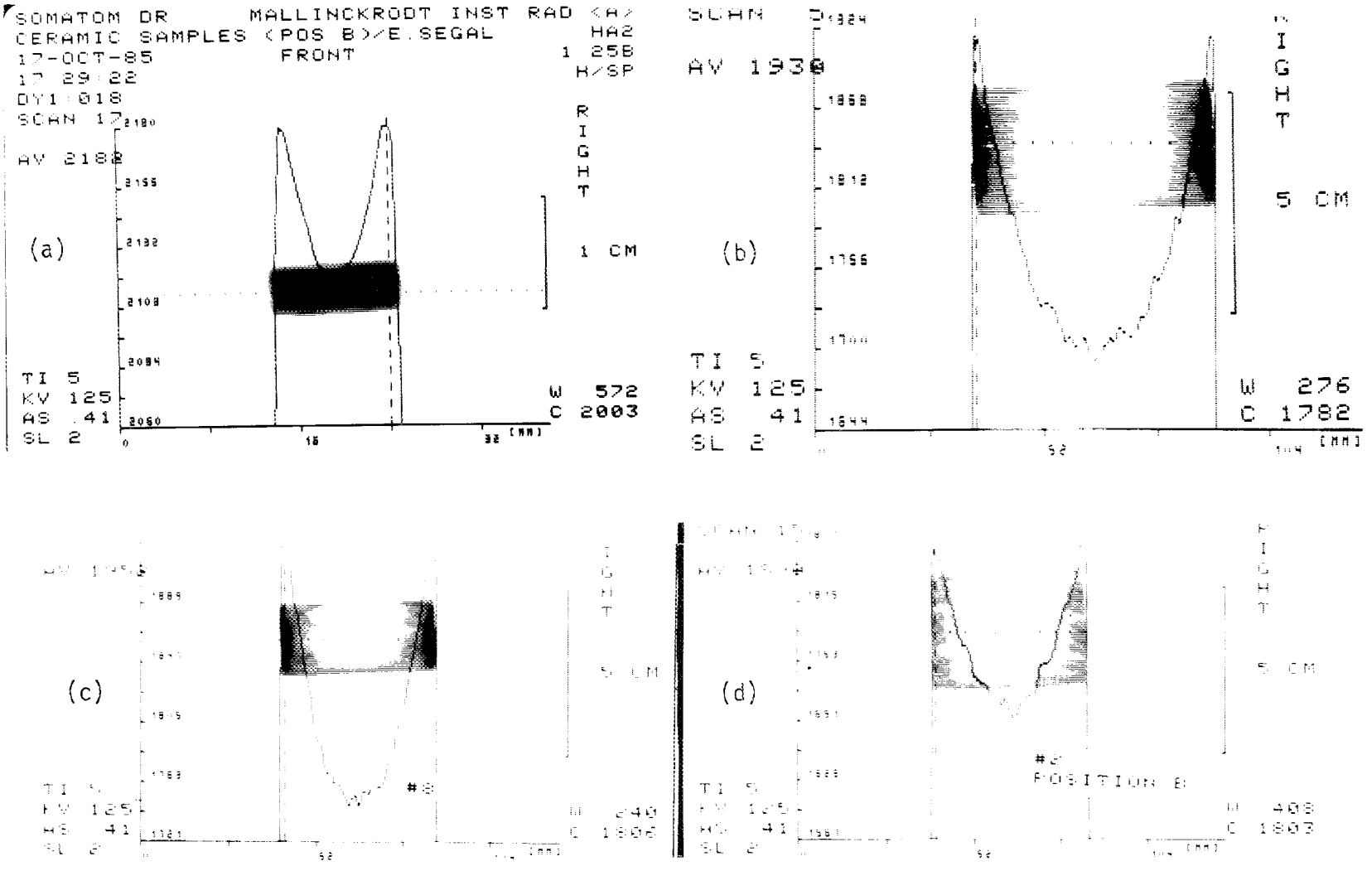

Figure 6. CT scans and density distributions for four of the samples of Table 1. (a) B&W sample 2 (small); (b) B&W sample 7 (large); (c) B&W sample 6 (medium); (d) B&W sample 4 (medium). Values C and W in lower right corners of panels represent, respectively, the middle HU and the range of HU values covered.

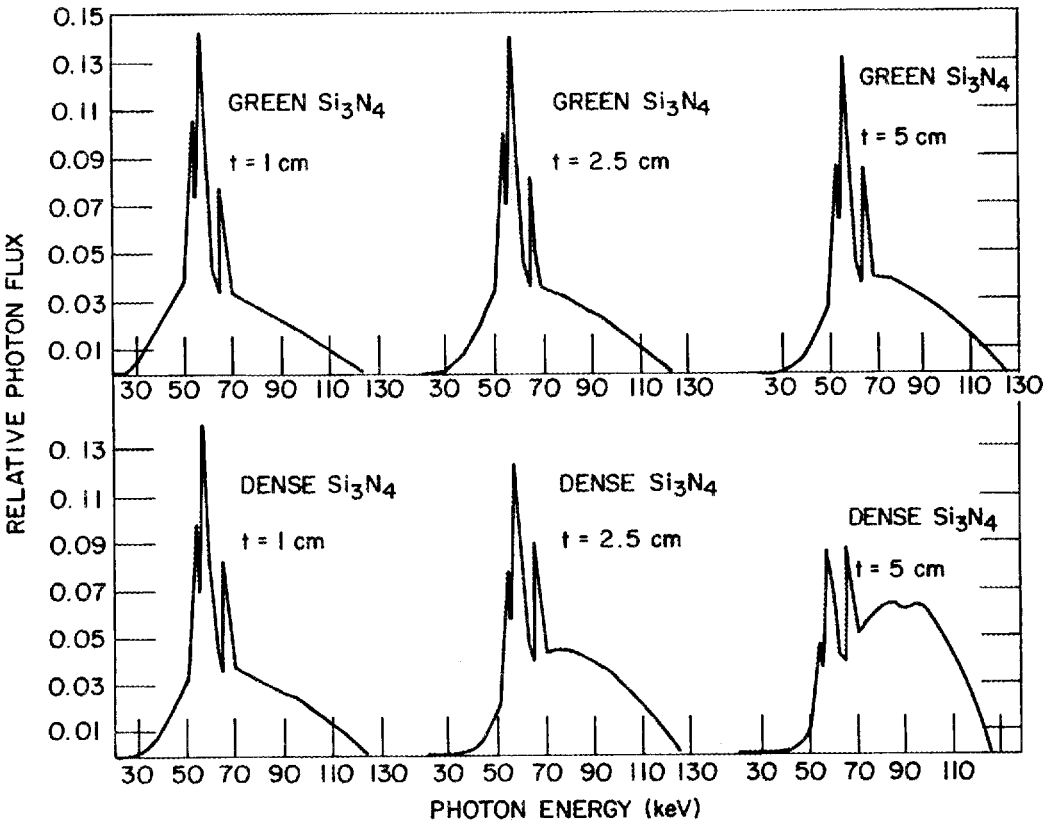

Figure 7. Photon energy spectrum of x-ray beam from Siemens Model DR CT scanner, with tube voltage of 125 kV, after passage through various thicknesses of green and densified Si_3N_4.

Calibration of CT scanner for beam hardening

A second part of this research program involves establishing proper calibration methods for the inspection of ceramic materials with CT scanners that have polychromatic x-ray sources. Because of the problem in obtaining uniform specimens, it is not clear whether ceramics are the best materials to use for calibration purposes. Thus, we conducted exploratory calibration studies with several possible alternative materials, in the form of homogeneous circular rods. Materials of widely different densities were chosen so that the calibration would cover the whole HU range relevant to ceramics. Table 2 gives the materials and diameters of the calibration rods. Aluminum was chosen to represent high-density ceramics, with HU values up to and exceeding the maximum value of 3000 for which regular medical CT scanners are designed. The Freon TF and Teflon represent the intermediate HU range (500-800), and Lucite encompasses the lower limit of the calibration. (The liquid Freon TF was contained in cylinders of styrofoam, which has a very low x-ray photon absorption compared to Freon.) A second-generation CT scanner, the Elscint model 2002, was used for the calibration tests.

Table 2. Samples Used for Calibration of Beam-Hardening Correction

Diameter (mm)	Material			
	Aluminum	Freon TF	Teflon	Lucite
5	x		x	x
10	x		x	x
20	x		x	x
30		x		
40		x		
50	x		x	x
70		x		
100	x	x	x	x

Before the specimens listed in Table 2 were tested in the CT scanner, a test was conducted with a 20-cm-diam water phantom. Since a standard beam-hardening correction for water is programmed into the scanner, one would not expect to see a beam-hardening effect. Figure 8 shows a CT scan of the water phantom. The dark outer region is the Lucite case used to contain the water. The square region in the center of the water scan is very uniform, but beam hardening is still evident near the outer surface of the Lucite case. The lack of a perfect beam-hardening correction causes a noise level (i.e., a variation in HU number) of about 0.3%.

Figure 9 shows a typical CT scan of a Lucite specimen. Since the image has been magnified, only the lower right quadrant of the rod is seen, although the entire rod was scanned. Very little beam hardening is evident. A measure of the amount of beam hardening (increased apparent density of the outer region) can be obtained by determining the difference between the HU value of the outer region and the average HU value over a typical inner region. For Fig. 9, the outer region has an HU value of 150. The average for the region bounded by the small rectangle is 141.9. This 8-HU difference, divided by the HU range (1200 in this case), represents an absolute hardening effect of 0.6%.

Figure 10 shows a CT scan of the 50-mm-diam Teflon rod. Using the same rationale as above, one obtains a hardening effect of 1.8% for this rod.

Figure 11 shows scans of the 30-, 40- and 70-mm-diam Freon cylinders. As the diameter increases from 30 to 70 mm, the beam-hardening effect increases from 6 to 14%. Figure 12 shows CT scans of the 100-mm-diam Freon cylinder. In the image of Fig. 12a, which was made without the standard correction, the beam-hardening effect is about 18%. Figure 12b shows the same material, but with the standard beam-hardening correction. This correction reduces the beam-hardening effect to about 15%.

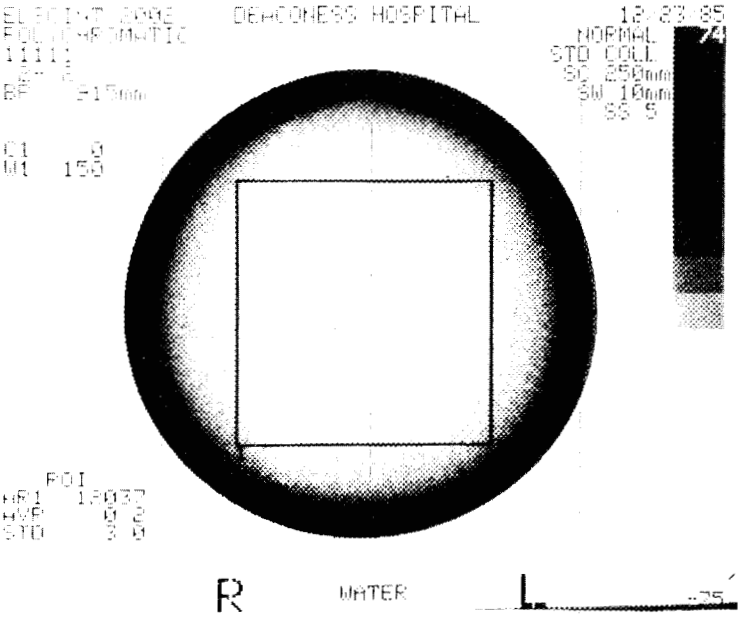

Figure 8. CT scan of 20-cm-diam water phantom (10-mm-thick slice). The noise level in the square region is about 3 HU or 0.3%. The dark outer region is the Lucite container used to hold the water.

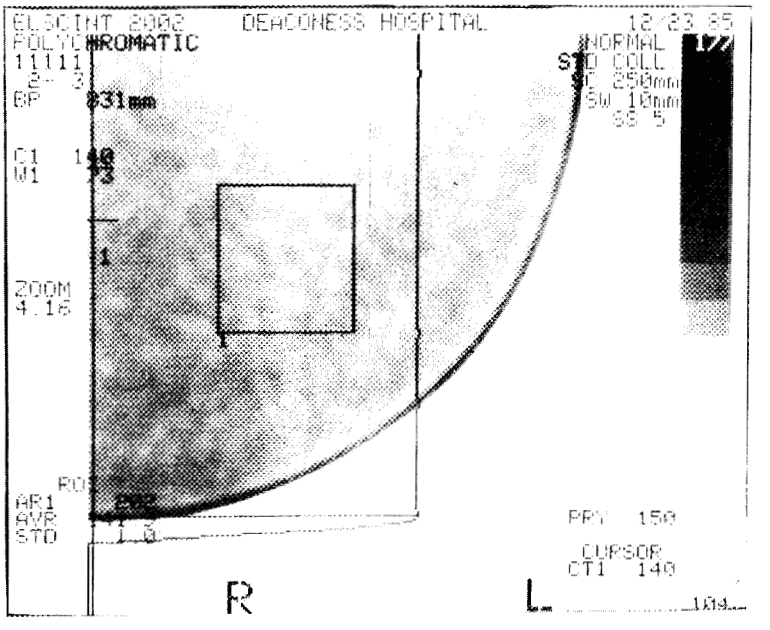

Figure 9. Portion of CT scan of 10-cm-diam Lucite rod, showing beam-hardening effect at the outer edge (10-mm-thick slice).

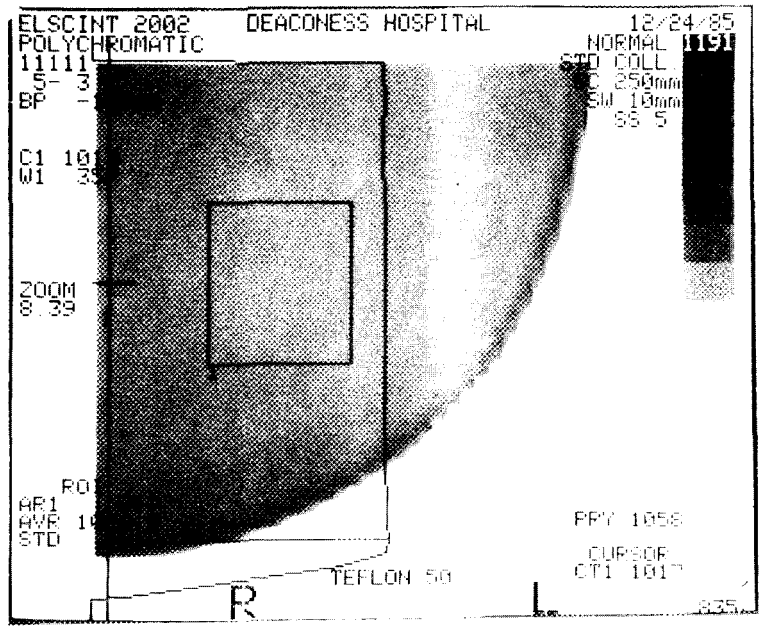

Figure 10. CT scan of 50-mm-diam Teflon rod (10-mm-thick slice).

A second, greatly exaggerated beam-hardening correction (produced by increasing the beam-hardening correction algorithm by a factor of 10) was also made on this test specimen (Fig. 13). This exaggerated correction reduced the beam-hardening effect to ~0.5%. This beam-hardening correction appears to be nearly appropriate for green-state ceramics. Close inspection of Fig. 13, however, reveals a significant apparent nonuniformity in the density of the Freon TF; thus, it seems that this beam-hardening correction significantly affects the imaged density distribution. Work will continue on incorporating an appropriate beam-hardening correction into the image reconstruction algorithm.

Status of milestones

All milestones are still on schedule.

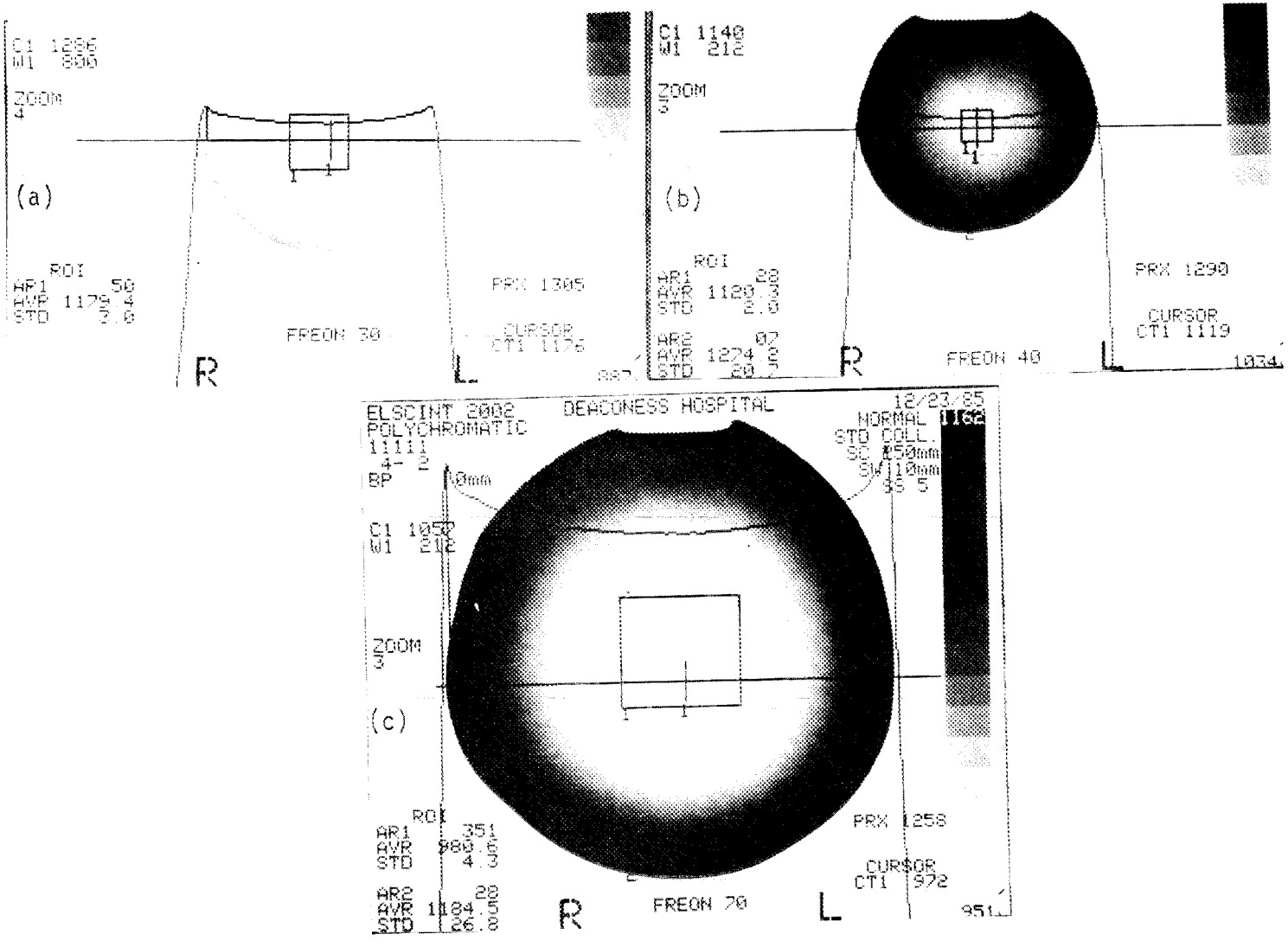

Figure 11. CT scans of liquid Freon TF (10-mm-thick slice). (a) 30-mm-diam cylinder; 6% beam-hardening effect. (b) 40-mm-diam cylinder; 8% beam-hardening effect. (c) 70-mm-diam cylinder; 14% beam-hardening effect.

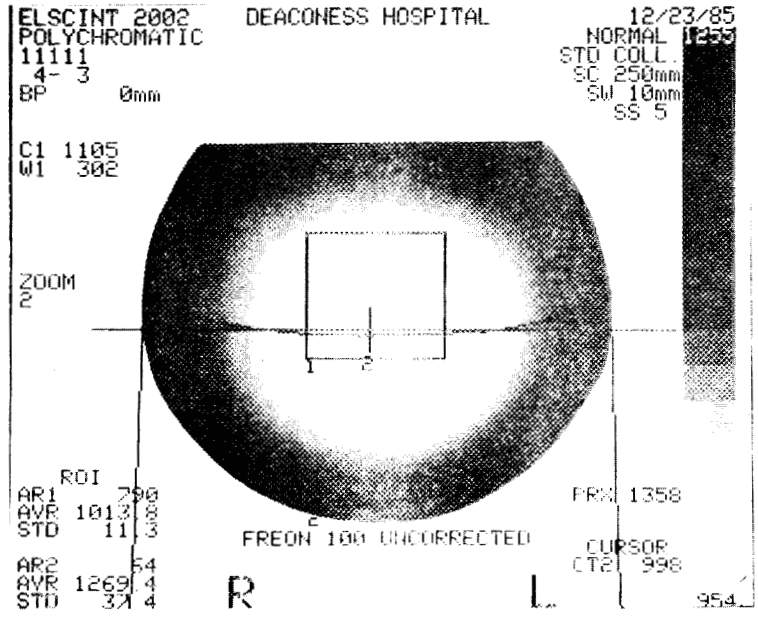

(a)

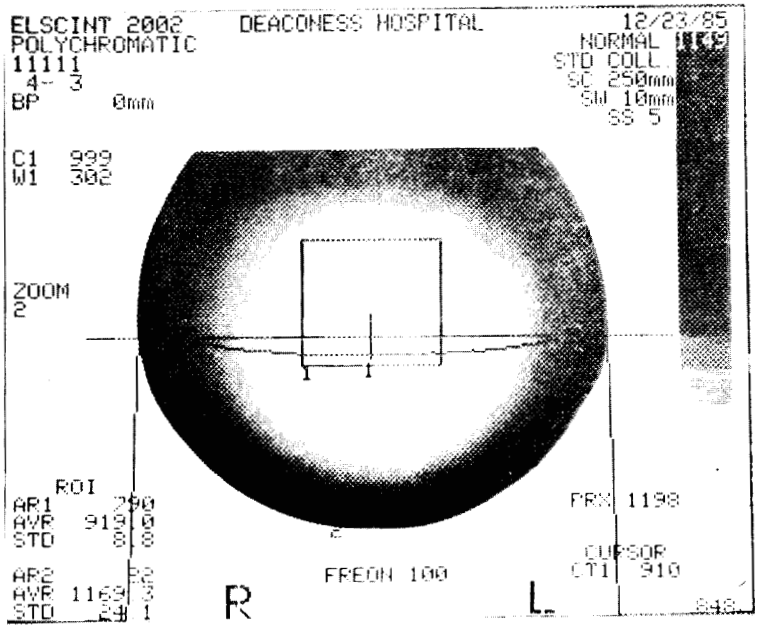

(b)

Figure 12. CT scans of 100-mm-diam liquid Freon TF (10-mm-thick slice). (a) No correction; 18% beam-hardening effect. (b) Standard correction; 15% beam-hardening effect.

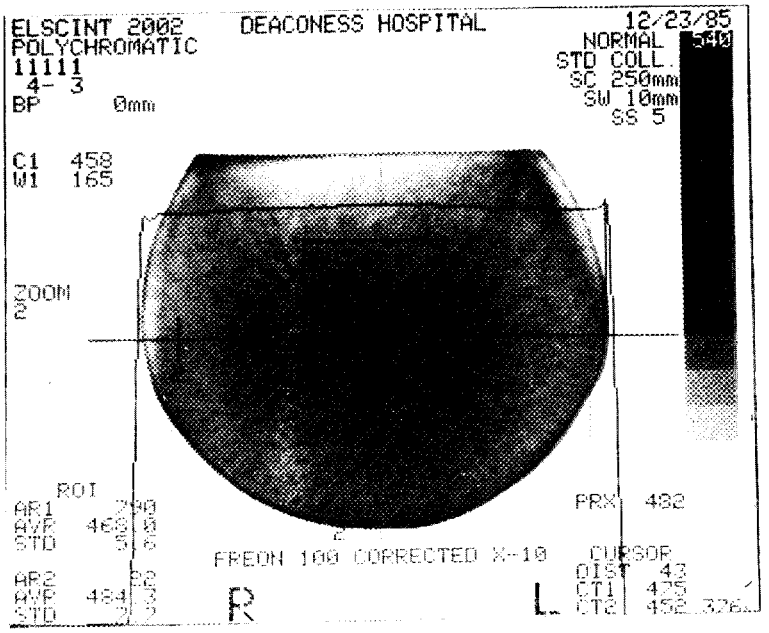

Figure 13. CT scan of 100-mm-diam Freon TF specimen with exaggerated beam-hardening correction (10-mm-thick slice).

References

1. R. A. Roberts, W. A. Ellingson, and M. W. Vannier, "A Comparison of X-Ray Computed Tomography, Through-Transmission Ultrasound, and Low-kV X-Ray Imaging for Characterizing Green-State Ceramics," in Proc. of the 15th Symposium on Nondestructive Evaluation, San Antonio, Tex., April 23-25, 1985 (in press).

2. T. Taylor, W. A. Ellingson, and W. D. Koenigsberg, "Evaluation of Engineering Ceramics by Computed Tomography," in Proc. of the American Ceramic Society Engineering Ceramics Division Meeting, Cocoa Beach, Fla., January 20-25, 1986 (in press).

3. H. Berger and W. A. Ellingson, "Three-Dimensional Radiographic Imaging," in Research Techniques in Nondestructive Testing, R. Sharpe, ed., Academic Press, New York, 1980, Vol. 4, Chapt. 1, pp. 1-38.

4. G. T. Herman, Image Reconstructions from Projections: The Fundamentals of Computerized Tomography, Academic Press, New York, 1980.

5. R. A. Brooks and G. DiChiro, "Theory of Image Reconstruction in Computed Tomography," Radiology 117, 561-572 (1975).

6. W. A. Ellingson, R. A. Roberts, J. L. Ackerman, and E. Segal, "Nondestructive Testing for Structural Ceramics," in Advanced Research and Technology Development Fossil Energy Materials Program Quarterly Progress Report for the Period Ending December 31, 1985, ORNL/FMP-86/1, Oak Ridge National Laboratory, Oak Ridge, Tenn. (in press).

4.0 TECHNOLOGY TRANSFER

4.1.1 Technology Transfer

Technology Transfer
D. R. Johnson (Oak Ridge National Laboratory)

Technology transfer in the Ceramic Technology Project is accomplished by a number of mechanisms including the following:

Trade shows. A portable display describing the program has been built and used at several trade shows and technical meetings, most recently at the Annual Meeting of the American Ceramic Society, May 5–7, 1985, in Cincinnati, Ohio.

Newsletter. A Ceramic Technology Newsletter is published bimonthly and sent to a large distribution.

Reports. Semiannual technical reports, which include contributions by all participants in the program, are published and sent to a large distribution. Informal bimonthly management and technical reports are distributed to the participants in the program. Open-literature reports are required of all research and development participants.

Direct Assistance. Direct assistance is provided to subcontractors in the program via access to unique characterization and testing facilities at the Oak Ridge National Laboratory.

Workshops. Topical workshops are held on subjects of vital concern to our community. During this period a workshop on material requirements for advanced heat engines was held during the Automotive Technology Development Contractors Coordination Meeting, October 21–24, 1985.

International Cooperation. Our program is actively involved in and supportive of the cooperative work being done by researchers in West Germany, Sweden, and the United States under an agreement with the International Energy Agency. That work, ultimately aimed at development of international standards, includes physical, morphological, and microstructural characterization of ceramic powders and dense ceramic bodies, and mechanical characterization of dense ceramics. Detailed planning and procurement of ceramic powders and flexural test bars were accomplished during this reporting period.

Standard Reference Materials

A. L. Dragoo (National Bureau of Standards)

Objective/scope

Ceramics have been successfully employed in engines on a demonstration basis. The successful manufacture and use of ceramics in advanced engines depends on the development of reliable materials that will withstand high, rapidly varying thermal stress loads. Improvement in the characterization of ceramic starting powders is recognized[1] as a critical factor in achieving reliable ceramic materials for engine applications. The production and utilization of such powders require characterization methods and property standards for quality assurance.

The objectives of the NBS program are (1) to assist with the division and distribution of five ceramic starting powders for an international round-robin on powder characterization; (2) to provide reliable data on physical (dimensional), chemical and phase characteristics of two silicon nitride powders: a reference and a test powder; and (3) to conduct statistical assessment and modeling of round-robin data. This program is directed toward a critical assessment of powder characterization methodology and toward establishment of a basis for the evaluation of fine powder precursors for ceramic processing. This work will examine and compare by a variety of statistical means the various measurement methodologies employed in the round-robin and the correlations among the various parameters and characteristics evaluated. The results of the round-robin are expected to provide the basis for identifying measurements for which Standard Reference Materials are needed and to provide property and statistical data which will serve the development of internationally accepted standards.

Technical Progress

Division and Distribution of Ceramic Starting Powders. The division of a bulk lot of powder into many samples requires the use of probability sampling. A detailed protocol was developed based on the recommended practice for probability sampling as described in ASTM Standard E105-58, "Probability Sampling of Materials," and the recommendations of statistical consultants at NBS. The protocol is intended to insure the use of a verifiable procedure, the maintenance of clean operating conditions and the use of randomization procedures throughout the operation. The general steps in the procedure are as follows:

1. Blending of bulk powder in cone blender;
2. Manual division of powder, approximate sample size 3.2 Kg (6.4 Kg for zirconia powder);

3. Random selection of sample;
4. Partial drying of sample to reduce caking;
5. First division of sample with spinning riffler, approximate sample size 400 g (800 g for zirconia powder);
6. Vacuum drying of powder followed by storing, powder stored under dry argon;
7. Second division with spinning riffler, approximate sample size 50 g (100 g for zirconia powder);
8. Vacuum drying, storage under dry argon;
9. Randomly selected samples withdrawn for distribution as 100 g samples;
10. Third division with spinning micro riffler operated in glovebox flushed with dry argon, approximate sample size 6.25 g (12.5 g for zirconia powder.

The superiority of the spinning riffler over other sampling techniques has been demonstrated by several investigators[2-7]. For sampling of a binary sand mixture it was found to give a relative standard deviation 0.125 percent and an estimated maximum relative sample error of 0.42 percent[2]. Sampling of powders by a spinning riffler is recommended in ASTM Standard F577B-78.

The spinning riffler to be used in steps "5." and "7." is shown in Figure 1. This apparatus is enclosed in a plastic shield, not shown in the photograph, to eliminate the possible introduction of airborne contaminates. Since this riffler divides the powder by a factor of 16, pairs of tubes are randomly selected and then combined to yield a riffled sampled.

Two types of packaging are shown in Figure 2. An example of the first type is labeled "(A)" in the figure and is shown near the lower right center of the photograph. This method uses inner and outer shell vials and consists of first packaging the powder in the smaller inner shell vial which is capped with a plastic stopper. The inner shell vial is inserted in the outer vial which is flame sealed. A flame-sealing apparatus, belonging to NBS, is available at CT Labs, Skokie, Illinois, which prepares powder samples for the NBS Office of Standard Reference Materials.

The use of the method would require packaging the samples in the inner vials at NBS. This operation would be performed in an dry argon atmosphere as samples are removed from the microriffler. Samples would be packed in containers filled with dry argon for transportation to CT Labs for the flame-sealing operation. A representative of NBS would participate in the flame-sealing operation.

Although flame-sealing offers the advantage of continuous, rigid hermetic enclosure, there are three disadvantages. First, in transporting the samples from NBS, Gaithersburg, Maryland, to Skokie, Illinois, there is the risk of loss or damage to samples. Second, samples must be maintained temporarily for several days in nonhermetic containers. Third, the flame-sealing operation may introduce a small amount of water vapor, carbon dioxide and oxygen into the outer vial during sealing. The possibility of contamination of the IEA samples by powder residues and dusts would be minimized by the initial sealing at NBS in the stoppered inner vials and by the participation of an NBS representative in the flame-sealing operation.

Figure 1. Spinning riffler.

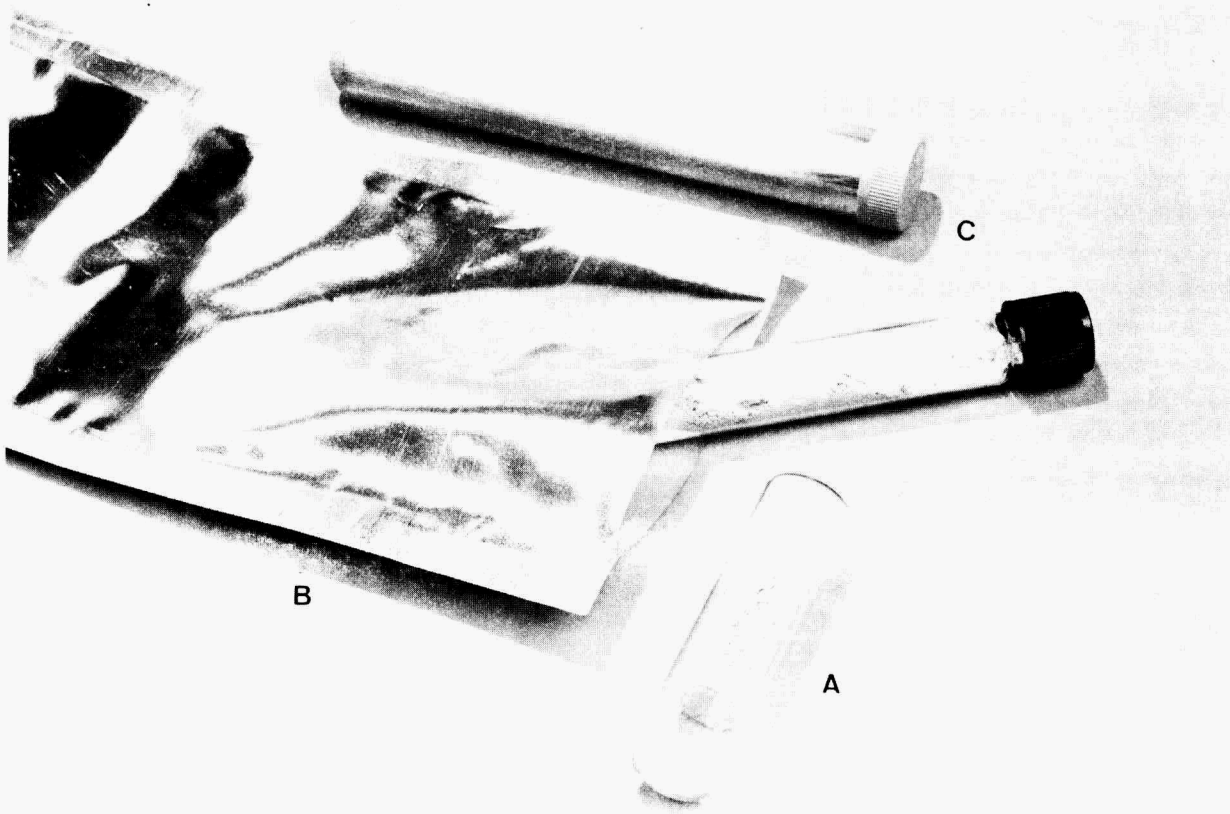

Figure 2. Packaging for powder samples.

The second method consists of first packaging the powder in a culture tube fitted with a screw cap having a styrene-butadiene liner faced with Teflon. Alternatively, a cone-shaped liner or Teflon-faced septum may be used to eliminate possible lodging of powder at the junction of the cap and bottle. This packaging step would be performed under dry argon as the tubes are removed from the microriffler. A culture tube with powder is shown near the center of the photograph in Figure 2.

Following the initial packaging step, the culture tube may be placed either in a polyfilm bag which is made of an aluminum-polymer laminate, labeled "(A)" in Figure 2, or in an extruded aluminum tube fitted with a gas-tight cap, labeled "(C)" in the figure. Packaging of the culture tubes can be carried out on site under dry argon immediately following the final riffling operation. Gas-tight seals are thermally formed at the closures.

Experimental Design and Statistical Assessment of Round-Robin Data. The powder characterization task undertaken by participants in Assignment II-O-1 of the IEA round-robin includes physical measurements, chemical measurements, determination of phase composition and defect measurements. The objectives of the task is to evaluate and compare current ceramic materials characterization methods and to recommend and conduct experimental and analytical studies to identify and remedy deficiencies in the data base.

For the analysis of data from the round-robin each observation reported can be considered to have five attributes:

1. Material
2. Sampling
3. Laboratory
4. Property
5. Measurement technique.

It is customary to analyze the statistics of an observation with respect to a property attribute, such as concentration of a component, to determine the effects of the other attributes. However, it is necessary to bear in mind that other comparisons may be desired to test hypotheses with respect to other variables.

The data will be first analyzed by frequency histograms, correlation plots, plots of residuals and analysis of major sources of variance. Computer-assisted analyses will be conducted as required by means of sophicated programs, such as the BMDP[8,9] developed by W. J. Dixon at the Health Sciences Computing Facility at the Medical Center of the University of California at Los Angeles, will be used for computer-assisted analyses. These programs provide an array of analysis methods, including robust estimators, backward stepping in regression analysis, nonparametric statistical tests, graphical outputs, factor analysis, bilinear correlations and cluster analysis.

The set of measured characteristics can be easily partitioned with respect to the five materials to be studied. Comparison of characteristics with respect to the material attribute will be used to identify measurement problems as well as similarities and differences.

Sampling errors will be minimized by use of spinning rifflers and probabilistic sampling methods. Certification of samples for homogeneity will be carried out on randomly selected samples to verify that all

samples are similar and to provide an estimate of the intralaboratory variance for the characteristics used for certification. The measurements will not establish absolute or preferred values. The following certification measurements are planned:

* Determination of particle size distribution by x-ray sedigraph or photon correlation spectroscopy;
* Determination of specific surface area by multipoint B.E.T.;
* Determination of relative crystalline phase compositions by x-ray diffraction;
* Determination of chemical composition and major impurities by neutron activation or spectrochemical methods.

Fifteen samples will be tested in each of the particle size measurements. Phase analyses and chemical analyses will be conducted on five samples. Independent duplicate measurements will be carried out on each sample.

The laboratory attribute can be clearly identified. However, since the participating laboraties will neither apply all of the same characterization methods nor measure all of the same properties, it will not be possible to compare all methods or properties over all laboratories. A balance design is not expected to be applicable to the data.

The generic attribute "Property" includes all of the physical and chemical attributes which will be measured in the round-robin. Both "fine-graining" - for example, concentration of a specific impurity - and "coarse-graining" - for example, total impurity content - of the data can be performed. Thus, comparisons with respect to both specific and generic properties is recommended.

The measured values for each property are expected to depend strongly on the method used for characterization ("Measurement Technique"). This is particularly the case with particle size measurements in which the size is not measured directly but is estimated from a size dependent property. The values obtained for a property may have both an observed value and a reduced or formal value. For example, measurement of the particle size distribution by x-ray sedigraph readily yields a median value from the analog output. However, this value is referenced to a mass-weighted distribution and the observed distribution may be decomposable into two or more modes. Data reduction is expected to be generally necessary to place all data for a property on an equal footing. It is advisable that a data table display both observed and formal values.

Status of Milestones

Subtask A, Milestone 1. Draft of sampling protocol prepared.

Subtask A, Milestone 2. Sampling of silicon nitride reference powder deferred pending Task Group decision on packaging.

Subtask A, Milestone 3. Sampling of zirconia powder to commence on or about April 15. Final riffling and packaging operations to be deferred until Task Group decision is obtained.

Subtask C, Milestone 1. Preliminary draft of document on experimental design and statistical analysis prepared. The document is summarized in the above report on technical progress.

Publications

None.

References

1.Charles River Associates, "Technological and Economic Assessment of Advanced Ceramic Materials," *Planning Report 19*, Vol. 1, NBS Gcr 84-470-1, Program Office, National Bureau of Standards, Gaithersburg, Maryland, p. 48.

2. T. Allen and A. A. Khan, "Critical Evaluation of Powder Sampling Procedures," *Chem. Engr. (London)* 238, CE108-CE112 (1970).

3. J. R. Montgomery, "Revolving Riffle for Subdividing Ground Magnesium Chips," *Analyt. Chem.* 40(8), 1399-1400 (1968).

4. B. H. Kaye, "An Investigation into the Relative Efficiency of Different Sampling Procedures," *Powder Metall.* 9, 213-34 (1962).

5. J. R. P. Clarke, "Sampling for On-Line Analysis," *Measurement and Control* 3, 241-4 (1970).

6. T. A. Hatton, "Representative Sampling of Particles with a Spinning Riffler. Stochastic Model," *Powder Technol.* 19, 227-33 (1978).

7. R. Charlier and P. J. D. Goossens, "Sampling a Heterogeneous Powder Using a Spinning Riffler," *Powder Technol.* 4, 351-59 (1970/71).

8. W. J. Dixon, ed., *BMDP Statistical Software*, University of California Press, Berkeley, 1981.

9. A. A. Afifi and S. P. Azen, *Statistical Analysis, A Computer Oriented Approach*, Second Edition, Academic Press, New York, 1979.

IEA Annex II Specimens and Support

V. J. Tennery (Oak Ridge National Laboratory)

Objective/scope

The IEA Annex II agreement between the United States, the Federal Republic of Germany, and Sweden concerning structural ceramics for advanced heat engines and other conservation applications was recently signed by all three countries. This agreement includes four subtasks: (1) information exchange, (2) ceramic powder characterization, (3) ceramic chemistry and structural characterization, and (4) ceramic mechanical property characterization. Each country has agreed to provide selected ceramic powders and sintered structural ceramics for study in all three participating countries. Participating laboratories in all three countries have agreed to share all resulting data with the intent of using the knowledge gained for the purpose of evolving standard measurement methods for characterizing ceramic powders and sintered structural ceramics.

The lack of such standard measurement methods has severly hampered the evolution and development of structural ceramics, and this new Annex II agreement will greatly accelerate the development of standard methods for determining important properties of these materials.

In the United States, many companies and their research laboratories have agreed to contribute significant resources in performing the required measurements. For example, in Subtask 2, a total of twelve laboratories are participating. In Subtask 3, a total of seven laboratories are participating, and for Subtask 4, a total of eight laboratories are participating.

For Subtask 2, a total of five ceramic powders are being studied in the initial phase of this work. For Subtasks 3 and 4, three sintered ceramics are being studied, including one from each of the three countries. The ceramic from the United States is a silicon nitride, SNW-1000 from GTE-Wesgo, that from Germany is a hipped SiC from ESK Kempton, and that from Sweden is a silicon nitride from Asea Cerama.

Technical progress

As a result of several meetings of representatives of the three countries over the past two years, it has been agreed that the ceramic powders to be studied in Subtask 2 will be provided by the United States and these will be distributed by the National Bureau of Standards. The first of these powders is scheduled to be distributed to the participating laboratories in October 1986. The sintered ceramics required for Subtasks 3 and 4 are in the form of machined flexure bars. The ESK SiC bars to be studied in the United States are anticipated to be shipped to the Oak Ridge National Laboratory by the end of August 1986. The requisite number of bars will then be reshipped to the participating U.S. laboratories. An indication from Sweden as to the anticipated shipping date for the Asea Cerama silicon nitride bars is expected by September 1986. ORNL is responsible for purchasing the GTE-Wesgo SNW-1000 bars and distributing them to all participants in Subtasks 3 and 4. In addition, ORNL (with assistance from Professor M. K. Ferber of the University of Illinois) is distributing a template written for LOTUS 1-2-3 for data

entry and statistical analysis of fracture strength data required in Subtask 4. This template has been prepared and will be distributed to all participants by the end of August 1986. In ddition, ORNL is responsible for providing metric four-point flexure fixtures on a loan basis to all U.S. participants who request them. These fixtures have been fabricated and will be distributed following certification testing during the latter part of August. The specimens to be utilized for this certification are of alumina and are being provided by NASA-Lewis Research Center, as this laboratory is also using this material to certify fixtures to be used at NASA-Lewis prior to fracturing specimens of nitride and carbide from the three countries.

The status of the SNW-1000 silicon nitride bars from GTE-Wesgo follows. The purchase order was placed on August 12, 1985, with a requirement that a total of 2875 bars be delivered to ORNL by January 1986. In January, ORNL was informed that a powder batch compositional error had occurred at Wesgo and that a delay in bar delivery was anticipated which may delay delivery until May 1986. In early June, ORNL was informed that the bars may be delayed until July. From the beginning of July until the present, Wesgo has been unsuccessful in sintering a "thick" billet of SNW-1000 which has the required Weibull modulus of 19–20 with a flexure strength of >100 ksi. A series of processing studies are now underway to identify the critical variables which have prevented achievement of the required properties, and it is anticipated that these problems will be resolved by the end of August. If this is done successfully, the silicon nitride bars will be distributed by ORNL in the first quarter of calendar year 1987, following ultrasonic and radiographic NDE characterization.

Status of Milestones

On schedule.

Publications

None

References

None

ORNL/TM-10079

INTERNAL DISTRIBUTION

1–2. Central Research Library
3. Document Reference Section
4–5. Laboratory Records Department
6. Laboratory Records, ORNL RC
7. ORNL Patent Section
8. S. Baik
9. P. F. Becher
10. J. Bentley
11. T. M. Besmann
12. A. Bleier
13. E. E. Bloom
14. K. W. Boling
15. W. D. Bond
16. R. A. Bradley
17. C. R. Brinkman
18. V. R. Bullington
19. A. J. Caputo
20. R. S. Carlsmith
21. P. T. Carlson
22. J. A. Carpenter, Jr.
23. J. V. Cathcart
24. R. H. Cooper
25. S. A. David
26. J. H. DeVan
27. W. P. Eatherly
28. J. I. Federer
29. W. Fulkerson
30. R. L. Graves
31. D. L. Greene
32. M. A. Janney
33–37. D. R. Johnson
38. R. R. Judkins
39. M. A. Karnitz
40. M. P. Kertesz
41. T. B. Lindemer
42. K. C. Liu
43. E. L. Long, Jr.
44. R. W. McClung
45. D. L. McElroy
46. A. J. Moorhead
47. J. L. Rich
48. C. R. Richmond
49. J M Robbins
50. M. W. Rosenthal
51–75. A. C. Schaffhauser
76. J. H. Schneibel
77. J. L. Scott
78. G. M. Slaughter
79. E. J. Soderstrom
80. D. P. Stinton
81. R. W. Swindeman
82. V. J. Tennery
83–85. P. T. Thornton
86. T. N. Tiegs
87. J. R. Weir, Jr.
88. F. W. Wiffen
89. C. S. Yust
90. A. Zucker

EXTERNAL DISTRIBUTION

91. Donald F. Adams
Composite Mat'ls. Research Group
Mechanical Engineering Dept.
University of Wyoming
Laramie, WY 82071

92. Jane W. Adams
Corning Glass Works
SP-DV-21
Corning, NY 14831

93. Richard T. Alpaugh
U.S. Department of Energy
Office of Transportation Systems
Forrestal Building CE-151
1000 Independence Avenue
Washington, DC 20585

94. H. Arbabi
Brunel University
Department of Materials Technology
Uxbridge Middlesex UB8 3PH
United Kingdom

95. James P. Arnold
U.S. Army Belvoir
R&D Center
ATTN: FTRBE-EMP
Fort Belvoir, VA 22060

96. V. S. Avva
North Carolina Agricultural and Technical State University
Department of Mechanical Engineering
Greensboro, NC 27411

97. John M. Bailey
Research Consultant
Research Department
Technical Center
Caterpillar Tractor Company
100 NE Adams
Peoria, IL 61629

98. Murray Bailey
NASA Lewis Research Center
21000 Brookpark Road, MS 77-6
Cleveland, OH 44135

99. R. R. Baker
34819 Lyndon Street
Livonia, MI 48154

100. J. Gary Baldoni
GTE Laboratories, Inc.
40 Sylvan Road
Waltham, MA 02254

101. Ken Baumert
Air Products and Chemicals, Inc.
Box 538
Allentown, PA 18105

102. Ronald L. Beatty
ARCO Chemicals, Silag Operation
Route 6, Box A
Greer, SC 29651

103. A. L. Bement, Jr., Vice President
Technical Resources
TRW, Inc.
23555 Euclid Avenue
Cleveland, OH 44117

104. M. Bentele
Xamag, Inc.
259 Melville Avenue
Fairfield, CT 06430

105. Clifton G. Bergeron
Head
Department of Ceramic Engineering
University of Illinois
204 Ceramics Building
Urbana, IL 61801

106. William D. Bjorndahl
TRW, Inc.
TRW Energy Development Group Group
Materials Characterization and Chemical Analysis Dept.
One Space Park
Building 01, Room 2060
Redondo Beach, CA 90278

107. James A. Black
Vice President
American Matrix, Inc.
118 Sherlake Drive
Knoxville, TN 37922

108. Paul N. Blumberg
President
Integral Technologies Inc.
415 E. Plaza Drive
Westmont, IL 60559

109. Wolfgang D. G. Boecker
Standard Oil Engineered Materials Company
Niagara Falls R&D Center
PO Box 832
Niagara Falls, NY 14302

110. Seymour A. Bortz
Manager
Nonmetallic Materials and Composites
Materials and Manufacturing Division
IIT Research Institute
10 West 35th Street
Chicago, IL 60616

111. H. K. Bowen
Department of Materials Science and Engineering, Room 12-009
Massachusetts Institute of Technology
Cambridge, MA 02139

112. Richard C. Bradt, Chairman
Materials Science and Engrg.
University of Washington
Dept. of Materials Science and Engineering
Roberts Hall, FB-10
Seattle, WA 98195

113. Raymond J. Bratton
Manager, Ceramic Science
Westinghouse Electric Corporation
R&D Center
1310 Beulah Road
Pittsburgh, PA 15235

114. Catherine E. Brown
E. I. DuPont de Nemours & Company
Experimental Station
Information Center E302/301
Wilmington, DE 19898

115. W. Bryzik
U.S. Army Tank Automotive Command
R&D Center
Propulsion Systems Division
Warren, MI 48090

116. S. T. Buljan
GTE Laboratories, Inc.
40 Sylvan Road
Waltham, MA 02254

117. John M. Byrne, Jr.
Manager, Business Development
Corporate Development Dept.
PPG Industries, Inc.
One PPG Place
Pittsburgh, PA 15272

118. Donald J. Campbell
Air Force Wright Aeronautical Laboratory
AFWAL/POX
Wright-Patterson AFB, OH 45433

119. Harry W. Carpenter
Rockwell International
Rocketdyne Division
J39-169-FB39
6633 Canoga Avenue
Canoga Park, CA 91304

120. David Carruthers
Garrett Turbine Engine Co.
111 South 34 Street
PO Box 5217
Phoenix, AZ 85010

121. Se-Tak Chang
GTE Laboratories
40 Sylvan Road
Dept. 312
Waltham, MA 02254

122. R. J. Charles, Manager
Ceramics Branch
Physical Chemistry Laboratory
General Electric Company
PO Box 8
Schenectady, NY 12301

123. En-sheng Chen
B&C Engineering Research
13906 Dentwood Drive
Houston, TX 77014

124. Albert A. Chesnes, Director
Heat Engine Propulsion Division
Office of Transportation Systems
U.S. Department of Energy
Forrestal Building CE-151
1000 Independence Avenue
Washington, DC 20585

125. Gilbert Y. Chin
Bell Telephone Laboratories
Research & Development
Murray Hill, NJ 07974

126. Melvin H. Chiogioji
Director
Office of Transportation Systems
U.S. Department of Energy
Forrestal Building CE-15
1000 Independence Avenue, SW
Washington, DC 20585

127. William J. Chmura
The Torrington Company
Corporate Research
59 Field Street
Torrington, CT 06790

128. William L. Cleary
Associate Division Director
ORI, Inc.
1375 Piccard Drive
Rockville, MD 20850

129. Jack L. Clem
General Manager
Carbon Black Division
Huber Technology Group
J. M. Huber Corporation
P.O. Box 2831
Borger, TX 79008-2831

130. Philip R. Compton
Energy Systems Office
National Aeronautics and
Space Administration
Code REC-1
Washington, DC 20546

131. Harry E. Cook
Director, Automotive Research
and Technical Planning
Chrysler Corporation
PO Box 857, CIMS: 414-01-22
Detroit, MI 48288

132. Stephen Copley
Professor and Chairman
Materials Science Department
University of Southern
California
Los Angeles, CA 90089-0241

133. John A. Coppola
Representative Director
Executive Vice President
Hitachi-Carborundum Company
Shinjuku-Mitsui Building
No. 1-1, 2-Chome,
Nishishinjuku
Shinjuku-ku, Tokyo 160
Japan

134. William J. Croft
U.S. Army Materials
Technology Laboratory
Arsenal Street
Watertown, MA 02172

135. Gary M. Crosbie
Ford Motor Company
PO Box 2053, Room S-2079
Ceramics Materials Department
Dearborn, MI 48121

136. Floyd W. Crouse, Jr.
U.S. Department of Energy
Morgantown Energy Technology
Center
PO Box 880
Morgantown, WV 26505

137. Raymond Cutler
Ceramatec, Inc.
163 W. 1700 South
Salt Lake City, UT 84115

138. Stanley J. Dapkunas
Ceramic Division
Institute for Material Science
and Engineering
National Bureau of Standards
Gaithersburg, MD 20899

139. Robert F. Davis
North Carolina State University
Materials Engineering
Department
232 Riddick Laboratory
Raleigh, NC 27607

140. Alan L. Dragoo
Materials Scientist, Inorganic
Materials Division
National Bureau of Standards
Center for Materials Science
Gaithersburg, MD 20899

141. Keith F. Dufrane
Battelle Columbus Laboratories
505 King Avenue
Columbus, OH 43201

142. Robert J. Eagan, Manager
Chemistry and Ceramics
Department 1840
Sandia National Laboratories
Albuquerque, NM 87185

143. Christopher A. Ebel
Program Manager
High Performance Ceramics
Norton Company
High Performance Ceramics
Goddard Road
Northboro, MA 01532-1545

144. J. J. Eberhardt
Office of Energy Utilization
Research
U.S. Department of Energy
Forrestal Building CE-12
1000 Independence Avenue
Washington, DC 20585

145. E. E. Ecklund
Office of Transportation
Systems
U.S. Department of Energy
Forrestal Building CE-151
1000 Independence Avenue
Washington, DC 20585

146. William A. Ellingson
Argonne National Laboratory
9700 South Cass Avenue
Argonne, IL 60439

147. Director
Applied Technology Laboratory
U.S. Army Research and
Technology Laboratory
(AVSCOM)
ATTN: SAVDL-ATL-ATP
(Mr. Graydon A. Elliott)
Fort Eustis, VA 23604

148. A. Erdely
Chemical Engineer
26 Av. Gare des Eaux-vives
1208 Geneva
Switzerland

149. Charles D. Estes
U.S. Senate
Professional Staff Member
Committee on Appropriations
SD-152 Dirksen Senate Office
Building
Washington, DC 20510

150. Anthony G. Evans
University of California
Santa Barbara, CA 93106

151. Robert C. Evans
Asst. Manager, Vehicular Gas
Turbine and Diesel Project
Office
NASA Lewis Research Center
21000 Brookpark Road
Cleveland, OH 44135

152. Katherine T. Faber
Assistant Professor
of Ceramic Engineering
Ohio State University
2041 College Road
Columbus, OH 43210

153. John Facey
National Aeronautics and
Space Administration
Energy Systems Office
Washington, DC 20546

154. John W. Fairbanks
Office of Transportation
Systems
U.S. Department of Energy
Forrestal Building CE-151
Washington, DC 20585

155. Larry Farrell
Babcock and Wilcox
PO Box 1260
Lynchburg, VA 24505

156. M. K. Ferber
University of Illinois
105 S. Goodwin Avenue
203 Ceramic Building
Urbana, IL 61801

157. R. E. Fisher
President
Amercom, Inc.
8948 Fullbright Avenue
Chatsworth, CA 91311

158. H. W. Foglesong
Dow Corning Corporation
3901 S. Saginaw Road
Midland, MI 48640

159. Thomas F. Foltz
Manager, Product Applications
Avco
Special Materials Division
Two Industrial Avenue
Lowell, MA 01851

160. Robert G. Frank, Manager
Non-Metallic Materials
General Electric Company
One Neumann Way
Mail Drop M-87
PO Box 156301
Cincinnati, OH 45215-6301

161. Frank Gac
Department of Materials Science
and Engineering
University of Washington
Seattle, WA 98195

162. George E. Gazza
U.S. Army Materials
Technology Laboratory
Arsenal Street
Watertown, MA 02172

163. Charles M. Gilmore
Department of Civil, Mechanical,
and Environmental Engineering
The George Washington University
Washington, DC 20052

164. Paul Glance
Director, R&D
Concept Analysis Corporation
9145 General Court
Plymouth, MI 48170

165. Joseph W. Glatz
Naval Air Propulsion Test
Center
Science and Technology Group
Systems Technology Division
Box 7176, PE 34
Trenton, NJ 08628

166. Stephen T. Gonczy
Allied Signal Research Center
Materials Science Department
50 UOP Plaza
Des Plaines, IL 60016-6187

167. Robert J. Gottschall
Office of Material Sciences
U.S. Department of Energy
ER-131 GTN
Washington, DC 20545

168. Kenneth Green
Senior Development Engineer
Coors Porcelain Company
17750 N. 32 Street
Golden, CO 80401

169. Michael Greenfield
National Aeronautics and
Space Administration
Energy Systems Office
Washington, DC 20546

170. Lance E. Groseclose
General Motors Corporation
Allison Gas Turbine Division
PO Box 420
Indianapolis, IN 46206-0420

171. T. D. Gulden, Manager
Ceramics and Chemistry
GA Technologies, Inc.
PO Box 81608
San Diego, CA 92138

172. M. D. Gurney
NIPER
PO Box 2128
Bartlesville, OK 74005

173. J. J. Habeeb, Senior Chemist
Research Division
Esso Petroleum Canada
PO Box 3022
Sarina, Ontario
Canada N7T 7M1

174. H. T. Hahn
Department of Mechanical Engineering
Washington University at St. Louis
Lindell and Skinker
Box 1087
St. Louis, MO 63130

175. Nabil S. Hakim
Staff Research Engineer
Engineering R&D
General Motors Corporation
Detroit Diesel Allison Division
36880 Ecorse Road
Romulus, MI 48174

176. John W. Halloran
Ceramic Process Systems
128 Spring Street
Lexington, MA 02173

177. John M. Halstead
Manager, Business Development
Structural Ceramics Division
Standard Oil Engineered Materials Company
1625 Buffalo Avenue
Bldg. 91-2
PO Box 1054
Niagara Falls, NY 14302

178. R. A. Harmon
25 Schalren Drive
Latham, NY 12110

179. Stephen D. Hartline
Norton Company
High Performance Ceramics
Goddard Road
Northboro, MA 01532-1545

180. Willard E. Hauth
Section Manager
Composite Development Ceramics Program
Dow Corning Corporation
Midland, MI 48640

181. Norman L. Hecht
University of Dayton Research Institute
300 College Park
Dayton, OH 45469-0001

182. S. S. Hecker
Deputy Division Leader
Material Science and Technology Division, G-756
Los Alamos National Laboratory
PO Box 1663
Los Alamos, NM 87545

183. Peter W. Heitman
General Motors Corporation
Allison Gas Turbine Operations
PO Box 420, W-5
Indianapolis, IN 46206-0420

184. H. E. Helms
General Motors Corporation
Allison Gas Turbine Operations
PO Box 420
Indianapolis, IN 46206-0420

185. Thomas L. Henson
Director of Research and Engineering
Chemical & Metallurgical Division
GTE Products Corporation
Hawes Street
Towanda, PA 18848-0504

186. Thomas P. Herbell
NASA Lewis Research Center
21000 Brookpark Road
MS 105-1
Cleveland, OH 44135

187. Ben Heshmatpour
Thermo Electron Corporation
101 First Avenue
Waltham, MA 02154

188. Hendrik Heystek
Bureau of Mines
Tuscaloosa Research Center
PO Box L
University, AL 35486

189. Robert V. Hillery
Manager
Coating Materials and Processes
General Electric Company
Cincinnati, OH 45215

190. Jonathan W. Hinton
Vice President and
General Manager
Structural Ceramics Division
Standard Oil Engineered
Materials Company
PO Box 1054
Niagara Falls, NY 14302

191. Stephen M. Hsu
Chief, Ceramics Division
Institute for Materials Science
and Engineering
National Bureau of Standards
Gaithersburg, MD 20899

192. Harold A. Huckins, President
Princeton Advanced
Technology, Inc.
56 Finley Road
Princeton, NJ 08540

193. Joseph E. Hunter, Jr.
General Motors Corporation
Research Labs
Metallurgy Department
12 Mile and Mound Roads
Warren, MI 48090-9055

194. Louis C. Ianniello
Director
Office of Materials Sciences
U.S. Department of Energy
ER-13 GTN
Washington, DC 20545

195. Curt A. Johnson
General Electric Company
PO Box 8, Ceramics Branch
Schenectady, NY 12301

196. Douglas C. Johnson
Technology Development Manager
Sundstrand Corporation
Turbomach Division
4400 Ruffin Road, PO Box 85757
San Diego, CA 92138-5757

197. Larry Johnson, Director
Center for Transportation
Research
Argonne National Laboratory
9700 S. Cass Avenue
Building 362
Argonne, IL 60439

198. R. A. Johnson
General Motors Corporation
Allison Gas Turbine Division
PO Box 420
Indianapolis, IN 46206-0420

199. L. A. Joo
Associate Director of Research
Great Lakes Research Corp.
PO Box 1031
Elizabethton, TN 37643

200. Roy Kamo, President
Adiabatics, Inc.
630 S. Mapleton
Columbus, IN 47201

201. Allan Katz
Air Force Wright Aeronautical
Laboratory
Materials Laboratory
AFWAL/MLLM
Metals and Ceramics Division
Wright-Patterson AFB, OH 45433

202. R. N. Katz, Chief
Ceramics Research Division
U.S. Army Materials Technology
Laboratory
Arsenal Street
Watertown, MA 02172

203. P. Victor Kelsey
Ceramics Technical Leader
Materials Science Division
Aluminum Company of America
Alcoa Technical Center B
Alcoa Center, PA 15061

204. Frederick L. Kennard, III
Supervisor, Ceramic Research
General Motors Corporation
AC Spark Plug Division
Dept. 32-24
1300 N. Dort Highway
Flint, MI 48556

205. J. R. Kidwell
AGT101 Assistant Project Engineer
Garrett Turbine Engine Company
111 S. 34th Street
PO Box 5217
Phoenix, AZ 85010

206. Max Klein
Senior Scientist
Thermodynamics
Gas Research Institute
8600 West Bryn Mawr Avenue
Chicago, IL 60631

207. C. E. Knapp
Norton Company
8001 Daly Street
Niagara Falls, Ontario
Canada

208. A. S. Kobayashi
University of Washington
Dept. of Mechanical Engineering
MS FU10
Seattle, WA 98195

209. David M. Kotchick
AiResearch Manufacturing Company
2525 W. 190th Street
Torrance, CA 90509

210. Bruce Kramer
George Washington University
Aerodynamic Center, Room T715
Washington, DC 20052

211. Saunders B. Kramer
Manager, AGT Program
Office of Transportation Systems
U.S. Department of Energy
Forrestal Building CE-151
1000 Independence Avenue
Washington, DC 20585

212. D. M. Kreiner
AGT 101 Project Manager
Garrett Turbine Engine Company
111 S. 34th Street, PO Box 5217
Phoenix, AZ 85010

213. Pieter Krijgsman
Ceramic Design Int. Hold., Ltd.
PO Box 68
8050 AB Hattem
The Netherlands

214. W. J. Lackey
Georgia Tech Research Institute
Energy and Materials Sciences Laboratory
Georgia Institute of Technology
Atlanta, GA 30332

215. Everett A. Lake
Air Force Wright Aeronautical Laboratory
AFWAL/POOS
Wright-Patterson AFB, OH 45433

216. Fred F. Lange
Science Center
Rockwell International
1049 Camino Dos Rios
PO Box 1085
Thousand Oaks, CA 91360

217. John G. Lanning
Corning Glass Works
Advanced Engine Components
HP-BB-2
Corning, NY 14830

218. David C. Larsen
Corning Glass Works
Materials Research Department
Sullivan Park, FR-51
Corning, NY 14831

219. Patrick Lauzon
Ontario Research Foundation
Glass and Ceramics Centre
Materials Division
Sheridan Park Research Community
Mississauga, Ontario
Canada L5K 183

220. Alan Lawley
Drexel University
Materials Engineering
Piladelphia, PA 19104

221. Daniel Lee
Temescon
2850 7th Street
Berkeley, CA 94710

222. E. M. Lenoe
Office of Naval Research
Air Force Office of Scientific Research
Liaison Office, Far East
APO San Francisco, CA 96503-0110

223. Stanley R. Levine
NASA Lewis Research Center
21000 Brookpark Road
Cleveland, OH 44135

224. David Lewis
Naval Research Laboratory
Code 6360, Materials Science and Technology Division
4555 Overlook Avenue, SW
Washington, DC 20375

225. Winston W. Liang
Project Manager
Industrial Materials Research
Gas Research Institute
8600 W. Bryn Mawr Avenue
Chicago, IL 60631

226. Bill Long
Babcock and Wilcox
PO Box 1260
Lynchburg, VA 24505

227. L. A. Lott
EG&G, Inc.
Idaho National Engineering Laboratory
PO Box 1625
Idaho Falls, ID 83415

228. Bryan K. Luftglass
Staff Consultant
Chem Systems, Inc.
303 S. Broadway
Tarrytown, NY 10591

229. Michael J. Lynch
General Electric Company
Medical Systems Group
PO Box 414, 7B-36
Milwaukee, WI 53201

230. Tai-il Mah
Technical Manager, Ceramics and Composites Research
Universal Energy Systems
4401 Dayton-Xenia Road
Dayton, OH 45432

231. William R. Martin
General Manager
Ceramic Packaging Business Unit
Cabot Technical Ceramics
87 John L. Dietsch Boulevard
Attleboro, MA 02110

232. John Mason
Vice President, Engineering
The Garrett Corporation
9851 Sepulveda Boulevard
PO Box 92248
Los Angeles, CA 90009

233. K. S. Mazdiyasni
Air Force Wright Aeronautical Laboratory
Materials Laboratory
AFWAL/MLLM
Metals and Ceramics Division
Wright-Patterson AFB, OH 45433-6533

234. J. McCauley
U.S. Army Materials Technology Laboratory
DRXMR-MC
Arsenal Street
Watertown, MA 02172

235. William J. McDonough
U.S. Department of Energy
Office of Transportation Systems
Forrestal Building CE-151
1000 Independence Avenue
Washington, DC 20585

236. Thomas D. McGee
Iowa State University
Department of Materials Science and Engineering
Ames, IA 50011

237. Malcolm G. McLaren
Head, Department of Ceramics
Rutgers University
Busch Campus
Bowser Road, Box 909
Piscataway, NJ 08854

238. Arthur F. McLean
Manager
Ceramics Materials Department
Ford Motor Company
20000 Rotunda Drive
Dearborn, MI 48121

239. Brian L. Mehosky
Development Engineer, R&D
Standard Oil Engineered Materials Company
4440 Warrensville Center Road
Cleveland, OH 44128

240. P. K. Mehrotra
Kennametal, Inc.
PO Box 639
Greensburg, PA 15601

241. Joseph J. Meindl
Reynolds International, Inc.
PO Box 27002
6603 W. Broad Street
Richmond, VA 23261

242. D. Messier
U.S. Army Materials Technology Laboratory
DRXMR-MC
Arsenal Street
Watertown, MA 02172

243. Arthur G. Metcalfe
Director, Research Department
Solar Turbines, Inc.
2200 Pacific Highway,
PO Box 80966
San Diego, CA 92138

244. Thomas N. Meyer
Senior Technical Specialist
Alumina
Chemicals and Ceramics Division
Aluminum Company of America
Alcoa Technical Center
Alcoa Center, PA 15069

245. W. Miloscia
Standard Oil Engineered Materials Company
Research and Development
4440 Warrensville Center Road
Cleveland, OH 44128

246. Bill Moehle
Ethyl Corporation
Ethyl Tower
451 Florida Blvd.
Baton Rouge, LA 70801

247. Helen Moeller
Babcock and Wilcox
PO Box 11165
Lynchburg, VA 24506

248. Peter E. D. Morgan
Member Technical Staff
Structural Ceramics
Rockwell International
Science Center
1049 Camino Dos Rios
PO Box 1085
Thousand Oaks, CA 91360

249. Solomon Musikant
General Electric Company
Space Systems Division
PO Box 8555
Mail Stop U-1219
Philadelphia, PA 19101

250. Pero Nannelli
Pennwalt Corporation
900 First Avenue, PO Box C
King of Prussia, PA 19406-0018

251. Dale E. Niesz
Manager, Materials Department
Battelle Columbus Laboratories
505 King Avenue
Columbus, OH 43201

252. William D. Nix
Stanford University
Department of Materials
Science and Engineering
Stanford, CA 94305

253. Dick Nixdorf
Vice President
American Matrix, Inc.
118 Sherlake Drive
Knoxville, TN 37922

254. W. Richard Ott
New York State College of
Ceramics
Alfred University
Alfred, NY 14802

255. Muktesh Paliwal
GTE Products Corporation
Hawes Street
Towanda, PA 18848

256. Hayne Palmour III
North Carolina State
University
Engineering Research
Services Division
2158 Burlington Engineering
Laboratories
PO Box 5995
Raleigh, NC 27607

257. Joseph N. Panzarino
Norton Company
Director
R&D, High Performance Ceramics
Goddard Road
Northboro, MA 01532-1545

258. Pellegrino Papa, Manager
Technical and Business
Development
Corning Technical Products Div.
Corning Glass Works
Corning, NY 14831

259. James G. Paschal
Reynolds Metals Company
P.O. Box 76154
Atlanta, GA 30358

260. Arvid E. Pasto
Member of Technical Staff
Precision Materials Technology
GTE Laboratories, Inc.
40 Sylvan Road
Waltham, MA 02254

261. James W. Patten
Director, Materials Engineering
Cummins Engine Company, Inc.
Box 3005, Mail Code 50183
Columbus, IN 47202-3005

262. Robert A. Penty
Development Engineer
Manufacturing Technology Dept.
Apparatus Division
Eastman Kodak Company
901 Elmgrove Road
Rochester, NY 14650

263. Dan Petrak
Babcock and Wilcox
PO Box 1260
Lynchburg, VA 24505

264. R. Byron Pipes
University of Delaware
Center for Composite Materials
2001 Spencer Laboratory
Newark, DE 19716

265. Robert C. Pohanka
Office of Naval Research
800 N. Quincy Street, Code 431
Arlington, VA 22217

266. Stephen C. Pred
Product Manager
ICD Group, Inc.
641 Lexington Avenue
New York, NY 10022

267. Karl M. Prewo
United Technologies Corporation
Research Center
Silver Lane, MS 24
East Hartford, CT 06108

268. Hubert B. Probst
Chief Scientist, Materials Div.
MS 49-1
NASA Lewis Research Center
21000 Brookpark Road
Cleveland, OH 44135

269. Carr Lane Quackenbush
Norton Company
High Performance Ceramics
Goddard Road
Northboro, MA 01532-1545

270. George Quinn
U.S. Army Materials Technology Laboratory
Arsenal Street
Watertown, MA 02172

271. Dennis T. Quinto
Kennametal, Inc.
Phillip M. McKenna Laboratory
PO Box 639
Greensburg, PA 15601

272. Dennis Readey
Department Chairman
Ceramic Engineering
Ohio State University
2041 College Road
Columbus, OH 43210

273. Robert R. Reeber
U.S. Army Research Office
PO Box 12211
Research Triangle Park, NC 27709

274. K. L. Reifsnider
Virginia Polytechnic Institute and State University
Department of Engineering Science and Mechanics
Blacksburg, VA 24061

275. Paul Rempes
Champion Spark Plug Company
Ceramic Division
20000 Conner Avenue
Detroit, MI 48234

276. K. T. Rhee
Rutgers University
College of Engineering
PO Box 909
Piscataway, NJ 08854

277. Roy W. Rice
W. R. Grace and Company
7379 Route 32
Columbus, MD 21044

278. David W. Richerson
Ceramatec, Inc.
163 West 1700 South
Salt Lake City, UT 84115

279. Paul Rieth
Ferro Corporation
661 Willet Road
Buffalo, NY 14218

280. Michael A. Rigdon
Babcock and Wilcox
1735 Eye Street, NW
Washington, DC 20006

281. John E. Ritter, Jr.
University of Massachusetts
Mechanical Engineering Dept.
Amherst, MA 01003

282. Giulio A. Rossi
Norton Company
High Performance Ceramics
Goddard Road
Northboro, MA 01532-1545

283. Barry R. Rossing
Aluminum Company of America
Alcoa Technical Center
Alcoa Center, PA 15069

284. David J. Rowcliffe
SRI International
333 Ravenswood Avenue
Menlo Park, CA 94025

285. Donald W. Roy
Manager
Carbide and Optical Material
Research and Development
Coors Porcelain Company
17750 N. 32 Street
Golden, CO 80401

286. Bruce Rubinger
Gobal
50 Milk Street, 15th Floor
Boston, MA 02109

287. Robert Ruh
Air Force Wright Aeronautical
Laboratory
Materials Laboratory
AFWAL/MLLM
Metals and Ceramics Division
Wright-Patterson AFB, OH 45433

288. Robert J. Russell, Sr.
Divisional Vice President
Technology and Planning
High Performance Ceramics
Norton Company
Goddard Street
Northboro, MA 01532-1545

289. George P. Safol
Westinghouse Electric
Corporation
R&D Center
Pittsburgh, PA 15235

290. J. Sankar
North Carolina Agricultural
and Technical State
University
Department of Mechanical
Engineering
Greensboro, NC 27411

291. Maxine Savitz
Assistant to Vice President
Engineering
The Garrett Corporation
PO Box 92248
Los Angeles, CA 90009

292. Richard Schapery
Texas A&M University
Civil Engineering Department
College Station, TX 77843

293. J. L. Schienle
Garrett Turbine Engine
Company
111 S. 34th Street
Phoenix, AZ 85034

294. L. J. Schioler
Aerojet Tech Systems Company
PO Box 13222
Dept. 9990, Bldg. 2001
Sacramento, CA 95813

295. Matthew Schreiner
Gas Research Institute
8600 W. Bryn Mawr Avenue
Chicago, IL 60631

296. John Schuldies
Industrial Ceramic Technology,
Inc.
141 Enterprise Drive
Ann Arbor, MI 48103

297–316. R. B. Schulz
U.S. Department of Energy
Office of Transportation
Systems
Forrestal Building CE-151
1000 Independence Avenue
Washington, DC 20585

317. Wesley J. C. Schuster
President
Thermo Electron Corporation
Metals Division
115 Eames Street, PO Box 340
Wilmington, MA 01887

318. Murray A. Schwartz
Bureau of Mines
2401 Eye Street, NW
Washington, DC 20241

319. Thomas M. Sebestyen
U.S. Army Tank-Automotive Command
AMSTA-RGRT
Warren, MI 48397-5000

320. Brian Seegmiller
Senior Development Engineer
Coors Porcelain Company
17750 North 32 Street
Golden, CO 80401

321. S. G. Seshadri
Research Associate
Standard Oil Engineered Materials Company
Niagara Falls R&D Center
PO Box 832
Niagara Falls, NY 14302

322. Peter T. B. Shaffer
Executive Vice President
Advanced Refractory Technologies, Inc.
699 Hertel Avenue
Buffalo, NY 14207

323. Maurice E. Shank, Director
Engineering Technology Assessment
United Technologies Corp.
Pratt and Whitney Engineering Div.
MS 162-31
East Hartford, CT 06108

324. Laurel M. Sheppard
Associate Editor
Advanced Materials and Processes
Metals Park, OH 44073

325. Dinesh K. Shetty
The University of Utah
Department of Materials Science & Engineering
Salt Lake City, UT 84112

326. Jack D. Sibold
Coors Porcelain Company
17750 North 32 Street
Golden, CO 80401

327. Neal Sigmon
Appropriations Committee
Subcommittee on Interior and Related Events
U.S. House of Representatives
Rayburn Building, Room B308
Washington, DC 20515

328. Richard Silberglitt
DHR, Inc.
6849 Old Dominion Drive
Suite 228
McLean, VA 22101

329. Maurice J. Sinnott
University of Michigan
Chemical and Metallurgical Engineering
438 W. Engineering Building
Ann Arbor, MI 48109

330. S. R. Skaggs
Los Alamos National Laboratory
PO Box 1663
MS F-682, Program Office
Los Alamos, NM 87545

331. Ed Skorupski
Air Products and Chemicals
PO Box 538
Allentown, PA 18105

332. J. Thomas Smith
Director
Precision Materials Tech.
GTE Laboratories, Inc.
40 Sylvan Road
Waltham, MA 02254

333. Jay R. Smyth
Senior Development Specialist
Garrett Turbine Engine Company
PO Box 5217, MS 93-172/1302-2K
Phoenix, AZ 85010

334. Rafal Sobotowski
Standard Oil Engineered Materials Company
Research and Development
3092 Broadway Avenue
Cleveland, OH 44115

335. Boyd W. Sorenson
E. I. DuPont de Nemours & Company
Planning Manager
New Ventures Dept.
Wilmington, DE 19898

336. Richard M. Spriggs
National Materials Advisory Board
National Research Council
2101 Constitution Avenue
Washington, DC 20418

337. M. Srinivasan
Standard Oil Engineered Materials Company
Niagara Falls R&D Center
PO Box 832
Niagara Falls, NY 14302

338. Gordon L. Starr, Manager
Metallic/Ceramic Materials Department
Cummins Engine Company, Inc.
Box 3005, Mail Code 50183
Columbus, IN 47202-3005

339. Harold L. Stocker, Manager
Low Heat Rejection Program
General Motors Corporation
Allison Gas Turbine Operations
PO Box 420, T-23
Indinapolis, IN 46206-0420

340. Roger Storm, Director
Niagara Falls R&D Center
Standard Oil Engineered Materials Company
PO Box 832
Niagara Falls, NY 14302

341. E. E. Strain
Program Manager AGT-101
Garrett Turbine Engine Company
111 S. 34th Street
PO Box 5217, Mail Stop 301-2N
Phoenix, AZ 85010

342. Thomas N. Strom
NASA Lewis Research Center
21000 Brookpark Road, 77-6
Cleveland, OH 44135

343. Karsten Styhr
AiResearch Casting Company
19800 Van Ness Avenue
Torrance, CA 90509

344. Paul Sutor
Midwest Research Institute
425 Volker Blvd.
Kansas City, MO 64116

345. J. J. Swab
U. S. Army Materials Technology Laboratory
Arsenal Street
Watertown, MA 02172

346. Lewis Swank
Ford Motor Company
PO Box 2053
Building SRL, Room E3172
Dearborn, MI 48121

347. Anthony C. Taylor
Staff Director
Subcommittee on Transportation, Aviation, and Materials
Committee on Science and Technology
U.S. House of Representatives
Rayburn Building, Room 2321
Washington, DC 20515

348. W. H. Thielbahr
Chief, Energy Programs Branch
U.S. Department of Energy
Idaho Operations Office
550 2nd Street
Idaho Falls, ID 83401

349. John K. Tien
Director of Center for
Strategic Materials
Columbia University
1137 SW Mudd Building
New York, NY 10027

350. T. Y. Tien
University of Michigan
Materials and Metallurgical
Engineering
Dow Building
Ann Arbor, MI 48109-2136

351. Nancy J. Tighe
National Bureau of Standards
Inorganic Materials
Division 420
Building 223, Room A331
Gaithersburg, MD 20899

352. Julian M. Tishkoff
Air Force Office
of Scientific Research
Directorate of Aerospace Sciences
Bolling AFB
Washington, DC 20332

353. Maurice L. Torti
Senior Scientist
High Performace Ceramics
Norton Company
Goddard Road
Northboro, MA 01532-1545

354. Louis E. Toth
National Science Foundation
Division of Materials Research
1800 G Street, NW
Washington, DC 20550

355. Richard E. Tressler
Chairman, Ceramic Science and
Engineering Department
The Pennsylvania State
University
201 Steidle Building
University Park, PA 16802

356. Donald R. Uhlmann, Professor
Ceramics and Polymers
Department of Materials
Science and Engineering
Massachusetts Institute of
Technology
Cambridge, MA 02139

357. Thomas Vasilos, Manager
Electro Chemical Facility
Avco Corporation
201 Towell Street
Wilmington, MA 01887

358. V. Venkateswaran
Standard Oil Engineered
Materials Company
PO Box 832
Niagara Falls, NY 14302

359. John B. Wachtman, Jr.
Director
Center for Ceramics Research
Rutgers University
PO Box 909
Piscataway, NJ 08854

360. Richard B. Wallace
Manager, Government Research
and Development Programs
General Motors Corporation
Detroit Diesel Allison
Division
36880 Ecorse Road
Romulus, MI 48174

361. Harlan L. Watson
Subcommittee on Energy
Research and Production
U.S. House of Representatives
Committee on Science and
Technology
Rayburn Building, Suite 2321
Washington, DC 20515

362. Steven G. Wax
Department of Defense
Advanced Research Projects
Agency
Materials Science Division
1400 Wilson Boulevard
Arlington, VA 22209

363. Albert R. C. Westwood
Corporate Director, R&D
Martin Marietta Laboratories
1450 South Rolling Road
Baltimore, MD 21227

364. Thomas J. Whalen
Principal Research Scientist
Ford Motor Company
Scientific Lab., Room 2023
Dearborn, MI 48121

365. Sheldon M. Wiederhorn
U.S. Department of Commerce
National Bureau of Standards
Inorganic Materials Division
Mechanical Properties Group
Gaithersburg, MD 20899

366. James C. Williams, Dean
Carnegie Institute of Technology
Carnegie-Mellon University
Schenley Park
Pittsburgh, PA 15213

367. Roger R. Wills, Manager
Advanced Ceramic Components
TRW, Inc.
Automotive Worldwide Sector
Valve Division
Cleveland, OH 44110

368. J. M. Wimmer, Supervisor
Nonmetallic Materials Group
Garrett Turbine Engine Company
111 S. 34th Street
PO Box 5217
Phoenix, AZ 85010

369. David Wirth, Vice-President
Technical Operations &
Engineering
Coors Porcelain Company
17750 North 32 Street
Golden, CO 80401

370. Thomas J. Wissing, Manager
Government Contract
Administration
Eaton Corporation
Engineering & Research Center
26201 Northwestern Highway
PO Box 766
Southfield, MI 48037

371. James C. Wood
NASA Lewis Research Center
21000 Brookpark Road
MS 500-210
Cleveland, OH 44135

372. Hun C. Yeh
Ceramic Supervisor
AiResearch Casting Company
19800 Van Ness Avenue
Torrance, CA 90509

373. Thomas M. Yonushonis
Cummins Engine Company, Inc.
Box 3005, Mail Code 50183
Columbus, IN 47202-3005

374. Don Zabierek
Air Force Wright Aeronautical
Laboratory
AFWAL/POTC
Wright-Patterson AFB, OH 45433

375. Charles Zeh
U.S. Department of Energy
Morgantown Energy Technology
Center
PO Box 880
Morgantown, WV 26505

376. Klaus M. Zwilsky
Executive Director
National Materials Advisory
Board
National Research Council
2101 Constitution Avenue
Washington, DC 20418

377. Department of Energy
Oak Ridge Operations Office
Office of Assistant Manager
for Energy Research and
Development
PO Box E
Oak Ridge, TN 37831

378-
405. Department of Energy
Technical Information Center
Office of Information Services
PO Box 62
Oak Ridge, TN 37831

For distribution by microfiche
as shown in DOE/TIC-4500,
Distribution Category UC-95
(Energy Conservation).